

Removal of organic compounds from aquatic environments by advanced oxidation processes.

MENEZES, I.

2024

The author of this thesis retains the right to be identified as such on any occasion in which content from this thesis is referenced or re-used. The licence under which this thesis is distributed applies to the text and any original images only – re-use of any third-party content must still be cleared with the original copyright holder.

Removal of organic compounds from aquatic environments by advanced oxidation processes

Indira Menezes

PhD

August 2024

Removal of organic compounds from aquatic environments by advanced oxidation processes

Indira Menezes

A thesis submitted in part fulfilment of the requirement of Robert Gordon
University for the degree of Doctor of Philosophy

August 2024

TABLE OF CONTENTS

TITLE PAGE.....	I
TABLE OF CONTENTS	III
DECLARATION	V
DEDICATION	VI
ACKNOWLEDGMENTS	VII
LITS OF ABBREVIATIONS	VIII
ABSTRACT	XII
1 INTRODUCTION	1
1.1 Water pollutants	3
1.2 Conventional water treatment	15
1.3 Advanced oxidation processes	16
1.4 Thesis aim and objectives	19
2 A TALE OF CAUTION: THE EFFECT OF MEDIA NUTRIENTS ON LIGHT- DRIVEN CYANOBACTERIA AND TOXIN REMOVAL	21
2.1 Introduction	23
2.2 Materials and methods	28
2.3 Results and discussion.....	44
2.4 Conclusion	66
3 PREPATION OF TiO₂, g-C₃N₄ AND g-C₃N₄/TiO₂ COATED GLASS BEADS FOR THE PHOTOCATALYTIC DEGRADATION OF A MODEL NATURAL POLLUTANT	67
3.1 Introduction	69
3.2 Materials and methods	80
3.3 Results and discussion.....	91

3.4	Conclusion	105
4	PHOTOCATALYTIC REMOVAL OF PESTICIDES BY g-C₃N₄ COATED BEADS AND UV-A LED IRRADIATION	107
4.1	Introduction	110
4.2	Materials and methods	123
4.3	Results and discussion	133
4.4	Conclusion	169
5	SCALE-UP OF A PHOTOCATALYTIC REACTOR FOR THE DEGRADATION OF PESTICIDES AT SOURCE FROM AQUATIC ENVIRONMENTS	171
5.1	Introduction	173
5.2	Materials and methods	175
5.3	Results and discussion	177
5.4	Conclusion	193
6	CONCLUSIONS AND FUTURE WORK.....	195
6.1	Conclusion and future work	196
7	REFERENCES	199
8	APPENDIX.....	256

DECLARATION

I declare that the work presented in this thesis is my own, except where otherwise acknowledged, and has not been submitted in any form for another degree or qualification at any other academic institution.

Information derived from published or unpublished work of others has been acknowledged in the text and a list of references is given.

Indira Menezes

DEDICATION

Aos meus pais, que foram guias para todos os
caminhos que trilhei.

ACKNOWLEDGEMENTS

I am grateful for the support, guidance and mentorship of my supervisory team, Dr Carlos Pestana, Professor Linda Lawton and Dr Bruce Petrie. I am also grateful to the Hydro Nation Scholar Programme funded by the Scottish Government through the Scottish Funding Council and managed by the Hydro Nation International Centre for funding this research.

I would like to thank the other members of CyanoSol group, Professor Christine Edwards, Dorothy McDonald, Len Montgomery, Jane Moore and Colin Sloan, for all their help and advice. In special, I would like to thank Dr Diana Souza Moura for being a true friend through my entire PhD.

I also would like to thank Dr Jianing Hui and Dr Nikoletta Gkoulemani from the University of St Andrews for the collaboration involving the preparation and characterisation of the coated beads.

I am also grateful for my friends who made my PhD journey a great experience, Nuruddin, Teo, Kam, Alenza, Shubhada, Kai and Katie.

I would like to thank my family for the constant love and support they have given me my entire life, my aunts Roseli, Rosilda, Veridiana, Roziane (*in memorium*) and Juliana, my uncles Antônio, Weuton, Vivica, Clerton and Elder, and my cousins Israel, Rodrigo, William, Lara, Lucas, Gabriela, Marina, Pedro, Wellen, Weuton and Carol.

More importantly, I would like to thank my parents Rozi and Galvan, who gave me the opportunity of becoming the best version I could be, by showing me their unconditional love. I love you more than everything. I would also like to thank my brother Nicolas Castro, for being my best friend no matter what.

Finally, the biggest thank you to my husband Nicolas Miranda, who has always been my biggest supporter and has always been by my side. Everything was possible because I had you. I love you more than yesterday and less than tomorrow.

LIST OF ABBREVIATIONS

λ	Wavelength
2,4-D	2,4-dichlorophenoxyacetic acid
Adda	3-amino-methoxy-10-phenyl-2,6,8-trimethyldeca-4,6-dienoic acid
AFW	Artificial freshwater
AOP	Advanced oxidation process
BMAA	β -N-methylamino-L-alanine
C_0	Initial concentration
C_{Eq}	Concentration at equilibrium
CFL	Compact fluorescent lamps
D-Ala	D-Alanine
D-Glu	D-Glutamate
D-MeAsp	D-Aspartate methyl
DDT	dichlorodiphenyltrichloroethane
DIP	Dual In-Line Package
e^-	Electron
EFSA	European Food Safety Authority
E_g	Band gap
EU	European Union
F_0	Minimal fluorescence

F_M	Maximal fluorescence
F_S	Steady-state fluorescence
F_V	Variable fluorescence
F_M'	True maximal fluorescence
FDA	Food and Drug Administration
g-C ₃ N ₄	Graphitic carbon nitride
h^+	Hole
HID	High intensity discharge
HPLC	High-performance liquid chromatography
$h\nu$	Energy of a photon (input of light)
k	Reaction rate constant
K_{ow}	Partition coefficient
LED	Light emitting diode
<i>M. aeruginosa</i>	<i>Microcystis aeruginosa</i>
MC	Microcystin
Mdha	N-Methyldehydroalanine
MS	Mass spectrometry
NOM	Natural organic matter
PDA	Photodiode array
PET	Polyethylene terephthalate
pKa	Acid dissociation constant

PS	Photosystem
PVDF	Polyvinylidene fluoride
RNS	Reactive nitrogen species
ROS	Reactive oxygen species
RV	Reactor volume
SD	Standard deviation
SRM	Selected reaction monitoring
SMD	Surface Mounted Diode
t	Time
T ₀	Time zero
T _{Eq}	Time at equilibrium
TBT	Tributyltin
TiO ₂	Titanium dioxide
UK	United Kingdom
UNSDG	United Nation Sustainable Development Goals
UPLC	Ultra-performance liquid chromatography
USA	United States of America
USEPA	United States Environmental Protection Agency
UV	Ultraviolet
Vis	Visible light
w/v	Weight/volume

WHO

World Health Organization

ABSTRACT

Agricultural practices and eutrophication contribute to cyanobacteria proliferation, cyanotoxin contamination and pesticide pollution in aquatic environments. Conventional treatments can be ineffective for the removal of high cell densities of cyanobacteria, dissolved toxins and pesticides. Therefore, complementary technologies are required to effectively remove these contaminants at source. The current study aims to apply photolysis and photocatalysis (advanced oxidation processes) as novel technologies for *in-situ* removal of harmful contaminants.

Photoinduced photolysis by UV-A 365 nm LED irradiation was explored during bench-scale experiments for the removal of *Microcystis aeruginosa* cells and microcystins. A common way of verifying the effects of light-driven treatments on cyanobacteria is by performing lab-scale experiments, where cyanobacteria are cultured in growth media. In the current study, six *Microcystis aeruginosa* strains (SCIENTO, NIES 1099, B2666, PCC 7820, 7813 and 7806) in BG-11 medium were exposed for seven days to UV-A (365 nm) irradiation.

Photosynthetic activity significantly decreased after 24 hours of irradiation with samples showing no photosynthetic activity by the end of the experiment. Intra- and extracellular microcystin (MC) concentrations were markedly decreased in UV-A treated samples with a combined microcystin removal of 86%. It was observed, however, that nutrients present in the BG-11 growth medium (e.g., nitrate and iron) enhanced the UV-A photolytic effects on microcystins concentration. Therefore, it is important to consider the media composition for lab-scale experiments focused on cyanobacterial removal to effectively evaluate light-driven strategies for cyanobacteria and toxin removal.

Photocatalysis was explored for the removal of pesticides at source. Bench-scale experiments were performed to demonstrate the effectiveness of graphitic carbon nitride (g-C₃N₄) coated glass beads and UV-A LED irradiation for the removal of a mixture containing nine pesticides (1 mg L⁻¹ each in artificial freshwater; acetamiprid, clothianidin, imidacloprid, thiacloprid, thiamethoxam, diuron, atrazine, dimethoate and 2,4-dichlorophenoxyacetic acid). The photocatalytic system was able to successfully remove a range of pesticides at the same time. Finally, a photocatalytic reactor prototype based on g-C₃N₄ coated beads and UV-A LED irradiation was developed to be applied at source for

pesticide removal from aquatic environments. The reactor could be deployed in different locations, which include storage tanks with residual pesticides, ponds, drainage systems, farmyards and other aquatic environments around farms to treat water contaminated with pesticides.

Both treatments based on photolysis and photocatalysis have the potential to be novel, long-lasting, environmentally safe, economical, modular and flexible approaches for the removal of contaminants at source from aquatic environments.

Chapter 1

Introduction

1	INTRODUCTION	1
1.1	Water pollutants	3
1.1.1	Cyanobacteria.....	4
1.1.2	Cyanotoxins	7
1.1.3	Pesticides.....	13
1.2	Conventional water treatment	15
1.3	Advanced oxidation processes	16
1.4	Thesis aim and objectives	19

1.1 Water pollutants

Water is an essential resource to life. Around 55% to 75% of the human body consists of water (Nicolaidis 1998). The water present in the body is responsible for a series of activities, such as regulating body temperature, preventing infections, delivering nutrients to cells and keeping organs functioning properly (Drayer 2017). In 2015, the United Nation established 17 Sustainable Development Goals (UNSDG) to improve the world. One of the proposed measures guarantees safe drinking water for all (goal number 6) (United Nations 2015), however, only 0.5% of the total water on Earth is available for human consumption in the form of aquifers, lakes, reservoirs, rivers, streams and rainfall (Baker, Aldridge and Omer 2016). Furthermore, the contamination of these aquatic environments by various pollutants increases issues related with availability of safe drinking water (Table 1.1).

Table 1.1: Types of pollutants responsible for water contamination.

Type of water pollutant	Definition	Examples	Reference
Organic	Contaminants containing carbon covalently bonded with other compounds in their chemical structure	Personal care products, pharmaceuticals, detergents and disinfection products	(Obinna and Ebere 2019)
Inorganic	Heavy metals are the main constituents of inorganic pollutants (metals with high density of at least 5 g cm ⁻³)	Arsenic, copper, cadmium, lead, chromium, nickel, mercury, zinc, cobalt, manganese, iron and vanadium	(Obinna and Ebere 2019; Borah, Kumar and Devi 2020)
Radioactive	Contain radioactive material that are usually emitted from nuclear power plants, nuclear weapons and application of radioactive material	Uranium, thorium and aluminium	(Singh et al. 2020; Speight 2020)
Suspended solids	Generated by improper disposal of materials or by the disruption of soil sediments	Solid waste, sand and plastics	(Speight 2020; Lin, Yang and Xu 2022)
Pathogens	Organisms that can cause diseases through water contamination	Bacteria, viruses, protozoa and helminths	(Toze 1999)
Thermal	Release of heat that results in alteration of the natural water temperature	Electric power plants, cooling towers used in industry	(Speight 2020)
Nutrients	Compounds rich in nutrients, for example, phosphorus and nitrogen	Fertilizers and pesticides	(Speight 2020)

The use of pesticides in agricultural practices leads to the introduction of nutrients and contamination of the environment. Nutrient enrichment in aquatic environments by nitrogen and phosphorus can contribute to eutrophication. Aquatic environments can be classified in different trophic status based on the nutrients as oligotrophic (phosphorus concentration $< 12 \mu\text{g L}^{-1}$), mesotrophic (phosphorus concentration $12 - 24 \mu\text{g L}^{-1}$), eutrophic (phosphorus concentration $24 - 96 \mu\text{g L}^{-1}$) or hypereutrophic (phosphorus concentration $> 96 \mu\text{g L}^{-1}$) (Beiras 2018).

The eutrophication of lakes, reservoirs, rivers and coastal oceans can lead to several potential negative effects. The increase in nutrients can promote the excessive growth (blooms) of phytoplankton (e.g., cyanobacteria and microalgae), algae and macrophytes (Dokulil and Teubner 2011), which can interfere in recreational activities such as boating services and swimming (Dodds et al. 2009), along with unacceptable odors from rotting biomass. Cyanobacteria tend to dominate phytoplankton communities in eutrophic waters (Wang et al. 2021b). Some cyanobacteria can produce toxic compounds, known as cyanotoxins, which can be harmful to both human and animal health (Dodds et al. 2009). Further, taste and odor compounds can also be released into the environment by cyanobacteria. The presence of these compounds can cause economic issues, especially when they are present in drinking water reservoirs, because of the potential increase in water treatment costs and a possible consumer refuse (Dodds et al. 2009). The subsequent death and decomposition of blooms leads to a rapid decline in dissolved oxygen. The low levels of oxygen can result in the death of fish and other aquatic animals, which could ultimately decrease species diversity (Yang et al. 2008). Therefore, commonly reported contaminants in aquatic environments are pesticides, cyanobacteria and their associated toxins.

1.1.1 Cyanobacteria

Climate change and eutrophication intensify the proliferation of cyanobacteria, also known as blue-green algae, due to temperature rise and the input of nutrients (e.g., nitrogen and phosphorus) in water bodies (Paerl and Otten 2013). Cyanobacteria first appearance was around 2.8 to 3.5 billion years ago (Adams 1997) and their presence persist until today. These organisms can occur in terrestrial environments such as soil, deserts and glaciers or they can be found

in symbiotic system with plants and animals (Paerl 1996; Van Den Hoek, Mann D.G. and Jahns 1997). They can be also found in any aquatic ecosystem, such as freshwater, estuarine and marine, even in extreme conditions of salinity, pH and temperatures (Varshney et al. 2015). Cyanobacteria are photosynthetic organisms that include about 2000 species in 150 genera that are morphologically and physiologically diverse. Cyanobacteria morphology can present with unicellular form, with spherical, ovoid or cylindrical cells; colonial, which are aggregated unicellular cells, or filamentous, formed of a chain of cells also known as trichome (WHO 1999).

In aquatic environments, cyanobacteria are important primary producers and are part of the phytoplankton community (Sivonen 2009), however, high densities of cyanobacterial cells can result in harmful algal blooms. During bloom events, cyanobacteria outcompete other phytoplanktonic species (e.g., green algae, diatoms and dinoflagellates) and become dominant. Environmental conditions such as temperature, pH and availability of nutrients in aquatic environments are favorable to the presence of cyanobacteria (Mur, Skulberg and Utkilen 1999; Oliver et al. 2012). Cyanobacterial blooms typically present green colour in the water body (Figure 1.1).

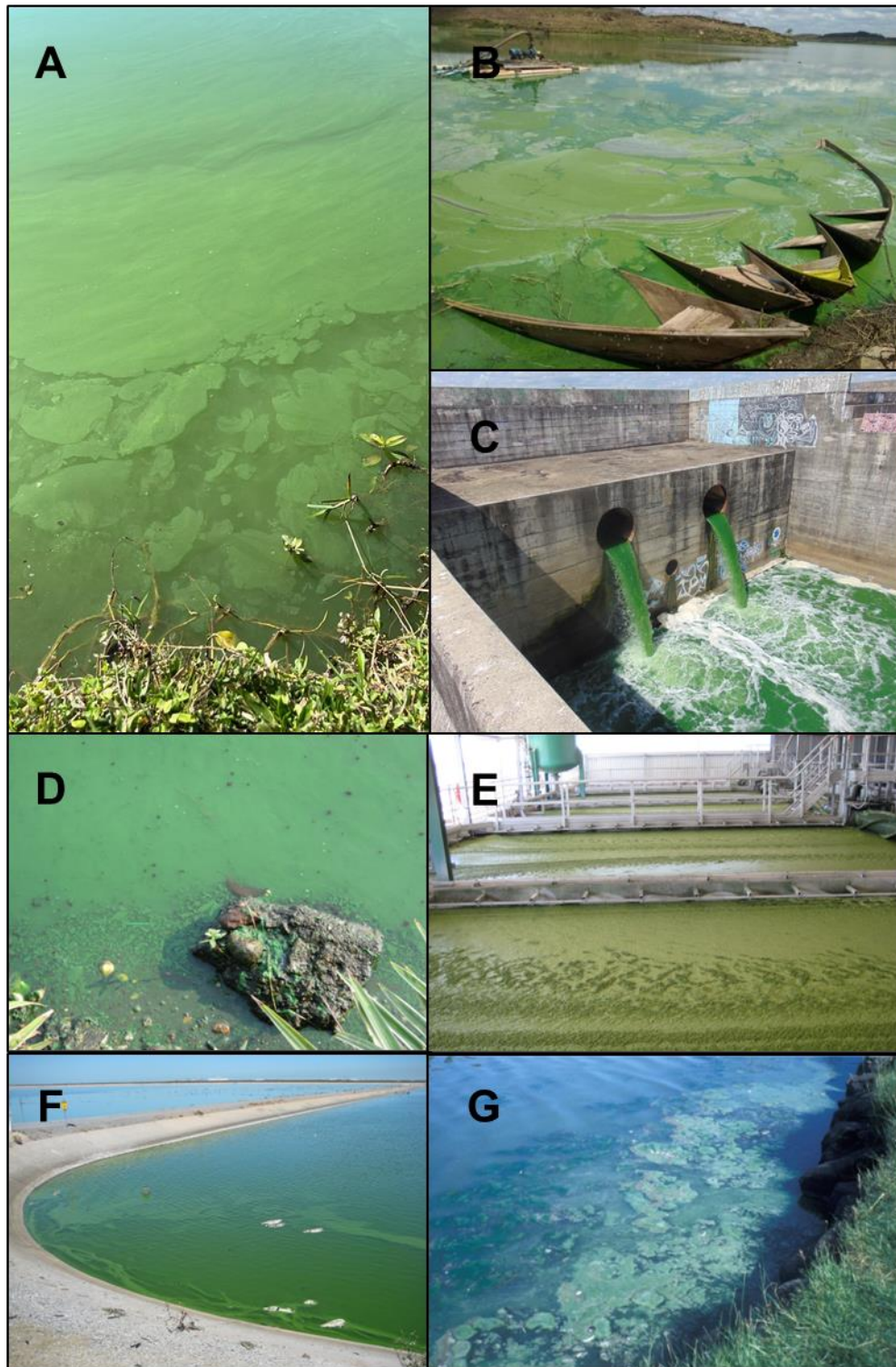


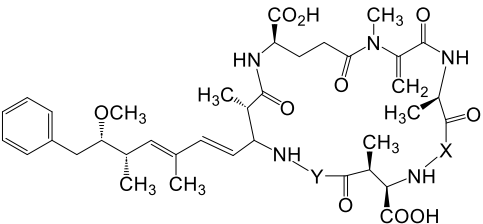
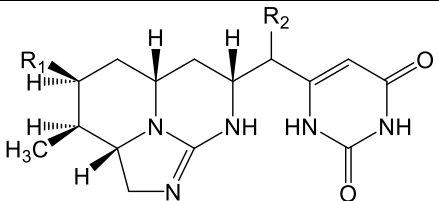
Figure 1.1: Cyanobacterial blooms typical green coloration in A) Barigui Park, Curitiba, South Brazil (copyright I. Carloto), B) Maranguapinho Reservoir, Maranguapinho, Northeastern Brazil (copyright M. Barros), C) Cocó River Dam, Fortaleza, Northeastern Brazil (copyright M. Barros), D) Beira Lake, Sri Lanka (copyright L. Lawton), E) Morgan Water Treatment Plant, South Australia (copyright C. Pestana), F) Myponga Reservoir, South Australia (copyright C. Pestana) and G) Holyrood Park, Edinburgh, United Kingdom (copyright L. Lawton). All used with permission.

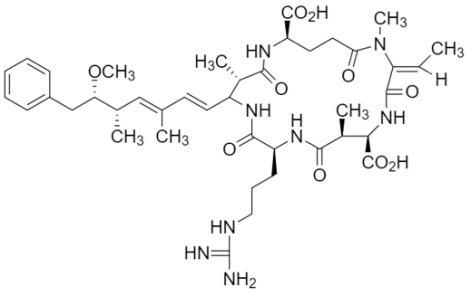
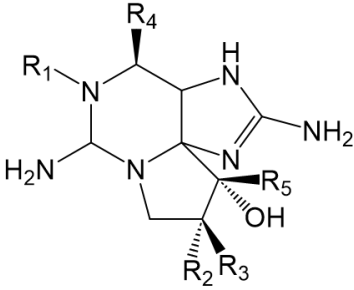
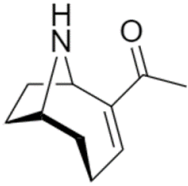
Cyanobacterial blooms can represent a challenge to water treatment when there is excessive cyanobacterial growth in the raw water, which can increase the costs of water treatment due to the increased use of treatment chemicals used during water purification, such as coagulants, disinfectants or algicides, or by reducing filter run times (De Julio et al. 2010; Pinkanjananavee et al. 2021; Jalili et al. 2022). After blooms collapse, a high amount of cyanobacterial biomass dies and decomposes, which then consumes a large amount of oxygen and reduces the dissolved oxygen in the water, causing the death of fish and other aquatic fauna (Zhang et al. 2022). Other socioeconomical impacts are also associated with cyanobacterial blooms, for example, there is normally a reduction in business associated with tourism in reservoir or lake areas contaminated by cyanobacteria, as well as a reduction in property values, causing heavy revenue losses (Cheung, Liang and Lee 2013; Carmichael and Boyer 2016). Cyanobacteria can produce taste and odor compound, such as geosmin and 2-methylisoborneol (MIB), which are two of the most reported taste and odor compounds that cause unpleasant earthy and muddy taste in drinking water. These compounds are not toxic, however, they can result in rejection of water or complaints by consumers due this strong smell and flavor (Suffet, Khiari and Bruchet 1999; Suurnäkki et al. 2015; Abd El-Hack et al. 2022). The other metabolites of concern are cyanotoxins, which are harmful to both animal and human health (Welker and Steinberg 1999; Heresztyn and Nicholson 2001; Liu et al. 2010; Merel et al. 2013; Yang et al. 2015; Machado et al. 2017).

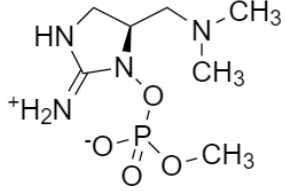
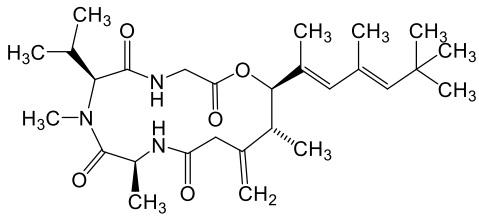
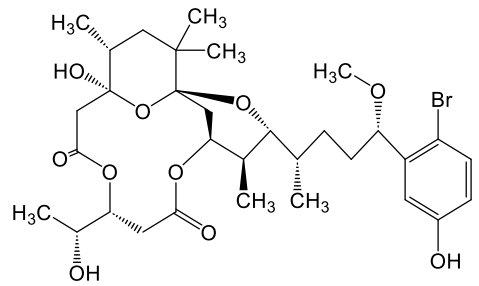
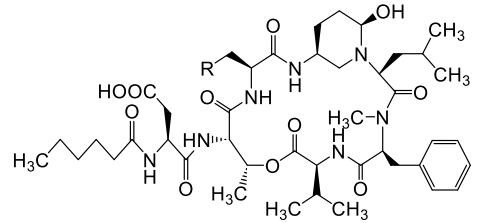
1.1.2 Cyanotoxins

The reason why cyanobacteria produce toxins has not been fully elucidated yet, however, possible reasons could be cellular signalling, defence mechanisms and ecological advantages over other organisms (Lawton and Edwards 2001; Kaebernick and Neilan 2006; Berry 2008; Rastogi, Madamwar and Incharoensakdi 2015). There is wide range of cyanotoxins with differing biological effects (Table 1.2).

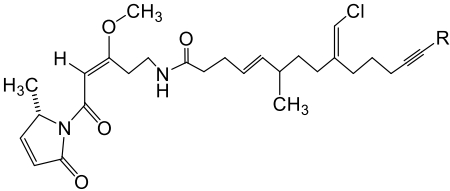
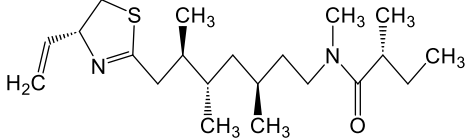
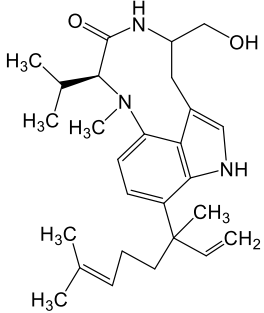
Table 1.2: Cyanotoxins produced by cyanobacteria, their main toxicity and reported cyanobacteria genera containing strains that are toxin producers.

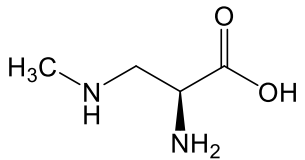
Cyanotoxin	Molecular structure	Toxicity	Producing cyanobacteria genera	Reference
Microcystin	 <p style="text-align: center;">*</p>	Hepatotoxic through inhibition of PP1 and PP2A protein phosphatases, tumor-promoted	<i>Microcystis</i> , <i>Dolichospermum</i> , <i>Planktothrix</i> , <i>Nostoc</i> , <i>Anabaenopsis</i> , <i>Aphanocapsa</i> , <i>Aphanizomenon</i> , <i>Arthrospira</i> , <i>Cyanobium</i> , <i>Hapalosiphon</i> , <i>Phormidium</i> , <i>Fischerella</i> , <i>Limnothrix</i> , <i>Lyngbya</i> , <i>Raphidiopsis</i> , <i>Rivularia</i> , <i>Synechocystis</i> and <i>Synechococcus</i>	(MacKintosh et al. 1990; Christiansen et al. 2003; Sivonen 2009; Rastogi, Madamwar and Incharoensakdi 2015; Beasley 2020)
Cylindrospermopsin	 <p style="text-align: center;">**</p>	Inhibitor of protein synthesis	<i>Raphidiopsis</i> , <i>Aphanizomenon</i> , <i>Dolichospermum</i> , <i>Umezakia</i> , <i>Lyngbya</i> and <i>Planktothrix</i>	(Sivonen 2009; Wimmer, Strangman and Wright 2014; Rastogi, Madamwar and Incharoensakdi 2015)

Nodularin	 <p>***</p>	Hepatotoxic through inhibition of PP1 and PP2A protein phosphates, carcinogenic	<i>Nodularia</i>	(Sivonen et al. 1989; Ohta et al. 2015; Akter et al. 2017)
Saxitoxin	 <p>**</p>	Neurotoxic, sodium channel blocker	<i>Dolichospermum</i> , <i>Aphanizomenon</i> , <i>Raphidiopsis</i> , <i>Lyngbya</i> and <i>Planktothrix</i>	(Landsberg 2002; Wiese et al. 2010)
Anatoxin-a	 <p>****</p>	Neurotoxic, neuromuscular blocker	<i>Dolichospermum</i> , <i>Aphanizomenon</i> , <i>Microcystis</i> , <i>Planktothrix</i> , <i>Raphidiopsis</i> , <i>Arthrospira</i> , <i>Cuspidothrix</i> and <i>Phormidium</i>	(Rastogi, Madamwar and Incharoensakdi 2015; Otero and Silva 2022)

Anatoxin-a(S)		Neurotoxic, neuromuscular blocker	<i>Dolichospermum</i>	(Carmichael, Mahmood and Hyde 1990)
Antillatoxin		Neurotoxic, sodium channels activator	<i>Lyngbya</i>	(Berman, Gerwick and Murray 1999)
Aplysiatoxin		Dermatotoxic	<i>Lyngbya, Schizothrix, Trichodesmium, Oscillatoria and Planktothrix</i>	(Rastogi, Madamwar and Incharoensakdi 2015)
Cyanopeptolin		Neurotoxic, serine proteases inhibitor.	<i>Microcystis, Lyngbya, Planktothrix and Dolichospermum</i>	(Welker and Von Döhren 2006)

**

Jamaicamide	 <p style="text-align: center;">**</p>	Neurotoxic, sodium channel blocker	<i>Lyngbya</i>	(Edwards et al. 2004)
Kalkitoxin		Neurotoxic, sodium channel blocker	<i>Lyngbya</i>	(Berman, Gerwick and Murray 1999)
Lyngbyatoxin	 <p style="text-align: center;">*****</p>	Dermatotoxic	<i>Lyngbya, Oscillatoria, Schizothrix</i>	(Fujiki et al. 1981; Welker and Von Döhren 2006; Rastogi, Madamwar and Incharoensakdi 2015)
Lipopolysaccharides	(Hong et al. 2021)	Dermatotoxic, gastrointestinal irritant	All cyanobacteria	(Wiegand and Pflugmacher 2005)

β-N-methylamino-l-alanine (BMAA)		Neurotoxic	<i>Dolichospermum, Microcystis, Nostoc and Planktothrix</i>	(Cox et al. 2005; Rastogi, Madamwar and Incharoensakdi 2015; Li et al. 2024)
----------------------------------	---	------------	---	--

*X and Y are two variable amino acids in the general microcystin chemical structure.

**General structure of cyanotoxin. R represents variable radical depending on cyanotoxin analogue.

***Chemical structure of nodularin-R. Most abundant nodularin analogue.

****Chemical structure of analogue anatoxin-a.

*****Chemical structure of analogue lyngbyatoxin-a.

A number of incidents involving cyanotoxin contamination of water have been reported over the years. In 1979, 128 people were hospitalized in Queensland, Australia due to abdominal pain and vomiting to kidney failure. This incident was known as Palm Island Mystery Disease, which then was discovered to be caused by cyanotoxin contamination, later proposed to be cylindrospermopsin (Bourke et al. 1983). Cases resulting in the development of pneumonia in soldiers were reported back in 1989 in Staffordshire, England, due to poisoning by ingestion of cyanotoxin contaminated water (Turner et al. 1990). In 1996, a total of 100 patients developed acute liver failure and other 52 patients died after a hemodialysis procedure in Caruaru, Brazil, caused by cyanotoxin (microcystins) contamination (Jochimsen et al. 1998; Azevedo et al. 2002). Another incident occurred in 2014 in Toledo, Ohio, where drinking or using tap water was considered unsafe by the authorities due to cyanotoxin contamination in Lake Erie, which led to the hospitalization of 60 people (Wolf, Georgic and Klaiber 2017). Also, the death of many dogs and other animals have been reported over the years (Wood 2016), for example, the death of dogs was associated with microcystin contamination during a *Microcystis aeruginosa* bloom in Lake Amstelmeer, the Netherlands, in 2011 (Lürling and Faassen 2013). In another incident, pets have died by suspected cyanotoxin poisoning in Aberdeenshire, United Kingdom, after a cyanobacterial bloom event in 2022 (Shanks 2022).

1.1.3 Pesticides

Pesticides are another example of water contaminants that are mainly used in agriculture for pest control. Pesticides are substances that can cause pollution in the environment due to their stability, mobility and long-term effects on living organisms (Nasiri, Ahmadzadeh and Amiri 2020), however, agriculture still requires the use of pesticides to reduce losses and improve the quality of products (Sharma et al. 2019; Thiour-Mauprivez et al. 2019; Tudi et al. 2021). Pesticides are widely applied in different regions of the world (Figure 1.2).

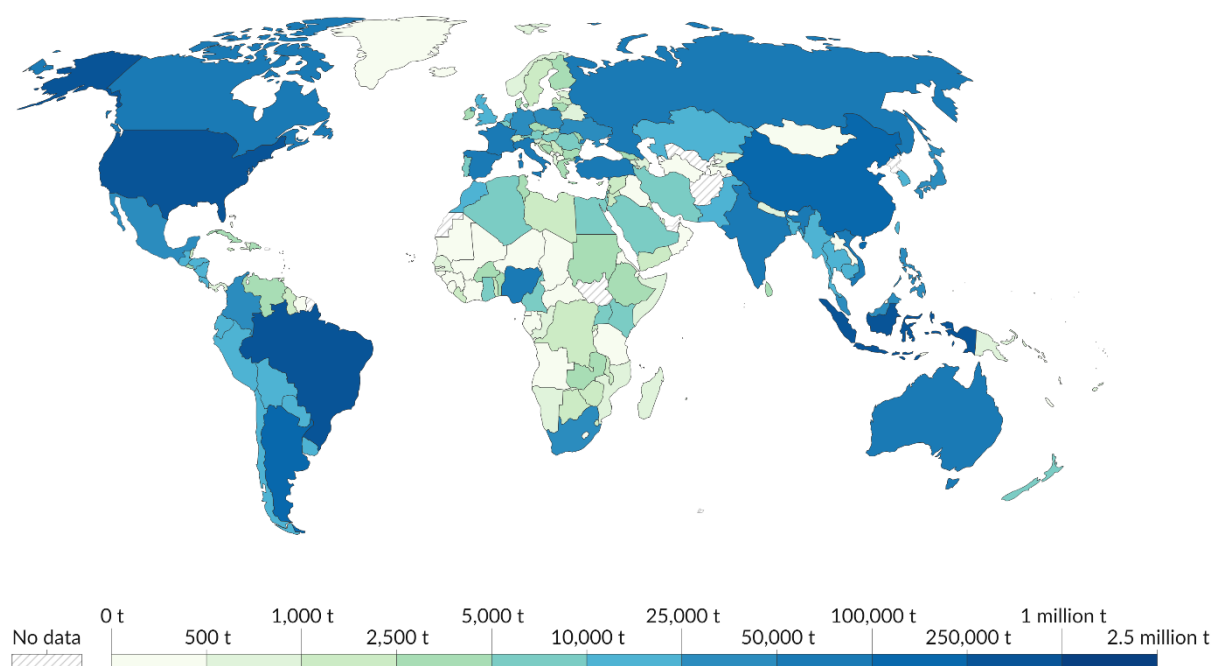


Figure 1.2: Total annual pesticide usage (tonnes) during 2021 (Ritchie, Roser and Rosado 2022).

Pesticides are mainly classified into herbicides, insecticides and fungicides according to their main usage in agriculture. Herbicides are used to prevent weeds or unwanted plant growth in crops, insecticides are used to destroy infesting insects and fungicides are applied to kill or inhibit the multiplication of fungi (Nasiri, Ahmadzadeh and Amiri 2020; Rani et al. 2020). Herbicides are the most widely used pesticides, constituting around 50% of total use, insecticides account for approximately 22% and fungicides represent less than 23% (Figure 1.3; Khatri and Tyagi 2015).

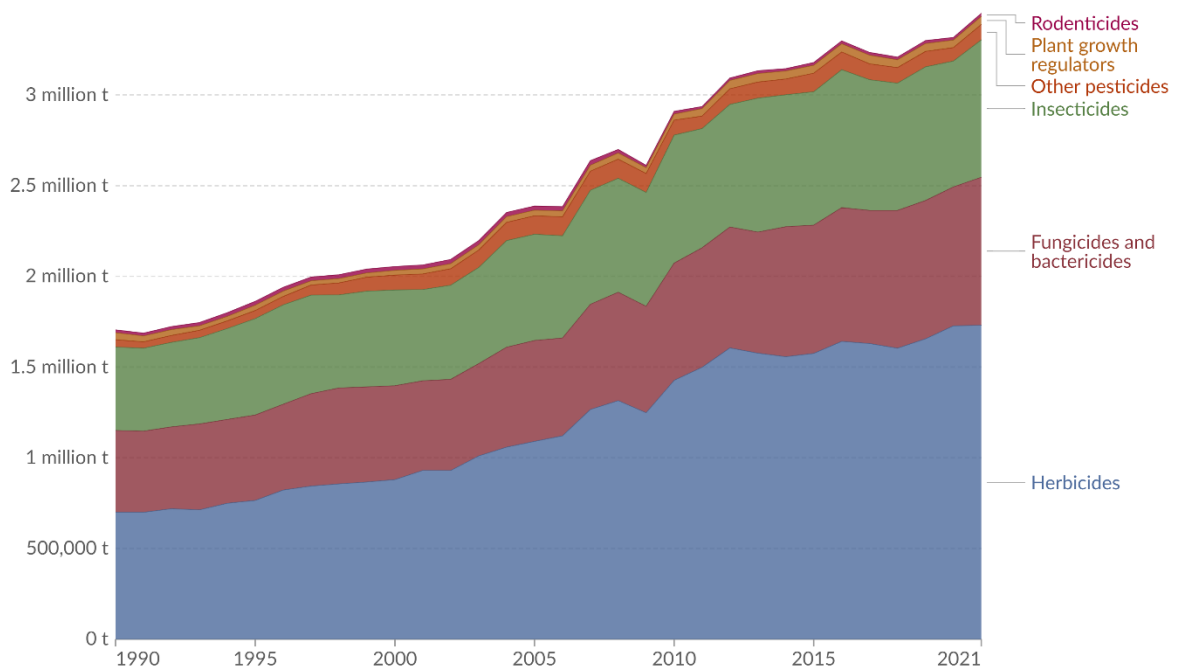


Figure 1.3: Pesticide usage in the world broken down by pesticide type from 1990 to 2021 (Ritchie, Roser and Rosado 2022).

Pesticides can be carried over during and after their application in agriculture through air, finding their way to aquatic environments such as surface and groundwaters and eventually end up in drinking water (Ribeiro et al. 2015; Nasiri, Ahmadzadeh and Amiri 2020). Effluents containing residual pesticides or other toxic degradation products can also contaminate freshwater environments (e.g., pesticide spray tank residuals, pesticide storage tanks, drainage channels next to crops and ponds) (Nasiri, Ahmadzadeh and Amiri 2020). Furthermore, rainfall runoff represents a primary pathway for the transport of pesticides (Stehle et al. 2019). Pesticide contamination in freshwater environments, such as rivers, lakes, estuaries, dams, streams and groundwater systems, may result in negative impacts to plants, animals and humans (Tudi et al. 2021). The input of nutrient into aquatic environments is strongly correlated with the use of pesticides and the presence of cyanobacteria and cyanotoxins. In order to promote safe drinking water, these contaminants need to be removed from aquatic environments.

1.2 Conventional water treatment

Conventional water treatment based on coagulation, flocculation, sedimentation/flotation and filtration is designed to treat suspended and colloidal

particles (Vilela et al. 2012; Chae et al. 2019; Saleh, Zouari and Al-Ghouti 2020; Anupam et al. 2022), however, it can be inefficient in removing dissolved compounds such as cyanotoxins and pesticides. Conventional water treatment can also result in cyanobacterial cell lysis and subsequent intracellular toxin release into the environment (Sakai et al. 2009; Ou et al. 2014; Pestana et al. 2019; Clemente et al. 2020). Due to the inefficiency of conventional water treatment in treating some pollutants, different technologies could be applied prior to the treatment plant or before the discharge of treated water into the environment to enhance the degradation of these compounds (Ribeiro et al. 2015; Saleh, Zouari and Al-Ghouti 2020). Advanced oxidation processes (AOPs) are based on the generation of oxidizing agents, such as reactive oxygen species (ROS), and have the potential of removing pollutants from aquatic environments (Schneider and Bláha 2020). These technologies are highly efficient and have the potential to be applied at source for the removal of contaminants.

1.3 Advanced oxidation processes

Advanced oxidation processes can be used for the removal of a range of compounds and microorganisms, including cyanobacteria, cyanotoxins and pesticides. All AOPs generate ROS, such as hydroxyl radical $\bullet\text{OH}$ and superoxide radical $\bullet\text{O}_2^-$, which are responsible for the non-targeted oxidation of contaminants (Tufail et al. 2021). Common AOPs are photolysis (ultraviolet alone), photolysis in combination with oxidants (e.g., hydrogen peroxide and chlorine), photocatalysis (light source in combination with photocatalysts), Fenton process and ozonation (Wols and Hofman-Caris 2012).

Photolysis is commonly applied in water treatment for the disinfection of water by ultraviolet (UV) irradiation. Photolysis can occur either directly or indirectly. Direct photolysis occurs when the compound is degraded by absorption of photons or when a chromophore present in the structure of the compounds absorbs energy to form an activated molecule that can undergo homolysis, heterolysis or photoionization. Indirect photolysis occurs when other compounds absorb light energy (photosensitizers, for example, dissolved organic matter, humic acid, fluvic acid, nitrate, ozone, nitrogen), which creates a series of reactions that ultimately degrade the target compound (Reddy and Kim 2015). The photolytic performance during water treatment depends on the wavelength of the light, which represents the energy applied (Schneider and Bláha 2020).

UV-C consists of a wavelength of 180 – 280 nm (shorter wavelength and higher energy), UV-B presents a wavelength of 280 – 315 nm and UV-A is in the wavelength range of 315 – 400 nm (longer wavelength and lower energy) (Saleh, Zouari and Al-Ghouti 2020). Furthermore, light intensity is another important parameter in the photolytic efficiency during water treatment. The high doses of UV energy usually required for disinfection of water can be energy demanding, therefore, expensive. Operating costs for photolysis need to be considered before large-scale water treatment applications (Schneider and Bláha 2020). Photolysis can also be combined with oxidants such as hydrogen peroxide (H_2O_2), chlorine or sulfate to enhance the production of radicals (e.g., $\bullet\text{OH}$, $\bullet\text{SO}_4^-$, $\bullet\text{OCl}$) (Reddy and Kim 2015; Schneider and Bláha 2020).

Ozone (O_3) in combination with hydrogen peroxide or UV radiation can also be an advanced oxidation process used for the removal of pollutants. During ozonation, the pollutants can be directly degraded by reactions with O_3 or indirectly removed by reactions with hydroxyl radicals $\bullet\text{OH}$ produced (Ribeiro et al. 2015; Rodriguez-Narvaez et al. 2017). The application of ozonation, however, can be expensive due to energy consumption and oxidant use (Ajiboye, Kuvarega and Onwudiwe 2020).

Photocatalysis is another AOP applied for water treatment. The application of photocatalysis started almost a century ago with water splitting, followed by artificial photosynthesis and other environmental applications, such as water treatment (Marcelino and Amorim 2019). Photocatalysis is based on the activation of a photocatalyst by light with a specific wavelength. Depending on the photocatalyst, the light source can be in the visible light or UV spectrum. The photocatalyst is activated when it is illuminated by light with energy higher than the band gap of the photocatalyst (energy difference between valence band and conduction band), which causes an electron to move to the conduction band (reducing site) and creates a hole in the valence band (oxidative site). The degradation of pollutants can occur by direct oxidation at the valence band caused by the generated hole (h^+) or by oxidation from reactive species generated in both valence and conduction band from H_2O or O_2 (Schneider and Bláha 2020).

Fenton reactions consist in the generation of ROS during the decomposition of H_2O_2 in the presence of iron(II) – Fe^{2+} (Equation 1.1). In Fenton-like reactions, other transition metals and oxidant can be applied in addition to H_2O_2 to produce

reactive species, for example, ferric iron or iron (III) – Fe^{3+} can be used instead of Fe^{2+} . Fenton reactions are efficient processes easy to implement and operate with low-cost reagents, however, the fast consumption of Fe^{2+} , the production of a sludge after treatment, the pH sensitivity (optimal pH range 2.5 – 3) and the necessity of addition oxidants are some disadvantages of this technology (Ribeiro et al. 2015).



During photo-Fenton and photo-Fenton like processes, UV or visible light irradiation is used to enhance the degradation of pollutants by increasing the generation of ROS. Even though costs associated with photo-Fenton and photo-Fenton like reactions might increase due to UV irradiation, less sludge is produced and less sludge treatment is required (Ribeiro et al. 2015).

Therefore, AOPs could be explored as water treatment technologies that can be applied at source for the removal of pollutants from aquatic environments. AOPs would be applied by developing reactors that are modular, scalable and flexible, hence able to remove contaminants from more localized areas (e.g., ponds near small farms, farmyards, storage tanks) or larger areas of contamination (e.g., lakes in industrial spaces), by changing the dimensions of the reactor or the number of treatment units.

1.4 Thesis aim and objectives

The aim of this study is to evaluate the application of different AOPs (photolysis and photocatalysis) as an effective and economical alternative for the removal of contaminants (cyanobacteria, cyanotoxins and pesticides) at source from aquatic environments. Therefore, the objectives are:

- Evaluation of the removal of cyanobacterial cells and toxins by a specific and economical UV-A 365 nm light emitting diodes photolytic treatment;
- Determination of optimal photocatalytic system based on coated glass beads and LEDs for the removal of contaminants from aquatic environments;
- Evaluation of the removal of pesticides including herbicides and insecticides by photocatalysis based on graphitic carbon nitride coated beads and UV-A light emitting diodes;
- Construction and evaluation of a photocatalytic treatment unit (reactor) that will promote the removal of pesticides at source from aquatic environments.

This thesis consists of six chapters based on the research rationale, the application of photolysis for the removal of cyanobacteria and cyanotoxins, the selection of a photocatalytic system for the removal of pollutants from aquatic environments at source, the selection and photocatalytic degradation of pesticides from water, the construction and evaluation of a reactor prototype for the removal of pesticides at source and a last chapter containing a conclusion of the findings of this thesis and proposal for future work (Table 1.3).

Table 1.3: Structure of the thesis according to the content of each chapter.

Thesis chapter	Content of the chapter
Chapter 1	Rationale, environmental background, aim and objectives
Chapter 2	Evaluation of the effects of media nutrients and UV-A (365 nm) LED irradiation on <i>Microcystis aeruginosa</i> and microcystins removal
Chapter 3	Preparation of g-C ₃ N ₄ , TiO ₂ and g-C ₃ N ₄ /TiO ₂ coated beads and evaluation of their photocatalytic efficiency on the removal of microcystin-LR as a model compound
Chapter 4	Evaluation of the photocatalytic degradation of selected pesticides by g-C ₃ N ₄ coated beads and UV-A LED irradiation in batch and flow-through systems and optimization of photocatalytic parameters, such as solution pH, catalyst load and catalyst reusability
Chapter 5	Rationale for the scale-up of a photocatalytic treatment unit (reactor) and evaluation of the pilot-scale removal of diuron as a model pesticide
Chapter 6	Conclusion and future work

Chapter 2

A tale of caution: the effect of media nutrients on light-driven cyanobacteria and toxin removal

2 A TALE OF CAUTION: THE EFFECT OF MEDIA NUTRIENTS ON LIGHT-DRIVEN CYANOBACTERIA AND TOXIN REMOVAL.....	21
2.1 Introduction.....	23
2.1.1 Cyanobacterium <i>Microcystis aeruginosa</i>	23
2.1.2 Microcystins	24
2.1.3 Water treatment technologies for cyanobacterial cells and toxins	25
2.1.4 Advantages of the proposed UV-A LED photolytic treatment for the removal of <i>Microcystis aeruginosa</i> cells and microcystins	27
2.2 Materials and methods.....	28
2.2.1 Reagents	28
2.2.2 <i>Microcystis aeruginosa</i> strains	28
2.2.3 Experimental design for the photolytic degradation of <i>Microcystis aeruginosa</i> cells	30
2.2.4 Photolytic degradation of dissolved microcystin-LR.....	30
2.2.5 Reactor design	31
2.2.6 Analysis	35
2.2.6.1 Determination of photosynthetic activity	35
2.2.6.2 <i>Microcystis aeruginosa</i> cell enumeration.....	36
2.2.6.3 Ultra-performance liquid chromatography tandem mass spectrometry analysis of intra- and extracellular microcystin concentrations.....	37
2.2.6.4 Statistical analysis	44
2.3 Results and discussion	44
2.3.1 Effects of UV-A irradiation on <i>Microcystis aeruginosa</i> photosynthetic activity..	44
2.3.2 Effect of UV-A irradiation on eleven microcystin analogues	52
2.3.3 Effects of UV-A irradiation on dissolved microcystin-LR	59
2.4 Conclusion	66

2.1 Introduction

2.1.1 Cyanobacterium *Microcystis aeruginosa*

The genus *Microcystis* is characterized morphologically by highly buoyant, unicellular, coccoid-shaped cells with a diameter ranging between 2 and 7 μm (Komárek et al. 2002). *Microcystis spp.* exhibits colonial morphology consisting of dense aggregations of cells under natural environmental conditions or of single cells when present within laboratory culture (Figure 2.1; Xiao, Li and Reynolds 2018).

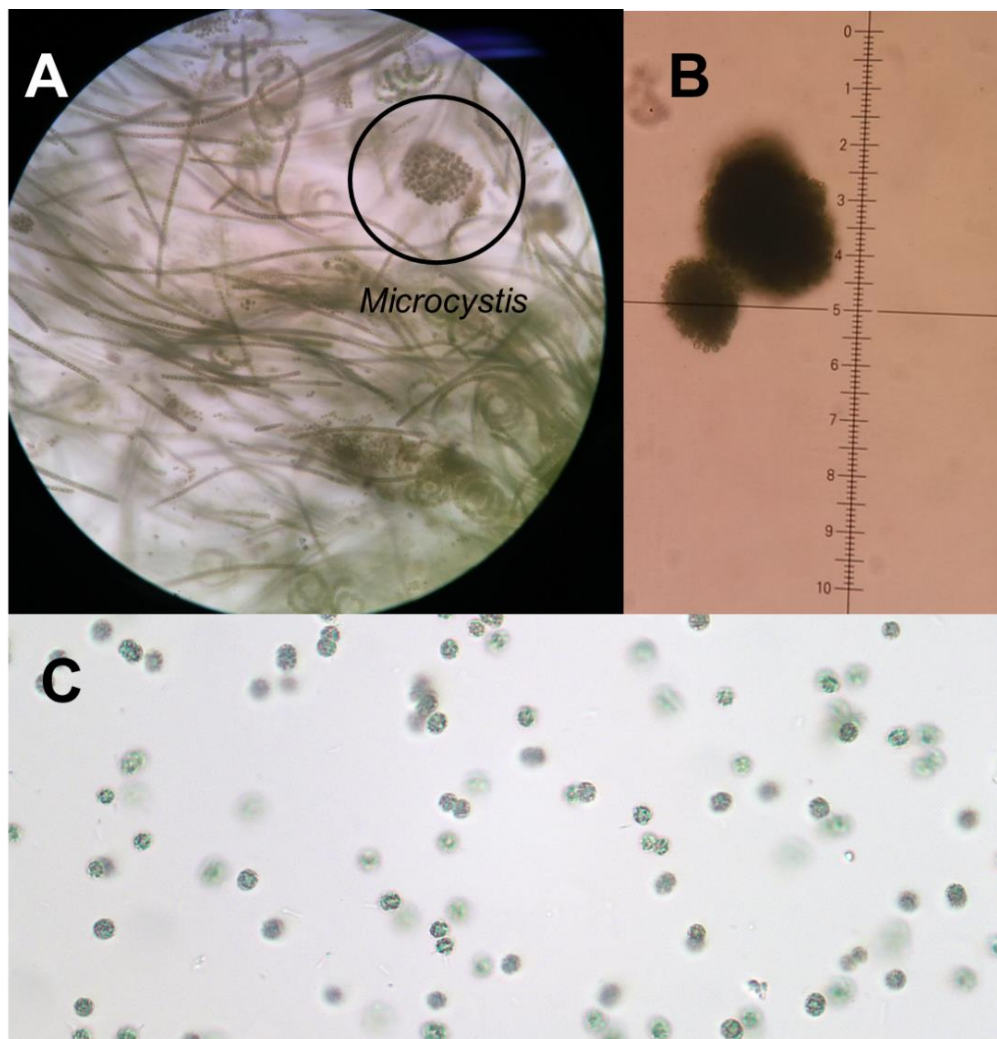


Figure 2.1: *Microcystis sp.* A) within a cyanobacterial bloom containing different species of cyanobacteria from environmental samples, B) isolated from environmental samples obtained from a freshwater reservoir in Brazil, both presenting colonial behaviour and C) in axenic laboratory conditions presenting single cellular behaviour.

The occurrence of *Microcystis* blooms in freshwater ecosystems is influenced by various environmental factors such as light, temperature, pH and nutrient levels (Jacoby et al. 2000), however, there are reports of toxic blooms of *Microcystis*

from all continents except Antarctica (Hodgson 2012). Different *Microcystis* species present both toxic and non-toxic strains (Janse et al. 2004). Between all *Microcystis* species, *Microcystis aeruginosa* is found to be the most predominant toxic species (Mohan et al. 2023), which can produce potent hepatotoxins that might cause death by liver injury and internal hemorrhages, also known as microcystins (Sivonen 2009).

2.1.2 Microcystins

The most reported cyanotoxins in freshwater environments are microcystins (MCs; Pinho et al. 2015) which present with over 247 analogues (Spoof and Catherine 2017). These toxins are cyclic heptapeptides that share a similar chemical structure: D-Glutamate (D-Glu), D-Alanine (D-Ala), D-Aspartate methyl (D-MeAsp), N-Methyldehydroalanine (Mdha) and 3-amino-methoxy-10-phenyl-2,6,8-trimethyldeca-4,6-dienoic acid (Adda). The other two amino acids are variable in positions 2 and 4 of the structure (Figure 2.2). The amino acid single letter abbreviation is used to differentiate the different types of microcystins (Table 2.1; Harke et al. 2016). The microcystin containing the amino acids leucine and arginine (MC-LR) is the most reported analogue. Microcystins are present inside cyanobacterial cells and can be released into the surrounding water through cell lysis (Tsai 2015).

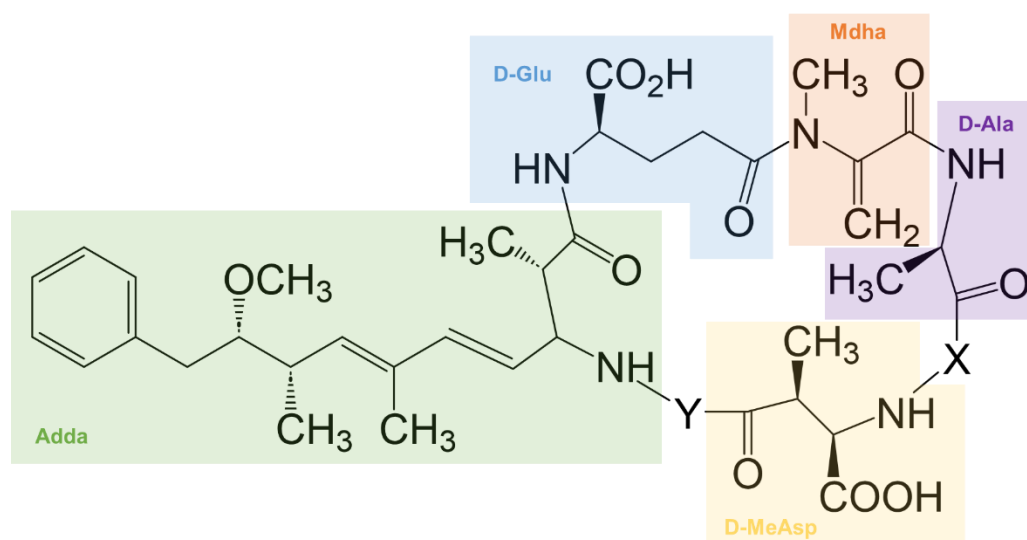


Figure 2.2: Microcystin general structure containing two variable amino acids X and Y, 3-amino-9-methoxy-2,6,8-trimethyl-10-phenyldeca-4,6-dienoic acid (Adda), D-Glutamic acid (D-Glu), N-Methylhydroalanine (M-dha), D-Alanine (D-Ala) and D-Aspartate methyl (D-MeAsp).

Table 2.1: Microcystin analogues with variable amino acids in position X and Y. All microcystins presented were incorporated within this thesis.

Microcystin analogue	Variable amino acid X	Variable amino acid Y
MC-HtyR	L-homotyrosine (Hty)	Arginine (R)
MC-LA	Leucine (L)	Alanine (A)
MC-LF	Leucine (L)	Phenylalanine (F)
MC-DmLR*	Leucine (L)	Arginine (R)
MC-LR	Leucine (L)	Arginine (R)
MC-LW	Leucine (L)	Tryptophan (W)
MC-LY	Leucine (L)	Tyrosine (Y)
MC-DmRR*	Arginine (R)	Arginine (R)
MC-RR	Arginine (R)	Arginine (R)
MC-WR	Tryptophan (W)	Arginine (R)
MC-YR	Tyrosine (Y)	Arginine (R)

*The D-MeAsp position is demethylated.

2.1.3 Water treatment technologies for cyanobacterial cells and toxins

Conventional water treatment based on coagulation, flocculation, sedimentation/flotation and filtration is designed to treat suspended and colloidal particles (Vilela et al. 2012; Chae et al. 2019), however, it can be inefficient in removing dissolved compounds such as cyanotoxins. Conventional water treatment can also result in cell lysis and subsequent intracellular toxin release into the environment (Sakai et al. 2009; Ou et al. 2014; Pestana et al. 2019; Clemente et al. 2020). Other technologies such as the application of algaecides and oxidants also present limitations during cyanobacteria treatment (Hanson and Stefan 1984; Huh and Ahn 2017; Pestana et al. 2020; Santos et al. 2021; Sukenik and Kaplan 2021; Zhan and Hong 2022).

Due to the inefficiency of some water treatment technologies in treating high cyanobacterial cell densities and cyanotoxins, other technologies emerged as alternatives for the removal of cyanobacteria and toxins. Advanced oxidation processes (AOPs) are water treatment technologies based on the generation of radicals with high oxidative power that have the potential to promote the degradation of pollutants, such as cyanobacterial cells and toxins (Kaminski et al. 2021; Munoz et al. 2021; Yu et al. 2024). Titanium dioxide (TiO₂) photocatalysis is one type of AOP that has been widely evaluated for the treatment of cyanobacteria and cyanotoxins from water. Pestana et al. (2015) evaluated the degradation of eleven microcystins and nodularin by photocatalysis using TiO₂

coated onto glass microspheres illuminated by a Xenon lamp (330 – 450 nm). The photocatalytic degradation of nodularin by powdered TiO₂ and a Xenon lamp (350 – 450 nm) was also demonstrated (Liu et al. 2005). Chang et al. (2015) reported the inactivation of *M. aeruginosa* cells by mixed phase silver (Ag) and TiO₂ co-coated on the surface of diatomite under sunlight. Pinho et al. (2015b) demonstrated the degradation of *M. aeruginosa* cells and two different cyanotoxins (microcystin-LR and cylindrospermopsin) by TiO₂ photocatalysis using a sunlight simulator (280 – 400 nm) in lab-scale and natural sunlight in a pilot scale experiment. Liao et al. (2009) investigated the successful control of *Dolichospermum* sp. PCC 7120 and *M. aeruginosa* growth by photocatalysis based on silver-doped TiO₂ and UV-C irradiation. Other studies also evaluated the effects of photocatalysis on *M. aeruginosa* cells by powdered TiO₂ and UV irradiation (Lu, Liu and Chen 2015).

Even though photocatalysis has been widely investigated for the removal of cyanobacteria and cyanotoxins, this technology has not yet been completely applied at large scale. In a previous study, Pestana et al. (2020) investigated the degradation of *M. aeruginosa* PCC 7813 and its four microcystins (microcystin-LR, -LY, -LW and -LF) by TiO₂ coated glass beads and UV light emitting diode (LED) irradiation as the first step (bench-scale experiments) of a large set of experiments that ultimately aimed to apply photocatalysis at source in reservoirs in Brazil (Pestana et al. 2022). Subsequently, Menezes et al. (2021a) used the same TiO₂ coated glass beads with UV-A LED irradiation for the photocatalytic removal of *M. aeruginosa* PCC 7813 and its four microcystins using a pilot-scale size photocatalytic treatment unit. When performing an experiment based in a typical photocatalysis treatment, three systems are investigated: a system containing the catalyst and the light source (treatment), a system containing only the catalyst in the solution (dark control) and a system with only the light source (light control). In the Menezes et al. (2021a) study, the authors actually observed that the light control system (only UV-A LEDs were used in the system) had a marked effect on both *M. aeruginosa* cells and toxins, which indicated that a photolytic treatment by UV-A LED irradiation resulted in the removal of cyanobacterial cells and toxins. These findings have demonstrated that *M. aeruginosa* PCC 7813 and four microcystin analogues MC-LR, MC-LF, MC-LY and MC-LW were effectively removed by photolytic UV-A irradiation at the specific wavelength of 365 nm by economical LEDs.

2.1.4 Advantages of the proposed UV-A LED photolytic treatment for the removal of *Microcystis aeruginosa* cells and microcystins

A promising measure to control cyanobacteria could be light-driven treatments such as UV photolysis. Previous investigations on the impact of UV-light on cyanobacterial cells and toxins at laboratory scale, particularly using UV-C (180 – 280 nm) and UV-B (280 – 315 nm) irradiation, have been evaluated. Both UV-B and UV-C irradiation can be applied for the removal of microorganisms by inducing DNA damage, however, this technology is non-specific and could damage other biota when applied *in situ* (Qin, Li and Li 2015). Yang et al. (2015) investigated the impacts of UV-B irradiation on a toxin- (FACHB 915) and a non-toxin- (FACHB 469) producing strains of *Microcystis aeruginosa* cells and microcystins. The authors observed a retarding effect on *M. aeruginosa* growth, however, cell numbers still increased at the end of 15 days of UV-B irradiation (from 2×10^5 to 8.7 and 6.6×10^6 cells mL⁻¹ after UV-B exposure compared to 10.3 and 9×10^6 cells mL⁻¹ from control samples). Yang et al. (2015) also showed intracellular microcystin degradation by UV-B of 40% after 6 days of exposure, which could be due to damage of the photosynthetic apparatus of cells. The extracellular microcystin content increased after 15 days of UV-B irradiation, however, it was significantly lower than the microcystins concentration from the control. Tao et al. (2013) observed that UV-C exposure could reduce photosynthetic activity and pigment concentration when evaluating the effects of UV-C irradiation on *M. aeruginosa* photosynthetic activity. The removal of microcystin from *M. aeruginosa* FACHB 905 by 185 nm UV-C irradiation was investigated (Liu et al. 2016). The authors observed a microcystin removal of 44% after 120 minutes.

Another disadvantage of the UV treatment application is the associated high costs (e.g., capital, running and maintenance), which also represent a challenge to the implementation of light-driven technologies *in situ* (Chae et al. 2019). LEDs have been widely used in the most diverse applications due to several advantages. Besides being an economical option as illumination source (~ USD 0.8 per LED), LEDs also have a long lifespan, low heat emission and low energy requirements, which highlights the low maintenance costs and high efficiency involved with LED application.

In order to determine if UV-A 365 nm irradiation degrades other *M. aeruginosa* strains and microcystin analogues and to better understand the mechanisms behind this technology, further exploration was required prior to *in situ* pilot testing. Therefore, UV-A (365 nm) LED irradiation was applied to treat six different *Microcystis aeruginosa* strains (SCIENTO, NIES 1099, B2666, PCC 7820, PCC 7813 and PCC 7806) and the range of eleven microcystins they produce (demethalated MC-RR, MC-RR, demethalated MC-LR, MC-LR, MC-LY, MC-LW, MC-LF, MC-Homotyrosine and MC-LA). Further, a common way of verifying the effects of light-driven treatments on cyanobacteria is by performing laboratory-scale experiments where cyanobacteria are cultured in growth media (e.g., BG-11 medium). It is important to consider the media composition for laboratory-scale experiments focused on cyanobacterial removal in order to effectively evaluate light-driven strategies for cyanobacteria and toxin removal. Therefore, the effects of media nutrients on cyanobacteria removal studies by UV-A irradiation were also evaluated.

2.2 Materials and methods

2.2.1 Reagents

Reagent grade chemicals (Fisher Scientific, UK) were used for the preparation of BG-11 culture medium (Stanier et al. 1971) and artificial freshwater (AFW) solution (Akkanen and Kukkonen 2003). Acetonitrile, methanol and formic acid (Fisher Scientific, USA) were used for ultra-performance liquid chromatography tandem mass spectrometry (UPLC-MS/MS) analysis of microcystins. Diuron (3-(3,4-dichlorophenyl)-1,1-dimethylurea) (Sigma-Aldrich, UK) was added to samples during photosynthetic activity determination. Isoton II Diluent was used for cell enumeration (Beckman Coulter, USA). Ultrapure water (18.2 M Ω) obtained by an ELGA PURELAB system (Veolia, UK) was used to prepare all solutions.

2.2.2 *Microcystis aeruginosa* strains

Six *M. aeruginosa* strains (Table 2.2) of geographically diverse origin were evaluated, including five *M. aeruginosa* strains with aerotopes (SCIENTO, NIES 1099, B2666, PCC 7820 and PCC 7806) and one strain without aerotopes (PCC 7813). Each strain of *M. aeruginosa* produced a range of microcystin analogues which included demethalated MC-RR (DmRR), MC-RR, demethalated MC-LR

(DmLR), MC-LR, MC-YR, MC-WR, MC-LY, MC-LW, MC-LF, MC-Homotyrosine (Htyr) and MC-LA.

Table 2.2: *Microcystis aeruginosa* strains, size range (μm), main microcystin analogues produced by each strain, presence of aerotopes (gas vesicles), location where culture was first isolated and respective culture collection.

<i>Microcystis aeruginosa</i> strain	Individual cell size range (μm)	Microcystin analogues	Aerotopes	Location of isolation	Culture collection
SCIENTO	2.6 – 5.4	MC-DmRR MC-RR MC-DmLR MC-LR MC-Htyr MC-YR MC-WR	Yes	England	Sciento, UK
NIES 1099	2.7 – 5.9	MC-DmRR MC-RR MC-DmLR MC-LR MC-YR MC-WR	Yes	Japan	National Institute of Environmental Studies (NIES), Japan
B2666	2.9 – 5.4	MC-LA MC-LR	Yes	South Africa	Culture Collection of Algae at the University of Texas at Austin (UTEX), USA
PCC 7820	2.7 – 4.6	MC-LR MC-LF MC-LY MC-LW	Yes	Scotland	Pasteur Culture Collection, France
PCC 7813	2.8 – 4.8	MC-LR MC-LF MC-LY MC-LW	No	Scotland	Pasteur Culture Collection, France
PCC 7806	2.4 – 4.9	MC-DmLR MC-LR	Yes	Netherlands	Pasteur Culture Collection, France

2.2.3 Experimental design for the photolytic degradation of *Microcystis aeruginosa* cells

M. aeruginosa strains were cultured in BG-11 medium (1400 mL of cyanobacteria in a 2000 mL borosilicate flask sparged with sterile air, kept at 21 ± 1 °C and illuminated by cool white fluorescent lights with an average light intensity of $30 \mu\text{mol photons m}^{-2} \text{s}^{-1}$) for 14 days. Prior to the beginning of the experiment, each strain of *M. aeruginosa* cells was diluted to a concentration of 10×10^6 cells mL^{-1} with sterile BG-11 medium. An aliquot of 100 mL was placed in a sterile 250 mL conical flask with a sample (3 mL) removed (equilibrium time – T_{EQ}). Samples were then incubated at 21 ± 1 °C and illuminated by cool white fluorescent light ($30 \mu\text{mol photons m}^{-2} \text{s}^{-1}$ or 7 W m^{-2}) for 72 hours to allow the cells to acclimate to the experimental conditions. After 72 hours, flasks were sampled (3 mL) again (time zero – T_0) and samples were continuously irradiated by UV light. Following this, 3 mL aliquots were removed at each sampling point at 1, 2, 3, 4, and 7 days. Aliquots were analysed for photosynthetic activity (1 mL), microcystins concentration (1 mL) and cell count (1 mL). Sample aliquots were evaluated immediately except for the aliquots for toxin determination, which were centrifuged at room temperature for 10 minutes at $13000 \times g$ and the supernatant was transferred to a fresh microcentrifuge tube (1.5 mL). Both, supernatants and cell pellets were stored at -20 °C until analysis. The experiment was performed in triplicate.

2.2.4 Photolytic degradation of dissolved microcystin-LR

Microcystin-LR was resuspended in ultrapure water ($50 \mu\text{g mL}^{-1}$) and the solution was filter sterilised using a PES filter membrane ($0.22 \mu\text{m}$ pore size). The filtered MC-LR solution was transferred into 100 mL of experimental medium (pure water, AFW, BG-11 or modified BG-11) in a sterile 250 mL conical flask until a final MC-LR concentration of 500 ng mL^{-1} was achieved. An aliquot T_{EQ} was removed (1 mL) and flasks were then incubated. After 72 hours of incubation at 21 ± 1 °C and illumination by cool white fluorescent light ($30 \mu\text{mol photons m}^{-2} \text{s}^{-1}$ or 7 W m^{-2}), flasks were sampled again (1 mL – T_0) and flasks were continuously irradiated by UV-A LEDs (maximum peak at 365 nm and 8 W m^{-2} light intensity). Additional samples were taken (1 mL) at each sampling point at 1, 2, 3, 4, and 7 days to determine MC-LR concentration. Aliquots were stored at -20 °C until analysis. On the day of analysis, aliquots were thawed and dried by rotary

evaporation in a Genevac (EZ-II evaporator, UK). Dried aliquots were resuspended in 1 mL of 50% methanol, placed in a dispersive extractor for 5 minutes at 2500 rpm followed by centrifugation at room temperature for 10 minutes at 13000 x g and then were immediately analysed for the determination of MC-LR concentration. The experiment was performed in triplicate.

2.2.5 Reactor design

Photolytic reactors were prepared for each of the tested systems: UV-A LED irradiation (Figure 2.3A), visible light (Vis) LED irradiation (Figure 2.3B), no LED irradiation (Figure 2.3C).

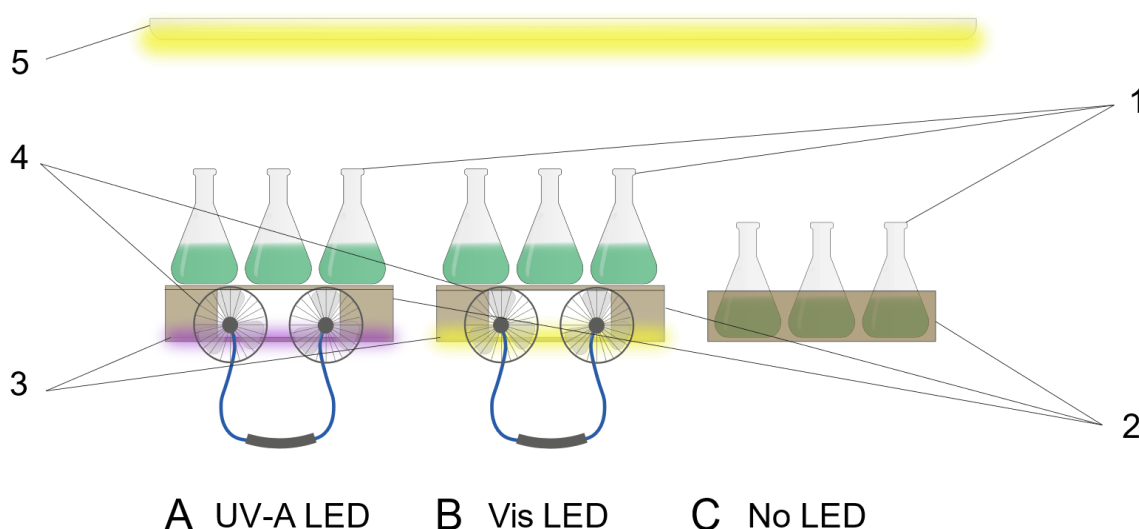


Figure 2.3: Schematic representation of experimental reactor systems containing (A) 600 individual UV-A LEDs (365 nm; 8 W m⁻²), (B) 600 individual visible light LEDs (400 – 700 nm; 6 W m⁻²) and (C) no LEDs that were used on six different *Microcystis aeruginosa* strains SCIENTO, NIES 1099, B2666, PCC 7820, PCC 7813 and PCC 7806. 1 – conical flasks containing *Microcystis aeruginosa* suspension, 2 – cardboard structure for respective reactors, 3 – LED-based irradiation of (A) UV-A and (B) visible light, 4 – portable fan for constant temperature and 5 – overhead cool fluorescent light of 30 μmol photons m⁻² s⁻¹ (7 W m⁻²).

Economical (~ USD 0.8 per LED) and long life of up to 100,000 working hours (Heering 2004a; Górecki 2013) UV-A LED strips were used for UV-A irradiation. Visible light LED irradiation was used to determine if the effects of the photolysis on cyanobacterial cells and toxins were caused due to the specific wavelength of UV-A (maximum peak at around 365 nm), therefore, a similar light output (i.e., similar light intensity) of both UV-A LEDs and visible light LEDs was required for the irradiation of *M. aeruginosa*. The base of the reactor (30 x 21 cm) contained either 600 UV-A LEDs on strips (9.6 W, 365 nm and light intensity of 8 W m⁻², Figure 2.4A) or 600 visible light LEDs on strips (400 – 700 nm and light intensity

of 1016 W m^{-2} , Figure 2.4B) or no LEDs depending on the tested system. Light spectra and light intensity were obtained with a StellarNet spectrometer (BLACK-Comet C-RS-50 model, USA).

Layers of cellulose paper were added over the visible light LED strips until a final light intensity of 6 W m^{-2} was achieved to mirror the light intensity of UV-A LEDs (Figure 2.4C). After the light intensity of visible light LEDs was adjusted to a similar light intensity that was used in UV-A LEDs, it was possible to observe that the layers of cellulose had an effect on the wavelength of the visible light LEDs. The wavelength obtained from the light spectrum initially was around 400 – 700 nm, however, the wavelength obtained was scattered after the adjustments (Figure 2.4C). Samples were kept at $22 \pm 1 \text{ }^{\circ}\text{C}$ with portable fans and overhead cool fluorescent light of $30 \text{ } \mu\text{mol photons m}^{-2} \text{ s}^{-1}$ (Figure 2.4D).

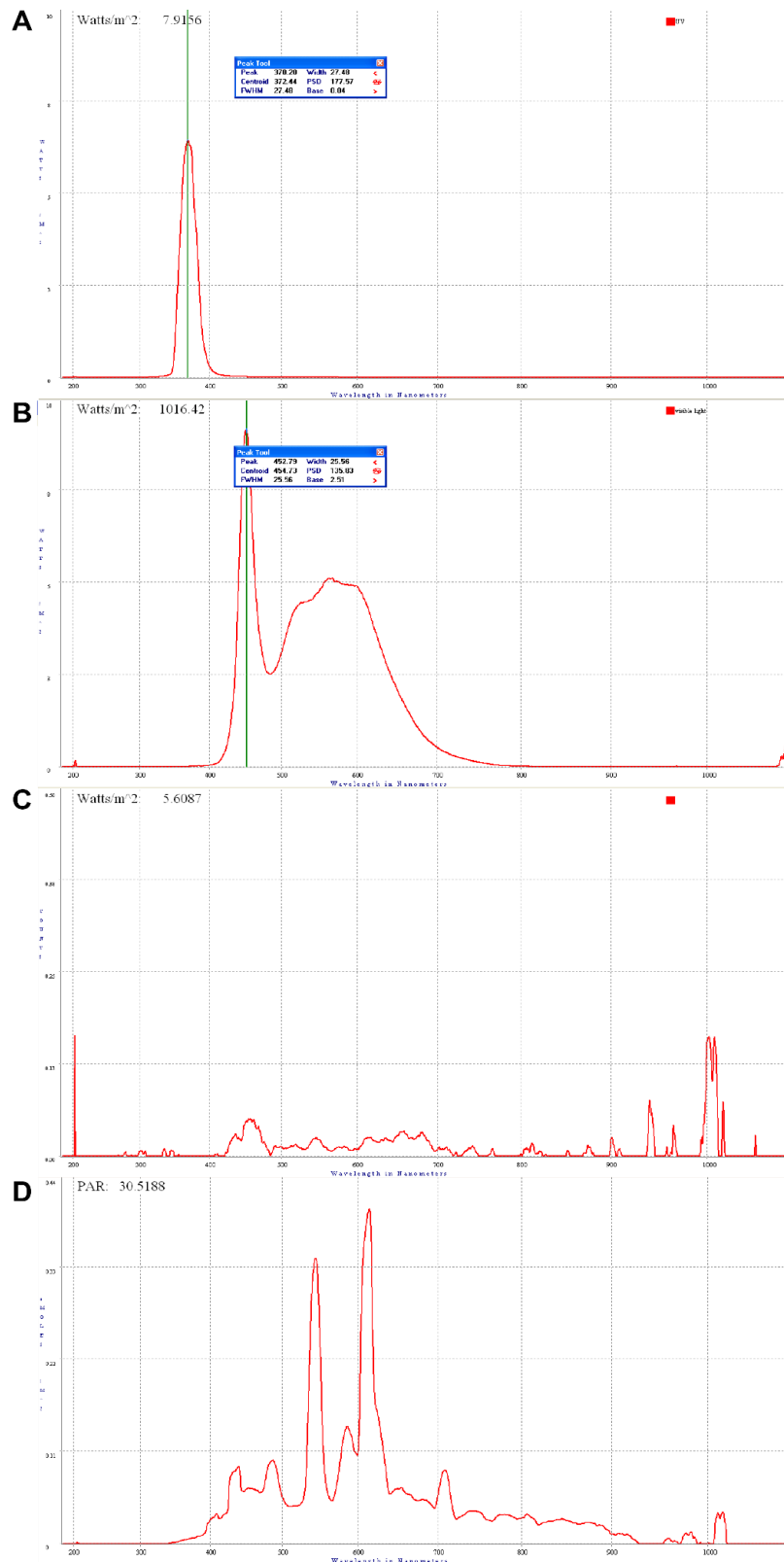


Figure 2.4: Full spectrum of A) ultraviolet-A light emitting diode (UV-A LED) strips presenting wavelength at a maximum peak at around 365 nm and light intensity of 8 W m^{-2} , B) visible light LED strips presenting wavelength range from 400 to 700 nm and light intensity of 1016 W m^{-2} , C) visible light LEDs with layers of cellulose with wavelength of 400-700 nm and light intensity of 6 W m^{-2} and D) overhead cool fluorescent light ($30 \mu\text{mol photons m}^{-2} \text{ s}^{-1}$ or 7 W m^{-2}).

Conical flasks containing samples (250 mL total volume) were placed on top of the reactor in triplicates on three openings of 8 cm of diameter each. Each conical flask presented an irradiated base area of 50.27 cm² which was illuminated by approximately 60 individual LEDs. UV-A and visible light LED irradiated samples were kept 3.5 cm from the base of the reactor containing LEDs. Non-LED irradiated samples were placed directly on the base of the reactor (Figure 2.5).

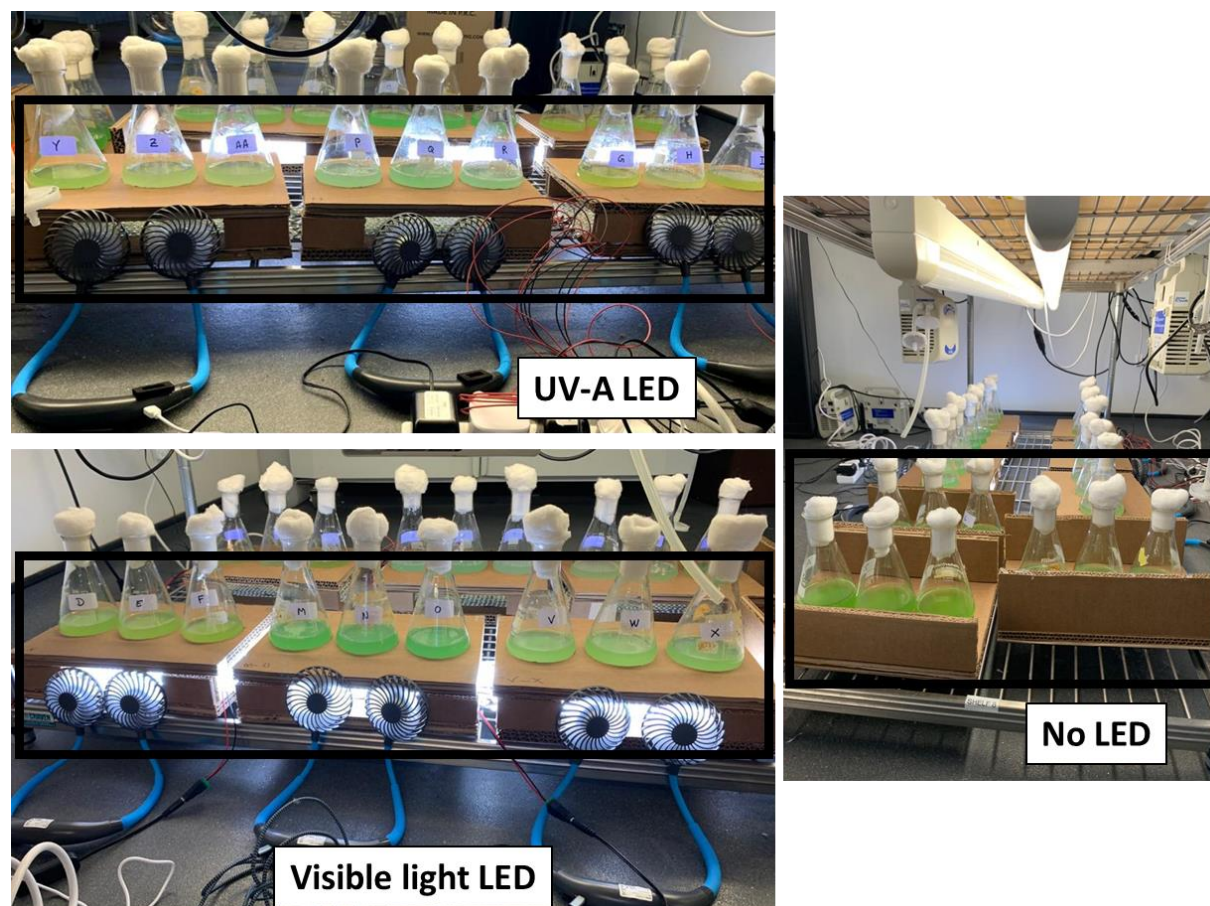


Figure 2.5: Photolytic experimental set-up with reactors containing ultraviolet-A light emitting diodes (UV-A LEDs), visible light LEDs and no LEDs to evaluate the effects of UV-A (365 nm) on the cells of different *Microcystis aeruginosa* strains and their respective microcynthins

2.2.6 Analysis

2.2.6.1 Determination of photosynthetic activity

Previous studies have indicated that photosynthetic activity is a rapid and reliable method of cell stress determination (Ou et al. 2011; Menezes et al. 2021b). A MINI-PAM-II fluorometer (Walz, Germany) was used to evaluate the effects of UV-A irradiation on the photosynthetic activity of six *M. aeruginosa* strains (Table 2.2), as per Menezes et al. (2021b). The chlorophyll present in the cells is able to absorb light energy, which can drive photosynthesis, be dissipated through heat or be re-emitted as fluorescence (Murchie and Lawson 2013). The fluorescence can be measured by the MINI-PAM fluorometer, which is an instrument able to measure the maximal values of quantum yield of photosystem II (PSII) in cyanobacteria by F_v/F_m , where F_v is the difference between the true maximal fluorescence (F_m) and the minimal fluorescence (F_0). The maximal values of quantum yield can be used as a proxy for photosynthetic activity of the cells. Samples (400 μL) were added into the MINI-PAM fluorometer cuvette. The F_0 was determined by emitting a low intensity measuring light ($0.1125 \mu\text{mol m}^{-2} \text{s}^{-1}$, at specified level 6 and frequency at 15 Hz) for 20 seconds (Figure 2.6). Then, a saturating pulse (light intensity at specified level 10, $5000 \mu\text{mol m}^{-2} \text{s}^{-1}$) was emitted to generate F_m . After 40 seconds of the saturating pulse, actinic light was activated (actinic light intensity at specified level 3, $65 \mu\text{mol m}^{-2} \text{s}^{-1}$), which allowed the determination of the steady-state fluorescence (F_s) (Ogawa, Misumi and Sonoike 2017). This methodology would be enough for higher plants and green algae, however, the photosynthetic complex in cyanobacteria functions differently due to an effect called state transition. This means that there is a change in energy allocation between the two photosystems (PSI and PSII) in the cells, resulting in more energy being transferred to PSI (Ogawa, Misumi and Sonoike 2017). Due to this, after determining F_s , it was necessary to add 20 μL of 0.5 μM diuron, an herbicide capable of inhibiting photosynthesis, under actinic light to detect the true maximal fluorescence in cyanobacteria (F_m') by a saturating pulse (Figure 2.6). The addition of diuron, however, could be misleading, as it indicates the possible maximal fluorescence emitted by cells and it can show a false representation of the photosynthetic activity. For this reason, the photosynthetic activity of each of the *M. aeruginosa* strains was determined by the maximal values of quantum yield of PS II calculated by the ratio of the variable fluorescence F_v' (difference between F_m' and F_0) and F_m' (Equation 2.1)

and the results were confirmed by calculating the photosynthetic activity of *M. aeruginosa* cells by the maximal theoretical quantum yield of PS II represented by the ratio of the variable fluorescence F_V (difference between F_M and F_0) and F_M (Equation 2.2) (Campbell et al. 1998; Stirbet et al. 2018).

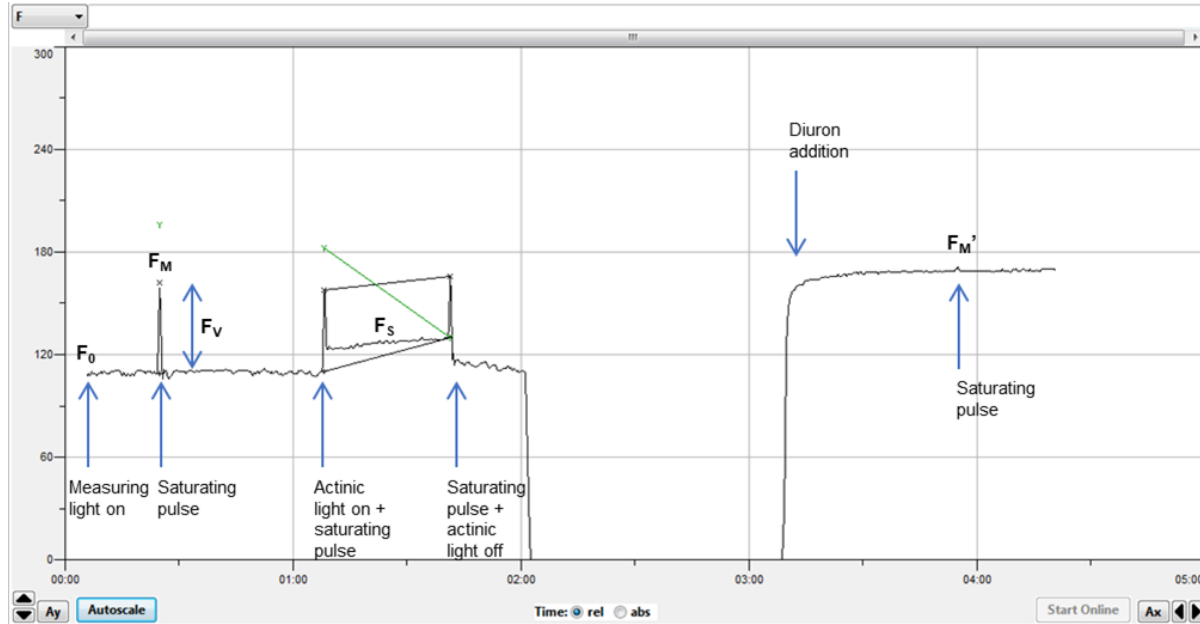


Figure 2.6: A typical spectrogram of *Microcystis aeruginosa* PCC7813 showing how F_0 , F_M , F_S and F_M' are formed. The measuring light excites chlorophyll and induces F_0 , the minimal level of fluorescence (reaction centres are open). A saturating pulse of light results in the formation of the maximal fluorescence, F_M (reaction centres are closed). Actinic light is applied generating a peak in the fluorescence of the cells, which then starts to decrease (photocatalysis is driven and energy is dissipated as heat because pigments start to protect the cells from damage caused by light). The steady-state level of fluorescence F_S is determined. Diuron is added to avoid energy transfer between the two photosystems in cyanobacteria and the true maximal fluorescence F_M' is determined.

$$\text{Maximal quantum yield} = \frac{F_M' - F_0}{F_M'} \quad (\text{Equation 2.1})$$

$$\text{Maximal theoretical quantum yield} = \frac{F_M - F_0}{F_M} \quad (\text{Equation 2.2})$$

2.2.6.2 *Microcystis aeruginosa* cell enumeration

A Multisizer 3 (Beckman Coulter, USA) can be used to measure any particulate material suspended in an electrolyte solution. This instrument allows the determination of particle number, volume, size (diameter) and surface area. An electric current flows through two electrodes, creating a resistance within the aperture where particles are collected. As particles pass through the aperture, the resistance changes creating pulses that are proportional to the particle

volume. The number of particles are determined by the number of pulses. Both surface area and particle diameter are determined based on the assumption that particles are perfect spheres.

A Multisizer 3 with a 50 µm aperture tube was used to determine *M. aeruginosa* cell density. Samples (200 µL) were diluted in 20 mL of Isoton carrier liquid (Beckman Coulter, USA). Cell counters are not a viability determination method, therefore, results only indicate particle enumeration. Particles in the range of 2.4 to 5.9 µm were considered intact cells, particles outwith this range were considered cell debris.

2.2.6.3 Ultra-performance liquid chromatography tandem mass spectrometry analysis of intra- and extracellular microcystin concentrations

After centrifugation for 10 minutes at 13000 x g, supernatant and cell pellet were separated and stored at -20 °C. On the day of analysis, the supernatant was thawed and dried by rotary evaporation in a Genevac (EZ-II evaporator, UK). Dried supernatant (extracellular/dissolved microcystins) and the cell pellet (intracellular microcystins) were resuspended in 1 mL of 50% methanol, placed in a dispersive extractor for 5 minutes at 2500 rpm followed by centrifugation for 10 minutes at 13000 x g, then final supernatants were immediately analysed (Figure 2.7).

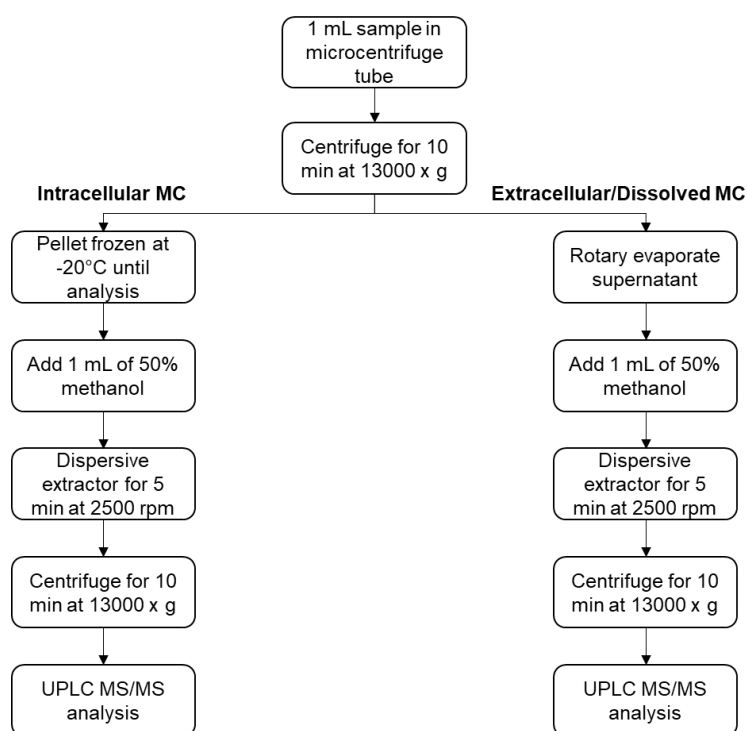


Figure 2.7: Schematic workflow for microcystins determination by ultra-performance liquid chromatography tandem mass spectrometry.

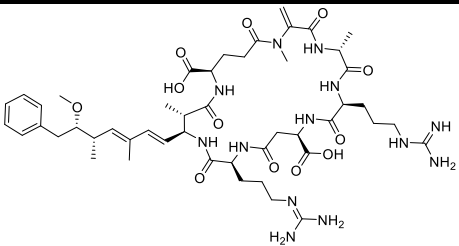
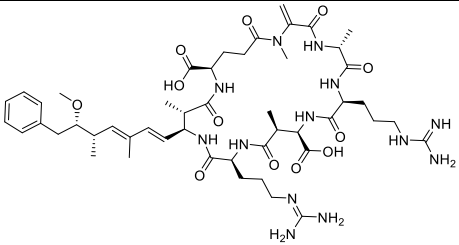
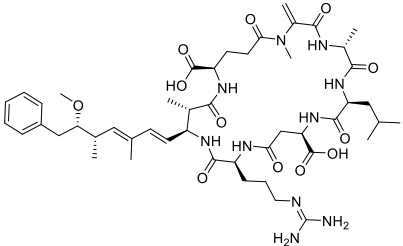
Quantification of microcystins was performed by a Waters Acquity UPLC system (Waters, UK) coupled to a triple quadrupole mass spectrometer (QqQ, Xevo TQ-XS, Waters, UK) with an electrospray ionization source (ESI) operated in positive ion mode (Table 2.3) as previously described by Turner et al. (2018).

Table 2.3: Analytical conditions of UPLC-MS/MS for microcystins quantification.

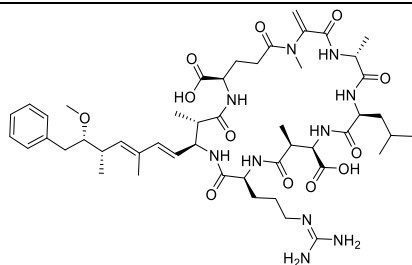
Parameters	Conditions									
Column	Waters Acquity UPLC BEH C18 column (2.1 x 50 mm, 1.7 µm particle size; Waters, UK)									
Mobile phase	A: 0.025% formic acid in ultrapure water (18.2 MΩ) B: 0.025% formic acid in acetonitrile									
Gradient	Time (min)	0	0.5	1.5	3	4	4.1	4.5	5	5.5
	Solvent B (%)	2	25	25	40	50	95	95	2	2
	Elution profile	6	6	6	6	6	6	6	6	6
Flow rate	0.6 mL min ⁻¹									
Injection volume	5 µL									
Column temperature	60 °C									

Samples were kept in the autosampler at 10 °C during analysis. The Xevo TQ-XS tune parameters were: capillary voltage 1.0 kV, desolvation gas flow 600 L h⁻¹ (N₂), collision gas flow 0.15 mL min⁻¹ (Ar), 150 °C source temperature and 600 °C desolvation temperature (Turner et al. 2018). The Multiple Reaction Monitoring (MRM) transitions, retention time, chemical structure and respective formula of all microcystin analogues evaluated were also determined (Table 2.4). Quantification was obtained by using standards (as per Enzo Life Sciences, USA) for calibration between 0.25 and 500 ng mL⁻¹. The limit of quantification was 0.25 ng mL⁻¹ for MC-DmLR, -YR, -Htyr, 0.5 ng mL⁻¹ for MC-LR, -LA and -WR and 1 ng mL⁻¹ for MC-DmRR, -RR, -LF, -LY and -LW.

Table 2.4: Chemical information of all microcystin analogues analyzed, considering their chemical structure, molecular formula, molecular weight, selected reaction monitoring (SRM) transitions and retention time in ultra-performance liquid chromatography tandem mass spectrometry system for the method.

Microcystin	Chemical structure	Molecular formula	Molecular weight (g mol ⁻¹)	MRM transitions ([M+H] ⁺ or [M+2H] ²⁺)	Retention time (min)
MC-DmRR		C ₄₈ H ₇₃ N ₁₃ O ₁₂	1024.2	513 ²⁺ >135	1.57
MC-RR		C ₄₉ H ₇₅ N ₁₃ O ₁₂	1038.2	520 ²⁺ >135.24	1.70
MC-DmLR		C ₄₈ H ₇₂ N ₁₀ O ₁₂	981.1	981.596 ⁺ >13.239	2.75

MC-LR

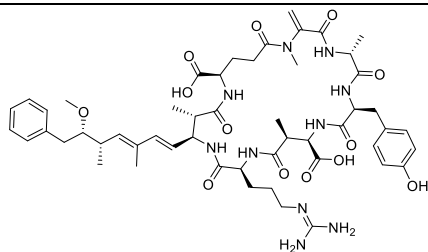
 $C_{49}H_{74}N_{10}O_{12}$

995.2

995.632*>135.243

2.69

MC-YR

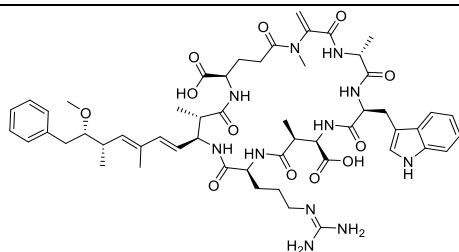
 $C_{52}H_{72}N_{10}O_{13}$

1045.2

1045.568*>135.303

2.51

MC-WR

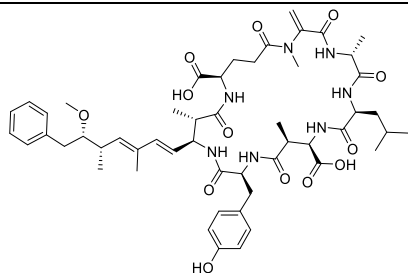
 $C_{54}H_{74}N_{11}O_{12}$

1069.2

1068.596*>135.242

2.86

MC-LY

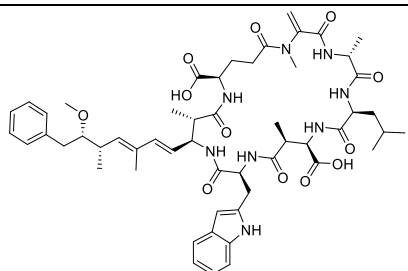
 $C_{52}H_{72}N_7O_{13}$

1003.2

1002.532*>135.368

3.81

MC-LW

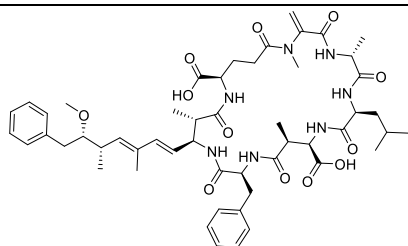
 $C_{54}H_{73}N_8O_{12}$

1026.2

1025.596*>135.24

4.30

MC-LF

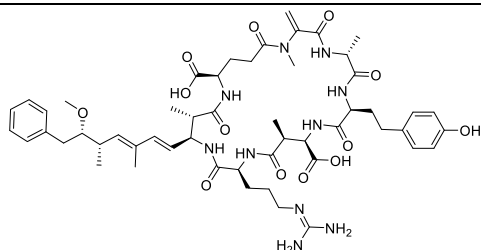
 $C_{52}H_{71}N_7O_{12}$

986.1

986.596*>135.245

4.37

MC-Htyr



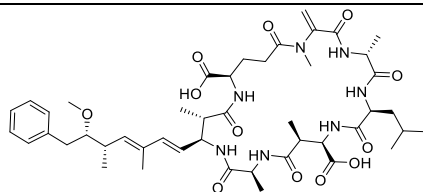
C₅₃H₇₅N₁₀O₁₃

1060.2

1059.632*>135.241

2.55

MC-LA



C₄₆H₆₈N₇O₁₂

911.1

910.579*>135.241

3.73

*Dominant ion observed in mass spectrometry analysis when singly protonated or **doubly protonated ion

2.2.6.4 Statistical analysis

The values shown are the results of the mean of triplicates for each treatment (UV-A LED, visible light LED and no LED samples). As three replicates were used during experiments ($n = 3$), testing for equal variance and normality was not seen as appropriate for a small level of replication as the results could be misleading, therefore, parametric assumptions were accepted as a low standard deviation was observed ($SD < 10\%$; Table A2.1). Two-way ANOVA was used to test for statistically significant differences caused by the effects of treatments on photosynthetic activity and total microcystins. A significance level of $p < 0.05$ was used to identify significant differences between the results. *Post hoc* Tukey analysis was applied to significant results.

2.3 Results and discussion

2.3.1 Effects of UV-A irradiation on *Microcystis aeruginosa* photosynthetic activity

An efficient and reliable way to evaluate the effects of a treatment on cyanobacteria is by photosynthetic activity measurements (Ou et al. 2011; Menezes et al. 2021b). The level of stress or damage caused by UV-A irradiation on *M. aeruginosa* cells can be observed by photosynthetic activity measurements as expressed as the F_V'/F_M' ratio (Figure 2.8.1) or as the F_V/F_M ratio (Figure 2.8.2). A decrease in the photosynthetic activity of cells can be explained by cyanobacterial stress. In the current study, cyanobacterial cells were considered stressed and/or damaged when the photosynthetic activity was below 0.3. According to Ogawa et al. (2017), cyanobacteria present photosynthetic activity values between 0.4 and 0.6, however, a photosynthetic activity value of 0.3 was still considered normal when observing the *M. aeruginosa* strains used in the current study, especially *M. aeruginosa* PCC 7806, which demonstrated an average photosynthetic activity value of 0.33 at time 0. When evaluating the photosynthetic activity of treated samples, the photosynthetic activity of all *M. aeruginosa* strains significantly decreased ($p < 0.05$) after only 24 hours of UV-A irradiation, except for *M. aeruginosa* B2666 ($p = 0.07$), which still demonstrated a photosynthetic activity reduction of 65% within 24 hours of UV-A LED irradiation (Figure 2.8.1A).

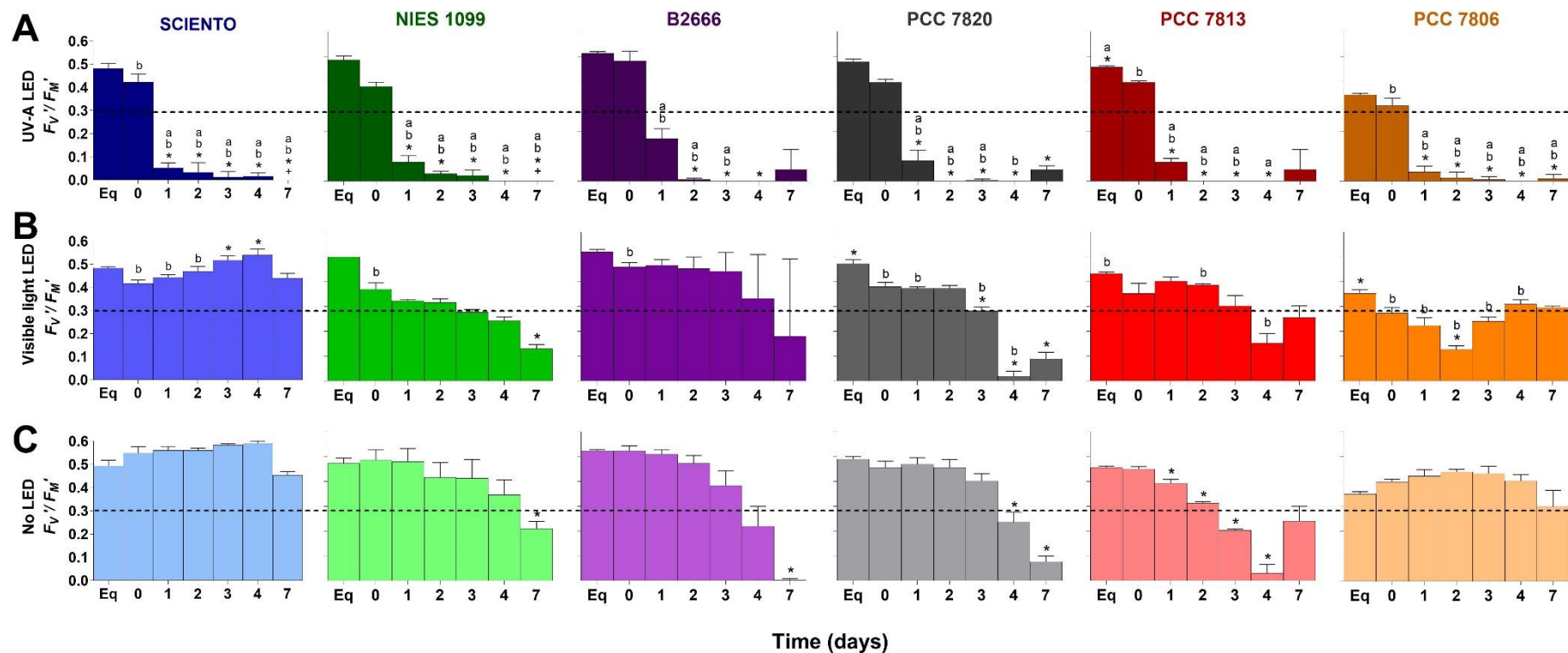


Figure 2.8.1: Photosynthetic activity (F_V/F_M') of six different *M. aeruginosa* strains exposed to overhead cool fluorescent light ($30 \mu\text{mol photons m}^{-2} \text{s}^{-1}$) in addition to (A) UV-A LEDs (365 nm and light intensity of 8 W m^{-2}); (B) visible light LEDs (400-700 nm and light intensity of 6 W m^{-2}); and (C) no additional LED irradiation over 7 days. F_M' was obtained after addition of diuron. UV-A LEDs were switched on after sampling at day 0. Dotted line represents the minimal photosynthetic activity value of healthy cyanobacterial cell. ($n = 3$, error bars = 1SD). *Significantly different from T_0 , ^aSignificantly different from visible light LED irradiated samples, ^bSignificantly different from no LED samples, +Data points with too few cells remaining for reliable quantification were considered below the limit of quantification.

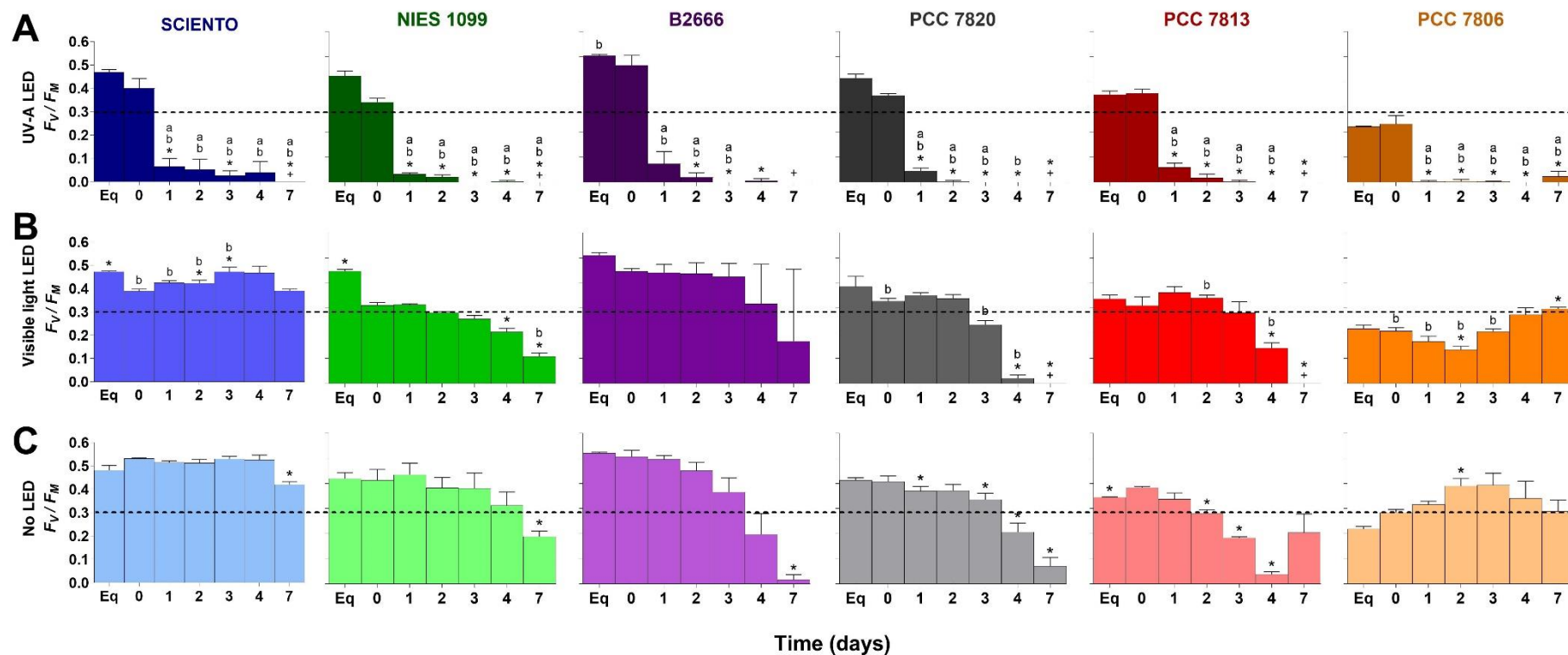


Figure 2.8.2: Photosynthetic activity (F_v/F_m) of six different *M. aeruginosa* strains exposed to overhead cool fluorescent light ($30 \mu\text{mol photons m}^{-2} \text{s}^{-1}$) in addition to (A) UV-A LEDs (365 nm and light intensity of 8 W m^{-2}); (B) visible light LEDs (400-700 nm and light intensity of 6 W m^{-2}); and (C) no additional LED irradiation over 7 days. UV-A LEDs were switched on after sampling at day 0. Dotted line represents the minimal photosynthetic activity value of healthy cyanobacterial cell. ($n = 3$, error bars = 1SD). *Significantly different from T_0 , ^aSignificantly different from visible light LED irradiated samples, ^bSignificantly different from no LED samples, ⁺Data points below the limit of quantification of MINI-PAM fluorometer.

The reduction on the photosynthetic activity of cultures within 24 hours of UV-A LED irradiation included a F_V'/F_M' value from 0.3 to 0.04 for PCC 7806, from 0.42 to 0.06 for SCIENTO, from 0.38 to 0.07 for NIES 1099, from 0.4 to 0.08 for both 7820 and 7813 and from 0.48 to 0.17 for B2666 (Figure 2.8.1A). It is possible that the UV-A LED irradiation caused a reduction in the photosynthetic activity of *M. aeruginosa* cells even earlier than 24 hours of UV-A irradiation, however, this was the first sampling point after UV-A LEDs were switched on. The photosynthetic activity remained very low for all samples irradiated by UV-A LEDs until day 7 of treatment (Figure 2.8.1A). *M. aeruginosa* SCIENTO and NIES 1099 appeared to have shown signs of recovery at day 7 of UV-A LED irradiation because of higher values of F_V'/F_M' initially observed, however, it is possible that the cell numbers were lower than the minimum cell density required for cell stress determination (Figure 2.9), as previously observed by Menezes et al. (2021a). The low cell numbers have resulted in an apparent photosynthetic activity recovery with higher F_V'/F_M' observed when using the MINI-PAM fluorometer, however, the uncharacteristically high statistical error for this sampling time suggests that cell number were below the quantification threshold.

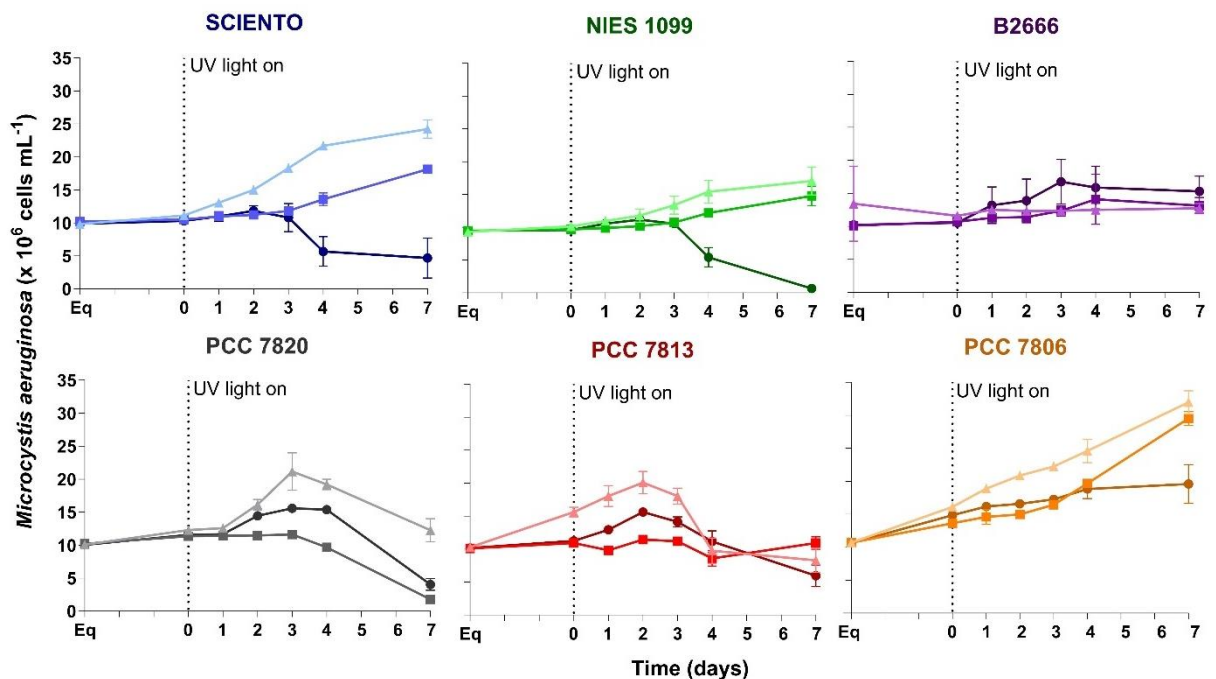


Figure 2.9: Cell density of six different *Microcystis aeruginosa* strains exposed to cool fluorescent light (30 $\mu\text{mol photons m}^{-2} \text{s}^{-1}$ or 7 W m^{-2}) and UV-A LEDs (365 nm, 8 W m^{-2} ; ● – dark shade), visible light LEDs (400–700 nm, 6 W m^{-2} , ■ – medium shade) and no additional irradiation (▲ – light shade) over 7 days. LEDs were switched on after 3 days acclimatization, prior to this a sample was removed (day 0). (n = 3, error bars = 1SD). Pictures show representative conical flasks containing *Microcystis aeruginosa* samples under different experimental conditions at day 7.

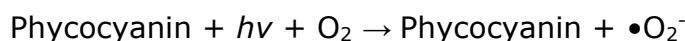
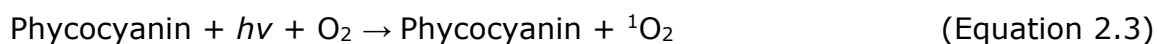
Although the *M. aeruginosa* photosynthetic activity of visible light LED irradiated samples (Figure 2.8.1B) was significantly different ($p < 0.05$) from some of the photosynthetic activity of no LED irradiated samples, especially for PCC 7820 and PCC 7806 (Figure 2.8.1C), it is possible to observe that both of these treatments (visible light LED and no LED irradiated samples) present the same trend of photosynthetic activity reduction or increase throughout the 11 days of experiment for all *M. aeruginosa* strains. For example, the F_v'/F_m' values obtained from *M. aeruginosa* NIES 1099 irradiated by visible light LED decrease from the beginning until the last day of the experiment and the same reduction trend is observed for *M. aeruginosa* NIES 1099 photosynthetic activity when no LED irradiation was used. Therefore, this indicates that the wavelength of the light used on photodegradation is a key factor for the treatment of *M. aeruginosa* cells.

The photosynthetic activity of *M. aeruginosa* cells was also estimated by evaluating the maximal theoretical quantum efficiency before the addition of diuron. The evaluation of the photosynthetic activity of *M. aeruginosa* cells using F_v/F_m demonstrated similar results as the ones obtained by F_v'/F_m' with the addition of diuron. A significant decrease ($p < 0.05$) in the photosynthetic activity of all *M. aeruginosa* strains was observed after only 24 hours of UV-A irradiation, except for *M. aeruginosa* B2666 ($p = 0.06$), however, a photosynthetic activity reduction of 84% was still observed for *M. aeruginosa* B2666 within 24 hours of UV-A LED irradiation (Figure 2.8.2A). Furthermore, the photosynthetic activity obtained from samples of treatment involving both visible light LED (Figure 2.8.2B) and no LED irradiated samples (Figure 2.8.2C) demonstrated a similar trend of photosynthetic activity change throughout the experiment for all *M. aeruginosa* strains. The results obtained by both F_v'/F_m' and F_v/F_m demonstrate the same pattern of treatment effects on *M. aeruginosa* cells.

Although the photosynthetic activity of most *M. aeruginosa* strains was significantly reduced ($p < 0.05$) from day 1 until the end of the experiment (Figure 2.8.1A), the UV-A effects were strain-dependent, which means different strains showed different photosynthetic activity response to UV-A irradiation. *M. aeruginosa* B2666 photosynthetic activity decreased by 65% after 24 hours of UV-A irradiation, whereas *M. aeruginosa* SCIENTO and PCC 7806 photosynthetic activity presented the higher response of 87%. Islam et al. (2019) observed different responses of two *Dolichospermum circinale* strains (CS451 and CS541)

when exposed to UV-B irradiation. During UV-B irradiation at 25°C, there was no significant photoinhibition rate for strain CS451, whereas the damage on photosynthetic activity was significant higher for CS537. Furthermore, the photoinhibition rate was higher for strain CS541 compared to CS537 at 30°C when high levels of UV-B irradiation were used (approximately 0.31 min⁻¹ for CS541 compared to 0.08 min⁻¹ for CS237). The different responses for each strain could be caused by variations in strain-specific photoreactive mechanisms (Islam, Beardall and Cook 2019). It is also possible that the effects caused by UV-A irradiation on each of the *M. aeruginosa* strains evaluated in the current study might be correlated with the intracellular concentration of phycocyanin, which means that the higher phycocyanin content inside the cells, the higher the UV-A effect on the cyanobacterial species. Commonly, studies select one specific strain of a species as a representative organism when evaluating the efficacy of a treatment. The difference in responses from different cyanobacterial strains of the same species highlight the importance of evaluating the impact of a treatment at strain, species and genus level before large-scale application.

A strategy that can be used for cyanobacteria control is UV photolysis by using UV-C (100 – 280 nm) and UV-B (280 – 315 nm) irradiation. In commonly studied UV-B and UV-C treatments, the cyanobacterial DNA absorbs the UV irradiation which result in DNA breakage and mutagenic lesions. Furthermore, UV-B and UV-C irradiation might cause cell membrane lysis due to oxidation of lipids and fatty acids (Ehling-Schulz and Scherer 1999; Sakai et al. 2007; Rastogi et al. 2014). UV-A irradiation, however, does not have the potential of causing direct damage to cyanobacterial DNA (Rastogi et al. 2010). It is likely that the photosynthetic apparatus of cells is involved in the photodegradation of cyanobacteria by UV-A irradiation and the photodegradation on the different *M. aeruginosa* strains was caused by the generation of intracellular reactive oxygen species (ROS). It is possible that UV-A irradiation passed through the cyanobacterial cell membrane without causing lysis reaching intracellular pigments, such as phycocyanin. Intracellular phycocyanin could have a photodynamic effect on the degradation of cells when exposed to UV-A irradiation. When phycocyanin is illuminated by UV-A irradiation, both singlet oxygen ¹O₂ (Equation 2.3) and the hydroperoxyl radical •O₂H (Equation 2.4) can be produced.



The hydroperoxyl radical has the potential to attack the cell structures from within, damaging the cells from the inside and causing subsequent degradation of the photosynthetic apparatus and removal of cells and toxins (Robertson, Lawton and Cornish 1999). The singlet oxygen, on the other hand, is more likely to attack the intracellular phycocyanin in preference to the other parts of the photosynthetic apparatus (Song, Bardowell and O'Shea 2007). Song et al. (2007) observed a photooxidative process caused by singlet oxygen on phycocyanin during microcystins removal by UV-A irradiation (350 nm). In the presence of sodium azide (NaN_3), which inhibits the singlet oxygen activity, the microcystin degradation was approximately 84%, whereas lower microcystin removal occurred (68%) when singlet oxygen was produced during phycocyanin illumination by UV-A (Song, Bardowell and O'Shea 2007). However, despite the fact that some phycocyanin is destroyed during UV photoinduced oxidation due to ${}^1\text{O}_2$, cells are destroyed and both intra- and extracellular toxins are removed, thus, this approach can be successfully applied for cyanobacteria control. Although phycocyanin maximum light absorption occurs at 620 nm, phycocyanin also presents a smaller absorbance peak at the range of 325-380 nm (Munawaroh et al. 2018). Light absorption at 620 nm does not contribute towards the generation of ROS and therefore, it has no influence on the removal of cells and toxins. On the other hand, the light absorbance peak at 325-380 nm lies completely within the UV-A spectrum. This allows phycocyanin to absorb UV-A irradiation at 365 nm and result in the photodynamic effect on both *M. aeruginosa* cells and microcystins. Beside phycocyanin, there are other phycobiliproteins present in cyanobacteria: phycoerythrin, phycoerythrocyanin and allophycocyanin. The phycobiliproteins are the major photosynthetic accessory pigments in cyanobacteria responsible for light harvesting. Phycobiliproteins present in cyanobacteria could also be involved in the photodynamic destruction of *M. aeruginosa* and microcystins. Allophycocyanin, for example, also presents a small absorption peak at 325-380 nm (Singh et al.

2015) and could also be responsible for photolytic destruction of cyanobacterial cells and toxins irradiated by UV-A by internal ROS generation.

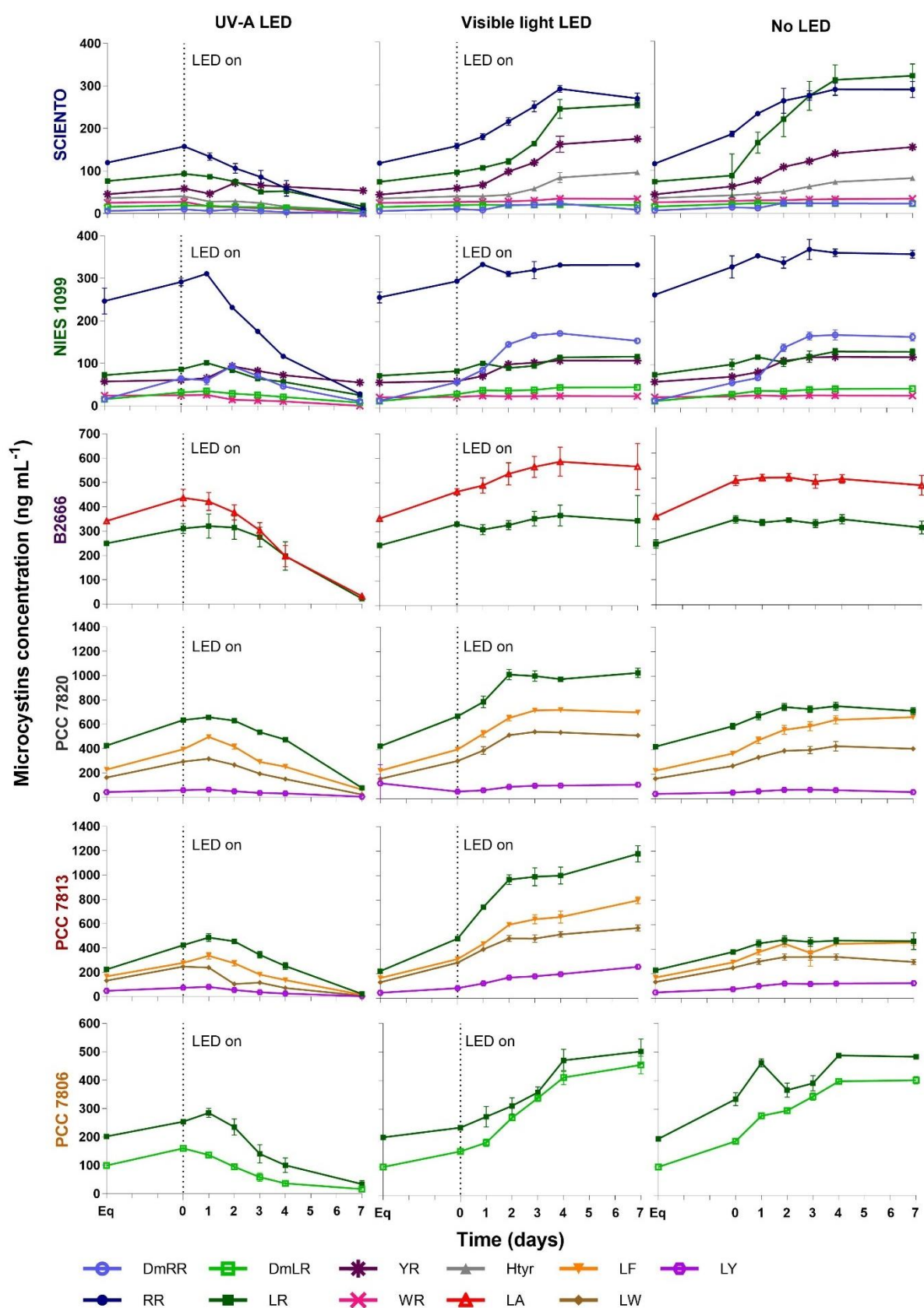
In the present study, cell enumeration was also carried out over 7 days of UV-A treatment (Figure 2.9), however, cell density did not provide a useful data of the effects caused by UV-A treatment on *M. aeruginosa* cells. As cells were damaged and lysed by UV-A irradiation, cell debris and other particles with the same size of viable cells were formed. The Multisizer particle counter was unable to differentiate healthy cells from other particles. To better understand the effects of UV irradiation on cyanobacteria, Noyma et al. (2021) studied the effects of a combination of UV-A (315 – 400) and visible light (400 – 700 nm) on *M. aeruginosa* and *Raphidiopsis raciborskii* over 5 days. Although there was a significant reduction in the photosynthetic activity of both species, the authors observed that both *M. aeruginosa* and *R. raciborskii* cell numbers increased by analysing cell density with an automated cell counter, with the inherent uncertainties that this method adds (Noyma et al. 2021). Both cyanobacterial species investigated in the Noyma et al. (2021) study were exposed to UV-A combined with visible light (light intensities of 10 W m^{-2} and $90 \mu\text{mol photon m}^{-2} \text{ s}^{-1}$ respectively), for only 4 hours per day over 5 days. In the current study, *M. aeruginosa* cultures were illuminated for 24 hours for 7 days (total irradiation time of 168 hours) by UV LEDs, whereas Noyma et al. (2021) only irradiated both *M. aeruginosa* and *R. raciborskii* cultures for a total of 20 hours by UV lamps. Considering one similarity that both studies applied UV-A light intensity of 10 W m^{-2} and 8 W m^{-2} , for Noyma et al. (2021) and the present study respectively, it is possible that the shorter UV-A exposure during Noyma et al. (2021) study allowed recovery of cells, whereas the continuous irradiation of UV-A over 7 days in the present study was able to damage the cells more permanently. This indicates that the amount of time for UV-A exposure or the application of a continuous UV-A treatment, as well as light source, has the potential to treat cyanobacteria *in situ*. One notable difference between both studies is the use of LEDs in the present study. Also, cyanobacteria present less ROS-scavenging enzymes as a mechanism for the protection against ROS generated by photolysis when compared with other eukaryotic phytoplankton. Ascorbate peroxidase and haem peroxidase are examples of two enzymes present in eukaryotes, however, none or little of these enzymes can be found in cyanobacteria (Sinha, Eggleton and Lochmann 2018). The application of LEDs as

an irradiation source of UV light is considered a safe approach for *in-situ* water treatment when compared to traditional lighting solutions e.g., compact fluorescent lamps (CFL) and incandescent bulbs. Those lights involve hazardous compounds such as mercury and other gases that can enter the environment (OSRAM 2009; de Souza et al. 2019). Furthermore, LEDs are more economical as only a small portion of the supplied energy is converted into heat, whereas incandescent lights convert more than 90% of the input energy into heat (Petroski 2002; Ying et al. 2014). Sodium vapor lighting and CFL can also be considered less efficient than LEDs since they require heat for a warm-up period to work (Peck, Ashburner and Schratz 2011). Another advantage on the use of LED is the lower energy requirement and therefore the lower associated costs. For example, while LEDs can present a luminous efficacy of around 150 lm W⁻¹, CFL and incandescent lights only show a luminous efficacy of 70 and 15 lm W⁻¹, respectively (Pattison, Hansen and Tsao 2018).

2.3.2 Effect of UV-A irradiation on eleven microcystin analogues

Microcystins are primarily inside cyanobacterial cells and become extracellular after release to the surrounding water due to cell wall lysis. The concentration of total microcystin analogues from six different *M. aeruginosa* strains (Table 2.2) was evaluated after UV-A irradiation. All *M. aeruginosa* strains were found to have a marked decrease of total combined microcystin content (sum of both intra- and extracellular microcystin analogues produced by a strain). The decrease was found to be 77% (SCIENTO), 77% (NIES 1099), 93% (B2666), 88% (PCC 7820), 95% (PCC 7813) and 88% (PCC 7806) after 7 days of UV-A exposure (Figure 2.10A). Tsuji et al. (1995) evaluated the degradation of microcystins during photolysis by sunlight, which irradiates the Earth surface at wavelengths higher than 295 nm. The authors observed that, under environmental conditions, around 7% of total microcystin was degraded when irradiated by sunlight for 15 days, whereas the addition of cyanobacterial pigments, including phycocyanin, increased their degradation by 55% over 15 days of exposure (Tsuji et al. 1995). Furthermore, Tsuji et al. (1995) showed that higher cyanobacterial pigment concentrations in solution resulted in higher microcystins degradation, corroborating the theory that the phycocyanin content inside of cells determines the level of degradation of both cyanobacterial cells

and toxins. During a study evaluating the TiO_2 photocatalytic decomposition of cyanobacterial toxins, Robertson, Lawton and Cornish (1999) observed that phycocyanin from cyanobacterial cells could promote the degradation of MC-LR by UV-A irradiation only. When no phycocyanin was present, UV light had no effect on the degradation of the toxin, however, phycocyanin behaved as a photodynamic molecule for MC-LR decomposition (Robertson, Lawton and Cornish 1999). These results support the hypothesis that the intracellular phycocyanin in conjunction with UV-A irradiation degrade both cyanobacterial cells and toxins.



Furthermore, the concentration of total combined microcystins from each *M. aeruginosa* strain exposed to UV-A irradiation at the end of the experiment was significantly lower ($p < 0.05$) compared to those exposed to either visible light LEDs or no LEDs (Figure 2.10). A detailed statistical analysis of the comparison of treatments was performed (Table A2.2). No significant difference was observed ($p > 0.05$) in the total combined microcystins of *M. aeruginosa* SCIENTO, NIES 1099 and B2666 between visible light LED samples and no LED samples for most of the sampling points. There was, however, a significant difference ($p < 0.05$) in the microcystins concentration between visible light LED and no LED samples for *M. aeruginosa* PCC 7820, PCC 7813 and PCC 7806. For the *M. aeruginosa* strains PCC 7820, PCC 7813 and PCC 7806, the microcystins concentration of no LED samples was 22%, 52% and 7% lower, respectively, than those from visible light LED treated samples at day 7 of irradiation. This indicates that the energy added into the system is not determinant on the photolytic degradation of *M. aeruginosa* cells and microcystins, but cells and toxins can be degraded depending on the wavelength of the light input.

Despite similarities in the chemical structure of microcystin analogues, different microcystins were found to have varying removal rates under UV-A irradiation. The removal was consistent for each microcystin analogue regardless of which cyanobacterial strain produced it, for example, MC-LR present in all *M. aeruginosa* strains used here was reduced by between 71% to 95% (Table 2.5). Furthermore, MC-DmRR was completely removed in *M. aeruginosa* SCIENTO and was found to decrease by 83% in *M. aeruginosa* NIES 1099 (Table 2.5). MC-WR was one of the analogues that had the lowest initial concentration in both *M. aeruginosa* SCIENTO and NIES 1099, and this analogue was completely eliminated in both strains by the end of the experiment (Table 2.5). MC-YR was notable with only 10% removal in *M. aeruginosa* NIES 1099 and 9% removal in *M. aeruginosa* SCIENTO after UV-A irradiation.

Table 2.5: Initial- and final concentrations as well as percent removal of total microcystin analogues by UV-A (365 nm) irradiation in six *Microcystis aeruginosa* strains.

SCIENTO											
Microcystin analogue	DmRR	RR	DmLR	LR	YR	Hytr	WR	LA	LF	LY	LW
Initial total concentration (ng mL ⁻¹)	9.9	157.7	19.0	93.4	58.8	40.4	27.5				
Final total concentration (ng mL ⁻¹)	0.0	9.8	5.9	16.8	53.8	8.1	0.0				
Removal (%)	100	94	69	82	9	80	100				
NIES 1099											
Microcystin analogue	DmRR	RR	DmLR	LR	YR	Hytr	WR	LA	LF	LY	LW
Initial total concentration (ng mL ⁻¹)	64.4	291.7	31.4	86.0	60.7		25.0				
Final total concentration (ng mL ⁻¹)	10.5	27.7	7.5	25.3	54.9		0.0				
Removal (%)	83	90	76	71	10		100				
B2666											
Microcystin analogue	DmRR	RR	DmLR	LR	YR	Hytr	WR	LA	LF	LY	LW
Initial total concentration (ng mL ⁻¹)				310.4				436.4			
Final total concentration (ng mL ⁻¹)				21.7				32.1			
Removal (%)				93				93			

PCC 7820											
Microcystin analogue	DmRR	RR	DmLR	LR	YR	Hytr	WR	LA	LF	LY	LW
Initial total concentration (ng mL ⁻¹)				633.8					393.3	58.0	292.0
Final total concentration (ng mL ⁻¹)				76.6					62.3	4.0	21.1
Removal (%)				88					84	93	93
PCC 7813											
Microcystin analogue	DmRR	RR	DmLR	LR	YR	Hytr	WR	LA	LF	LY	LW
Initial total concentration (ng mL ⁻¹)				423.4					276.6	73.0	246.5
Final total concentration (ng mL ⁻¹)				21.7					15.1	3.3	7.4
Removal (%)				95					95	95	97
PCC 7806											
Microcystin analogue	DmRR	RR	DmLR	LR	YR	Hytr	WR	LA	LF	LY	LW
Initial total concentration (ng mL ⁻¹)			159.8	253.6							
Final total concentration (ng mL ⁻¹)			16.4	33.6							
Removal (%)			90	87							

Microcystins are cyclic heptapeptides that share a common chemical structure with two variable amino acids (Rinehart, Namikoshi and Choi 1994). Amino acids can be photo-oxidated by direct photo-oxidation of the structure from the adsorption of UV irradiation or by indirect oxidation caused by the formation of ROS. Igarashi, Onoue and Tsuda (2007) observed the production of superoxide radical $\bullet\text{O}_2^-$ from tryptophan (W) and tyrosine (Y) irradiated by UV-A/B. Tryptophan produced the highest level of the superoxide radical, whereas other amino acids including alanine (A), leucine (L), arginine (R), and phenylalanine (F) did not produce any ROS (Igarashi, Onoue and Tsuda 2007). Both MC-WR and MC-LW have the amino acid tryptophan (W), so it is possible that the presence of tryptophan enabled superoxide radical production which resulted in the complete removal of MC-WR in both *M. aeruginosa* SCIENTO and NIES 1099 and high removal rates of MC-LW in PCC 7820 of 93% and PCC 7813 of 97% (Table 2.5). It is important to keep in mind that the experimental conditions evaluated represent a complex system with different microcystin analogues within each of the different *M. aeruginosa* strains. Other factors such as molecular conformations could have also influenced the removal of microcystins (He et al. 2015), which could explain why MC-YR was only degraded by 9-10%, whereas MC-LY was removed by 93-95%, even though both present tyrosine (Y) in their structure. It is also possible that the initial relative abundance of microcystins played a role in the degradation of each analogue. Both Dm-RR in *M. aeruginosa* SCIENTO and MC-WR presented a relatively low initial concentration when compared with other microcystin analogues and they were completely removed by UV-A irradiation after 7 days. Therefore, microcystin analogues with lower initial concentration may be removed faster by UV-A irradiation than other analogues with relative higher initial concentration (Chintalapati and Mohseni 2018; Chen, Ding and Zhou 2020).

2.3.3 Effects of UV-A irradiation on dissolved microcystin-LR

MC-LR was irradiated by UV-A (365 nm) LEDs over 7 days to further investigate the photo-oxidation effects of UV-A irradiation on toxins. Initially, pure water, AFW and BG-11 medium were used as experimental matrices. BG-11 medium was used as *M. aeruginosa* growth medium when evaluating the photolytic effects of UV-A LED irradiation on cells and toxins. When samples were irradiated by UV-A LEDs, there was a significant removal ($p < 0.05$) of MC-LR from day 1 of UV-A LED irradiation until the end of the experiment with a total MC-LR removal of 53% when BG-11 was used as experimental medium, however, a significant MC-LR removal ($p < 0.05$) of only 21% and 6% was observed at the end of the experiment when pure water and AFW were used, respectively (Figure 2.11). When no additional LED irradiation was applied to samples, there was a decrease in the MC-LR concentration of only 7% when BG-11 was used in comparison with an actual increase in the MC-LR concentration of 13% and 12% when pure water and AFW were used as experimental media, respectively (Figure 2.11). It is also possible to observe a difference in the MC-LR total degradation by UV-A LED irradiation when comparing dissolved MC-LR and intracellular MC-LR obtained from *M. aeruginosa* cell extracts. There was an average decrease of 86% in the MC-LR content (Table 2.5) when evaluating the degradation of MC-LR from cyanobacterial cell extracts, in comparison with a 53% MC-LR degradation when dissolved microcystin was used (Figure 2.11). These results indicate that besides the photodynamic effects caused by the *M. aeruginosa* intracellular content (e.g., phycocyanin), one or more nutrients present in BG-11 growth medium might be able to promote the generation of ROS and the subsequent degradation of microcystis by UV-A (365 nm) LED irradiation.

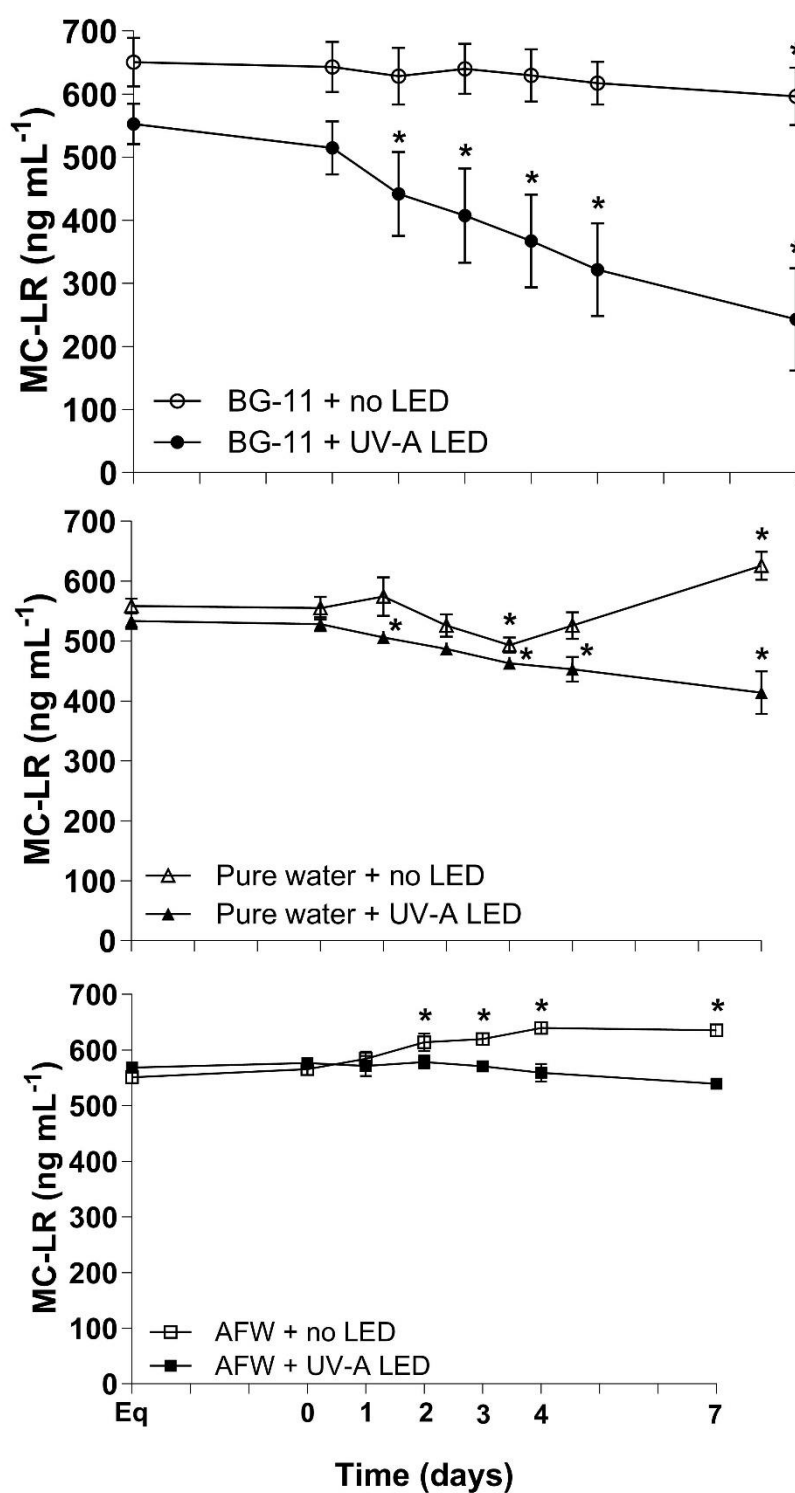


Figure 2.11: Dissolved microcystin-LR concentration (ng mL⁻¹) in different experimental media (● – BG-11 growth medium, ▲ – pure water and ■ – artificial freshwater) exposed to overhead cool fluorescent light (30 $\mu\text{mol photons m}^{-2} \text{s}^{-1}$) in addition to UV-A LEDs (365 nm and light intensity of 8 W m⁻²) or no additional LED irradiation over 7 days. Samples were incubated for 72 hours prior to UV-A LED irradiation. UV-A LEDs were switched on after sampling at day 0. (n = 3, error bars = 1SD). *Significantly different from T₀.

The iron from $\text{FeSO}_4 \cdot 7\text{H}_2\text{O}$ in BG-11 (Table 2.6) could have led to photo-fenton-like reactions when illuminated by UV-A LEDs, which then promoted ROS generation and enhanced the degradation of cells and toxins. Park et al. (2018) evaluated the MC-LR degradation by UV-A (352 nm) irradiation with a light intensity of 5.9 W m^{-2} over 5 minutes and the authors observed a degradation rate of 0.04 min^{-1} when a solution of $100 \mu\text{g L}^{-1}$ MC-LR in deionized water was used. When UV-A irradiation was combined with hydrogen peroxide (H_2O_2), a similar MC-LR degradation rate of 0.05 min^{-1} was observed, however, when both Fe(II) and H_2O_2 were used with UV-A, there was an increase in the MC-LR degradation rate to 0.065 min^{-1} . Even though only a small irradiation time was applied in the Park et al. (2018) study in comparison with the current study (5 minutes vs. 7 days of UV-A irradiation, respectively), it is possible to notice a difference in the MC-LR degradation rates when Fe(II) was present (Park et al. 2018), which indicates that iron from $\text{FeSO}_4 \cdot 7\text{H}_2\text{O}$ in BG-11 medium also plays a role in the UV-A light-driven oxidation of *M. aeruginosa* cells and microcystins. The production of ROS in photo-fenton-like systems can also be stimulated by the presence of ethylenediaminetetraacetic acid – EDTA (Šnyrychová, Pospíšil and Nauš 2006), which can also be found in BG-11 growth medium, even if only present in small concentrations (Table 2.6).

Table 2.6: Chemical composition of BG-11 growth medium, which is commonly used for the cultivation of cyanobacteria, based on Stanier et al. (1971).

Stock solution	Nutrient	Amount (g L ⁻¹)
1	NaNO_3	150
2	K_2HPO_4	40
3	$\text{MgSO}_4 \cdot 7\text{H}_2\text{O}$	75
4	$\text{CaCl}_2 \cdot 2\text{H}_2\text{O}$	36
5	Na_2CO_3	20
6	Citric acid	6
7	$\text{FeSO}_4 \cdot 7\text{H}_2\text{O}$	6
8	EDTA (di sodium)	1
	H_3BO_3	2.86
	$\text{MnCl}_2 \cdot 4\text{H}_2\text{O}$	1.81
Trace elements	$\text{ZnSO}_4 \cdot 7\text{H}_2\text{O}$	0.222
	$\text{Na}_2\text{MoO}_4 \cdot 2\text{H}_2\text{O}$	0.390
	$\text{CuSO}_4 \cdot 5\text{H}_2\text{O}$	0.079
	$\text{Co}(\text{NO}_3)_2 \cdot 6\text{H}_2\text{O}$	0.049

To further investigate the role of iron on the photolytic degradation of toxins by UV-A 365nm LED irradiation, dissolved MC-LR was irradiated by UV-A LEDs over 7 days using modified BG-11 as the experimental medium. The first experimental matrix used contained just the iron(II) sulfate heptahydrate usually used in BG-11 growth medium ($6 \text{ g L}^{-1} \text{ FeSO}_4 \cdot 7\text{H}_2\text{O}$ in pure water) and the second experimental matrix consisted of BG-11 growth medium without the $\text{FeSO}_4 \cdot 7\text{H}_2\text{O}$ content (Figure 2.12). There was a significant decrease ($p < 0.05$) in the MC-LR concentration from day 1 which then continued to decrease until the last day of UV-A LED irradiation when both modified BG-11 experimental matrices were used, however, a reduction of 82% on the MC-LR concentration was observed when the experimental medium containing $\text{FeSO}_4 \cdot 7\text{H}_2\text{O}$ was used, whereas 68% of MC-LR concentration decreased when no $\text{FeSO}_4 \cdot 7\text{H}_2\text{O}$ was present in the experimental medium (BG-11 - $\text{FeSO}_4 \cdot 7\text{H}_2\text{O}$). The increased MC-LR removal of 82% when the $\text{FeSO}_4 \cdot 7\text{H}_2\text{O}$ containing experimental medium was used demonstrates that the iron content in the BG-11 growth medium plays an important role in the degradation of *M. aeruginosa* cells and microcystins by UV-A irradiation (Figure 2.12). The 62% MC-LR removal when BG-11 - $\text{FeSO}_4 \cdot 7\text{H}_2\text{O}$ experimental medium was used, however, indicates that it is not iron exclusively that is important in the photooxidation of cells and toxins by UV-A irradiation, but other nutrients present in BG-11 growth medium must also be involved in the reaction.

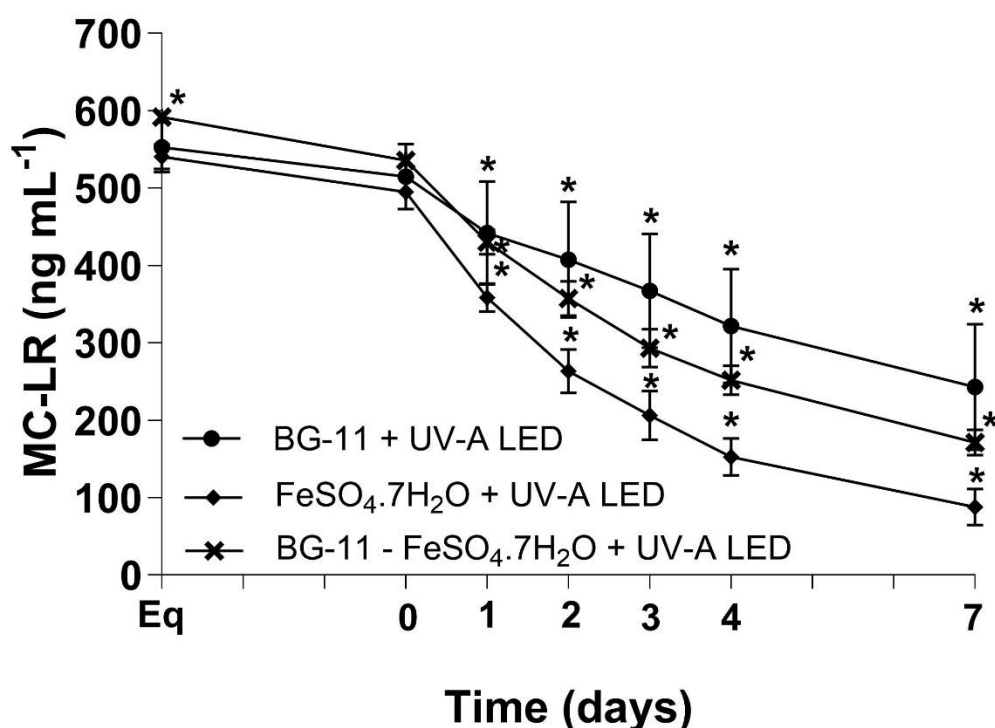
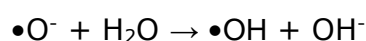


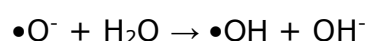
Figure 2.12: Dissolved microcystin-LR concentration (ng mL⁻¹) in ● – BG-11 and modified BG-11 experimental media (◆ – FeSO₄.7H₂O solution and × – BG-11 growth medium without FeSO₄.7H₂O content) exposed to overhead cool fluorescent light (30 μmol photons m⁻² s⁻¹) in addition to UV-A LEDs (365 nm and light intensity of 8 W m⁻²) over 7 days. Samples were incubated for 72 hours prior to UV-A LED irradiation. UV-A LEDs were switched on after sampling at day 0. (n = 3, error bars = 1SD). *Significantly different from T₀.

Reactive nitrogen species (RNS) and ROS such as hydroxyl radical (•OH) can be produced when nitrate is irradiated by UV light during water treatment and these radicals are responsible for degrading contaminants present in the water (Mack and Bolton 1999; Goldstein and Rabani 2007; Vinge et al. 2020). Under UV-A irradiation, the nitrate photolysis is very complex, however, the overall reaction can generate O₂ (Equation 2.3) (Mack and Bolton 1999). Further, nitrate photolysis can also generate •O (Equation 2.4) or nitrogen dioxide NO₂ and •O⁻, which can be protonated to generate •OH (Equation 2.5) (Goldstein and Rabani 2007).





Nitrite presents a small absorption peak around 360 nm (Mack and Bolton 1999; Goldstein and Rabani 2007) which means it can then absorb UV-A irradiation and produce more RNS ($\bullet\text{NO}$) and ROS, such as $\bullet\text{O}^-$, which is protonated to form hydroxyl radical $\bullet\text{OH}$ (Equation 2.6).



Sodium nitrate (NaNO_3) is the most abundant chemical present in BG-11 growth medium (Table 2.6), therefore, NaNO_3 might also be a contributing factor on the degradation of *M. aeruginosa* cells and microcystins by UV-A LED irradiation treatment.

Growth media is used for cultivation of microalgae, including cyanobacteria, to provide all micro and macronutrients required to the organisms. There are different types of growth media and they are usually selected based on the reason for cultivation (e.g., harvesting of any product) and if the organisms come either from freshwater or seawater (Pandey et al. 2023). BG-11 medium is one of the most widely used media for laboratory scale experiments involving cyanobacteria, however, other media are also used such as Kuhl, Chu-10 and ASM-1 medium, which all contain components in common with BG-11 medium (Table 2.7; Neelam and Chand Rai 2003; Kumar, Tyagi and Jha 2004; Yadav, Prajapati and Atri 2016; El-Sheekh et al. 2021; Jacinavicius et al. 2021). The nutrients present in the growth media of cyanobacteria (e.g., iron and nitrate) can interfere with the results of light-driven treatments for the removal of cyanobacterial cells and toxins, therefore, cyanobacteria growth media are not a suitable matrix for light-driven experiments. It is important to take these results into consideration when selecting the experimental matrix for water treatment experiments, especially these involving light-driven removal of cyanobacteria and cyanotoxins, because a controlled system with an inert matrix is desirable.

Table 2.7: Chemical composition and common nutrients of BG-11, Kuhl, Chu-10 and ASM-1 growth medium, commonly used for the cultivation of cyanobacteria.

Nutrient	BG-11 (Stanier et al. 1971)	Kuhl (Kuhl and Lorenzen 1964)	Chu-10 (Chu 1942)	ASM-1 (Gorham et al. 1964)
NaNO ₃	x			x
K ₂ HPO ₄	x			x
MgSO ₄ .7H ₂ O	x	x	x	x
CaCl ₂ .2H ₂ O	x	x		x
Na ₂ CO ₃	x		x	
Citric acid	x			
FeSO ₄ .7H ₂ O	x	x		
EDTA (di sodium)	x	x	x	x
H ₃ BO ₃	x	x	x	x
MnCl ₂ .4H ₂ O	x	x	x	x
ZnSO ₄ .7H ₂ O	x	x		
Na ₂ MoO ₄ .2H ₂ O	x			
CuSO ₄ .5H ₂ O	x	x		
Co(NO ₃) ₂ .6H ₂ O	x			
KNO ₃		x		
NaCl		x		
Na ₂ HPO ₄		x		x
NaHPO ₄		x		
(NH ₄) ₆ Mo ₇ O ₂₄ .4H ₂ O		x	x	
MnSO ₄ .H ₂ O		x		
Ca(NO ₃) ₂ .4H ₂ O			x	
KH ₂ PO ₄			x	
Na ₂ SiO ₃			x	
HCl			x	
FeCl ₃			x	x
MgCl ₂				x
ZnCl ₂				x
CoCl ₂				x
CuCl ₂				x

2.4 Conclusion

The role of nutrients from cyanobacterial growth media on light-driven experiments for the removal of *M. aeruginosa* cells and microcystins in laboratory was demonstrated. It was shown that nutrients, such as iron, interfere in the experimental results, which can be misleading when evaluating the efficacy of light-driven treatments for the degradation of cells and toxins.

The efficacy of economical low energy LED-based UV-A (365 nm) photolysis treatment for removal of cyanobacterial cells and toxins was demonstrated. Since this technology works in conjunction with a cell component specific to cyanobacteria (phycocyanin), it allows targeted removal for *in situ* application, easing the burden on potable water treatment.

Before the application of UV-A LED photolysis at full scale, the effects of this treatment on other cyanobacterial species and phytoplankton also need to be investigated. After full optimization, this treatment has real promise of providing a bespoke, scalable *in situ* treatment for toxic cyanobacteria. One option is the application of reactors based on UV-A photolysis in reservoirs prior to the intake of treatment plants or before the discharge of treated water into the environment as a polishing step of water treatment plants to enhance the degradation of these compounds.

Chapter 3

Preparation of TiO_2 , g- C_3N_4 and g- $\text{C}_3\text{N}_4/\text{TiO}_2$ coated glass beads for the photocatalytic degradation of a model natural pollutant

3	PREPATION OF TiO₂, g-C₃N₄ AND g-C₃N₄/TiO₂ COATED GLASS BEADS FOR THE PHOTOCATALYTIC DEGRADATION OF A MODEL NATURAL POLLUTANT	67
3.1	Introduction.....	69
3.1.1	Photocatalysts	69
3.1.2	Titanium dioxide as photocatalyst.....	71
3.1.3	Graphitic carbon nitride as photocatalyst	72
3.1.4	Light sources for photocatalyst activation	76
3.1.5	Nanopowdered photocatalysts coated onto immobilization matrices ..	78
3.2	Materials and methods.....	80
3.2.1	Reagents	80
3.2.2	Preparation of titanium dioxide (TiO ₂) and graphitic carbon nitride (g-C ₃ N ₄) coated beads and g-C ₃ N ₄ /TiO ₂ co-coated beads as catalysts for heterogenous photocatalysis	80
3.2.3	Photocatalytic removal of microcystin-LR	84
3.2.4	Visible light light emmiting diode (LED) selection for activation of g-C ₃ N ₄ coated beads.....	86
3.2.5	High-performance liquid chromatography analysis of microcystin-LR.	89
3.2.6	Statistical analysis.....	90
3.3	Results and discussion	91
3.3.1	Photocatalytic degradation of microcystin-LR by g-C ₃ N ₄ and g-C ₃ N ₄ /TiO ₂ coated beads and UV-A LED irradiation.....	91
3.3.2	Photocatalytic degradation of microcystin-LR by g-C ₃ N ₄ coated beads and visible light LED irradiation	96
3.3.3	Photocatalytic degradation of microcystin-LR by TiO ₂ coated beads and UV-A LED irradiation	101
3.4	Conclusion	105

3.1 Introduction

3.1.1 Photocatalysts

Heterogenous photocatalysis, when the photocatalyst and the medium are not in the same phase, is usually applied for the removal of contaminants from water, in comparison with homogenous photocatalysis (photocatalyst and medium are in the same phase) (Baruah et al. 2019). Photocatalysts are semiconductors capable of conducting electricity. The presence of a catalyst and light are determining factors for photocatalysis to occur. When illuminated by light of sufficient energy and at a specific wavelength, the catalyst absorbs the photon energy, which promotes one electron (e^-) from the valence band to the conduction band of the catalyst and creates a positively charged hole (h^+) in the valence band (Herrmann 1999). The electron transfer process is also known as photoexcitation state (Ameta et al. 2018). The electrons and holes react with oxygen and water to form radicals with high oxidative power that are responsible for degrading pollutants. These pollutants are degraded by being directly adsorbed onto the catalyst surface or indirectly by the action of radicals in close proximity to the catalyst (Qamar and Muneer 2005; Qamar, Muneer and Bahnemann 2006; Reddy and Kim 2015; Xing et al. 2018; Hassaan et al. 2023). The energy difference between the valence band and the conduction band is called band gap (E_g). The band gap depends on the type of materials, for example, conductors (metals) present a band gap lower than 1 eV ($E_g < 1.0$ eV), semiconductors present a band gap between 1.5 and 3 electron volts ($1.5 < E_g < 3.0$ eV) and insulators present a band gap higher than 5 electron volts ($E_g > 5.0$ eV) (Ameta et al. 2018).

Photocatalysts can be divided in oxide photocatalysts, for example, titanium dioxide (TiO_2), and non-oxide photocatalysts, such as copper sulfide (CuS), cadmium sulfide (CdS), zinc sulfide (ZnS) and carbon nitride (C_3N_4) (Herrmann 1999; Dalhat and Ahmad 2021). Each catalyst present different band gap (Table 3.1).

Table 3.1: Semiconductors and their respective band gaps (E_g).

Semiconductor	Band gap (eV)	Reference
Titanium dioxide (TiO_2)	3.0 (rutile) 3.2 (anatase)	(Mills and Le Hunte 1997; Toma et al. 2014; Mamba and Mishra 2016a; Ameta et al. 2018; Dalhat and Ahmad 2021)
Bismuth oxide (Bi_2O_3)	2.5 (tetragonal β - Bi_2O_3) 2.8 (monoclinic α - Bi_2O_3)	(Leontie et al. 2002; Dalhat and Ahmad 2021)
Iron (III) oxide or hermatite (Fe_2O_3)	2.2	(Mills and Le Hunte 1997; Sulania et al. 2016; Dalhat and Ahmad 2021)
Zinc oxide (ZnO)	3.2	(Mamba and Mishra 2016a; Dalhat and Ahmad 2021; Junaid et al. 2023)
Cadmium oxide (CdO)	2.1	(Ameta et al. 2018; Hussein et al. 2022)
Cuprous oxide (Cu_2O)	2.1	(Zhang, McMillon and McNatt 2013; Ameta et al. 2018; Pham et al. 2023)
Tin (IV) oxide or stannic oxide (SnO_2)	3.5	(Mamba and Mishra 2016a)
Tungsten trioxide (WO_3)	2.8	(González-Borrero et al. 2010; Vemuri, Engelhard and Ramana 2012; Mamba and Mishra 2016a; Dalhat and Ahmad 2021)
Molybdenum sulfide (MoS_2)	1.3	(Mak et al. 2010; Tongay et al. 2012)
Copper sulfide (CuS),	2.2	(Nagcu et al. 1997; Dalhat and Ahmad 2021; Shaikh et al. 2022; Escobar-Sánchez et al. 2023).
Zinc sulfide (ZnS)	3.7	(Madkour et al. 2016; Dalhat and Ahmad 2021; Wang et al. 2022; Liu et al. 2023).
Cadmium sulfide (CdS)	2.4	(Mills and Le Hunte 1997; Ameta et al. 2018; Dalhat and Ahmad 2021).
Carbon nitride (C_3N_4)	2.7	(Fagan et al. 2016a; Mamba and Mishra 2016a; Ong et al. 2016; Dalhat and Ahmad 2021; Gao et al. 2022; Wierzyńska et al. 2023).

3.1.2 Titanium dioxide as photocatalyst

Titanium dioxide (TiO_2) is an abundant material that is used in several commercial applications such as food industry, paint fabrication, sunscreen and toothpaste production (Fagan et al. 2016b). TiO_2 acts as a catalyst when light activates it with energy that is either equal to or greater than its band gap width of 3.2 eV. After energy is absorbed by TiO_2 , electrons (e^-) and holes (h^+) are produced and ultimately generate reactive oxygen species (ROS) with high oxidative power. The generated electron reacts with oxygen to produce superoxide radicals ($\bullet\text{O}_2^-$) and the hole reacts with H_2O to generate hydroxyl radicals ($\bullet\text{OH}$). Both types of ROS ultimately are responsible for degrading contaminants (Figure 3.1).

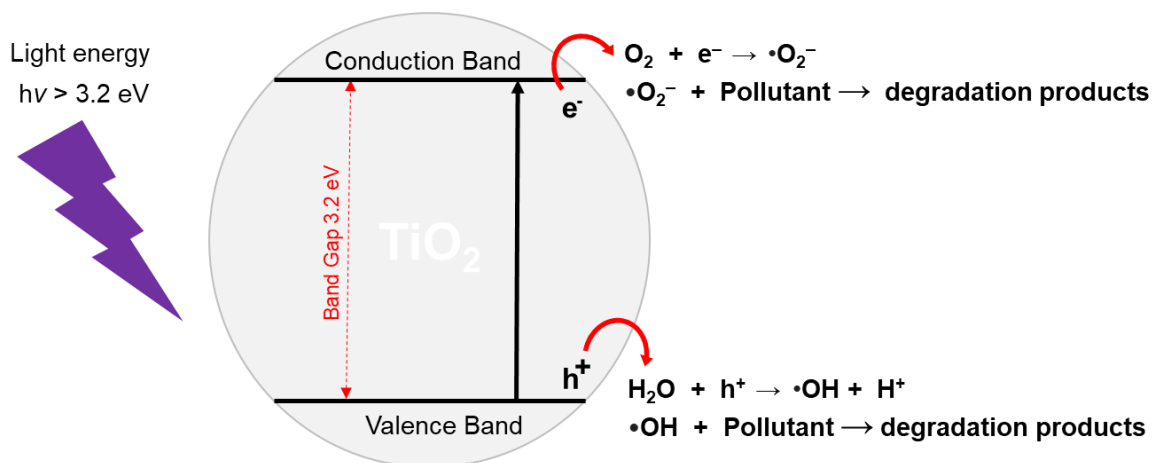


Figure 3.1: Activation of titanium dioxide (TiO_2) catalyst during heterogenous photocatalysis with the production of hydroxyl and superoxide radicals to degrade pollutants during water treatment.

Since around 1980, TiO_2 has been proposed as a photocatalyst during the photocatalytic degradation of cyanide (Frank and Bard 1977), which promoted the further development of TiO_2 in photocatalytic studies. Since then, TiO_2 has been commonly used as a photocatalyst in photocatalysis for the removal of pollutants, such as pesticides (Černigoj, Štangar and Trebše 2007; Affam and Chaudhuri 2013; Vicente et al. 2014; Yang et al. 2014; Camacho-Muñoz et al. 2020), pharmaceuticals (Elmolla and Chaudhuri 2010; Fawzi Suleiman Khasawneh and Palaniandy 2019; Silva et al. 2022), cyanobacteria and their secondary metabolites (Robertson, Robertson and Bahnemann 2012; Jacobs et al. 2013; Rodriguez-Gonzalez et al. 2019), bacteria and other contaminants of emerging concern (Fagan et al. 2016b).

TiO₂ presents three crystal forms: rutile, brookite and anatase, however, only anatase and rutile are commonly used as photocatalysts (Eddy et al. 2023). Because of the wide band gap energy required for the activation of TiO₂ of approximately 3.2 eV for anatase and 3.0 eV for rutile (Chen et al. 2015; Pinho et al. 2015; Hu et al. 2017), TiO₂ requires ultraviolet (UV) light to act as a catalyst (Zhao et al. 2014; Hu et al. 2017; Chang, Huo and Lin 2018). Solar irradiation can be used to achieve the energy required for TiO₂ activation, however, UV irradiation only corresponds to around 5% of sunlight radiation in comparison with 45% corresponding to visible light irradiation (Dong et al. 2015; Ola and Maroto-Valer 2015; Yang et al. 2017; Du, Lian and Zhang 2022), which limits the application of TiO₂ catalyst in the visible light spectrum range. Further, the low percentage of UV present in solar irradiation limits the photocatalytic efficiency when sunlight is used as light source in comparison with other sources of UV illumination (Pinho et al. 2015; Kanan et al. 2020). TiO₂ was previously considered non-toxic by the Food and Drug Administration (FDA), however, the European Food Safety Authority (EFSA) has stated that TiO₂ is no longer safe for food application due to possibility of inflammation and neurotoxicity effects (Younes et al. 2021). The toxicity of TiO₂ should also limit its application as photocatalyst during water treatment of contaminants.

3.1.3 Graphitic carbon nitride as photocatalyst

A more economic heterogenous photocatalysis process can be achieved when visible light is used for the activation of the photocatalyst. Graphitic carbon nitride (g-C₃N₄) is a metal-free semiconductor that can be used as photocatalyst for the degradation of contaminants because it presents chemical and thermal stability, low-cost and abundance (Dorrajati et al. 2017; Wang et al. 2018a; Li et al. 2020; Tang et al. 2020). g-C₃N₄ has been used as a photocatalyst in more recent photocatalysis studies for the removal of dyes (Paul et al. 2019; Aljuaid et al. 2023; Luo et al. 2023; Ganesan et al. 2024) and other pollutants, such as pesticides (Dorrajati et al. 2017; Raizada et al. 2019; Liu et al. 2020a; Ejeta and Imae 2021), pharmaceuticals (Niu et al. 2020; Luo et al. 2023) and cyanotoxins (Pestana et al. 2023) from aquatic environments.

g-C₃N₄ can be synthesized from the thermal treatment (pyrolysis) of different nitrogen-rich precursors that present direct bonding of C-N. g-C₃N₄ can be formed from urea, thiourea through cyanamide, melamine, dicyandiamide and

their polymerized derivatives (Figure 3.2). The precursors result in a molecular structure containing carbon and nitrogen atoms arranged in either a s-triazine or a tri-s-triazine (heptazine) unit (Inagaki et al. 2019; Prasad et al. 2020; Anjumol et al. 2022; Sharma et al. 2022; Luo et al. 2023). Both s-triazine or tri-s-triazine (heptazine) basic structures are planar and the g-C₃N₄ final structure can be formed by layers of these basic structures, hence the final structure is called graphitic carbon nitride (Figure 3.2).

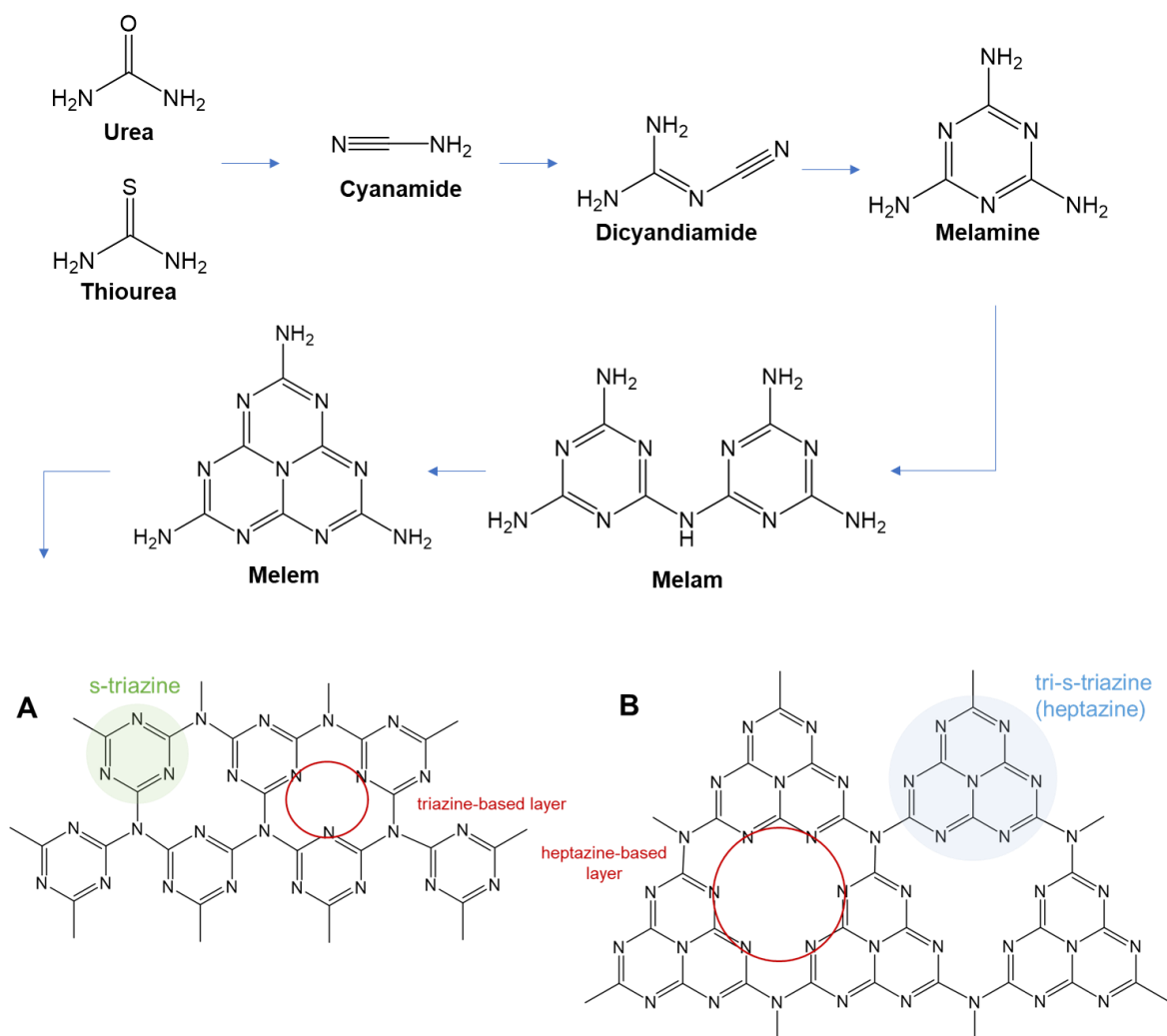


Figure 3.2: Graphitic carbon nitride (g-C₃N₄) precursors and g-C₃N₄ chemical structure containing A) s-triazine and B) tri-s-triazine (heptazine) basic unit. Characteristic intrinsic vacancies surrounded by nitrogen atoms are emphasized by red circles for each g-C₃N₄ basic unit.

g-C₃N₄ presents a band gap of 2.7 eV (-1.4 eV for the conduction band and 1.3 eV for the valence band), making g-C₃N₄ a catalyst favorable to visible light activation up to 460 nm (Tang et al. 2020; Hui et al. 2021). When energy is absorbed by g-C₃N₄, the electron shifts from the valence to the conduction band, resulting in a hole in the valence band. The electron reacts with oxygen to produce superoxide radicals ($\bullet\text{O}_2^-$) which are able to oxidize contaminants in water (Figure 3.3) (Xu et al. 2022). The hole created in the valence band can be responsible for directly oxidizing pollutants, but it can also oxidize the superoxide radicals produced, generating singlet oxygen ($^1\text{O}_2$). Singlet oxygen, however, presents short lifetime and therefore cannot present a main role in the degradation of pollutants (Figure 3.3) (Liu et al. 2015b; Grando et al. 2023).

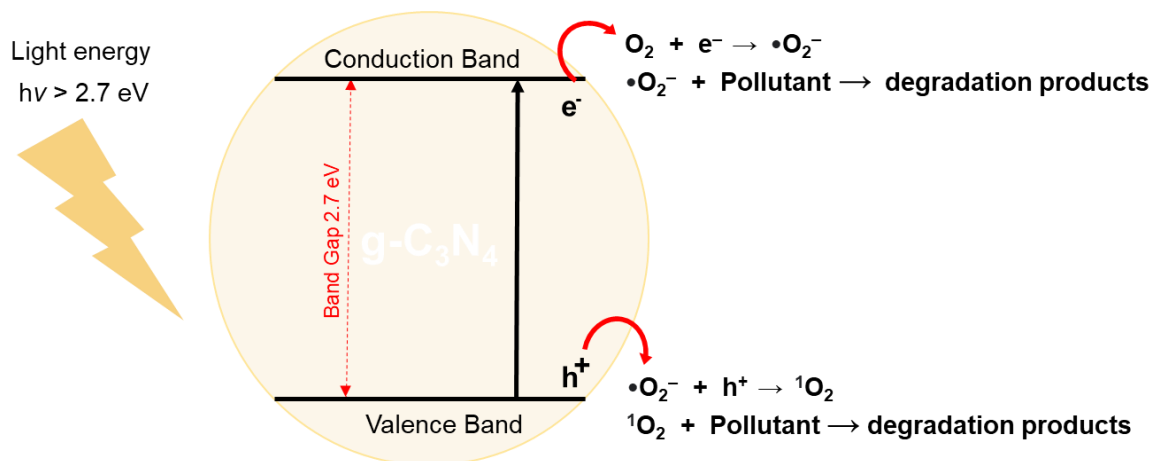


Figure 3.3: Activation of graphitic carbon nitride dioxide (g-C₃N₄) catalyst during heterogenous photocatalysis with the production of superoxide radical and singlet oxygen to degrade pollutants during water treatment.

Superoxide radicals generated by the reduction of oxygen can also promote the formation of other ROS, especially in more acidic conditions when there is a higher concentration of protons (h^+) (Dorrajati et al. 2017; Grando et al. 2023). The ROS are produced through a multiple electron-reduction mechanism that ultimately contributes to the degradation of contaminants. Superoxide radical $\bullet\text{O}_2^-$ can be protonated to generate hydroperoxyl radical $\bullet\text{O}_2\text{H}$ (Equation 3.1), which, in turn, can also be protonated and reduced to hydrogen peroxide H_2O_2 (Equation 3.2). Finally, hydrogen peroxide can be further reduced by an electron (e^-) to generate hydroxyl radicals $\bullet\text{OH}$ (Equation 3.3).



Despite the fact that g-C₃N₄ can be used as catalyst in the photocatalytic degradation of pollutants, there are some drawbacks associated with the application of bulk g-C₃N₄. The high recombination rate of the photogenerated electron-hole charged and the small specific surface area of the catalyst (Ismael 2020; Niu et al. 2020; Bairamis, Rapti and Konstantinou 2023), which occur due to structural defects from the stacking of the layers of bulk g-C₃N₄, can be a challenge (Rono et al. 2021). Further, bulk g-C₃N₄ as photocatalyst can also represent a challenge for water treatment applications. The recovery of the bulk g-C₃N₄ from water after treatment can be a hurdle due to the size of the photocatalyst, usually in micrometres or even nanometres (Liu et al. 2020b; Hui et al. 2021).

Photocatalysis can demonstrate superior performance when a heterojunction interaction is created using two different semiconductors (Pawar and Lee 2015). Heterojunction is the interface region between semiconductors that results in the presence of multiple valence and conduction bands. The different valence and conduction bands result in a lower band gap of the catalyst and it prevents recombination of charge carriers (electrons and holes) that ultimately are responsible for the production of ROS (Shetgaonkar et al. 2023). Heterojunctions allow photocatalysts that can only be activated by UV irradiation, such as TiO₂, to develop a visible light response due to the change in the electronic structures of metal oxides caused by the narrow band gap resulted from joining semiconductors. A heterojunction can be created when using g-C₃N₄ combined with TiO₂ as a photocatalyst (Li et al. 2017; Song et al. 2018a; Pestana et al. 2023). In this case, g-C₃N₄ is responsible for harvesting photons from visible light and generates electrons that can be transferred to TiO₂. This induces the activation of TiO₂ catalyst even when using visible light (Liu et al. 2015a). Therefore, the photocatalytic efficiency of combined g-C₃N₄ and TiO₂ should be enhanced and both g-C₃N₄ and TiO₂ will be responsible for producing ROS, resulting in a higher degradation of pollutants.

3.1.4 Light sources for photocatalyst activation

Solar irradiation can be used to activate catalysts during the photocatalytic removal of contaminants from water because sunlight is inexpensive, clean and sustainable. Sunlight, however, is not always available throughout the year, especially in areas further from the Equator (Weaver et al. 2001). Further, some photocatalysts (e.g., TiO_2) can only be activated with UV irradiation, which corresponds to only 5% of the sunlight spectrum (Dong et al. 2015; Ola and Maroto-Valer 2015; Yang et al. 2017; Du, Lian and Zhang 2022). As an alternative, other types of artificial light sources, such as light-emitting diodes, fluorescent lamps, incandescent bulbs and high intensity discharge (HID) lamps, can be used as continuous source of light supply for photocatalysis.

Incandescent lamps consist of a glass bulb with an inert gas and a metal filament usually made of tungsten, because of the high melting point of tungsten of 3,422 °C. An electric current is passed through the tungsten filament and the filament is heated to emit electromagnetic radiation and ultimately light. Incandescent bulbs have been widely applied in household and commercial lighting, however, only 10% of the electrical energy is converted into light, whereas the rest of the energy is released as heat (Petroski 2002; Ying et al. 2014). Incandescent light also present with low luminous efficacy of around 15 lm W^{-1} (Flesch 2006; Pattison, Hansen and Tsao 2018) and have short lifetime of around 1,000 hours (Sangwan et al. 2014) in comparison with other light sources (Table 3.2).

HID lamps emit light by sending an electrical discharge between two tungsten electrodes and through an ionized gas (plasma). The type of gas determines the type of HID lamp: mercury, sodium or metal halide. HID lamps are more efficient in emitting light than incandescent lamps (Table 3.2), because HID lamps do not lose a lot of energy due to heat (Pisupati 2022a). HID lamps present high luminous efficiency that can range from 50 to 140 lm W^{-1} (Flesch 2006). These lamps are mainly used for street lighting and industry applications where a higher luminous efficacy is required (Chakraborty, Goswami and Roy 2023), however, these lamps are usually not used in daily applications where lights are turned on and off regularly because some HID bulbs require an extended warm up time (Pisupati 2022a). HID lamps can also be considered toxic due to the production of radioactive substances such as krypton-85 and thorium (HERCA WG 2014) in the arc tube of the lamp.

In fluorescent lamps, an electric current passes through two metal electrodes that are placed on each side of a tube coated with phosphorous and containing an inert gas and some mercury. The inert gas usually consists of argon or krypton. Light is produced by energy release from excited mercury atoms, which is absorbed by the phosphorus coating to produce visible light. Fluorescent lamps present higher lifespan of 10,000 – 20,000 hours (Pisupati 2022b) and luminous efficacy of 70 – 80 lm W^{-1} (Flesch 2006) in comparison with only 1,000 hours lifespan and 15 lm W^{-1} luminous efficacy from incandescent light (Table 3.2). Fluorescent lamps, however, lose efficiency due to the warm-up period required in order to produce light (Peck, Ashburner and Schratz 2011). There are also extra costs associated with fluorescent lamps, for example, ballasts are devices responsible for controlling the electricity of the lamp that require energy and need to be replaced when the lamp is left on for long periods of time (Pisupati 2022b). Also, spent fluorescent lamps are hazardous waste, due to presence of mercury and radioactive substances such as krypton (OSRAM Opto Semiconductors 2009; de Souza et al. 2019).

Light emitting diodes (LEDs) consist of semiconductors. The color of the emitted light is determined by the energy required for the electron to pass through the band gap of the semiconductor. When an electric current passes through the semiconductor, electrons recombine with holes and release energy in the form of photons (light). Therefore, different semiconductors will generate light with different wavelength and each wavelength will present an unique color. LEDs have long lifespan of up to 100,000 hours (Heering 2004; Górecki 2013), they can be manufactured in very small sizes (Lin 2012), which allow the most various applications, and present fast switching on with no warmup time required. LEDs have lower power consumption and a very high luminous efficiency of 150 lm W^{-1} (Pattison, Hansen and Tsao 2018; Pisupati 2022c), however, lumen depreciation might occur in some systems. Lumen depreciation is the decrease of the LED lumen output (light intensity) over time. This could be aggravated by overheating of the system (Quan et al. 2015), therefore, an external heat sink or LEDs containing a heat sink at the back of the LED microchip might be required. Further, LEDs are a directional light source, which means LEDs are more efficient in their light irradiation by emitting light in a specific direction, whereas traditional light sources can lose around 50% of the energy output by emitting light in all directions (Alabaani 2013). To overcome the limitations from solar

irradiation and other conventional light sources, low-cost UV LEDs were evaluated as an alternative source of illumination for catalyst activation during photocatalysis experiments.

Table 3.2: Comparison of different light source for the activation of photocatalysts during the photocatalytic degradation of contaminants in aquatic environments.

Light source	Advantages	Disadvantages
High intensity discharge (HID)	<ul style="list-style-type: none"> • High luminous efficacy (50 – 140 lm W⁻¹) • Relatively high lifespan (5,000 – 24,000 hours) 	<ul style="list-style-type: none"> • Production of radioactive substances • Production of hazardous substances • Warm up time required
Sunlight	<ul style="list-style-type: none"> • Inexpensive • Sustainable light source 	<ul style="list-style-type: none"> • Only small percentage of spectrum corresponds to UV irradiation • Limited availability in some regions
Incandescent	<ul style="list-style-type: none"> • Widely applied 	<ul style="list-style-type: none"> • Short lifespan (1,000 hours) • Low luminous efficacy (15 lm W⁻¹)
Fluorescent light	<ul style="list-style-type: none"> • Relatively high lifespan (10,000 – 20,000 hours) • Good luminous efficacy (70 – 80 lm W⁻¹) 	<ul style="list-style-type: none"> • Production of hazardous substances • Associated costs with replacement of components (e.g., ballasts) • Warm up time required
Light emitting diode (LED)	<ul style="list-style-type: none"> • High luminous efficacy (150 lm W⁻¹) • Long lifespan of up to 100,000 hours • No warmup time required • Available in small sizes • Directional light source 	<ul style="list-style-type: none"> • Lumen depreciation

3.1.5 Nanopowdered photocatalysts coated onto immobilization matrices

Photocatalysts are usually applied in the form of a slurry during photocatalytic removal of pollutants, where the catalyst is present in the form of suspended particles (powdered catalyst) in aqueous solution due to a higher catalyst surface area that enhances the photocatalytic activity. The use of powdered catalyst, however, might interfere in the light penetration for catalyst activation

(Marcelino and Amorim 2019). Also, most photocatalysts present higher density than water, leading to their sinking and subsequent accumulation at the bottom of the aquatic environment (Hui et al. 2021). Further, this might represent loss of the powdered photocatalyst and secondary pollution of aquatic environments by the photocatalyst (Mamba and Mishra 2016b), hence the necessity to recover the catalyst from water after treatment. Alternative methods of catalyst application or separation during photocatalysis are required to overcome the challenges of recovering powdered photocatalyst from water after the photocatalytic treatment. Magnetic photocatalysts (e.g., haematite, maghemite, magnetite and ferrites) have been developed to allow catalyst recovery from the treated water by using an external magnetic force (Mamba and Mishra 2016b; Miceli et al. 2021), however, this alternative does not seem feasible on a larger scale or during at source applications of photocatalysis since the photocatalyst remains in the powdered form after incorporation of magnetic nanoparticles. Further, the use of magnets is required to recover the catalyst from solution. Catalyst recovery from water can also be achieved by centrifugation and filtration of the water during laboratory scale experiments (Marcelino and Amorim 2019; Odling and Robertson 2019), however, the application of this methodology at large scale also becomes impractical. An effective approach for photocatalyst recovery is to immobilize powdered photocatalysts onto a substrate (immobilization matrix) that can easily be removed from water. The textile dye orange solimax was successfully degraded by photocatalysis using ZnO immobilized in alginate beads as photocatalyst (Gonçalves et al. 2021). Cunha et al. (2018) used borosilicate glass spheres immobilized with TiO₂ (P25) for the degradation of 96% of the dye methylene blue. Borosilicate glass was also coated with TiO₂ in El Yadini et al. (2014) study which used two types of TiO₂ (Millennium PC500 and Degussa P25) and in the study from Akbari Shorgoli and Shokri (2017) to degrade pesticides. Beads made of polyethylene terephthalate (PET) were used as TiO₂ immobilization matrix for the photocatalytic degradation of the pharmaceutical pregabalin (Evgenidou et al. 2023). TiO₂ was also immobilized onto other materials such as glass slides (Žabar et al. 2012; Pišková et al. 2015), silica gel (Echavia, Matzusawa and Negishi 2009; Negishi et al. 2012), clay beads (Sraw et al. 2018), stainless steel mesh (Byrne, Subramanian and Pillai 2018) and aluminium plates (Gar Alalm et al. 2018) for the photocatalytic removal of organic pollutants. Nieto-Sandoval et al. (2023)

evaluated the photocatalytic degradation of pharmaceuticals from water using g-C₃N₄ immobilized in a polyvinylidene fluoride (PVDF) polymeric membrane. g-C₃N₄/TiO₂ was immobilized onto a glass substrate (Zhao et al. 2020) and onto a cement paste (Feng and Li 2021) for the removal of the dye rhodamine B and the pharmaceutical tetracycline hydrochloride, respectively.

In the current study, TiO₂ and g-C₃N₄ were coated onto floating glass beads made of recycled glass to overcome some hurdles for photocatalysis application, such as catalyst recovery from water and costs associated with irradiation. The evaluation of the photocatalytic system containing TiO₂, g-C₃N₄ or g-C₃N₄/TiO₂ coated beads and economical LEDs was performed using the water contaminant, microcystin-LR, as a model natural compound for other organic pollutants.

3.2 Materials and methods

3.2.1 Reagents

Reagent grade chemicals (Fisher Scientific, UK) were used for the preparation of artificial freshwater (AFW) solution (Akkanen and Kukkonen 2003). Acetonitrile, methanol and trifluoroacetic acid (Fisher Scientific, USA) were used for high-performance liquid chromatography tandem photo diode array (HPLC-PDA) analysis of microcystin-LR. Ultrapure water (18.2 MΩ) obtained by an ELGA PURELAB system (Veolia, UK) was used to prepare all solutions. Microcystin-LR was acquired as per Enzo Life Sciences, >95% purity.

3.2.2 Preparation of titanium dioxide (TiO₂) and graphitic carbon nitride (g-C₃N₄) coated beads and g-C₃N₄/TiO₂ co-coated beads as catalysts for heterogenous photocatalysis

Porous foamed glass beads made with recycled glass (2 – 4 mm diameter; Poraver, Germany) were used as the immobilization matrix for the coating processes with TiO₂, g-C₃N₄ and g-C₃N₄/TiO₂.

Initially, uncoated glass beads were sieved to achieve a desired diameter of 3 – 4 mm. Beads were prepared by a bead wash followed by a pre-calcination of the beads. Uncoated beads were washed using a solution of 50% acetone in an ultrasonic bath (Decon FS Minor Ultrasonic Bath) for 20 minutes. Beads were removed from the 50% acetone solution and placed in an oven at 100 °C for 2 hours until beads were dry. Beads were washed with distilled water, placed in an

alumina crucible and pre-calcinated in a muffle furnace (Carbolite Gero RHF 15/3 with EPC3008P10 programmer) at 500°C for 5 hours (heating and cooling ramp rate of 5 °C min⁻¹).

TiO₂ coated glass beads were prepared by using a wet coating process (Pestana et al. 2020). TiO₂ (P25, Rutile/Anatase: 85/15, 99.9%, 20 nm particle size; Degussa Evonik, Germany) was used as the precursor for the TiO₂ coated beads. Pre-calcinated beads (3 g) were placed in a beaker containing a 0.1 g mL⁻¹ TiO₂ P25 degussa in deionized water with 2 drops of Hypermer KD6 (dispersant for aqueous system; Croda, United Kingdom) for 10 minutes (Figure 3.4A). Beads were removed from the TiO₂ suspension (Figure 3.4B and Figure 3.4C) and placed in the oven at 100 °C for 2 hours until beads were dry. Beads were placed in an alumina crucible and calcinated in a muffle furnace for 1 hour at 500 °C (ramp rate of 5 °C min⁻¹). This coating process deposits approximately 2% (w/w) of TiO₂ onto the beads (Figure 3.4D).

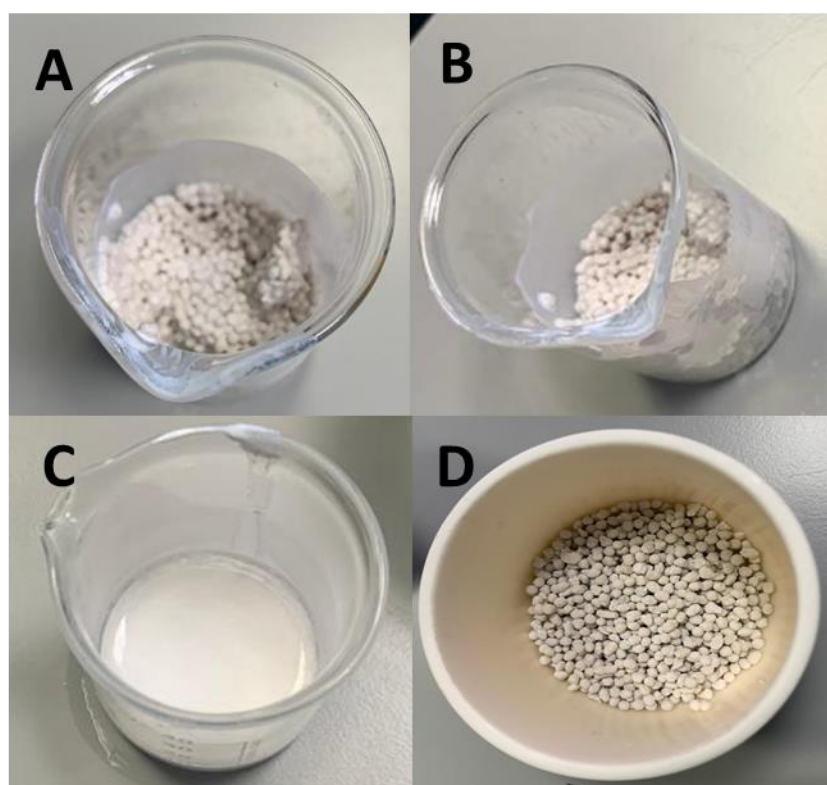


Figure 3.4: Preparation of titanium dioxide (TiO₂) coated beads preparation. A) beads submerged in TiO₂ suspension, B) wet beads after submersion in TiO₂ suspension, C) TiO₂ suspension and D) TiO₂ coated beads after one coating procedure with approximately 2% (w/w) of TiO₂ onto the bead surface.

The process consisting of adding beads to the TiO_2 suspension, removing, drying and calcinating was repeated five times until a final TiO_2 concentration of around 10% (w/w) was achieved, as a final step, beads were placed in a muffle furnace for 10 hours at 500 °C (ramp rate of 5 °C min⁻¹) during the final calcination process. TiO_2 coated beads were washed with ultrapure water to remove any residual precursor that was not immobilized onto the bead surface and dried in the oven at 100 °C for 2 hours (Figure 3.5A).



Figure 3.5: A) Titanium dioxide (TiO_2) and graphitic carbon nitride ($\text{g-C}_3\text{N}_4$) coated glass beads to be used as catalysts during heterogenous photocatalysis.

For $\text{g-C}_3\text{N}_4$ coated glass beads, melamine (99%, Fisher Scientific, United Kingdom) was the precursor (Hui et al. 2021). Melamine (8 g) was sieved onto 20 g of pre-calcinated beads wetted with ultrapure water (Figure 3.6A). Beads were transferred to an alumina crucible (Figure 3.6B) and placed in a drying oven for 2 hours at 100 °C until beads were dry (Figure 3.6C). The alumina crucible was sealed with a lid and aluminium foil and then placed in the muffle furnace at 500 °C for 10 hours (calcination time) at ramp rate of 5 °C min⁻¹. The coating procedure deposits approximately 10% (w/w) of $\text{g-C}_3\text{N}_4$ onto the bead surface (Figure 3.6D). Coated beads were then submerged in deionized water and removed until the water was clear for fines removal (Figure 3.6E and Figure 3.6F). Coated beads were placed in the oven at 100 °C for 2 hours until dryness (Figure 3.5B).

The production of $\text{g-C}_3\text{N}_4/\text{TiO}_2$ co-coated beads consisted of submerging $\text{g-C}_3\text{N}_4$ coated beads in the same TiO_2 P25 suspension prepared for the wet coating of TiO_2 coated beads. Beads were then kept in the drying oven at 100 °C until dryness. The beads were then placed in an alumina crucible and placed in the

muffle furnace at 500 °C for only 1 hour. g-C₃N₄/TiO₂ co-coated beads were then washed and dried in the oven as previously described. This coating procedure deposits approximately 12% (w/w) of catalyst onto the bead surface (10% w/v g-C₃N₄ + 2% w/v TiO₂).

The amount of uncoated glass beads and precursors (melamine and TiO₂ P25) used during the techniques for the coating of g-C₃N₄, TiO₂ and g-C₃N₄/TiO₂ represent ratios and can be scaled up as long as the proportions are followed.

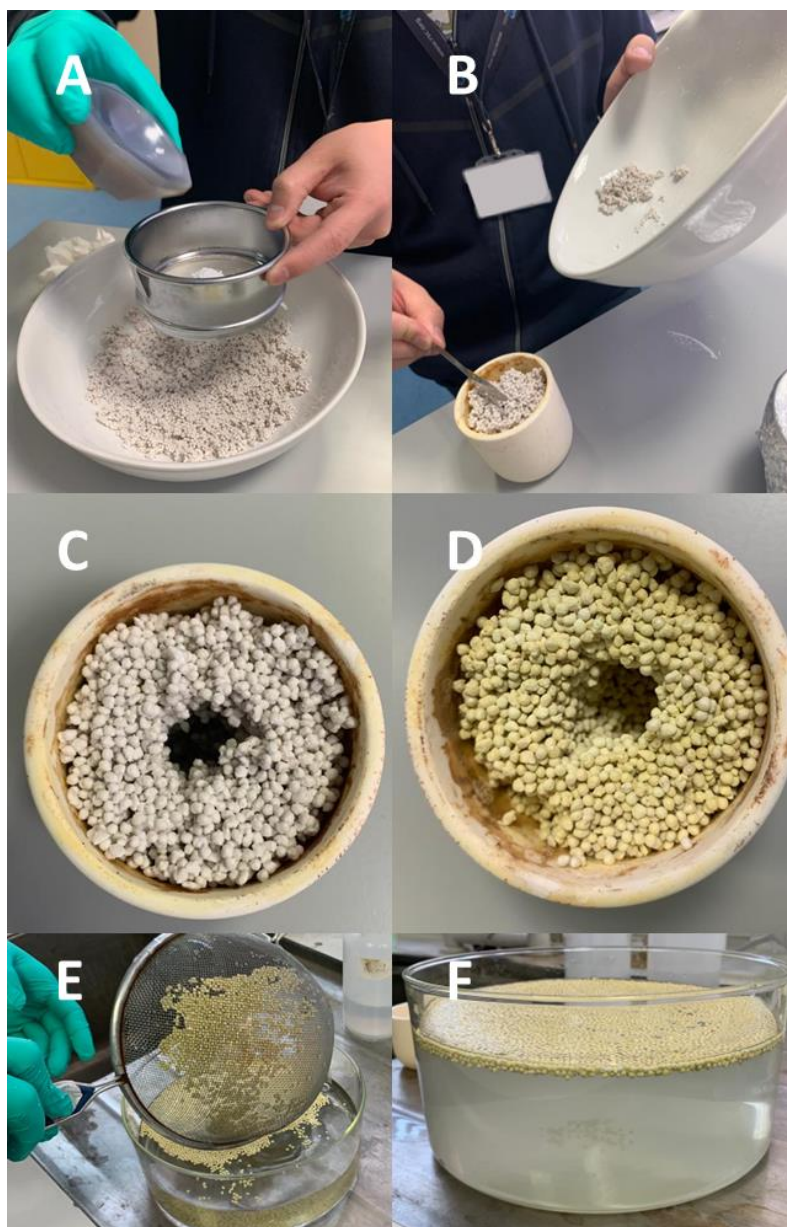


Figure 3.6: Graphitic-carbon nitride (g-C₃N₄) coated beads preparation. A) Adding the melamine precursor onto the beads surface, B) beads containing melamine added to alumina crucible, C) beads inside alumina crucible before calcination in the muffle furnace, D) beads inside alumina crucible after calcination in the muffle furnace, E) beads added to deionized water for washing procedure and F) cloudy deionized water due to free g-C₃N₄ that was not coated onto the bead surface.

3.2.3 Photocatalytic removal of microcystin-LR

The efficiency of g-C₃N₄ coated beads for the photocatalytic removal of MC-LR was evaluated. Reactors made of cardboard (30 x 21 cm) were prepared containing UV-A 365 nm light emitting diode (LED) irradiation (600 individual UV-A LEDs 365 nm; 8 W m⁻²). Each reactor was placed on top of beakers (100 mL; irradiated area of 19.6 cm² illuminated by approximately 30 individual LEDs), irradiating the g-C₃N₄ coated beads from above at a distance of 6 cm from the experimental solution. Each beaker contained 50 mL of 5 mg L⁻¹ MC-LR in artificial fresh water (AFW; Akkanen and Kukkonen 2003) with gentle agitation using a magnetic stirrer (Figure 3.7).

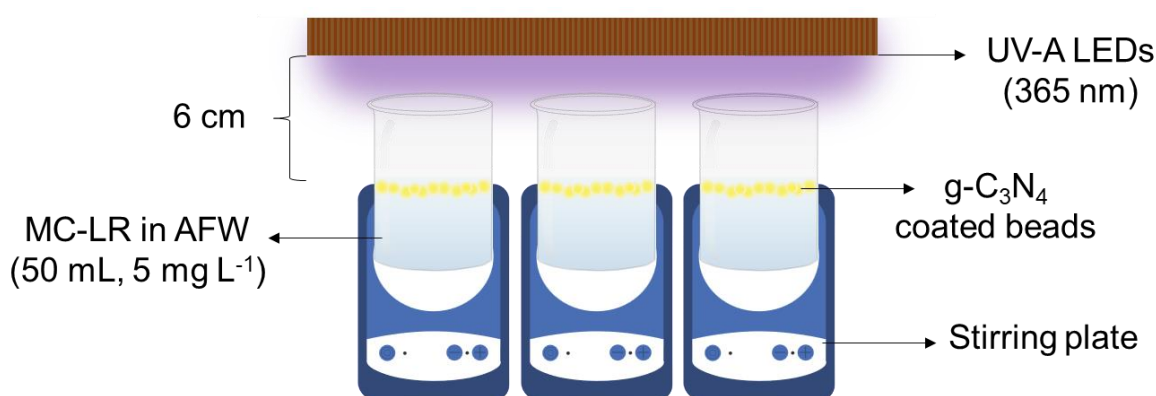


Figure 3.7: Representation of UV-A/g-C₃N₄ photocatalytic system used for the removal of microcystin-LR. Representation of the photocatalytic reactor used, stirring plates and beakers containing microcystin-LR experimental solution and g-C₃N₄ coated beads.

An initial sample (500 µL) was removed from the MC-LR experimental solution for analysis (C_0) and 700 mg of coated beads were added (0.14% g-C₃N₄ w/v). The amount of beads was established based on previous studies were 0.15% (w/v) g-C₃N₄ beads were used for the photocatalytic degradation of MC-LR by natural sunlight (Pestana et al. 2023). Dark adsorption occurred for 15 minutes and another sample was removed (C_{Eq}). Samples were then exposed to UV-A LED irradiation, removed at pre-determined intervals (Table 3.3), placed in 1.5 mL Eppendorf tubes, centrifuged for 30 seconds at 13000×*g* and the supernatant analyzed by high-performance liquid chromatography with photodiode array detector (HPLC-PDA; Waters, United States) for MC-LR quantification. Light control samples were prepared using 5 mg L⁻¹ MC-LR in AFW solution irradiated with UV-A LEDs and without any g-C₃N₄ coated beads. Dark control samples were prepared using the 5 mg L⁻¹ MC-LR experimental solution and 700 mg of g-C₃N₄

coated beads with beakers completely enclosed by aluminium foil to avoid any light exposure. Each treatment was performed in triplicate.

Table 3.3: Sampling intervals for the photocatalytic degradation of microcystin-LR by UV-A LED irradiation (365 nm) and g-C₃N₄ coated beads.

Sample	Time (min)
1 (C ₀)	Not applicable
Dark adsorption (15 minutes)	
2 (C _{Eq})	0
UV-A LED irradiation	
3	1
4	3
5	5
6	7
7	10
8	15
9	30
10	45
11	60
12	90
13	120
14	180

3.2.4 Visible light light emitting diode (LED) selection for activation of g-C₃N₄ coated beads

Graphitic carbon nitride can be activated by both UV-A and visible light. UV-A LED irradiation was initially used for the photocatalytic removal of MC-LR by g-C₃N₄ coated beads (Figure 3.8), however, visible light is usually more economical than UV irradiation.

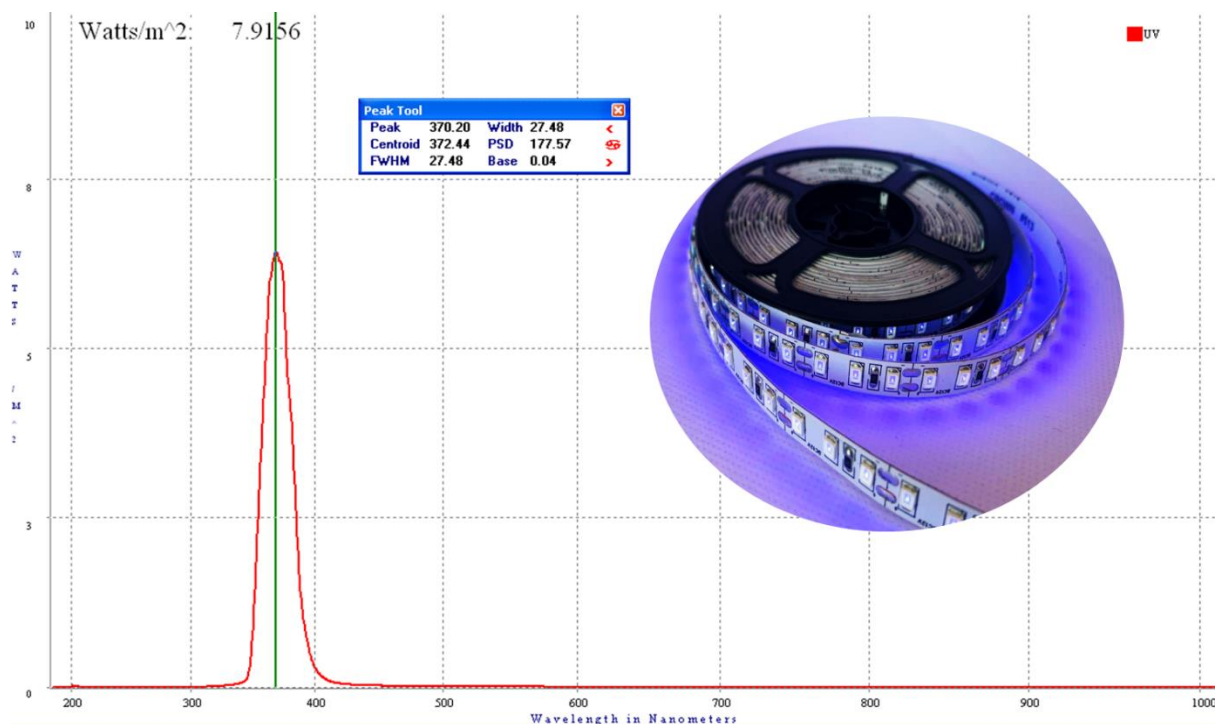


Figure 3.8: UV-A light emitting diode (LED) used for the photocatalytic activation of graphitic carbon nitride (g-C₃N₄) coated beads.

Visible light LED options were explored for the activation of g-C₃N₄ coated beads. Visible light presents a wide range of spectra (400 – 700 nm) and each light source has a specific light spectrum. Four different visible light sources (Figure 3.9) were evaluated (blue LEDs from a red/blue LED-panel, white LED strip, blue LED strip and white warm LED strip) and the light spectrum of each was characterized by a BLACK-Comet Concave Grating Spectrometer (StellarNet Inc, United States).

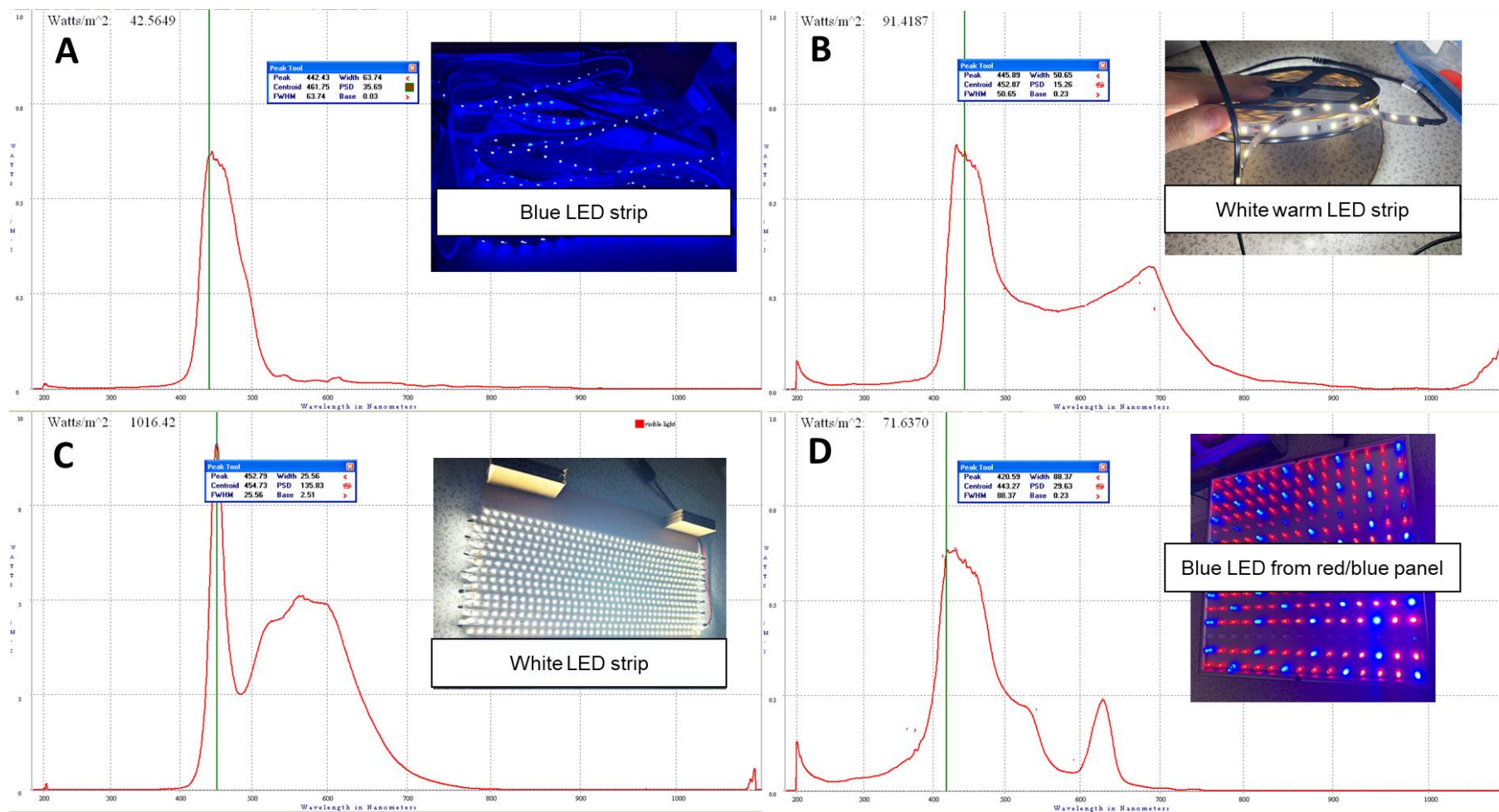


Figure 3.9: Visible light sources (white LED strip, white warm LED strip, blue LED bulbs from red/blue panel and blue LED strip) and respective light spectra evaluated for the photocatalytic activation of graphitic carbon nitride (g-C₃N₄) coated beads.

The first light source evaluated was the blue LED strip (Figure 3.9A), which presented a main peak around 430 – 500 nm. Another option was the white warm LED strip (Figure 3.9B), which had a wider main peak starting at 430 nm until the end of the visible light spectrum at 700 nm. The white LED strip (Figure 3.9C) presented a higher narrow peak at around 450 nm and a broader, but less intense peak at 480 – 650 nm. The spectrum from the blue LED strip, the white warm LED and the white LED strip had a starting peak at 430 nm and a similar main peak at around 450 nm, therefore, the white LED strip was selected as visible light option for the activation of g-C₃N₄ coated beads due to its higher light intensity of 1016 W m⁻² in comparison to 91 W m⁻² and 42 W m⁻² from white warm LED strip and blue LED strip, respectively (Figure 3.9). The blue LED bulbs from the red/blue panel were the visible light option that presented a peak closest to the beginning of the visible light spectrum (400 nm) until around 530 nm. The small peak after 600 nm was an interference from the spectrum of the red LED present in the same panel (Figure 3.9D). Because of the spectrum from 400 nm, which is closer to the end of UV spectrum, the blue LED bulbs from red/blue panel might be able to activate the g-C₃N₄ coated beads for the photocatalytic degradation of MC-LR. Therefore, the white LED strip and the blue LED bulbs from the red/blue panel were selected as visible light sources in the investigation of MC-LR removal by photocatalysis using g-C₃N₄ coated beads. To avoid spectrum interference from the red LEDs in the red/blue LED panel and intensify the energy from the blue LEDs, a new panel was constructed containing only the blue LEDs bulbs (Figure 3.10).

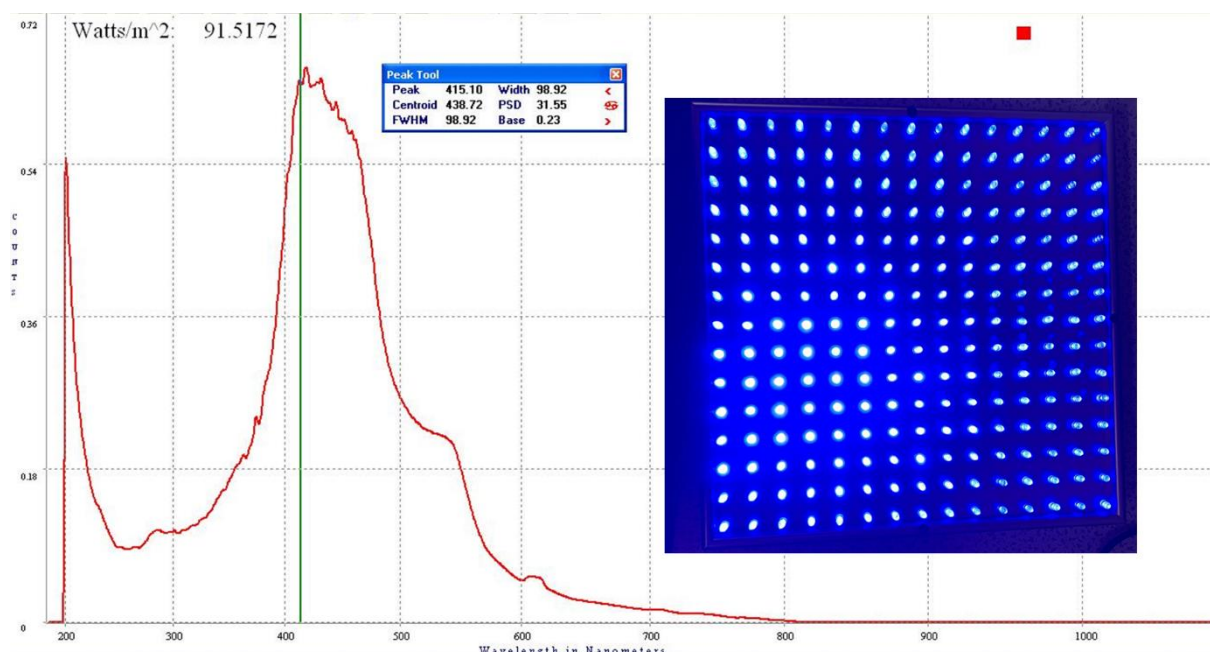


Figure 3.10: Visible light panel containing blue LED bulbs for the activation of graphitic carbon nitride (g-C₃N₄) coated beads during the photocatalytic removal of microcystin-LR and its respective light spectrum (light intensity 91 W m⁻²).

3.2.5 High-performance liquid chromatography analysis of microcystin-LR

Quantification of MC-LR was achieved by a Waters Corporation HPLC with a 2965 separation module and a 2996 photodiode array (PDA) detector (Waters, United States). All chromatograms were extracted at 238 nm (Table 3.4). The limit of quantification of MC-LR was 0.05 mg L⁻¹.

Table 3.4: Analytic conditions of high-performance liquid chromatography for microcystin-LR quantification.

Parameters	Conditions
Column	Symmetry C18 column (2.1 x 150 mm, 5 µm particle size; Waters, UK)
Mobile phase	A: 0.05% trifluoroacetic acid in ultrapure water (18.2 MΩ) B: 0.05% trifluoroacetic acid in acetonitrile
Gradient	Time (min) 0 0.1 9 10 12 15 Solvent B (%) 30 30 60 100 100 30 Elution profile 1 6 6 1 1 1
Flow rate	0.3 mL min ⁻¹
Injection volume	10 µL
Column temperature	40 °C

3.2.6 Statistical analysis

The values shown are the results of the mean of triplicates for each treatment (photocatalysis, light control and dark control). As three replicates were used during experiments ($n = 3$), testing for equal variance and normality was not seen as appropriate for a small level of replication as the results could be misleading, therefore, parametric assumptions were accepted as a low standard deviation was observed ($SD < 10\%$; Table A3.1). Two-way ANOVA was used to test for statistically significant differences. A significance level of $p < 0.05$ was used to identify significant differences between the results. *Post hoc* Tukey analysis was applied to significant results.

Further, the kinetics of experiments were evaluated by linear regression and the experimental data were fitted to pseudo-first order and pseudo-second order models (Table 3.5). The correlation coefficient (R^2) was determined as a goodness-of-fit measure for linear regression models. A significance level of $R^2 > 0.7$ (high level of correlation) was used during kinetics determination.

Table 3.5: Kinetic models applied to the photocatalytic degradation of microcystin-LR.

Kinetics model	Linear equation	Model	Plot	Rate constant
Pseudo-first order	$\ln C = -kt + \ln C_0$	$C = C_0 \times e^{kt}$	$\ln C \text{ vs } t$	$k = \text{-slope}$
Pseudo-second order	$\frac{1}{C} = kt + \frac{1}{C_0}$	$C = \frac{1}{kt + \left(\frac{1}{C_0}\right)}$	$\frac{1}{C} \text{ vs } t$	$k = \text{slope}$

Where:

- C is the microcystin-LR concentration (mg L^{-1}) at a given time of photocatalytic degradation t .
- C_0 is the microcystin-LR concentration (mg L^{-1}) at T_0 .
- k is the pseudo-first order and pseudo-second order reaction rate constant (min^{-1}).

3.3 Results and discussion

3.3.1 Photocatalytic degradation of microcystin-LR by g-C₃N₄ and g-C₃N₄/TiO₂ coated beads and UV-A LED irradiation

The photocatalytic removal of MC-LR by UV-A LEDs and g-C₃N₄ coated beads was evaluated. It was possible to observe a significant decrease ($p=0.046$) of approximately 62% in the MC-LR concentration from 45 minutes of UV-A LED/g-C₃N₄ coated beads photocatalysis, which continued to reduce until MC-LR was completely removed at 180 minutes (Figure 3.11). No significant changes ($p>0.05$) in the MC-LR concentration were observed during both light and dark control throughout the experiment (Figure 3.11).

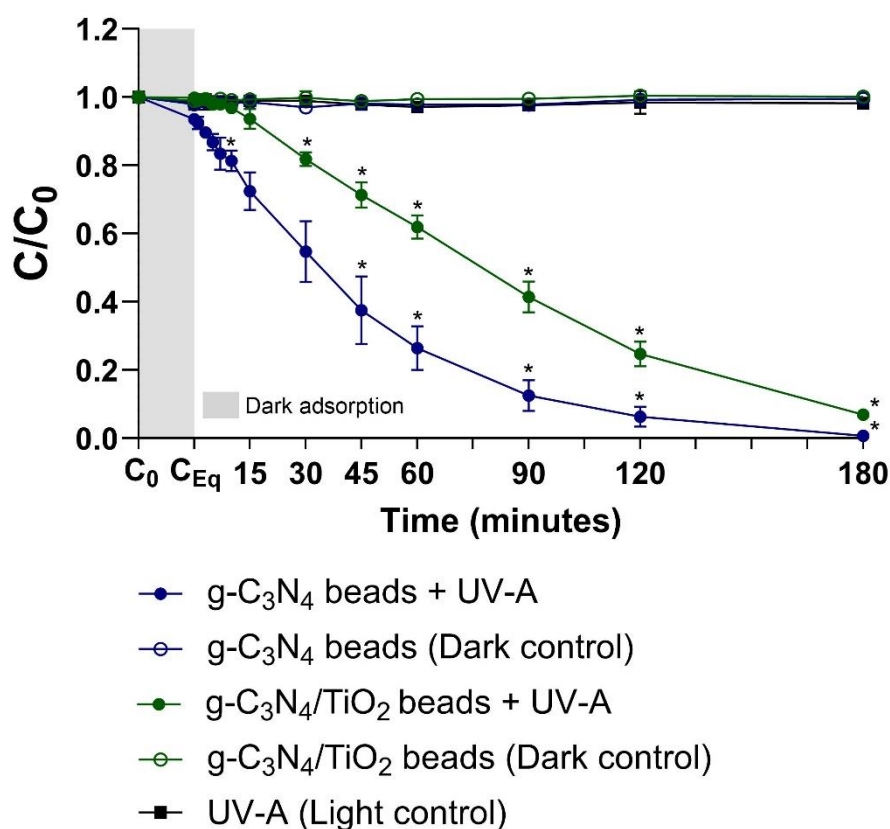


Figure 3.11: Microcystin-LR degradation after photocatalysis by UV-A LED irradiation and glass beads coated with graphitic carbon nitride (g-C₃N₄) or glass beads co-coated with graphitic carbon nitride and titanium dioxide (g-C₃N₄/TiO₂) over 180 minutes. LEDs were placed 6 cm away from MC-LR solution ($n = 3$, error bars = 1SD). *Significantly different from T_{Eq}.

When comparing the MC-LR concentration during photocatalysis with both dark and light control, the photocatalytic treatment was significantly different ($p<0.05$) from the light control from the first minute of irradiation and it was also significantly different ($p<0.05$) from the dark control during all sampling points,

except at 7 minutes of photocatalysis. There were no significant differences ($p > 0.05$) between light and dark control samples during any of the experiment (Table A3.2). This indicates that photocatalytic oxidation was the process responsible for MC-LR removal and no other mechanisms such as adsorption of the toxin onto g-C₃N₄ coated beads and photolysis by UV-A LED irradiation were involved in the oxidation of MC-LR.

The kinetics of MC-LR (5 mg L⁻¹) degradation by UV-A LED/g-C₃N₄ coated beads photocatalysis was also evaluated. The reaction order depends on the rate that the concentration of reactants react. For instance, a reaction presents zero order if the rate of the reaction is independent of reactants, a first order reaction depends on the concentration of one reactant and a second order reaction is proportional to the square of the concentration of one reactant. A pseudo-order reaction is usually applied when one of the reactants is present in excess or the reactant concentration remains constant throughout the reaction, altering the kinetics behavior to a lower order (Chemistry Steps 2016; Toppr 2024). During photocatalysis experiments, a pollutant is degraded by the oxidation of radicals produced by a catalyst under irradiation. By definition, a catalyst is not consumed in a reaction, which means that the catalyst concentration remains constant throughout the reaction. Therefore, photocatalysis can be considered a pseudo-order reaction, since the concentration of the catalyst does not change over time and ROS are produced in excess.

The degradation rate of MC-LR by photocatalysis can be evaluated by determining the reaction rate constant k by fitting the data into either a pseudo-first order or a pseudo-second order model. The experimental data for the photocatalytic degradation of MC-LR did not fit the pseudo-second order rate ($R^2 = 0.6326$), however, the data adjusted to the pseudo-first order ($R^2 = 0.9214$) and the degradation rate constant obtained was $k = 0.02239 \text{ min}^{-1}$ (Figure 3.12). Other studies evaluating the MC-LR degradation by photocatalysis also observed the data fitted pseudo-first order kinetics best (Chen et al. 2012; Peng et al. 2015; Wang et al. 2020; Zhan et al. 2023).

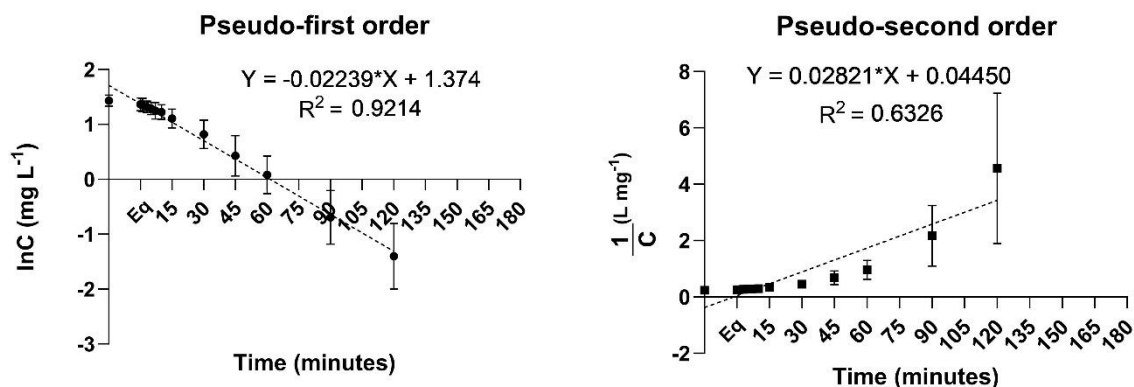


Figure 3.12: Kinetics of microcystin-LR (MC-LR) photocatalytic degraded by graphitic carbon nitride (g-C₃N₄) coated beads and UV-A LED irradiation. Kinetic models were calculated following pseudo-first order and pseudo-second order reactions. MC-LR initial concentration was 5 mg L⁻¹. (n = 3, error bars = 1SD).

The interaction of g-C₃N₄ coated on the surface of glass beads with other catalysts, such as TiO₂, should enhance the generation of radicals during photocatalysis and, therefore, increase the MC-LR degradation (Wang et al. 2021). In order to optimize the photocatalytic efficiency during the degradation of MC-LR, g-C₃N₄/TiO₂ co-coated beads were prepared and the photocatalytic removal of MC-LR by UV-A LEDs and g-C₃N₄/TiO₂ co-coated beads was evaluated. The same experimental protocol used with g-C₃N₄ coated beads was applied, except g-C₃N₄/TiO₂ co-coated beads were used as the photocatalyst instead of g-C₃N₄ coated beads. g-C₃N₄/TiO₂ co-coated beads were also efficient in the photocatalytic removal of MC-LR by UV-A LED irradiation (Figure 3.11). A significant decrease ($p=0.04$) of 18% in the MC-LR concentration was observed from 30 minutes of photocatalysis by g-C₃N₄/TiO₂ beads and UV-A LED irradiation. MC-LR continued to degrade over 180 minutes with a MC-LR removal of 93% by the end of the experiment (Figure 3.11). The MC-LR concentration during g-C₃N₄/TiO₂ beads/UV-A LED irradiation photocatalysis was significantly different ($p<0.05$) from the MC-LR concentration during both dark and light control from 30 minutes until 180 minutes of treatment, however, there was no significant differences ($p>0.05$) between MC-LR concentration from light and dark control samples during the whole experiment (Table A3.2). Other photocatalytic studies have also used g-C₃N₄/TiO₂ as catalyst for the successful degradation of dyes, such as rhodamine B, methylene blue and methyl orange (Yan, Li and Zou 2010; Ma et al. 2016; Mohini and Lakshminarasimhan 2016;

Zhou et al. 2016; Gu et al. 2017; Hao et al. 2017; Lu et al. 2018; Yang et al. 2019), however, dyes have the capacity of causing photosensitization during photocatalysis, which means that dyes can enhance the photodegradation efficiency of catalysts by transferring electrons to the catalyst and achieving the excited state required for photocatalysis (Diaz-Angulo, Lara-Ramos and Machuca-Martínez 2021; Gahlot et al. 2021). The degradation of other organic compounds, for example, pharmaceuticals (Yang et al. 2016; Wang et al. 2017, 2019b; Hussien and Yahia 2021; Kane et al. 2022), formaldehyde (Tan et al. 2023) and pyridine (Liu, Feng Tian and Long Chang 2020) by g-C₃N₄/TiO₂ photocatalysis was also demonstrated, confirming that g-C₃N₄/TiO₂ is effective in the removal of pollutants.

During photocatalysis experiments using g-C₃N₄/TiO₂ co-coated beads as photocatalyst, the experimental data also did not fit the pseudo-second order ($R^2 = 0.6956$), however, the data was well adjusted ($R^2 = 0.9388$) to the pseudo-first order reaction and presented a degradation rate constant k of 0.01341 min⁻¹ (Figure 3.13). The MC-LR degradation rate k was lower when g-C₃N₄/TiO₂ co-coated beads were applied as catalyst (Figure 3.13), in comparison with the MC-LR degradation rate k of 0.02239 min⁻¹ when g-C₃N₄ coated beads were used. Even though g-C₃N₄/TiO₂ co-coated beads were efficient in the degradation of MC-LR with almost complete removal at the end of the experiment, g-C₃N₄ coated beads were still more effective on the degradation of MC-LR.

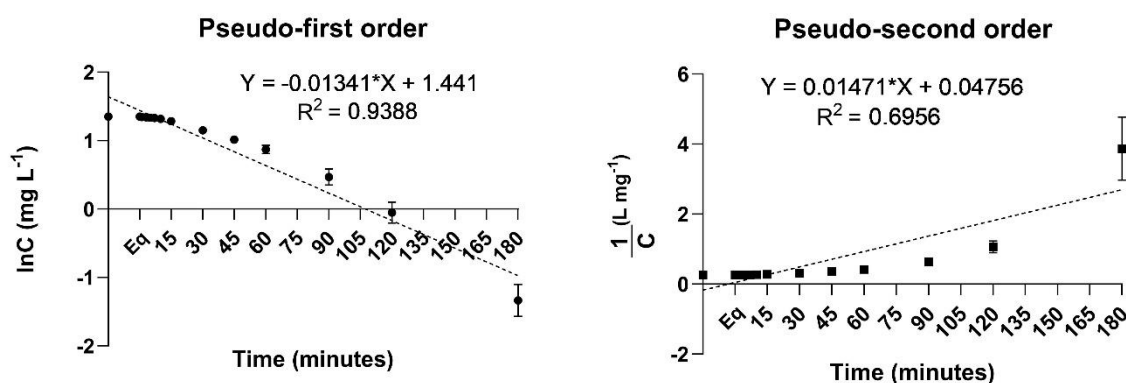


Figure 3.13: Kinetics of microcystin-LR (MC-LR) photocatalytic degraded by graphitic carbon nitride (g-C₃N₄)/Titanium dioxide (TiO₂) co-coated beads and UV-A LED irradiation. Kinetic models were calculated following pseudo-first order and pseudo-second order reactions. MC-LR initial concentration was 5 mg L⁻¹. (n = 3, error bars = 1SD).

Titanium dioxide is an abundant and economical photocatalyst that used to be considered non-toxic (Weir et al. 2012), however, TiO_2 was recently considered not to be safe for food applications according to the European Food Safety Authority (EFSA), due to possibility of causing inflammation and neurotoxicity (Younes et al. 2021). Therefore, besides the fact that using TiO_2 co-coated with g- C_3N_4 beads did not enhance MC-LR degradation during photocatalysis experiments in comparison with when g- C_3N_4 coated beads, TiO_2 is now considered hazardous and its use should be avoided during water treatment, especially for at source applications.

Contrary to the current study, Liu, Feng Tian and Long Chang (2020) observed that g- $\text{C}_3\text{N}_4/\text{TiO}_2$ was more efficient than g- C_3N_4 (around 98% removal compared to 12% over 8 hours of photocatalysis, respectively) on the photocatalytic degradation of pyridine under sunlight irradiation. Kobkeatthawin et al. (2022) made similar observations in the photocatalytic degradation of monochlorophenols (2-chlorophenol, 3-chlorophenol and 4-chlorophenol) by g- $\text{C}_3\text{N}_4/\text{TiO}_2$ and UV-visible light lamp (spectrum scattered around 300 – 600 nm). Less than 50% of monochlorophenols was removed over 2 hours when bulk g- C_3N_4 and g- C_3N_4 coated onto nanosheets were used, whereas higher photocatalytic efficiencies were demonstrated over 2 hours of photocatalysis when g- $\text{C}_3\text{N}_4/\text{TiO}_2$ was used (Kobkeatthawin et al. 2022).

On the other hand, Pestana et al. (2023) observed similar efficiencies in the degradation of MC-LR by natural sunlight when using g- C_3N_4 coated beads or g- $\text{C}_3\text{N}_4/\text{TiO}_2$ co-coated beads, with complete removal of MC-LR (initial concentration of 1.5 mg L^{-1}) over 2 hours of photocatalysis for both catalysts. In another study, Wang et al. (2018b) evaluated the degradation of the dye rhodamine B by g- $\text{C}_3\text{N}_4/\text{TiO}_2$ and g- C_3N_4 using a fluorescent lamp (300 – 700 nm). The removal efficiency of rhodamine B was very similar when g- $\text{C}_3\text{N}_4/\text{TiO}_2$ and g- C_3N_4 were used as catalysts (around 91% and 96% degradation, respectively), especially at longer photocatalysis times (72 hours to 120 hours of photocatalysis). However, the removal efficiency of rhodamine B varied when different ratios of g- C_3N_4 and TiO_2 were used. The degradation rate of rhodamine B improved as the g- C_3N_4 content in the g- $\text{C}_3\text{N}_4/\text{TiO}_2$ catalyst increased (Wang et al. 2018b). Therefore, the different ratios of g- C_3N_4 and TiO_2 in g- $\text{C}_3\text{N}_4/\text{TiO}_2$ catalyst might affect the photocatalytic efficiency for the removal of pollutants. Also, different light sources were used for the activation of g- $\text{C}_3\text{N}_4/\text{TiO}_2$ catalysts. The junction of g-

C₃N₄ and TiO₂ changes the light absorption range and subsequent light response of the catalyst in comparison to the light response range when only g-C₃N₄ is used as catalyst, therefore, different light sources might result in various removal efficiencies observed in the different studies (Wang et al. 2018b; Liu, Feng Tian and Long Chang 2020; Kobkeatthawin et al. 2022; Pestana et al. 2023).

3.3.2 Photocatalytic degradation of microcystin-LR by g-C₃N₄ coated beads and visible light LED irradiation

Graphitic carbon nitride was shown to be activated by UV-A light, however, it can also be activated by visible light irradiation up to 460 nm (Tang et al. 2020; Hui et al. 2021). Therefore, the possibility of using visible light LEDs to activate g-C₃N₄ coated beads was explored as visible light LEDs are more economical than UV-A LEDs. The MC-LR solution containing g-C₃N₄ coated beads was also irradiated by visible light LEDs for 180 minutes. White LED strips (Figure 3.8) were initially used to evaluate the photocatalytic efficiency of g-C₃N₄ coated beads in the removal of MC-LR. A reactor (30 x 21 cm) was prepared with white LED strips (600 individual visible light LEDs; 1016 W m⁻²; Figure 3.9), which illuminated g-C₃N₄ coated beads from above at a distance of 6 cm from the experimental solution (5 mg L⁻¹ MC-LR in AFW). No significant changes ($p < 0.05$) were observed in the MC-LR concentration during photocatalytic treatment (g-C₃N₄ coated beads irradiated by the white visible light LED used in the present study), except for 45 minutes of photocatalysis, during light control (white LED irradiation only) and during dark control (g-C₃N₄ coated beads with no irradiation) (Figure 3.14).

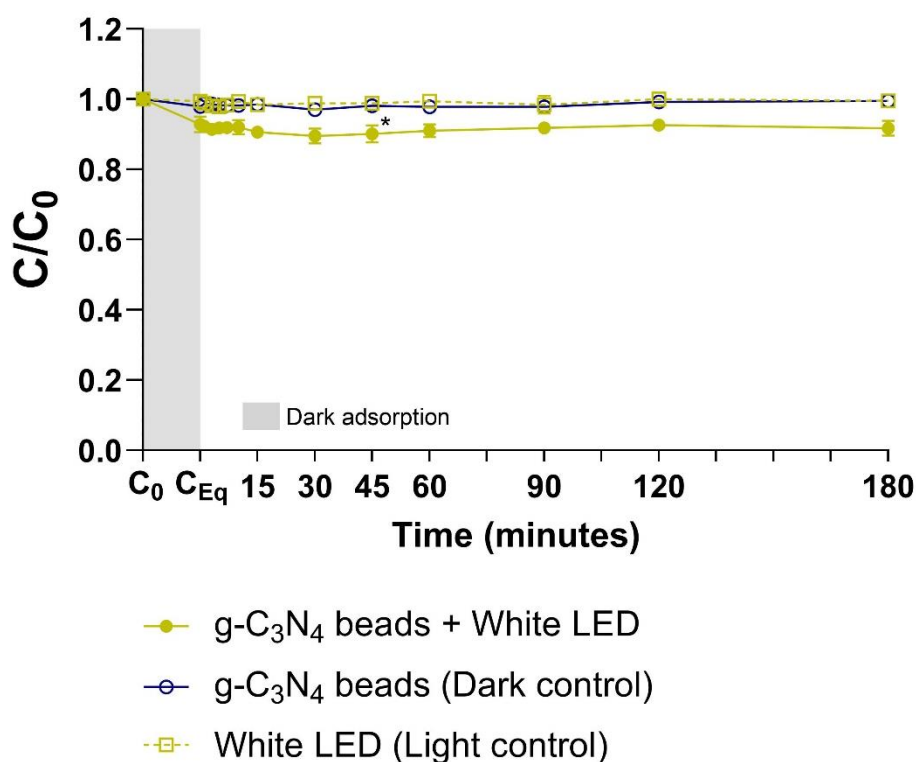


Figure 3.14: Microcystin-LR degradation after evaluation of the exposure of MC-LR to graphitic carbon nitride (g-C₃N₄) coated beads and visible light irradiation from white LEDs over 180 minutes. LEDs were placed 6 cm away from MC-LR solution (n = 3, error bars = 1SD). *Significantly different from T_{Eq}.

Even though the MC-LR concentration during photocatalytic treatment (g-C₃N₄ coated beads and white LED irradiation) was significantly different ($p < 0.05$) from the MC-LR concentration during both dark and light control for almost all the sampling points (Table A3.2), it seems that the specific wavelength from white LEDs was not sufficient to activate g-C₃N₄ coated beads and subsequently cause photocatalytic oxidation of MC-LR. There were no significant differences ($p > 0.05$) in the MC-LR concentration between light and dark control samples (Table A3.2). In contrast to the findings reported in the current study, Song et al. (2018) performed a photocatalysis experiment using g-C₃N₄ coated on expanded perlite and a xenon lamp (20 W m⁻²) with a UV filter as light source and the authors demonstrated approximately 55% removal of MC-LR after 6 hours. Visible light presents a broad range of spectra ranging from 400 to 700 nm, with each light source demonstrating its specific light spectrum. In the current study, the visible light spectrum from white LED strips was spread from 430 to 700 nm, with the majority of the total emitted energy concentrated at a peak around 450 nm and between 500 to 650 nm (Figure 3.9). The spectrum of xenon lamps is usually

around 300 – 1000 nm wavelength, therefore, scattered through the entire visible light wavelength range, therefore, it is possible that the light source used in the Song et al. (2018) study had sufficient energy in a specific wavelength range of the visible light spectrum to activate the catalyst based on g-C₃N₄. Blue LED bulbs were also tested for the activation of g-C₃N₄ coated beads on the degradation of MC-LR during photocatalysis experiments (Figure 3.9). A reactor (31 x 31 cm) was prepared with blue LED bulbs (225 individual LED bulbs; 91 W m⁻²; Figure 3.10), which illuminated g-C₃N₄ coated beads from above at a distance of 6 cm from the experimental solution (50 mL of 5 mg L⁻¹ MC-LR in AFW placed in 100 mL beakers; irradiated area of 19.6 cm² illuminated by approximately 6 individual LED bulbs). g-C₃N₄ coated beads were completely submerged using a stainless-steel mesh (aperture of 1.2 x 1.2 mm and 0.4 mm wire strength) to mimic the position of g-C₃N₄ coated beads during at source applications. There were no significant changes ($p>0.05$) in the MC-LR concentration over 180 minutes of photocatalysis when g-C₃N₄ coated beads and blue LED bulbs were used, except for MC-LR concentration at 120 minutes when the MC-LR content increased by 2% (Figure 3.15). The small increase in the MC-LR concentration at the end of the experiment can be attributed to some evaporation caused by heating from LED bulbs.

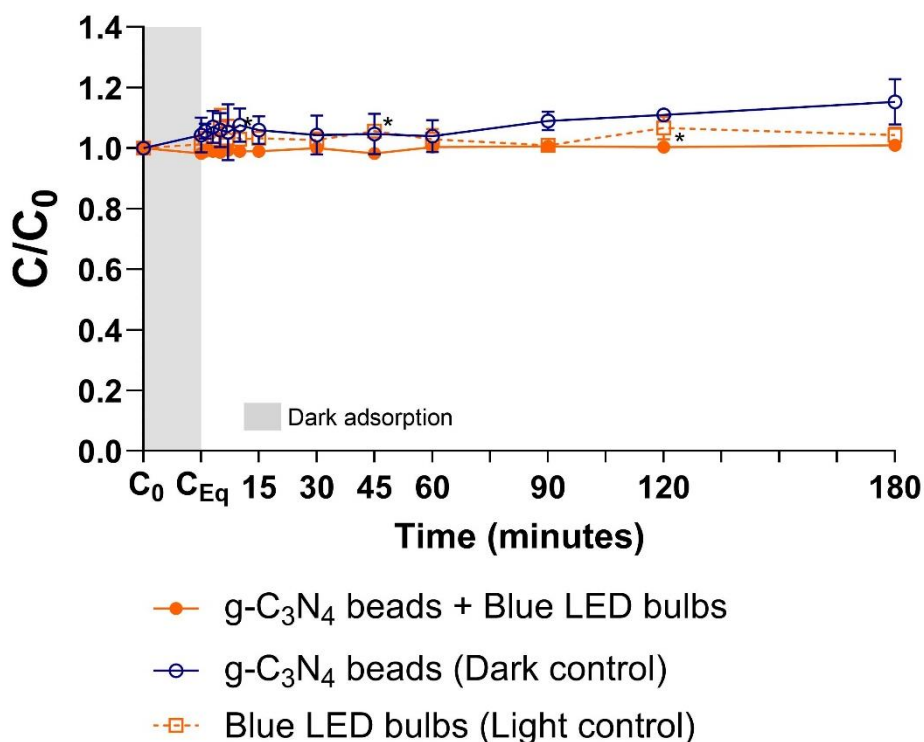


Figure 3.15: Microcystin-LR degradation after photocatalysis by blue LED bulbs irradiation and glass beads coated with graphitic carbon nitride (g-C₃N₄) over 180 minutes. LEDs were placed 6 cm away from MC-LR solution and g-C₃N₄ coated beads were submerged (n = 3, error bars = 1SD). *Significantly different from T_{Eq}.

During light control samples (no g-C₃N₄ coated beads were placed in the MC-LR solution), significant changes were observed in the MC-LR concentration at 15 minutes ($p < 0.0001$) and 45 minutes ($p = 0.0355$) of LED irradiation, however, the MC-LR concentration increased around only 2% from T_{Eq} during both sampling times. No significant changes ($p > 0.05$) were observed in the MC-LR concentration for dark control samples (no LED irradiation on samples). The blue LED bulbs appeared to have no effect on the photocatalysis of MC-LR when g-C₃N₄ coated beads were used as photocatalyst, however, the blue LED bulbs were placed 6 cm away from the experimental solution. As the distance increases by each cm, the light intensity varies proportionally with the inverse of the square of the distance (Voudoukis and Oikonomidis 2017). Therefore, the inverse correlation between distance of the light and light intensity leads to a reduction of light energy and, consequently, decreases the photocatalytic efficiency as the distance increases. In order to improve the photocatalytic efficiency when visible light was used to activate g-C₃N₄ coated beads, a new photocatalysis experiment was performed using the same g-C₃N₄ coated beads and blue LED bulbs,

however, in this case, the blue LED bulbs panel was placed only 3 cm away from the MC-LR experimental solution and no mesh was used. Since the distance between the blue LED bulbs panel was halved, the emitted light energy should be four times higher than the previous setup, however, no significant differences ($p>0.05$) were observed in the MC-LR content during either photocatalytic treatment (g-C₃N₄ coated beads and blue LED bulbs), light control (blue LED bulbs only) and dark control (g-C₃N₄ coated beads), except from the MC-LR concentration at 120 minutes of dark control, which presented a significant increase ($p<0.0001$) of 0.9% in MC-LR content (Figure 3.16).

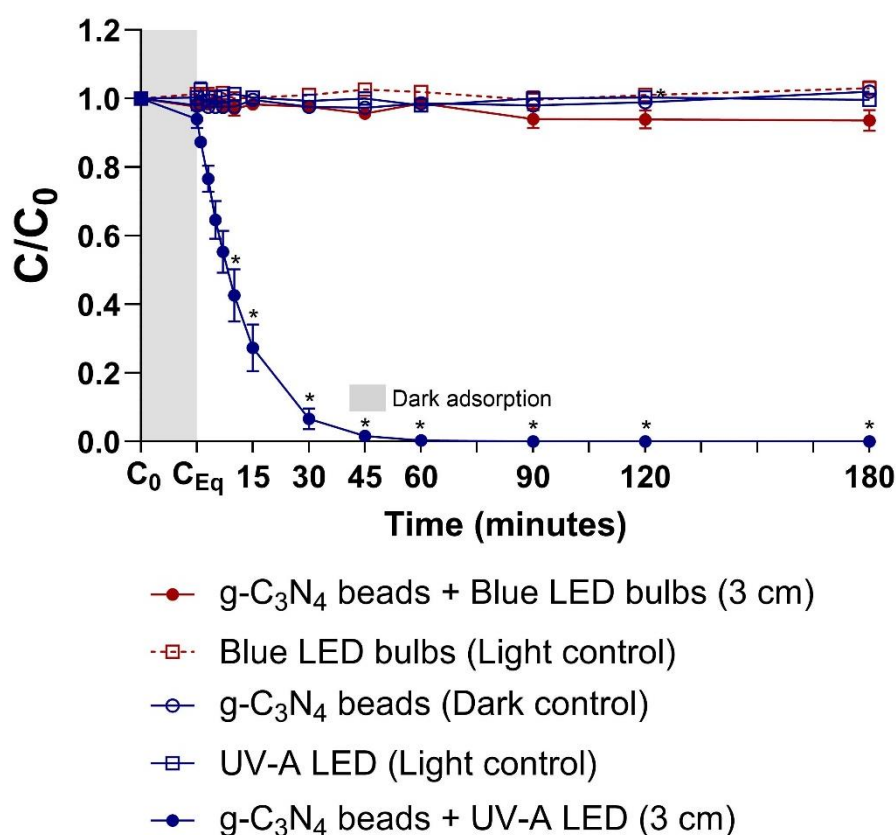


Figure 3.16: Microcystin-LR degradation after photocatalysis by blue LED bulbs or UV-A LED irradiation and glass beads coated with graphitic carbon nitride (g-C₃N₄) over 180 minutes. LEDs were placed 3 cm away from MC-LR solution (n = 3, error bars = 1SD). *Significantly different from T_{Eq}.

The experimental setup containing LEDs placed 3 cm from experimental solution and no mesh was used to confirm an increase in the photocatalytic removal of MC-LR when UV-A LEDs were used to activate g-C₃N₄ coated beads by decreasing the light distance between light source and catalyst. The MC-LR concentration significantly decreased ($p<0.05$) from 10 minutes of photocatalysis when g-C₃N₄ coated beads were used and UV-A LEDs were placed only 3 cm from

the experimental solution. MC-LR concentration continued to reduce until it was completely removed at 60 minutes of photocatalysis (Figure 3.16). No significant changes were observed when only UV-A LEDs were used (light control), demonstrating that photolysis did not occur (Figure 3.16). The experimental data did not adjust to the pseudo-second order ($R^2 = 0.7248$), however, the data was well fitted to the pseudo-first order ($R^2 = 0.9123$) reaction (Figure 3.17). The reduction in the distance between the UV-A LED panel to the MC-LR experimental solution from 6 to 3 cm increased the MC-LR degradation rate constant k to 0.07038 min^{-1} more than 3-fold in comparison with the MC-LR degradation rate constant k of 0.02239 min^{-1} previously demonstrated at 6 cm illumination distance (Figure 3.12).

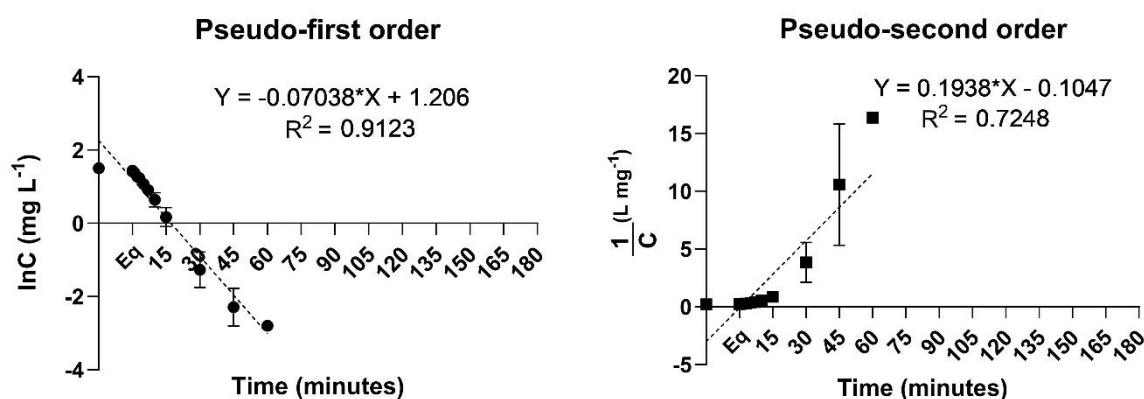


Figure 3.17: Kinetics of microcystin-LR (MC-LR) photocatalytic degraded by graphitic carbon nitride ($\text{g-C}_3\text{N}_4$) coated beads and UV-A LED irradiation. LEDs were placed 3 cm away from MC-LR solution. Kinetic models were calculated following pseudo-first order and pseudo-second order reactions. MC-LR initial concentration was 5 mg L^{-1} . ($n = 3$, error bars = 1SD).

3.3.3 Photocatalytic degradation of microcystin-LR by TiO_2 coated beads and UV-A LED irradiation

TiO_2 coated beads were used in the same photocatalytic experimental setup previously described (UV-A LEDs placed 3 cm from MC-LR experimental solution and no mesh) in order to verify if TiO_2 coated beads would be more effective than $\text{g-C}_3\text{N}_4$ coated beads in the degradation of MC-LR. TiO_2 coated beads in the MC-LR solution without the presence LEDs were used as dark control samples and no significant changes ($p > 0.05$) were observed over 180 minutes of photocatalysis (Figure 3.18). This suggests that significant adsorption of the MC-LR onto TiO_2 coated beads did not occur during photocatalysis experiments. TiO_2 coated beads were illuminated by UV-A LEDs and a significant decrease ($p < 0.05$) in the MC-LR concentration was observed from 5 minutes of photocatalysis. The

MC-LR content continued to decrease until around 88% of MC-LR was removed during 180 minutes of treatment (Figure 3.18).

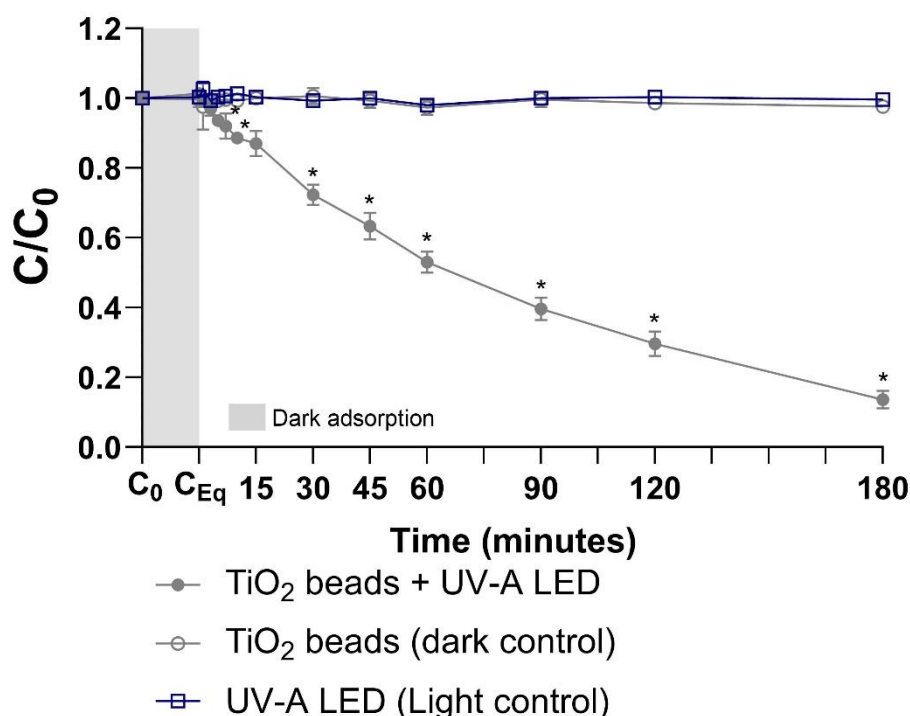


Figure 3.18: Microcystin-LR degradation after photocatalysis by UV-A LED irradiation and glass beads coated with titanium dioxide (TiO₂) over 180 minutes. LEDs were placed 3 cm away from MC-LR solution (n = 3, error bars = 1SD). *Significantly different from T_{Eq}.

The experimental data did not adjust to the pseudo-second order reaction ($R^2 = 0.8468$), however, the data was well fitted to the pseudo-first order reaction ($R^2 = 0.9829$) and presented a degradation rate constant k of 0.01059 min^{-1} even though full degradation was not achieved (Figure 3.19).

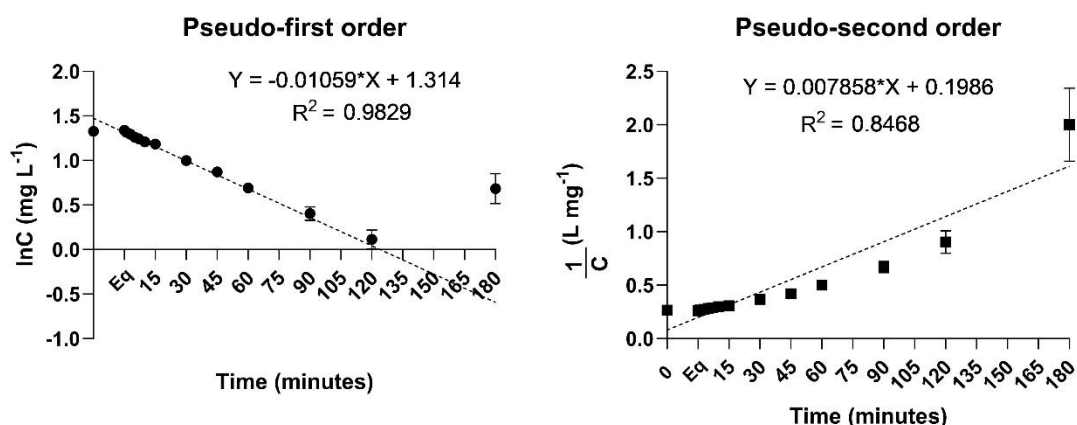


Figure 3.19: Kinetics of microcystin-LR (MC-LR) photocatalytic degraded by titanium dioxide (TiO₂) coated beads and UV-A LED irradiation. LEDs were placed 3 cm away from MC-LR solution. Kinetic models were calculated following pseudo-first order and pseudo-second order reactions. MC-LR initial concentration was 5 mg L^{-1} . (n = 3, error bars = 1SD).

Even though TiO_2 coated beads were also efficient in the photocatalytic oxidation of MC-LR, the highest degradation rate of MC-LR was obtained when $\text{g-C}_3\text{N}_4$ coated beads were used and activated by UV-A LED irradiation. Hui et al. (2021) observed a similar photocatalytic performance of $\text{g-C}_3\text{N}_4$ coated beads when compared with TiO_2 coated beads on the degradation of MC-LR (10 mg L^{-1}) and cylindrospermopsin (10 mg L^{-1}) by UV light irradiation from fluorescent lamps. MC-LR was completely removed at 15 minutes when both $\text{g-C}_3\text{N}_4$ coated beads and TiO_2 coated beads were used. $\text{g-C}_3\text{N}_4$ coated beads and TiO_2 coated beads also presented similar photocatalytic activity with a complete removal of cylindrospermopsin by 100 minutes of photocatalysis (Hui et al. 2021). During cylindrospermopsin degradation by TiO_2 coated beads, however, a dark period adsorption of 25% of cylindrospermopsin was observed, while only 5% of cylindrospermopsin was adsorbed onto $\text{g-C}_3\text{N}_4$ coated beads, which indicates that adsorption also played a role on the photocatalytic oxidation of cylindrospermopsin by TiO_2 coated beads and $\text{g-C}_3\text{N}_4$ coated beads presented a better photocatalytic efficiency.

MC-LR is a cyanotoxin commonly found in freshwater environments, which in this study was selected as a model compound to verify the efficiency of coated glass beads and LED irradiation of the photocatalytic degradation of pollutants. $\text{g-C}_3\text{N}_4$, TiO_2 coated beads and $\text{g-C}_3\text{N}_4/\text{TiO}_2$ co-coated beads were compared and $\text{g-C}_3\text{N}_4$ coated beads were shown to be the most effective catalyst in the removal of MC-LR. Furthermore, UV-A LEDs and different types of visible light LEDs were also evaluated for the activation of $\text{g-C}_3\text{N}_4$ coated beads, however, only UV-A LED were able to achieve MC-LR degradation in the presence of $\text{g-C}_3\text{N}_4$ coated beads. Therefore, $\text{g-C}_3\text{N}_4$ coated beads and UV-A LEDs (365 nm) were selected for further photocatalysis studies of other pollutants. It is important to keep in mind that the LED technology has been improving in the past years and more affordable LED options have been put on the market, for example, UV/Visible light LEDs (Figure 3.20) could be a suitable and economical (£0.075 per LED) alternative for the activation of $\text{g-C}_3\text{N}_4$ coated beads since it presents a peak starting from the end of the UV range and finishing at the beginning of the visible light spectrum (360 – 420 nm).

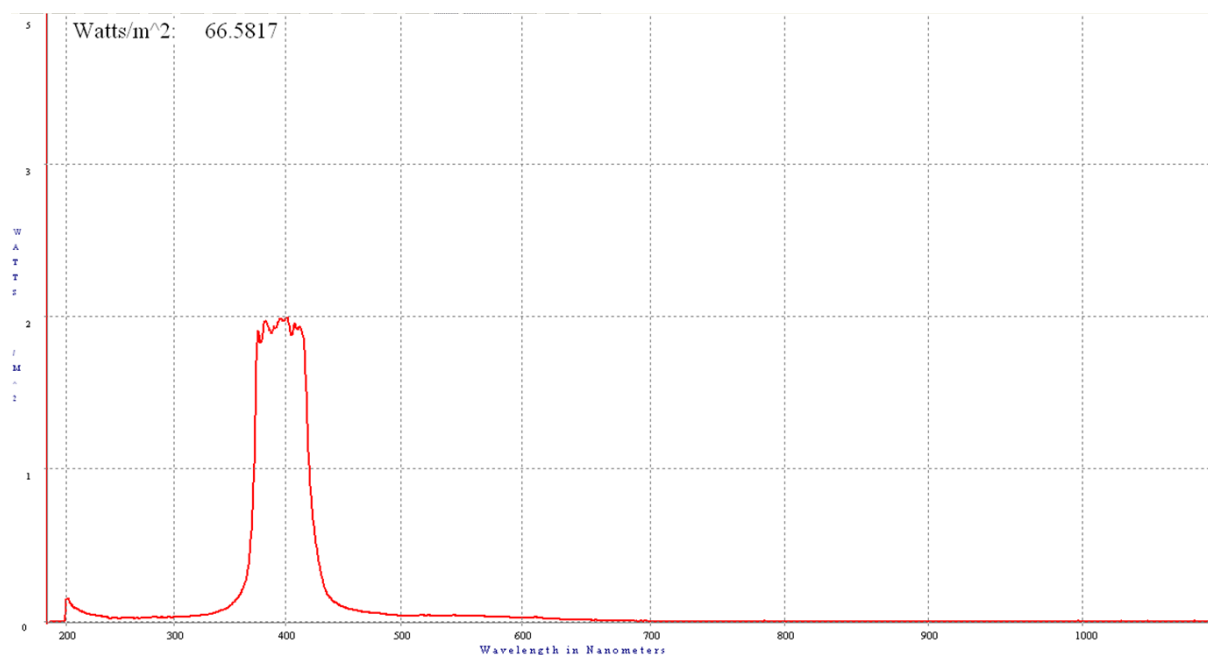


Figure 3.20: Spectrum of UV/Visible light light emitting diode (LED) that could be explored as a potential alternative for the activation of graphitic carbon nitride (g-C₃N₄) coated beads during the photocatalysis experiments (light intensity 66 W m⁻²).

3.4 Conclusion

The photocatalytic degradation of the cyanotoxin microcystin-LR was demonstrated when economical low energy LED-based UV-A (365 nm) were used in the presence of TiO_2 , g- C_3N_4 and g- $\text{C}_3\text{N}_4/\text{TiO}_2$ coated onto floating glass beads. Floating coated glass beads can easily be separated from water after photocatalytic treatment. The photocatalytic efficiencies were compared and g- C_3N_4 coated beads demonstrated the highest microcystin-LR degradation rate when illuminated by UV-A LEDs. A very similar degradation rate was observed when g- $\text{C}_3\text{N}_4/\text{TiO}_2$ coated beads were used and both g- C_3N_4 and g- $\text{C}_3\text{N}_4/\text{TiO}_2$ coated beads demonstrated superior photocatalytic efficiency when compared to TiO_2 coated beads. Further research is required to investigate the photocatalytic removal of other pollutants by coated beads and UV-A LEDs as well as the use of natural water samples before application at source.

g- C_3N_4 coated beads used in the current study were prepared using a facile calcination process, which requires a single affordable precursor (melamine), instead of a multi-step process that requires expensive compounds, such as noble metals. The preparation of g- C_3N_4 coated beads can easily be scaled up for quantities required for at source water treatment, considering the capacity of the muffle furnace available for production.

LEDs are an affordable, environmentally safe light source that can be used to activate photocatalysts during at source water treatment of contaminants. Other LED options providing different wavelengths should be further explored in order to identify a visible light source capable of activate and improve the photocatalytic efficiency of g- C_3N_4 coated beads. The possibility of using alternative LED energy supplies such as photovoltaic cells or wind power with storage capacity should also be explored to decrease the costs associated with the activation of g- C_3N_4 coated beads at source. Floating g- C_3N_4 coated beads and LED photocatalysis is a promising technology for a scalable treatment of contaminants at source.

Chapter 4

Photocatalytic removal of pesticides by g-C₃N₄ coated beads and UV-A LED irradiation

4 PHOTOCATALYTIC REMOVAL OF PESTICIDES BY G-C₃N₄ COATED BEADS AND UV-A LED IRRADIATION.....	107
4.1 Introduction.....	110
4.1.1 Pesticide selection	110
4.2 Materials and methods.....	123
4.2.1 Reagents	123
4.2.2 Determination of the photocatalytic experimental setup for pesticide degradation.....	123
4.2.3 Effect of g-C ₃ N ₄ catalyst load on the photocatalytic degradation of diuron under UV-A LED irradiation	125
4.2.4 Effect of pH on the photocatalytic degradation of diuron	126
4.2.5 Effect of g-C ₃ N ₄ coated beads calcination time on the photocatalytic degradation of diuron	127
4.2.6 Photocatalytic degradation of a pesticide mixture by g-C ₃ N ₄ coated beads and UV-A LED irradiation.....	127
4.2.7 Reusability of g-C ₃ N ₄ coated beads	128
4.2.8 Photocatalytic degradation of diuron by graphitic carbon nitride (g-C ₃ N ₄) coated beads and UV-A LED irradiation in a continuous flow reactor ...	129
4.2.9 Ultra-performance liquid chromatography analysis of pesticides	131
4.2.10 Statistical analysis.....	132
4.3 Results and discussion	133
4.3.1 Comparison of photocatalytic reactor designs for degradation of the herbicide diuron	133
4.3.2 g-C ₃ N ₄ coated beads catalyst load optimization using solution pH 7 .	136
4.3.3 Optimization of initial solution pH for the photocatalytic degradation of diuron by g-C ₃ N ₄ coated beads.....	142
4.3.4 g-C ₃ N ₄ coated beads catalyst load optimization with pH 5 and phosphate buffer initial solution.....	147
4.3.5 Optimization of muffle furnace calcination time for g-C ₃ N ₄ coated beads preparation	151
4.3.6 Pesticide mixture degradation by photocatalysis using g-C ₃ N ₄ coated beads and UV-A LED irradiation.....	155

4.3.7	Reusability analysis of g-C ₃ N ₄ coated beads during the photocatalytic degradation of diuron	163
4.3.8	Diuron degradation by photocatalysis using g-C ₃ N ₄ coated beads and UV-A LED irradiation in a continuous-flow system	165
4.4	Conclusion	169

4.1 Introduction

4.1.1 Pesticide selection

Pesticides are widely applied in agriculture for pest control, which can result in the contamination of the environment (Tudi et al. 2021). During application in agriculture, pesticides can be carried through air or by rainfall runoff, finding their way to aquatic environments (Nasiri, Ahmadzadeh and Amiri 2020) and eventually end up in drinking water (Ribeiro et al. 2015). Pesticides can also find their way into aquatic environments by the disposal of residual pesticides in storage tanks, drainage systems, waste gutters and ponds (Nasiri, Ahmadzadeh and Amiri 2020). Conventional water treatment (coagulation, flocculation, sedimentation and filtration) can be ineffective in degrading pesticides as they are not developed for the removal of dissolved compounds (Ribeiro et al. 2015; Sousa et al. 2018; de Souza et al. 2020). Therefore, it is important to develop strategies for the removal of pesticides at source.

Pesticides can be divided in herbicides, insecticides and fungicides according to their main use in agriculture (Nasiri, Ahmadzadeh and Amiri 2020; Rani et al. 2020). Each type of pesticide can also be classified in different classes according to their chemical structure, such as carbamates, triazines, organochlorines, organophosphates, pyrethroidstriazines, chloroacetanilides, chlorophenoxy acids, phenylurea, polyaromatic hydrocarbon and neonicotinoids (Murray, Thomas and Bodour 2010; Ribeiro et al. 2015; Pietrzak et al. 2019; Sharma et al. 2019; de Souza et al. 2020). Since there are a large number of pesticides that can be used, a selected number of pesticides were investigated in the current study as representative compounds of other widely used pesticides. A prioritization strategy of pesticides was created based on the toxicity, worldwide occurrence in the environment, persistence, ecological risk, environmental impact and usage in Scottish farms. Pesticides were also investigated considering their physical-chemical characteristics, usage, World Health Organization (WHO) toxicity classification from 2019 (World Health Organization 2019) and impacts on humans and other organisms (Table 4.1).

Table 4.1: Evaluated pesticides and their physico-chemical characteristics, WHO classification, usage, impacts as compelling reasons for selection. Type = herbicide (H), insecticide (I) or fungicide (F). The selected pesticides are highlighted in yellow.

Pesticide	Type	Molecular weight (g mol ⁻¹)	Solubility (mg L ⁻¹ , 20°C)	log K _{ow}	Group	Use in agriculture	Other uses	Persistence	WHO classification	Impacts
Diuron	H	233.09 [1]	42 [1]	2.8 [1]	Phenylurea [1]	Fruit, cotton, sugar cane and wheat [2]	Antifouling paint [2]	Half-life of 43–2180 days for hydrolysis. Moderately persistent in soil and persistent in water [1]	Class III = slightly hazardous [3]	Anaemia, bone marrow damage, abnormal blood pigment, skin and eye irritation [4]. It is slightly toxic to mammals, slightly toxic to birds, moderately toxic to fish and slightly toxic to aquatic invertebrates [2]
Isoproturon	H	206.28 [1]	70.2 [1]	2.5 [1]	Phenylurea [1]	Grass weeds in wheat, cereal, sugarcane, citrus, cotton, and asparagus [5]		Not persistent in soil, very persistent in water with half-life of 1560 days of hydrolysis [1]	Class II = moderately hazardous [3]	Damage to the spleen, liver, kidney, and testes [6]
Simazine	H	201.66 [1]	5 [1]	1.9 [1]	Triazines [1]	Selective systemic herbicide [7]	Pot-plant and tree production (orchards, Christmas trees and in areas for recreation) [7]		Unlikely to present acute hazard in normal use [3]	Reproductive disorder, kidney failure [4]

Chlorfenvinphos	I	359.6 [1]	145 [1]	3.8 [1]	Organo-phosphate [1]	Livestock [8]	Household pests – flies, fleas and mites [8]		Class Ib = highly hazardous [3]	
Chlorpyrifos	I	350.58 [1]	1.05 [1]	4.7 [1]	Organo-phosphate [1]	Control foliage and soil borne pests (ants, slugs, snails, etc.) [9]		Half-life of 53.5 days of hydrolysis [1]	Class II = moderately hazardous [3]	Nerve disorders, headache, nausea, muscle twitching and convulsions and in extreme cases death. Human birth defects have also been associated with its exposure. It also affects the male reproductive system. It is toxic to a variety of beneficial arthropods, including bees, ladybird beetles, parasitic wasps and fish [10]
Tributyltin (TBT)	F	596.15 [1]	100 [1]	3.1 [1]	Organotin [1]		Antifouling agent in boat paints, disinfectant of circulating industrial cooling waters, slime control in paper mills and wood preservative [11]		Class II = moderately hazardous [3]	

Trifluralin	H	335.28 [1]	0.221 [1]	5.2 [1]	Dinitroaniline [12]	Control of grasses and broadleaf weeds on crops of cotton, soybeans, fruits and vegetables [13]		Unlikely to present acute hazard in normal use [3]	Nausea, irritation in eyes, skin disease [4]
Cypermethrin	I	416.3 [1]	0.009 [1]	5.5 [1]	Pyrethroid [1]	Used in bell pepper and white cabbage crops [9]		Class II = moderately hazardous [3]	
Pendimethalin	H	281.31 [1]	0.33 [1]	5.4 [1]	Dinitroaniline [12]	Applied in woody plants and broadleaf weeds [14]		Class II = moderately hazardous [3]	
Permethrin	I	391.3 [1]	0.2 [1]	6.1 [1]	Pyrethroid [1]	Control of insects in crops and livestock [15]	Control of mosquitos and residential use (indoor spaces and pets) [15]	Class II = moderately hazardous [3]	

Atrazine	H	215.69 [1]	35 [1]	2.7 [1]	Triazines [1]	Broadleaf and grassy weeds in mainly soybean, corn and sugar cane, and sorghum, pineapple, roses, raspberries, young woodlands [16]	Landscaping [16]	Low solubility, making atrazine moderate persistent in aqueous solution. It is poorly adsorbed in the organic fraction of the soil, consequently presenting high leaching potential [16]	Class III = slightly hazardous [3]	Kidney failure, heart failure, endocrine disrupting chemical that retardates sexual and embryonic development and variations in pubertal growth. It reduces cellular metabolism and influences the formation of reactive oxygen species, altering the antioxidant activity in fish, crustaceans and chironomid larvae [16]
Tebuconazole	F	307.82 [1]	36 [1]	3.7 [1]	Triazole [1]	Soybean crops and vegetables (e.g., onions and potatoes) and fruit trees [17]	Human and animal illness [17]	Although it has low solubility, it is moderately persistent in water [1,11]	Class II = moderately hazardous [3]	
Carbendazim	F	191.21 [1]	8 [1]	1.4 [1]	Benzimidazole [1]	Control of fungi on crops (banana, cereal, cotton, fruit, mushrooms, peanuts, sugarbeet, soybeans, tobacco and vegetables) [18]	Anthelmintic and antiulcer medicine [17]	Although it has low solubilization, it is persistent in water with a half-life of 350 days of hydrolysis. Low persistence in soil [1]	Unlikely to present acute hazard in normal use [3]	

Dimethoate	I	229.26 [1]	25900 [1]	0.7 [1]	Organo-phosphate [1]	Pre- and post-harvest fruit fly control [17]	Despite low Kow and high solubility, it has low persistence in water with a half-life of 68 days of hydrolysis [1]	Class II = moderately hazardous [3]	Change in oxidative stress biomarkers. Also causes neurological damage in mice, histopathological changes in the liver and brain of the animals, carcinogenic [17]
2,4-dichlorophenoxyacetic acid (2,4-D)	H	221.03 [1]	24300 [1]	-0.8 [1]	chloro-phenoxy acid [1]	Soybean, corn and wheat crops [19]	Home lawns and public parks, controls broad-leaved weeds and other vegetation on rangeland, lawns, golf courses, forests, roadways and parks [20]	High persistence in water and low persistence in soil (mobile in aqueous systems because of its acidic carboxyl group and low soil adsorption that), half-life from 20 to 312 days for hydrolysis [21]	Class II = moderately hazardous [3]. Intellectual disability, miscarriage, defects in tissues, failure of the central nervous system, failure of the liver, ear damage, and carcinogenic effects. Also associated with the development of Parkinson's disease and autism. Endocrine disruption, reproductive disorders, genetic alterations and carcinogenic effects in other organisms. It can reduce growth rates, induce reproductive problems and produce changes in appearance or behaviour or could cause death of nontarget species, including plants, animals and microorganisms [21]

dichlorodiphenyl-trichloroethane (DDT)	I	354.49 [1]	0.006 [1]	6.9 [1]	Organo-chlorine [1]	Insect control in crop and livestock production [22]	Against insect-borne human diseases (malaria, typhus) [22]		Class II = moderately hazardous [3]
Glyphosate	H	169.1 [1]	10500 [1]	-3.2 [1]	Organo-phosphate [1]	Before planting of crops and after planting of genetically modified glyphosate-resistant crops, desiccation on grain crops, broadleaf weed control [23]	Widely used between trees in orchards and groves, urban areas for weed control along streets and in parks, applied in waterways to eliminate invading aquatic plants [23]	Highly persistent in soil, half-life of 91 days for hydrolysis [23]	Class III = slightly hazardous [3] (the WHO reclassified as probably carcinogenic to humans in 2015) [23] Cancer, kidney damage and mental conditions, autism, Alzheimer's and Parkinson's disease, miscarriages, dermatological and respiratory illnesses in humans. Infertility and malformation among pigs. Liver, kidney damage and tumors in laboratory rats. Negative impacts in the health of a variety of animals in the aquatic food web, including protozoa, mussels, crustaceans, frogs and fish [23]
Acetamiprid	I	222.7 [1]	2950 [1]	0.8 [1]	Neo-nicotinoid [1]	Foliar spray to control insects on fruit, vegetables, ornamental plants, and flowers [25]		Half-life of 420 days for hydrolysis degradation (high persistence in water), low persistence in soil [25]	Class II = moderately hazardous [3] Adverse effects on vertebrate and invertebrate species, as well as mammals [25]

Clothianidin	I	249.4 [1]	340 [1]	0.9 [1]	Neo-nicotinoid [1]	Crops of pome fruits, stone fruits and fruit trees, as well as vegetables and turf grass [25]	High persistence in water (stable), low persistence in soil [25]	Class II = moderately hazardous [3]	Adverse effects on vertebrate and invertebrate species, as well as mammals. It is highly toxic to honeybees and other pollinators [25]
Imidacloprid	I	255.7 [1]	610 [1]	0.5 [1]	Neo-nicotinoid [1]	Sucking, soil and chewing insects that attack vegetables and fruit crops [24]	High persistence in water (stable), low persistence in soil [25]	Class II = moderately hazardous [3]	Adverse effects on vertebrate and invertebrate species, as well as mammals. It is highly toxic to honeybees and other pollinators [25]
Thiacloprid	I	252.7 [1]	184 [1]	1.2 [1]	Neo-nicotinoid [1]	Crops of pome fruits, stone fruits and fruit trees, as well as vegetables and turf grass [25]	High persistence in water (stable), low persistence in soil [25]	Class II = moderately hazardous [3]	Adverse effects on vertebrate and invertebrate species, as well as mammals [25]
Thiamethoxam	I	291.7 [1]	4100 [1]	-0.1 [1]	Neo-nicotinoid [1]	Used against termites, cockroaches, fleas, ants, adult flies, and larvae and is used on corn, vegetables, and fruit trees [25]	High persistence in water (stable), low persistence in soil [25]	Class II = moderately hazardous [3]	Adverse effects on vertebrate and invertebrate species, as well as mammals. It is highly toxic to honeybees and other pollinators [25]

[1] (Agriculture and Environment Research Unit 2007) , [2] (Giacomazzi and Cochet 2004), [3] (World Health Organization 2019), [4] (Rani et al. 2020), [5] (Liu 2010), [6] (Ighalo, Adeniyi and Adelodun 2020), [7] (Strandberg and Scott-Fordsmand 2004), [8] (ATSDR 1997), [9] (EPA 2024a), [10] (Amalraj and Pius 2015), [11] (Sousa et al. 2018), [12] (Fernandes, Pizano and Marin-Morales 2013), [13] (EPA 2000), [14] (Greim 2024), [15] (EPA 2006), [16] (de Albuquerque et al. 2020), [17] (de Souza et al. 2020), [18] (National Center for Biotechnology Information 2024) [19] (Horak, Horn and Pieters 2021), [20] (Islam et al. 2018), [21] (Zuanazzi, Ghisi and Oliveira 2020), [22] (EPA 2024b), [23] (Meftaul et al. 2020), [24] (Muñoz, Bleak and Calaf 2020), [25] (Pietrzak et al. 2019).

Initially, pesticides were identified according to their use in the world and presence in the environment. The most frequent pesticides in the environment were the herbicide atrazine, the insecticide dimethoate and the fungicides tebuconazole and carbendazim (Table 4.1; de Souza et al. 2020). Atrazine is the mostly used herbicide from the triazine class usually applied in pre- and post-emergent applications. Further, atrazine degradation can result in toxic transformation products, such as deisopropylatrazine and deethylatrazine, which are persistent in water (de Albuquerque et al. 2020). Dimethoate is an insecticide commonly detected in surface waters around the world at higher concentrations (Carazo-Rojas et al. 2018). Both tebuconazole and carbendazim have low water solubility of 36 and 8 mg L⁻¹, respectively, which could represent an issue when performing experiments with these compounds in terms of solution preparation. Further, carbendazim is unlikely to present acute hazard in normal use (World Health Organization 2019).

The Watch List of priority substances for EU monitoring launched in the EU Directive from 2018 (Commission Implementing Decision (EU) 2018/840 2018) was also evaluated. Five neonicotinoids (acetamiprid, clothianidin, imidacloprid, thiacloprid and thiamethoxam) and other biocidal agents (diuron, isoproturon, simazine, chlorfenvinphos, chlorpyrifos, tributyltin, trifluralin, cypermethrin, pendimethalin and permethrin) were present in the 2018 Watch List of priority substances for monitoring (Table 4.1).

Neonicotinoids are a group of insecticides with similar chemical structure based on nicotine (Seifert 2005). The neonicotinoids have been used as replacements of many existing conventional insecticide classes (Thompson et al. 2020), however, neonicotinoids cause adverse impacts on pollinators, especially bees (Morrissey et al. 2015). This class of insecticides can also cause damage to humans and other mammals (e.g., reproductive toxicology, hepatotoxicity, neurotoxicity and genotoxicity) (Han, Tian and Shen 2018). Further, neonicotinoids are persistent in the environment and have high leaching and runoff potential. Therefore, neonicotinoids represent a risk to surface waters and the aquatic and terrestrial fauna (Pietrzak et al. 2019). Even though neonicotinoid usage was banned in Europe, they have been widely used in Latin America, Asia, and North America (Han, Tian and

Shen 2018) and some are approved in the United Kingdom (Agriculture and Environment Research Unit 2007).

Diuron has been widely reported in aquatic environments (Sharma et al. 2019) and it can be harmful to humans causing anaemia, bone marrow damage, abnormal blood pigmentation and skin and eye irritation (Giacomazzi and Cochet 2004). Despite being a herbicide, diuron can also be toxic to other non-target organisms, for example, fish and birds (de Souza et al. 2020). Further, diuron was classified as a slightly hazardous pesticide (World Health Organization 2019) and diuron degradation can generate toxic transformation products, such as 3,4-dichloroaniline (3,4-DCA), 1-(3,4-Dichlorophenyl)-3 methylurea (DCPMU) and 1-(3,4-Dichlorophenyl)-urea (DCPU). 3,4-DCA is highly toxic and is classified as a secondary poisonous substance (Giacomazzi and Cochet 2004).

Simazine is an herbicide unlikely to present acute hazard in normal use (World Health Organization 2019), even though simazine can generate toxic transformation products, such as desethylsimazine (Strandberg and Scott-Fordsmand 2004). Also, simazine has a low solubility in water of 5 mg L^{-1} and would not be a suitable compound to be used during water treatment experiments due to analytical constraints (Agriculture and Environment Research Unit 2007).

Tributyltin (TBT) is usually not applied in agriculture and it is mainly used as an antifouling agent in boat paints, disinfectant of circulating industrial cooling waters and wood preservative (Sousa et al. 2018). Pesticides that are not used in agriculture were not selected.

The n-octanol-water partition coefficient (K_{ow}) is the partition coefficient for a system consisting of two phases: n-octanol and water, therefore, K_{ow} could be an indicative of the hydrophilicity of a compound. The bioaccumulation and toxicity of a compound can also be estimated by the K_{ow} (Hodges et al. 2019). K_{ow} values present many orders of magnitude, therefore, these values can also be represented using the decadic logarithm of K_{ow} ($\log K_{ow}$). $\log K_{ow}$ values can vary from -3 where compounds are very hydrophilic to 10 where compounds are hydrophobic (Cumming and Rücker 2017). The relatively high $\log K_{ow}$ of 4.7 and low solubility in water of 1.05 mg L^{-1} from chlorpyrifos indicate low persistence and low contamination of this compound in water. A high $\log K_{ow}$ and low solubility in water can also

be found in other evaluated pesticides such as trifluralin (log K_{ow} 5.27 and solubility of 0.221 mg L⁻¹), cypermethrin (log K_{ow} 5.55 and solubility of 0.009 mg L⁻¹) and permethrin (log K_{ow} 6.1 and solubility of 0.2 mg L⁻¹), which is not commonly detected in surface water (Agriculture and Environment Research Unit 2007; Fernandes, Pizano and Marin-Morales 2013).

Chlorfenvinphos is from the same class of insecticides organophosphate as dimethoate, however, chlorfenvinphos presents lower solubility in water of 145 mg L⁻¹ in comparison with a higher solubility of 25900 mg L⁻¹ for dimethoate.

Isoproturon is from the same herbicide class of phenylurea as diuron. Both isoproturon and diuron were banned in the United Kingdom, however, diuron is used in Australia and in the United States. Therefore, diuron is more representative than isoproturon in terms of usage in the world (Agriculture and Environment Research Unit 2007).

Other pesticides that are commonly studied were also investigated, for example, 2,4-dichlorophenoxyacetic acid (2,4-D) and dichloro-diphenyl-trichloroethane (DDT) (Handford, Elliott and Campbell 2015; Loomis et al. 2015; Reddy and Kim 2015; Ribeiro et al. 2015; Guerrero-Estévez and López-López 2016; Islam et al. 2018; Sousa et al. 2018; Stehle et al. 2019; Zuanazzi, Ghisi and Oliveira 2020; Horak, Horn and Pieters 2021) (Table 4.1).

2,4-D can be used as a substitution for glyphosate (Zuanazzi, Ghisi and Oliveira 2020). An increase in 2,4-D use in crops of soybean, corn and wheat can be expected, due to the development of new resistant genetically modified crops, which have been registered by the United States Environmental Protection Agency since 2014 (Zuanazzi, Ghisi and Oliveira 2020). Further, 2,4-D can cause disruption of the endocrine system (Guerrero-Estévez and López-López 2016; Islam et al. 2018), reproductive disorders (Pattanasupong et al. 2004) and carcinogenic effects (Loomis et al. 2015) on plants, animals and microorganisms.

DDT presents a relatively high log K_{ow} 6.91 and low water solubility of 0.006 mg L⁻¹. Pesticides with low solubility and persistence in water were not selected.

When evaluating pesticide usage in Scotland, glyphosate and pendimethalin were the herbicides most used in arable crops and thiacloprid was the insecticide (neonicotinoid) most used in some soft fruits (Scottish Government 2019). Glyphosate degradation can generate transformation products such as aminomethyl phosphonic acid (AMPA), which can be more toxic and more persistent in the environment than glyphosate (Meftaul et al. 2020). Currently, glyphosate is used as an active component in many other formulations of pesticides, also known as glyphosate-based herbicides (Muñoz, Bleak and Calaf 2020). The detection of glyphosate by liquid chromatography, however, requires derivatization of glyphosate before liquid chromatography detection (Islas et al. 2014; Sun et al. 2017; Pimenta et al. 2020), which could also represent analytical constraints. Pendimethalin demonstrates high log K_{ow} 5.4 and low solubility of 0.33 mg L⁻¹ in water, therefore, pendimethalin was not further evaluated for this research. Thiamethoxam is a neonicotinoid that is currently applied in the United Kingdom. The use of neonicotinoids was restricted in Europe in 2018 (McGrath 2018) because of their high toxicity to bees and other pollinating insects, however, the United Kingdom has been approving emergency use of thiamethoxam since 2021 (Marshall 2021). The last emergency use of thiamethoxam was approved in the beginning of 2024 (Prior 2024). The pesticides selected as representative compounds were the herbicides diuron, atrazine, 2,4-D and the insecticides dimethoate, acetamiprid, clothianidin, imidacloprid, thiacloprid and thiamethoxam (Figure 4.1).

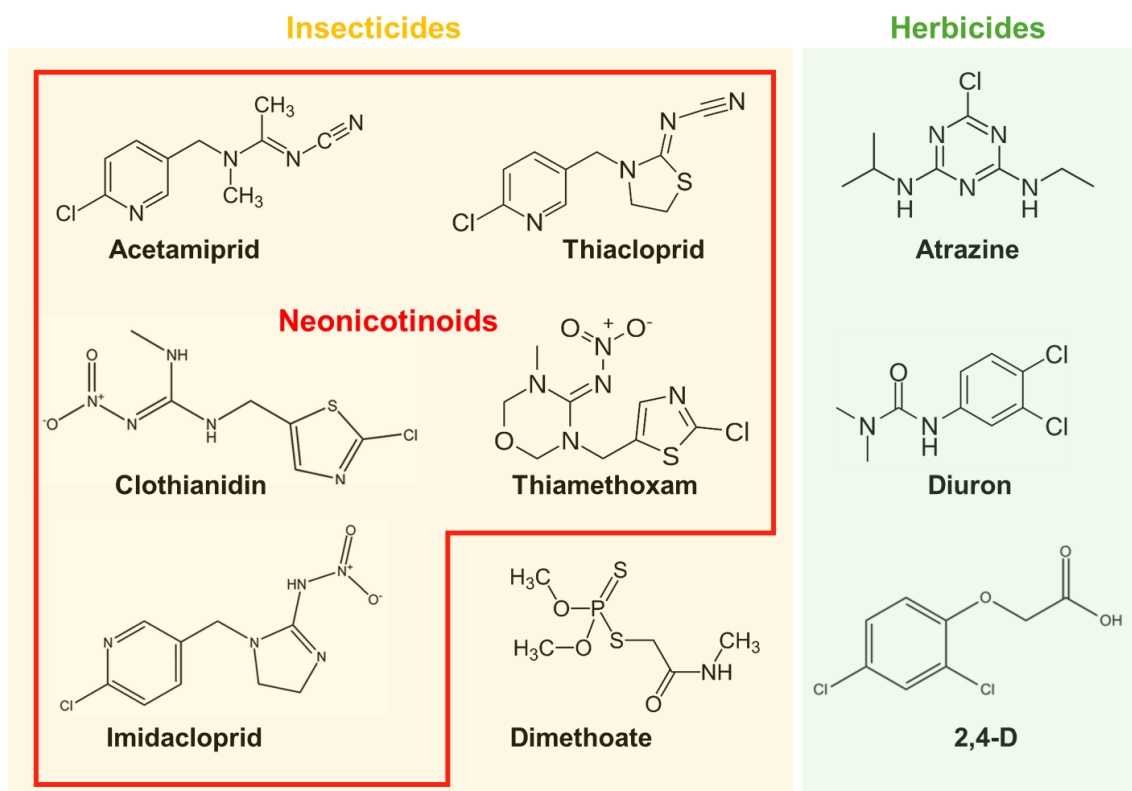


Figure 4.1: Selected pesticides to be used as pesticide representatives in the current research.

The photocatalytic system based on g-C₃N₄ coated beads and UV-A irradiation was evaluated for the removal of a pesticide mixture containing nine different compounds (herbicides diuron, atrazine, 2,4-D and the insecticides dimethoate, acetamiprid, clothianidin, imidacloprid, thiacloprid and thiamethoxam). The effect of solution pH (pH 2, 5, 8 and 10), catalyst load (0.14% – 0.70% w/v g-C₃N₄) and g-C₃N₄ coated beads calcination time (2 – 10 hours) on the removal of diuron was also investigated. Reusability and stability studies of g-C₃N₄ coated beads were performed to evaluate the applicability of the system at a large-scale water treatment.

4.2 Materials and methods

4.2.1 Reagents

Reagent grade chemicals (Fisher Scientific, UK) were used for the preparation of artificial freshwater (AFW) solution (Akkanen and Kukkonen 2003). pH was adjusted to 7 with 1 M hydrochloric acid or 1 M sodium hydroxide of reagent grade (Fisher Scientific, UK) when required. Acetonitrile, methanol and trifluoroacetic acid (Fisher Scientific, USA) were used for ultra-performance liquid chromatography tandem photo diode array (UPLC-PDA) analysis of pesticides. Ultrapure water (18.2 M Ω) obtained by an ELGA PURELAB system (Veolia, UK) was used to prepare all solutions. Solutions containing the pesticides diuron, dimethoate, acetamiprid (Fisher Scientific, UK), 2,4-D, atrazine, clothianidin, imidacloprid, thiacloprid and thiamethoxam (Tokyo Chemical Industry, Japan) were prepared, >95% purity.

4.2.2 Determination of the photocatalytic experimental setup for pesticide degradation

The reactor for the photocatalytic degradation of pesticides was initially evaluated to determine a simplified and optimized setup to be used during experiments to be carried out throughout the current study. Diuron was the pesticide selected as a model compound. Reactors made of cardboard (30 x 21 cm) were prepared containing UV-A light emitting diode (LED) irradiation (600 individual UV-A LEDs, 365 nm; 8 W m⁻²).

In the first design evaluated, each reactor was placed on top of beakers (100 mL; irradiated area of 19.6 cm² illuminated by approximately 30 individual LEDs), irradiating g-C₃N₄ coated beads (700 mg, 0.14% w/v g-C₃N₄) from above at 3 cm from the experimental solution containing 50 mL of 5 mg L⁻¹ diuron in AFW with gentle agitation using a magnetic stirrer at 100 rpm (Figure 4.2A). The other design evaluated consisted of placing each reactor on top of crystallizing dishes (150 mL, 80 mm x 45 mm; irradiated area of 50.3 cm² illuminated by approximately 60 individual LEDs), irradiating g-C₃N₄ coated beads (700 mg, 0.14% w/v g-C₃N₄) from above at 3 cm from the experimental solution (50 mL of 5 mg L⁻¹ diuron in AFW). No agitation was used, but a gentle swirl was performed before each sampling point (Figure 4.2B).

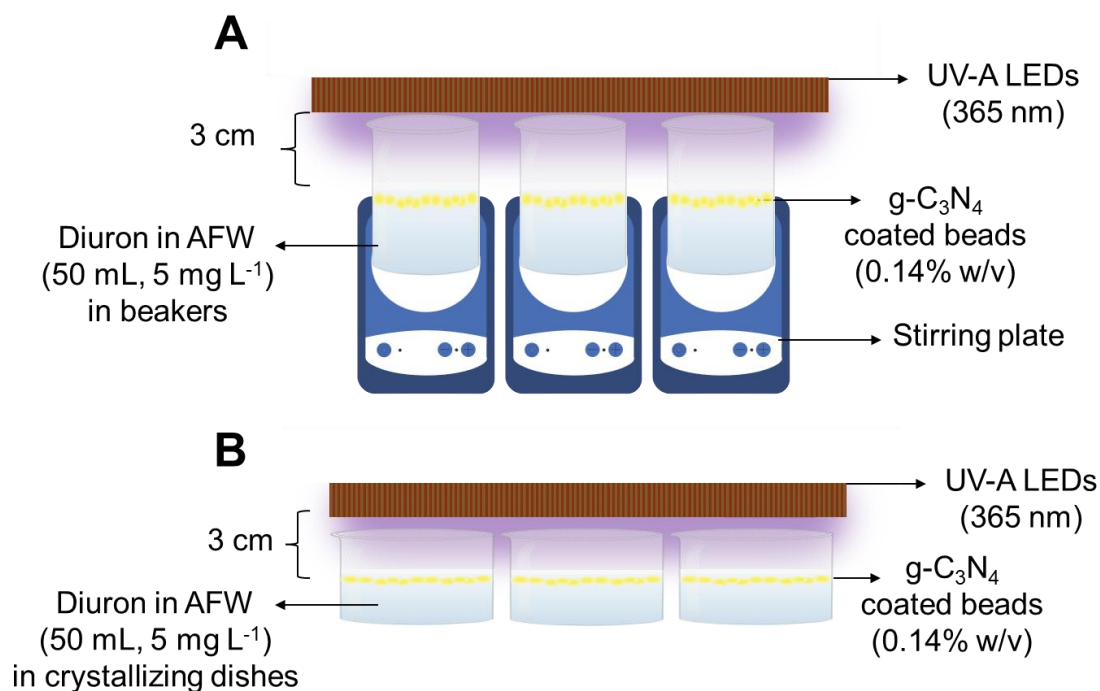


Figure 4.2: Representation of UV-A/g-C₃N₄ photocatalytic system using A) beakers or B) crystallizing dishes for the removal of diuron as a model pesticide.

An initial sample of 500 μL was taken from the diuron experimental solution (C_0) for analysis and g-C₃N₄ coated beads were added. Dark adsorption (no illumination) occurred for the first 15 minutes, then another sample was removed (500 μL ; C_{Eq}). Samples for UV-A LED irradiation were removed at pre-determined intervals (Table 4.2), placed in 1.5 mL Eppendorf tubes, centrifuged for 30 seconds at 13000 $\times g$ and the supernatant analyzed by ultra-performance liquid chromatography with photodiode array detector (UPLC-PDA; Waters, UK) for diuron quantification. Experiments were performed in triplicate. AFW was added to the solution when necessary to compensate for evaporation.

Table 4.2: Sampling intervals for the photocatalytic degradation of diuron by UV-A LED irradiation (365 nm) and g-C₃N₄ coated beads using two different setups.

Sample	Time (minutes)
1 (C ₀)	Not applicable
Dark adsorption (15 minutes)	
2 (C _{Eq})	0
UV-A LED irradiation	
3	5 (0.083 h)
4	15 (0.25 h)
5	30 (0.5 h)
6	45 (0.75 h)
7	60 (1 h)
8	240 (4 h)
9	1440 (24 h)

4.2.3 Effect of g-C₃N₄ catalyst load on the photocatalytic degradation of diuron under UV-A LED irradiation

Crystallizing dishes (80 mm x 45 mm) with 50 mL of diuron solution (5 mg L⁻¹ in AFW) were used. The catalyst load varied from 0.14% to 0.7% (w/v) g-C₃N₄ (Table 4.3). Reactors containing UV-A 365 nm LEDs were used to activate the g-C₃N₄ coated beads. A reactor containing UV-A LEDs was placed 3 cm from the level of the diuron solution as previously described.

Table 4.3: Catalyst load of graphitic carbon nitride (g-C₃N₄) coated beads applied in the photocatalytic degradation of diuron with UV-A LED irradiation.

Catalyst load (% w/v)	g-C ₃ N ₄ coated beads weight (mg)
0.14	700
0.28	1400
0.42	2100
0.56	2800
0.70	3500

Samples were taken (500 µL) at pre-determined intervals (Table 4.2), placed in 1.5 mL Eppendorf tubes, centrifuged for 30 seconds at 13000×g and the supernatant analyzed by a UPLC-PDA for diuron quantification. A gentle swirl was performed before each sampling point. Experiments were performed in triplicate. AFW was added to the solution when necessary to compensate for evaporation.

When using the maximum g-C₃N₄ coated beads catalyst load (0.70% w/v g-C₃N₄), the surface of solution in the crystallization dish was completely covered with a few double layers of g-C₃N₄ coated beads (Figure 4.3).

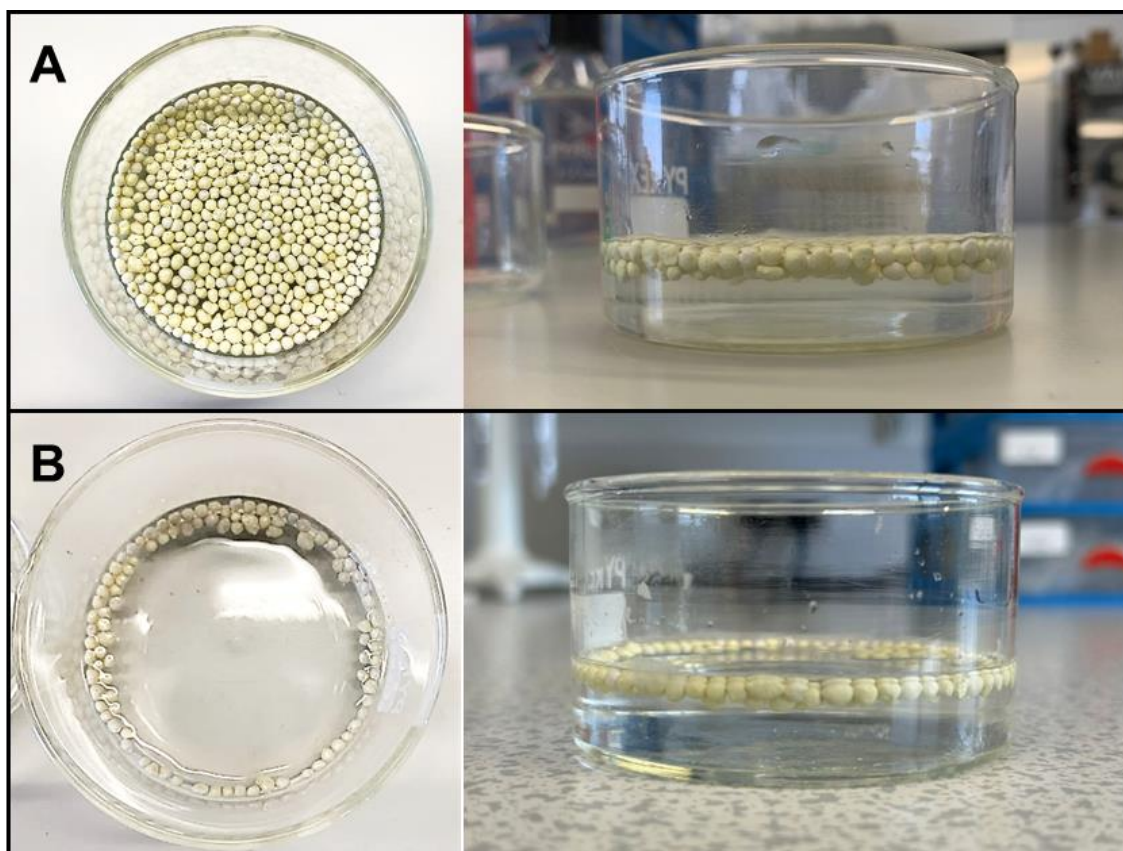


Figure 4.3: Crystallizing dishes containing A) 3500 mg (maximum catalyst load evaluated – 0.70% w/v g-C₃N₄) and B) 700 mg (minimum catalyst load evaluated – 0.14% w/v g-C₃N₄) of g-C₃N₄ coated beads in 50 mL of experimental solution.

4.2.4 Effect of pH on the photocatalytic degradation of diuron

Crystallizing dishes (80 mm x 45 mm) with 50 mL of diuron solution (5 mg L⁻¹ in AFW) were used. Initial pH of the diuron solution was set to varying pH of 2, 5, 8 and 10 by adjusting with 1M hydrochloric acid (HCl) or 1M sodium hydroxide (NaOH). g-C₃N₄ coated beads with catalyst load of 0.14% w/v (700 mg) were applied. Reactors containing UV-A 365 nm LEDs were used to activate the g-C₃N₄ coated beads. A reactor containing UV-A LEDs was placed 3 cm from the level of the diuron solution as previously described. The pH of the solution was determined using pH Indicator Paper Sticks (Fisher Scientific, UK) at pH range 0 to 14.

Samples were taken (500 μL) at pre-determined intervals (Table 4.2), placed in 1.5 mL Eppendorf tubes, centrifuged for 30 seconds at $13000\times g$ and the supernatant analyzed by a UPLC-PDA for diuron quantification. A gentle swirl was performed before each sampling point. Experiments were performed in triplicate. AFW was added to the solution when necessary to compensate for evaporation.

4.2.5 Effect of g-C₃N₄ coated beads calcination time on the photocatalytic degradation of diuron

Crystallizing dishes (80 mm x 45 mm) with 50 mL of diuron solution (5 mg L^{-1} in AFW) were used. g-C₃N₄ coated beads with catalyst load of 0.28% w/v (1400 mg) were applied. g-C₃N₄ coated beads were prepared using with different calcination times of 2, 4, 6, 8 and 10 hours. The preparation of g-C₃N₄ coated beads was previously described (Chapter 3, Section 3.2.2). Reactors containing UV-A 365 nm LEDs were used to activate the g-C₃N₄ coated beads. A reactor containing UV-A LEDs was placed 3 cm from the level of the diuron solution as previously described.

Samples were taken (500 μL) at pre-determined intervals (Table 4.2), placed in 1.5 mL Eppendorf tubes, centrifuged for 30 seconds at $13000\times g$ and the supernatant analyzed by a UPLC-PDA for diuron quantification. A gentle swirl was performed before each sampling point. Experiments were performed in triplicate. AFW was added to the solution when necessary to compensate for evaporation.

4.2.6 Photocatalytic degradation of a pesticide mixture by g-C₃N₄ coated beads and UV-A LED irradiation

The efficiency of g-C₃N₄ coated beads and UV-A LEDs on the photocatalytic removal of a pesticide mixture was evaluated. The solution containing the pesticide mixture consisted of acetamiprid, clothianidin, imidacloprid, thiacloprid, thiamethoxam, dimethoate, diuron, atrazine and 2,4-D in AFW (1 mg L^{-1} each, total combined concentration of 9 mg L^{-1}). Reactors made of cardboard (30 x 21 cm) were prepared containing UV-A 365 nm light emitting diode (LED) irradiation (600 individual UV-A LEDs 365 nm; 8 W m^{-2}). Each reactor was placed on top of crystallizing dishes (150 mL, 80 mm x

45 mm; irradiated area of 50.3 cm² illuminated by approximately 60 individual LEDs), irradiating g-C₃N₄ coated beads (0.28% g-C₃N₄ w/v) from above at a distance of 3 cm from the experimental solution. Each crystallizing dish contained 50 mL of the pesticide mixture solution. An initial sample (500 µL) was removed from the pesticide mixture experimental solution for analysis (C₀) and g-C₃N₄ coated beads were added. Dark adsorption occurred for 15 minutes and another sample was removed (C_{Eq}). Samples were then exposed to UV-A LED irradiation and removed at 5, 15, 30, 45 and 60 minutes followed by samples at 4, 7, 24 and 48 hours. A gentle swirl was performed before each sampling point. Samples were then placed in 1.5 mL Eppendorf tubes, centrifuged for 30 seconds at 13000×g and the supernatant analyzed by UPLC-PDA for pesticide quantification. Light control samples were prepared using the pesticide mixture experimental solution irradiated with UV-A LEDs and without any g-C₃N₄ coated beads to evaluate the occurrence of photolysis by UV-A LED irradiation. Dark control samples were prepared using the pesticide mixture experimental solution and g-C₃N₄ coated beads with beakers completely enclosed by aluminium foil to avoid any light exposure to evaluate dark adsorption of pesticides onto the g-C₃N₄ coated beads. Each treatment was performed in triplicate. AFW was added to the solution when necessary to compensate for evaporation.

4.2.7 Reusability of g-C₃N₄ coated beads

Crystallizing dishes (80 mm x 45 mm) with 50 mL of diuron solution (5 mg L⁻¹ in AFW) were used. Reactors containing UV-A 365 nm LEDs, 3 cm from the level of the diuron solution, were used to activate g-C₃N₄ coated beads 0.28% w/v of g-C₃N₄ (1400 mg of g-C₃N₄ coated beads).

Samples were taken (500 µL) at T₀, T_{Eq} (dark adsorption) then at 5, 15, 30, 45 and 60 minutes followed by samples at 4, 7 and 24 hours, placed in 1.5 mL Eppendorf tubes, centrifuged for 30 seconds at 13000×g and the supernatant analyzed by a UPLC-PDA for diuron quantification. A gentle swirl was performed before each sampling point. After the last sampling point (24 hours), the g-C₃N₄ coated beads were removed from the diuron solution and rinsed with distilled water to be used in a repeated photocatalytic cycle. A total of 5 cycles were performed. Experiments were

performed in triplicate. AFW was added to the solution when necessary to compensate for evaporation. The pH of the solution was determined using pH indicator paper sticks (Fisher Scientific, UK) at pH range 0 to 14.

4.2.8 Photocatalytic degradation of diuron by graphitic carbon nitride (g-C₃N₄) coated beads and UV-A LED irradiation in a continuous flow reactor

A continuous flow reactor was prepared with a cylindrical reactor made of glass and stainless-steel end-fittings (150 mm height, 31.8 mm internal diameter, 9.1 mm wall thickness and total volume of 84 mL). The reactor was filled with 13 g of g-C₃N₄ coated beads (catalyst load of 4.64% w/v) with void volume of 28 mL. A 75 cm UV-A LED strip (365 nm) was placed around the cylindrical reactor with a total of 90 individual LEDs (Figure 4.4). A 2 L flask containing the diuron experimental solution (5 mg L⁻¹ in AFW) was prepared as the pesticide reservoir. The diuron solution then flowed through the reactor via an inlet tube at the bottom of the reactor using a peristaltic pump (KrosFlo Research Iii TFF system, Model 900-1893, Spectrum Laboratories) at different flow rates (5 and 10 mL min⁻¹). The treated solution was collected in the outlet reservoir (Figure 4.4).

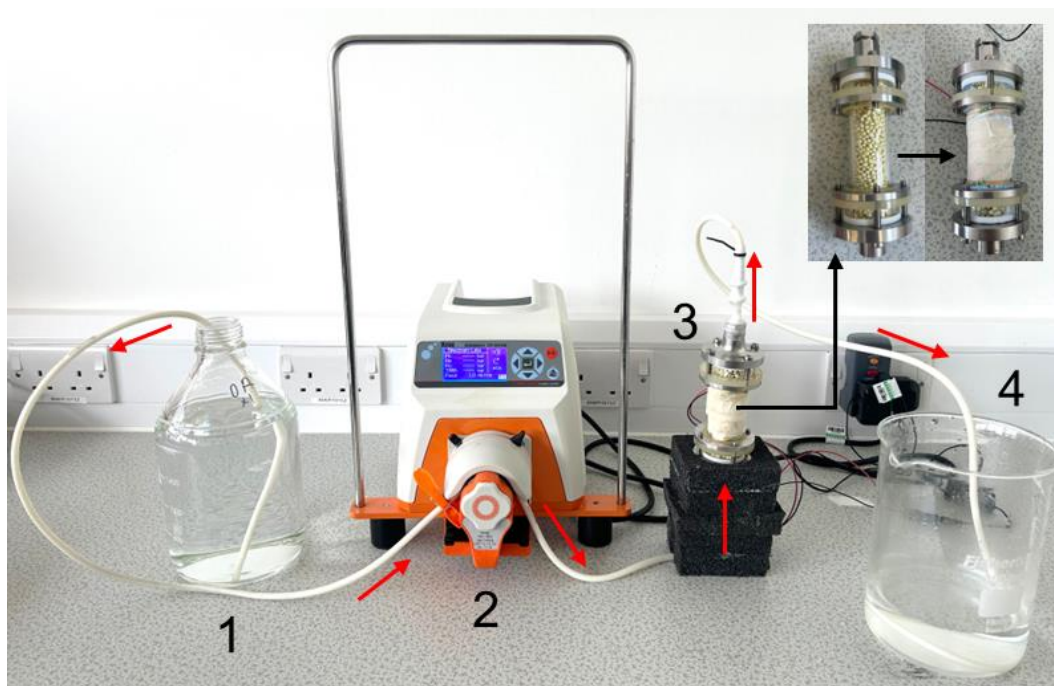


Figure 4.4: Continuous flow system for the photocatalytic degradation of diuron consisting of a 1) pesticide reservoir, 2) peristaltic pump, 3) photocatalytic reactor with graphitic carbon nitride ($\text{g-C}_3\text{N}_4$) coated beads and UV-A LEDs and 4) outlet reservoir. Red arrow indicates experimental solution flow.

An initial sample (1 mL) was removed for analysis (C_0). One reactor volume (RV) passed through the reactor (retention time: 5 minutes and 36 seconds at 5 mL min^{-1} and 2 minutes and 48 seconds at 10 mL min^{-1}) and another sample was taken (C_{Eq}) from the outlet tube before reaching the outlet reservoir. Following this, the UV-A LEDs were switched on and another sample was collected for analysis after one RV. Further samples were removed at pre-determined intervals (Table 4.4). Samples were then placed in 1.5 mL Eppendorf tubes, centrifuged for 30 seconds at $13000 \times g$ and the supernatant analyzed by UPLC-PDA for diuron quantification. Light control samples were prepared using the diuron experimental solution irradiated with UV-A LEDs, however, no $\text{g-C}_3\text{N}_4$ coated beads were placed inside of the reactor, instead uncoated beads with no catalyst (13 g) were used to investigate the effect of UV-A LED irradiation on diuron concentration. Uncoated beads were pre-treated with a fines removal step by washing with ultrapure water before the first set of light control experiments. Dark control samples were prepared using the diuron experimental solution and $\text{g-C}_3\text{N}_4$ coated beads with the reactor system completely enclosed by cardboard to avoid illumination. Each treatment was performed in triplicate.

The system was flushed with 3 RV of AFW at 5 mL min⁻¹ and UV-A LED irradiation before each experiment to remove any residual diuron.

Table 4.4: Sampling intervals for the photocatalytic degradation of diuron by UV-A LED irradiation (365 nm) and g-C₃N₄ coated beads in a continuous flow reactor at 5 and 10 mL min⁻¹ flow rate.

Sample	Time (minutes)	5 mL min ⁻¹	10 mL min ⁻¹
		Volume passed through the reactor (mL)	
1 (C ₀)	n/a	0	0
Dark adsorption (RV – varies according to flow rate)			
2 (C _{Eq})	0	28	28
UV-A LED on			
3	RV	28	28
4	15	75	150
5	30	75	150
6	60	150	300
7	120	300	600
8	240	600	1200
9	360	600	1200
		1856 mL	3656 mL

4.2.9 Ultra-performance liquid chromatography analysis of pesticides

Quantification of nine pre-selected pesticides (acetamiprid, clothianidin, imidacloprid, thiacloprid, thiamethoxam, dimethoate, diuron, atrazine and 2,4-D) was achieved by a Waters Acquity UPLC system (Waters, UK) and an Acquity photodiode array (PDA) eλ detector (Waters, UK) (Table 4.5). All chromatograms were extracted at wavelengths appropriate to each analyte (Table 4.6). The limit of quantification for all pesticides was 0.01 mg L⁻¹, except for dimethoate and 2,4-D which was 0.05 mg L⁻¹.

Table 4.5: Analytic conditions of ultra-performance liquid chromatography for the quantification of nine pesticides (acetamiprid, clothianidin, imidacloprid, thiacloprid, thiamethoxam, dimethoate, diuron, atrazine and 2,4-D).

Parameters	Conditions
Column	Acquity UPLC BEH C18 column (2.1 x 50 mm, 1.7 μ m particle size; Waters, UK)
Guard column	Acquity UPLC BEH C18 VanGuard pre-column (2.1 x 5 mm, 1.7 μ m particle size; Waters, UK)
Mobile phase	A: 0.05% trifluoroacetic acid in ultrapure water (18.2 M Ω) B: 0.05% trifluoroacetic acid in acetonitrile
Gradient	Time (min) 0 0.5 5 5.6 8 Solvent B (%) 5 5 80 5 5 Elution profile 6 6 6 6 6
Flow rate	0.5 mL min ⁻¹
Injection volume	10 μ L
Column temperature	40 $^{\circ}$ C

Table 4.6: Wavelength used for extraction of pesticide chromatograms after ultra-performance liquid chromatography analysis. The detection wavelength was selected according to the maximum UV absorption of each compound.

Pesticide	Chromatogram extraction (nm)	Retention time (min)
Acetamiprid	245	2.63
Clothianidin	265	2.38
Imidacloprid	269	2.48
Thiacloprid	245	2.91
Thiamethoxam	250	2.16
Dimethoate	211	2.54
Diuron	250	3.69
Atrazine	222	3.52
2,4-D	228	3.72

4.2.10 Statistical analysis

The values shown are the results of the mean of triplicates for each treatment (g-C₃N₄/UV-A LED photocatalysis, light control or dark control). As three replicates were used during experiments (n = 3), testing for equal variance and normality was not seen as appropriate for a small level of replication as the results could be misleading, therefore, parametric assumptions were accepted as a low standard deviation was observed (SD<10%; Table A4.1). Two-way ANOVA was used to test for statistically significant differences. A significance level of $p<0.05$ was used to identify significant differences between the results. *Post hoc* Tukey analysis was applied to significant results.

Further, the kinetics of experiments was evaluated and the experimental data were fitted to pseudo-first order and pseudo-second order models (Table 4.7). The correlation coefficient (R^2) was determined as a goodness-of-fit measure for linear regression models. A significance level of $R^2 > 0.7$ (high level of correlation) was used during kinetics determination.

Table 4.7: Kinetic models applied to the photocatalytic degradation of microcystin-LR.

Kinetics model	Linear equation	Model	Plot	Rate constant
Pseudo-first order	$\ln C = -kt + \ln C_0$	$C = C_0 \times e^{kt}$	$\ln C \text{ vs } t$	$k = \text{-slope}$
Pseudo-second order	$\frac{1}{C} = kt + \frac{1}{C_0}$	$C = \frac{1}{kt + \left(\frac{1}{C_0}\right)}$	$\frac{1}{C} \text{ vs } t$	$k = \text{slope}$

Where:

- C is the pesticide concentration (mg L^{-1}) at a given time of photocatalytic degradation t .
- C_0 is the pesticide concentration (mg L^{-1}) at T_0 .
- k is the pseudo-first order and pseudo-second order reaction rate constant (min^{-1}).

4.3 Results and discussion

4.3.1 Comparison of photocatalytic reactor designs for degradation of the herbicide diuron

A simplified and optimized reactor design for bench-scale experiments based on the photocatalytic degradation of pesticides by $\text{g-C}_3\text{N}_4$ coated beads and UV-A LEDs was evaluated. The first design was previously used for the photocatalytic degradation of the toxin microcystin-LR (Chapter 3, Section 3.2.1), however, beakers (100 mL) were used in this reactor, which demonstrated a small irradiation area of 19.6 cm^2 that could possibly limit the activation of $\text{g-C}_3\text{N}_4$ coated beads by UV-A irradiation. Also, magnetic stirrers at 100 rpm were used and often a change in the rotation speed of the stirrers was observed over time, especially during longer photocatalytic experiments (e.g., 24 hours of photocatalysis). Furthermore, the magnetic stirrer would eventually stop for a few seconds and abruptly restart,

resulting in shedding of the g-C₃N₄ coated beads, which could be identified by the experimental solution becoming cloudy.

The improved reactor design consisted of crystallizing dishes which presented a larger irradiated area of 50.3 cm², over 2-fold increase compared to the beakers, and mixing was achieved by a gently swirl performed before sampling to reduce damage to the catalyst coating. The lack of a more intense mixing could result in a non-uniformity of the experimental solution and it could limit the mass transport of pesticides in solution (Tokode 2014) and consequently decrease the photocatalytic efficiency of the system. Therefore, the two designs were tested in photocatalytic experiments for diuron degradation to verify the efficiency of each design and to investigate the influence of magnetic mixing during photocatalysis. There was complete degradation of diuron over 24 hours of photocatalysis when both crystallizing dishes with no magnetic mixing and beakers in the presence of magnetic mixing were used (Figure 4.5).

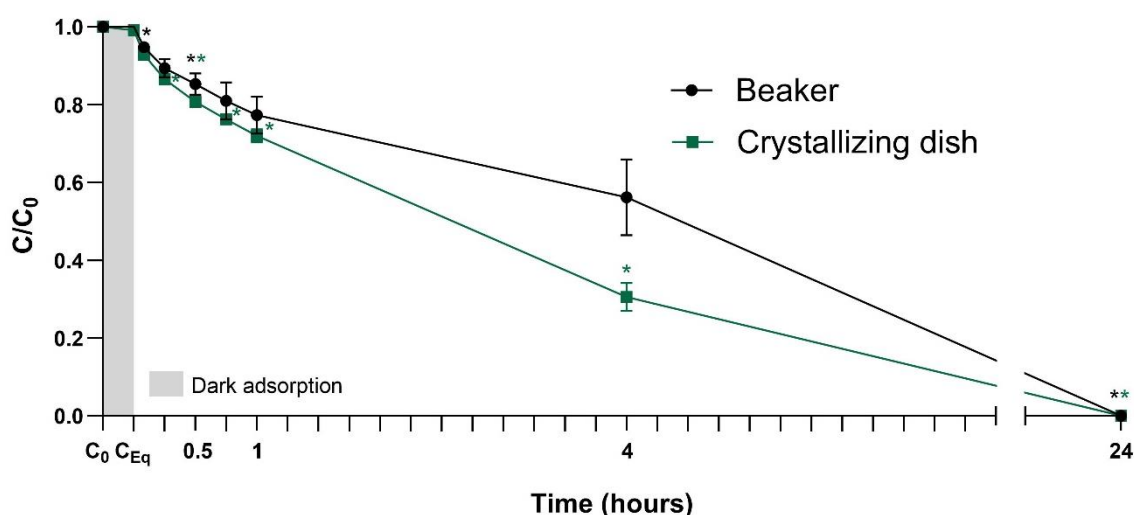


Figure 4.5: Diuron degradation after photocatalytic treatment by UV-A LED irradiation and glass beads coated with graphitic carbon nitride (g-C₃N₄) over 24 hours using two different reactor designs (crystallizing dish with no magnetic mixing vs. beaker with magnetic mixing). (n = 3, error bars = 1SD). *Significantly different from T_{Eq}.

The diuron kinetics was evaluated and both set of data were best fit into a pseudo-first order reaction with a R² = 0.9871 when crystallizing dishes were used (Figure 4.6) and a R² = 0.8643 when beakers were used (Figure 4.7). Other studies evaluating diuron degradation by photocatalysis also observed a pseudo-first order reaction kinetics (Bouquet-Somrani et al. 2000; Katsumata et al. 2009; Fenoll et al. 2013; Meephon et al. 2019).

When crystallizing dishes were used, however, diuron degradation demonstrated a faster reaction rate constant $k = 0.004738 \text{ min}^{-1}$ (Figure 4.6) in comparison with a reaction rate constant $k = 0.0023 \text{ min}^{-1}$ when beakers were used (Figure 4.7), even though no magnetic mixing was present in the crystallizing dish experimental setup. Therefore, a gentle swirl before each sampling point was sufficient to ensure the diuron experimental solution was homogenous and did not interfere negatively in the photocatalytic performance of diuron degradation. The reactor design using crystallizing dishes with no magnetic mixing was selected as standard for all following photocatalytic experiments involving the degradation of pesticides.

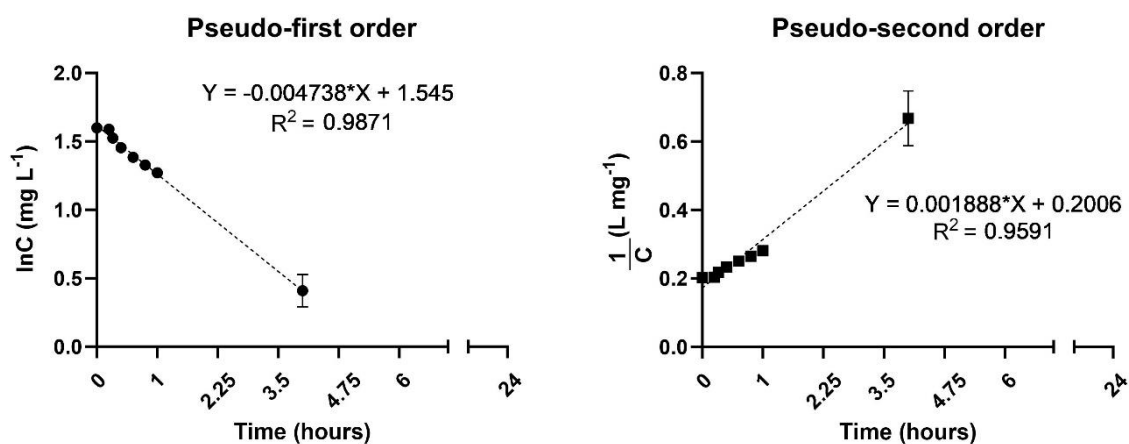


Figure 4.6: Kinetics of diuron photocatalytic degradation by graphitic carbon nitride (g-C₃N₄) coated beads and UV-A LED irradiation using crystallizing dishes and no magnetic mixing. Kinetic models were calculated following pseudo-first order and pseudo-second order reactions. Diuron initial concentration was 5 mg L⁻¹. (n = 3, error bars = 1SD).

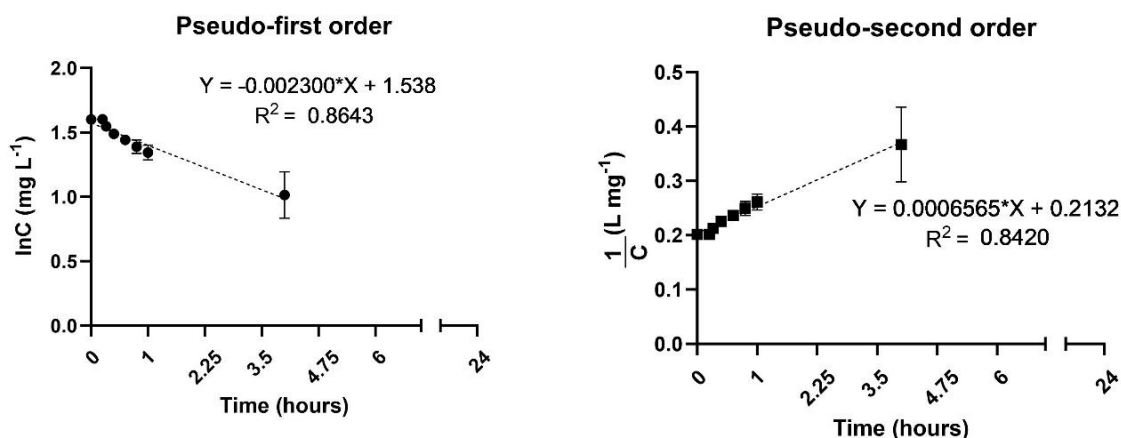


Figure 4.7: Kinetics of diuron photocatalytic degradation by graphitic carbon nitride (g-C₃N₄) coated beads and UV-A LED irradiation using beakers in the presence of magnetic mixing. Kinetic models were calculated following pseudo-first order and pseudo-second order reactions. Diuron initial concentration was 5 mg L⁻¹. (n = 3, error bars = 1SD).

4.3.2 g-C₃N₄ coated beads catalyst load optimization using solution pH 7

The g-C₃N₄ catalyst load of 0.14% (w/v) from g-C₃N₄ coated beads was initially selected based on previous investigations where g-C₃N₄ coated beads (0.15% w/v of g-C₃N₄) were used for the photocatalytic degradation of microcystin-LR by natural sunlight (Pestana et al. 2023). Further investigation, however, was necessary to determine the optimal g-C₃N₄ catalyst load for the degradation of pesticides in the current study. A diuron solution (5 mg L⁻¹) was prepared in AFW at an initial pH 7. Photocatalytic experiments were performed where the catalyst load of g-C₃N₄ coated beads varied from 0.14% to 0.7% (w/v) of g-C₃N₄. The diuron concentration significantly decrease ($p < 0.05$) from 15 minutes of photocatalysis and continued to reduce until diuron was completely removed the end of the experiment for all catalyst loads evaluated (Figure 4.8).

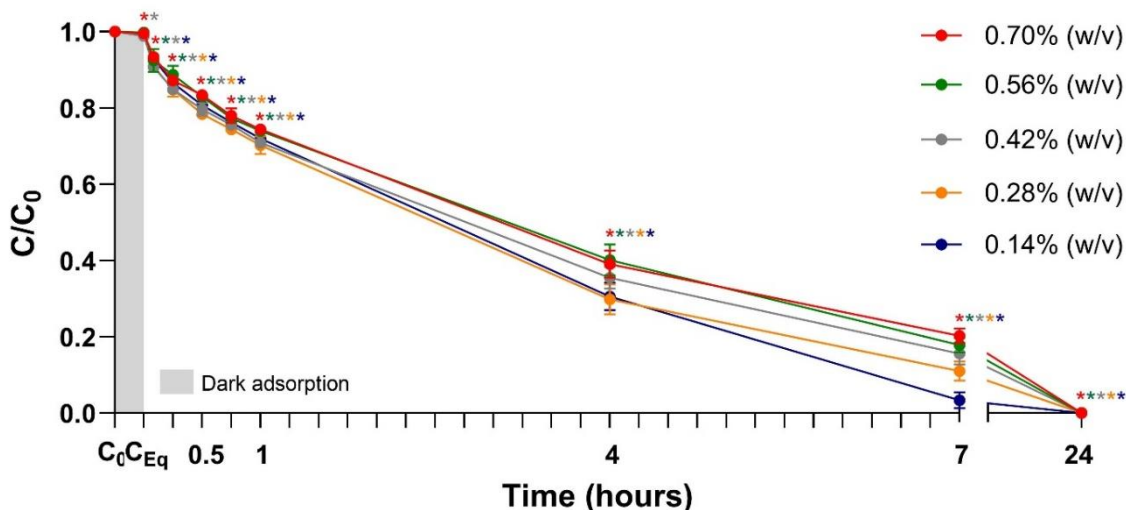


Figure 4.8: Diuron degradation after photocatalytic treatment by UV-A LED irradiation and glass beads coated with graphitic carbon nitride (g-C₃N₄) at different catalyst loads (0.14% – 0.70% w/v) and initial solution pH 7 over 24 hours. (n = 3, error bars = 1SD). *Significantly different from T_{Eq}.

To determine the optimal g-C₃N₄ catalyst load, the reaction rate constant k of diuron was determined for each catalyst load evaluated. The data used to determine the diuron kinetics of all g-C₃N₄ catalyst load investigated best fit into a pseudo-first order reaction with $R^2 = 0.9114$ for 0.14% (w/v) g-C₃N₄ catalyst load, $R^2 = 0.9850$ for 0.28% (w/v) g-C₃N₄, $R^2 = 0.9870$ for 0.42% (w/v) g-C₃N₄, $R^2 = 0.9897$ for 0.56% (w/v) g-C₃N₄ and $R^2 = 0.9933$ for 0.70% (w/v) g-C₃N₄ (Figure 4.9). Contrary to what may have been expected, lower g-C₃N₄ catalyst loads showed higher diuron degradation rates with a reaction rate constant $k = 0.007699 \text{ min}^{-1}$ when 0.14% (w/v) g-C₃N₄ was used $> k = 0.005078 \text{ min}^{-1}$ for 0.28% (w/v) g-C₃N₄ $> k = 0.004238 \text{ min}^{-1}$ for 0.42% (w/v) g-C₃N₄ $> k = 0.003911 \text{ min}^{-1}$ for 0.56% (w/v) g-C₃N₄ $> k = 0.003679 \text{ min}^{-1}$ for 0.70% (w/v) g-C₃N₄ (Figure 4.9). Vela et al. (2015) investigated the effects of powdered TiO₂ concentration on the photocatalytic degradation of the herbicides metamitron and metribuzin by UV-A irradiation. The catalyst loads used for herbicide degradation were 50, 100, 150, 200 and 300 mg L⁻¹ which represented 0.005%, 0.01%, 0.015%, 0.02% and 0.03% (w/v) TiO₂ respectively. Contrary to the findings of the present study, it is possible to observe that higher degradation of both metamitron and metribuzin over 60 minutes of photocatalysis occurred when higher TiO₂ concentrations were applied, even

though reaction rate constants were not determined (Vela et al. 2015). Kumar et al. (2022) also used TiO_2 to investigate the effects of the catalyst load on the photocatalytic degradation of the insecticide dichlorvos. The authors observed an increase in the dichlorvos degradation rate constant k as the catalyst concentration increased from 0.002% to 0.006% w/v TiO_2 (Kumar et al. 2022). Further, the degradation kinetics of the herbicide isoproturon was showed to increase as the TiO_2 concentration increased from 0.0125% to 0.25% (w/v) TiO_2 in another photocatalytic study (Verma, Prakash and Toor 2014).

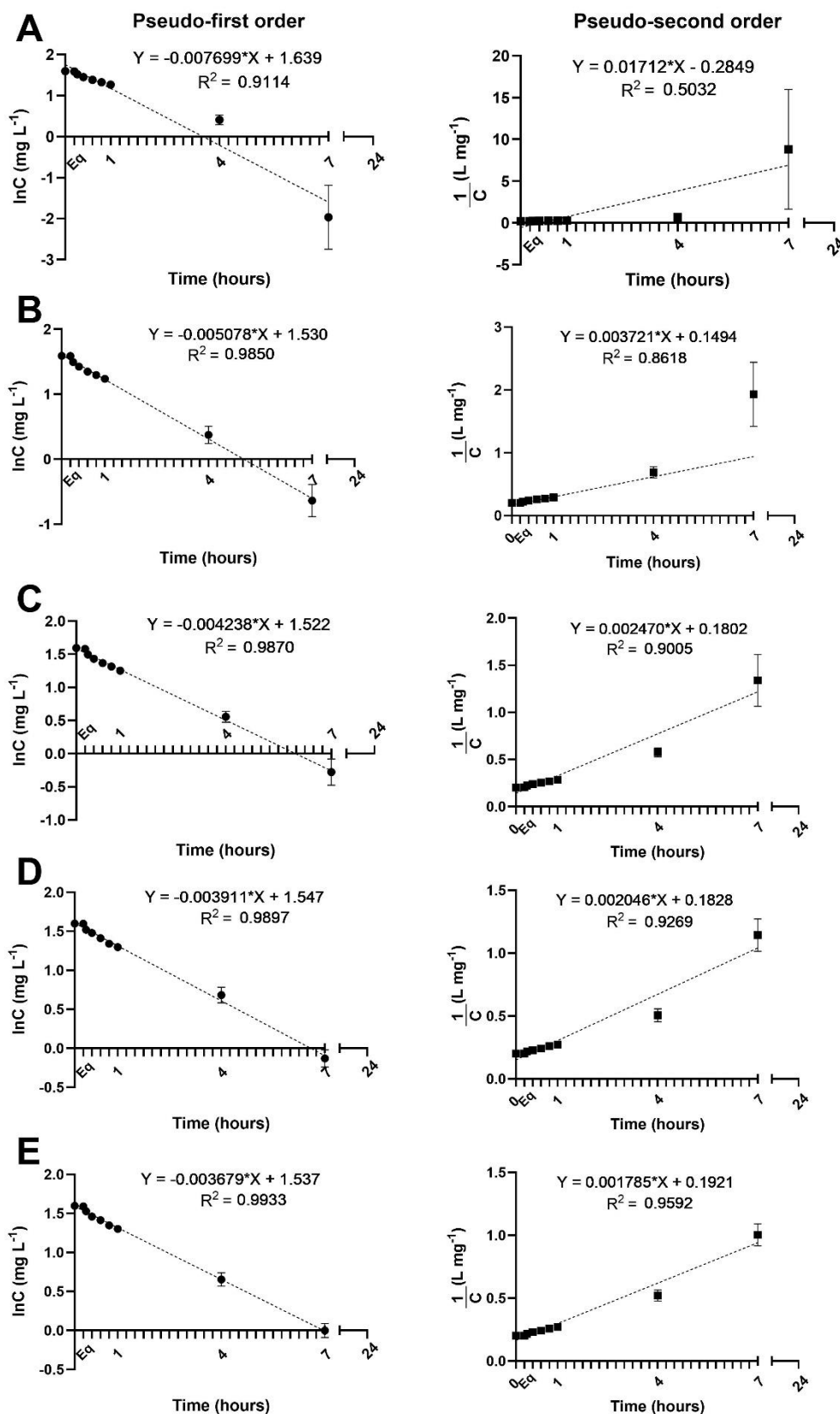


Figure 4.9: Kinetics of diuron photocatalytic degradation by graphitic carbon nitride (g-C₃N₄) coated beads at of A) 0.14%, B) 0.28%, C) 0.42%, D) 0.56% and E) 0.70% (w/v) catalyst load and UV-A LED irradiation at initial solution pH 5. Kinetic models were calculated following pseudo-first order and pseudo-second order reactions. Diuron initial concentration was 5 mg L⁻¹. (n = 3, error bars = 1SD).

A faster degradation of diuron was expected when higher catalyst loads were applied, however, lower catalyst loads were more effective in the photocatalytic degradation of diuron. The photocatalytic degradation of pesticides can be dependent on the solution pH value. Zhang et al. (2021) observed that the solution pH had different effects on the photocatalytic degradation of nine triazine pesticides by g-C₃N₄ doped with phosphorus and boron irradiated by visible light. While the photocatalytic performance was favored by acidic pH during the degradation of simazine, atrazine, terbuthylazine, cyanazine, metribuzin and hexazinone, the solution pH seemed to not interfere in the photocatalytic degradation of simetryne and simeton (Zhang et al. 2021). To further investigate why lower g-C₃N₄ catalyst loads presented higher photocatalytic efficiency in the degradation of diuron, a simple evaluation of the solution pH was performed. 50 mL of pure water were placed inside of crystallizing dishes containing 0.14% w/v of g-C₃N₄ coated beads (minimum catalyst load investigated) and 0.70% w/v of g-C₃N₄ coated beads (maximum catalyst load investigated) and the solution pH was recorded at 1, 4 and 72 hours by an Universal pH indicator paper (Fisher Scientific, UK). After 1 hour, the solution containing 0.14% w/v of g-C₃N₄ coated beads presented a pH of 7, while the solution containing 0.70% w/v of g-C₃N₄ coated beads showed an increase pH of 8, which continued to increase until 4 hours with a pH of 9 and a final pH of 10 at 72 hours (Figure 4.10). The solution pH only increased from pH 7 to pH 8 at 72 hours when 0.14% (w/v) g-C₃N₄ coated beads were used. It is possible that the pH was interfering in the photocatalytic efficiency when different catalyst loads were used, therefore, the optimal solution pH should be determined to better understand the photocatalytic conditions of the system based on g-C₃N₄ coated beads and UV-A LED irradiation.

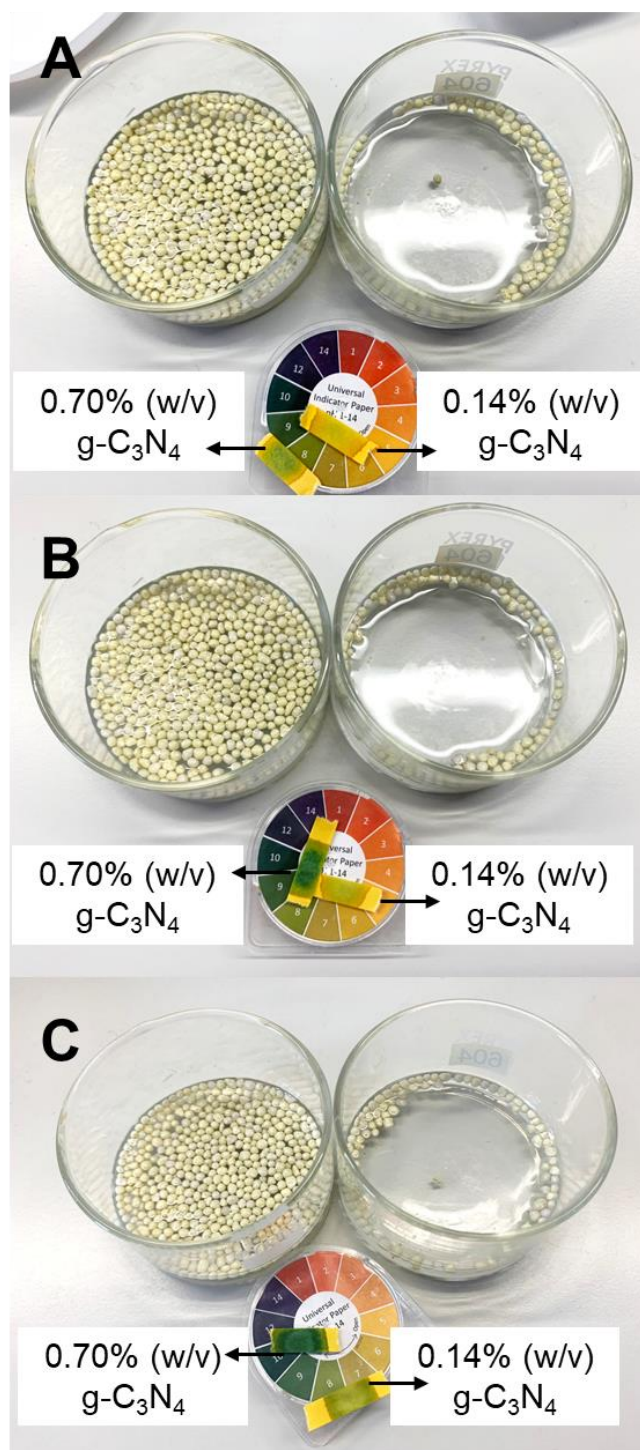


Figure 4.10: Solution pH from crystallizing dishes containing graphitic carbon nitride (g-C₃N₄) catalyst load of 0.14% (w/v) and 0.7% (w/v) in pure water after A) 1 hour, B) 4 hours and C) 72 hours contact time.

4.3.3 Optimization of initial solution pH for the photocatalytic degradation of diuron by g-C₃N₄ coated beads

The effects of the solution pH on the photocatalytic efficiency of g-C₃N₄ coated beads (0.14% w/v) illuminated by UV-A LED was investigated to better understand the optimal conditions in which this photocatalytic system occurs. The herbicide diuron (5 mg L⁻¹) was used as a model pesticide. The initial pH of the diuron solution in AFW was set to 2, 5, 8 and 10 by adjusting with 1 M HCl or 1 M NaOH. The photocatalytic performance towards diuron degradation was affected by the change of the initial solution pH. Diuron was significantly degraded ($p < 0.05$) from 5 minutes (0.083 hours) for solutions containing initial pH 2, 5 and 10 and from 15 minutes (0.25 hours) for solution containing initial pH 8 and diuron concentration continued to decrease until it was completely degraded (Figure 4.11).

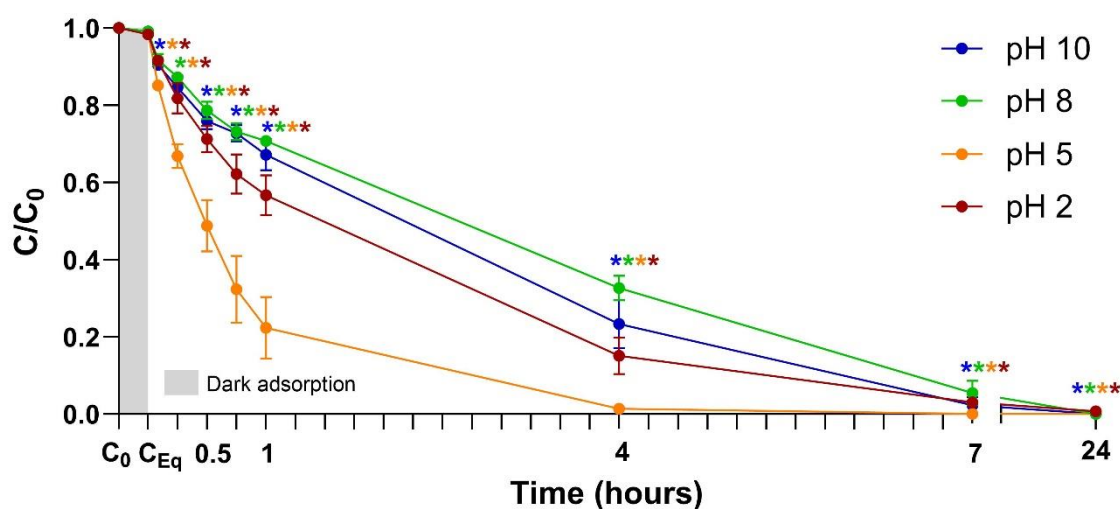


Figure 4.11: Diuron degradation after photocatalytic treatment by UV-A LED irradiation and graphitic carbon nitride (g-C₃N₄) coated beads containing different initial pH solutions (pH 2, 5, 8 and 10) over 24 hours. (n = 3, error bars = 1SD). *Significantly different from T_{Eq}.

Diuron degradation rates, however, were differently affected by the solution initial pH. The diuron reaction rate constant k was determined for each treatment. All data best fit into a pseudo-first order reaction with $k = 0.01639 \text{ min}^{-1}$ ($R^2 = 0.9433$) for pH 5, $k = 0.006633 \text{ min}^{-1}$ ($R^2 = 0.9180$) for pH 8 and $k = 0.007334 \text{ min}^{-1}$ ($R^2 = 0.9679$) for pH 10, except for solution initial pH 2 data which were best fit into a pseudo-second order

with $R^2 = 0.9162$ in comparison with a $R^2 = 0.7719$ for pseudo-first order. However, all data were considered to follow pseudo-first order and initial pH 2 reaction demonstrated a diuron degradation rate $k = 0.003473 \text{ min}^{-1}$ (Figure 4.12). Therefore, a higher g-C₃N₄ photocatalytic activity was observed when the initial pH of the diuron solution was adjusted to acidic to neutral pH range (pH 5), in comparison with a lower g-C₃N₄ photocatalytic activity when the initial pH was adjusted to basic pH of 8 and 10 or very acidic pH 2.

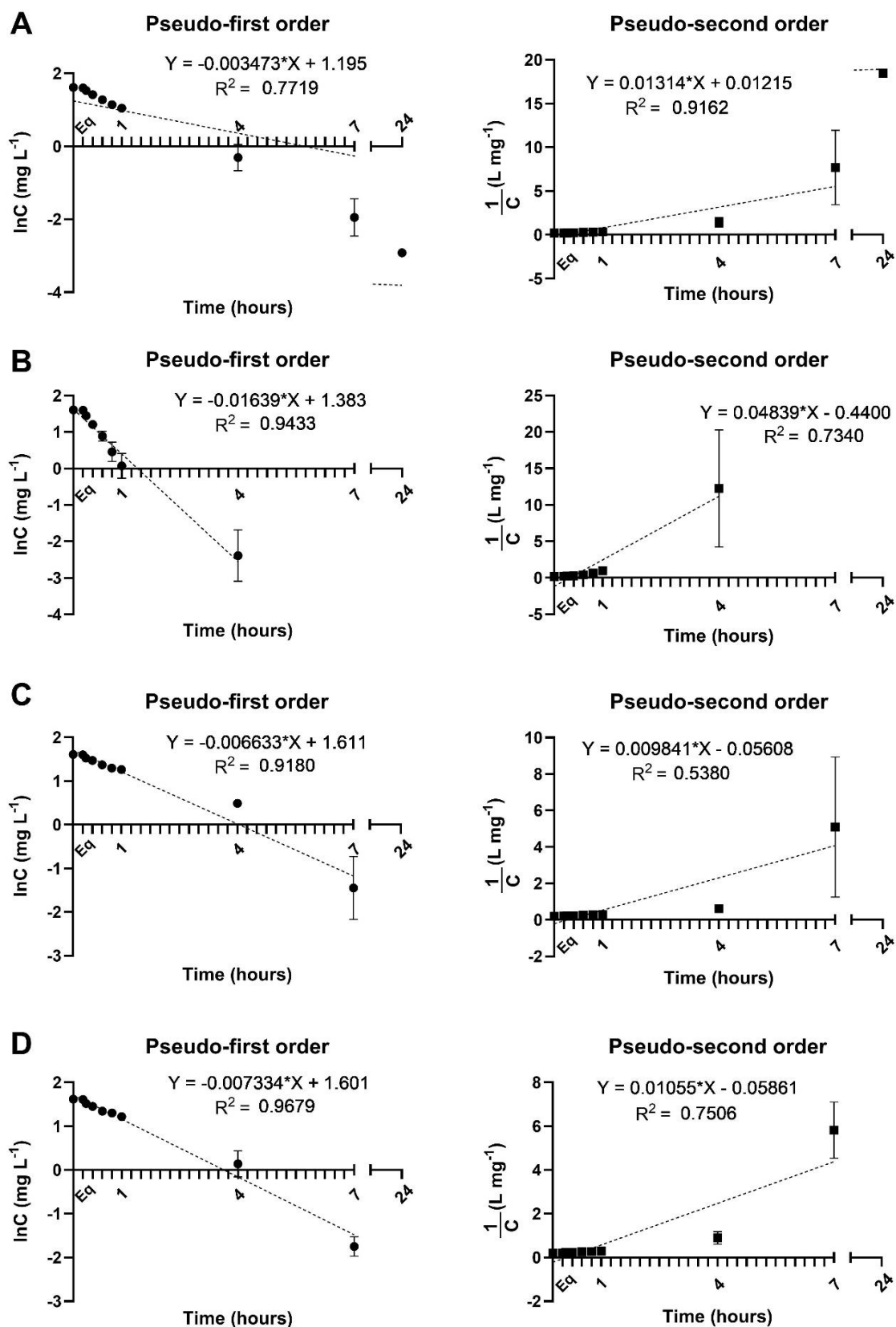


Figure 4.12: Kinetics of diuron photocatalytic degradation by graphitic carbon nitride (g-C₃N₄) coated beads and UV-A LED irradiation in solutions containing initial pH of A) 2, B) 5, C) 8 and D) 10. Kinetic models were calculated following pseudo-first order and pseudo-second order reactions. Diuron initial concentration was 5 mg L⁻¹. (n = 3, error bars = 1SD).

The solution pH can be an important factor in photocatalytic performance and it can influence the adsorption of pollutants onto the catalyst surface (Bruckmann et al. 2022; Gao et al. 2022). Although diuron was completely degraded by g-C₃N₄ coated beads and UV-A irradiation over 24 hours for all the initial pH conditions evaluated, the most efficient photocatalytic degradation of diuron occurred for initial pH 5, which presented the fastest degradation rate. The rate constant k was determined as follows: pH 5 (0.01639 min⁻¹) > pH 10 (0.007334 min⁻¹) > pH 8 (0.006633 min⁻¹) > pH 2 (0.003473 min⁻¹), with significant differences ($p < 0.05$) between photocatalytic treatments at initial pH 5 and 10 from 5 minutes to 1 hour of photocatalysis and between pH 5 and 8 from 5 minutes to 4 hours of photocatalysis. However, no significant differences were observed in the diuron degradation between initial pH 2 and pH 8 ($p > 0.05$), except at 4 hours of photocatalysis, and between initial pH 8 and pH 10 (Table A4.2). This might be related to the fact that diuron has a pK_a of 3.7, therefore, diuron shows a negative charge at solution pH 5, since the solution pH is higher than the diuron pK_a of 3.7 (Lopes and Salgado 2021). The diuron negative charge at pH 5 may result in a strong electrostatic attraction among diuron and the positively charged g-C₃N₄ particles (Martin et al. 2014; Paul et al. 2019), which may explain the higher photocatalytic degradation by g-C₃N₄ coated beads. Furthermore, the production of more powerful reactive oxygen species (ROS) such as hydroperoxyl radical •O₂H, hydrogen peroxide H₂O₂ and hydroxyl radical •OH from the protonation and reduction reactions of superoxide radicals (•O₂⁻) generated during g-C₃N₄ photocatalysis could have been enhanced in acidic conditions because of the presence of protons H⁺ (Dorraj et al. 2017; Andrés et al. 2023; Grando et al. 2023), hence the higher photocatalytic performance observed at solution pH 5.

The solution pH was also monitored during photocatalytic experiments. The solution pH increased after the addition of the g-C₃N₄ coated beads into solution and it continued to increase until the end of the photocatalytic reaction (Figure 4.13). There was a higher pH variation between T₀ and 24 hours of photocatalysis for solutions with lower initial pH (pH 2 and pH 5), which demonstrated a pH increase of 3 pH units (from pH 2 to pH 5 for initial (Figure 4.13). The decrease in the solution pH at 24 hours could have

been caused by a dilution of the diuron solution when AFW was added into the crystallizing dishes to compensate for evaporation.

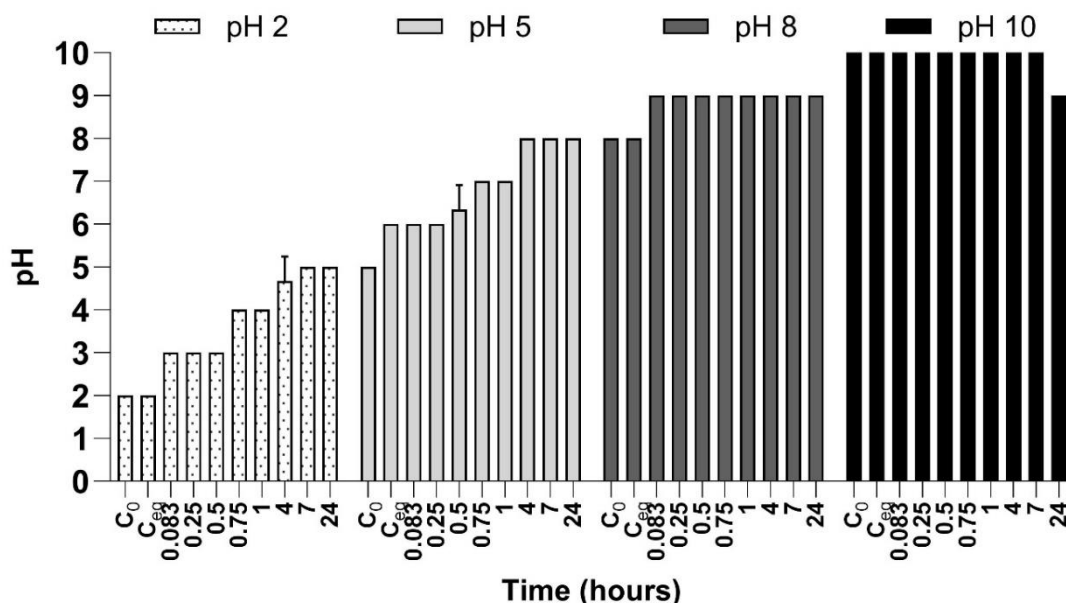


Figure 4.13: Solution pH determined during photocatalytic degradation of diuron by graphitic carbon nitride (g-C₃N₄) coated beads and UV-A LED irradiation in solutions containing initial pH of 2, 5, 8 and 10.

The increase in the solution pH might have been caused due to the generation of intermediate products such as heptazine and poly(triazine imide) created during the calcination of melamine during the preparation of g-C₃N₄ coated beads (Pestana et al. 2023). Furthermore, the washing procedure during the preparation of g-C₃N₄ coated beads is an important step responsible for removing impurities and uncoated (loose) g-C₃N₄ particles from the glass bead surface. It is possible that not all loose g-C₃N₄ particles were removed during the washing step during the preparation of g-C₃N₄ coated beads, which could have then been released into solution during pH optimization experiments and therefore responsible for increasing the solution pH over time.

4.3.4 g-C₃N₄ coated beads catalyst load optimization with pH 5 and phosphate buffer initial solution

In order to determine the optimal g-C₃N₄ coated beads catalyst load for the photocatalytic degradation of diuron at a constant solution pH, the diuron experimental solution (5 mg L⁻¹) was prepared in phosphate buffer pH 5 instead of AFW. The phosphate buffer solution was prepared using 6.8 g L⁻¹ sodium dihydrogen phosphate (NaH₂PO₄) and 10M potassium hydroxide (KOH) to adjust the pH to 5. The catalyst load of g-C₃N₄ coated beads varied from 0.14% to 0.7% (w/v) g-C₃N₄. Diuron was significantly ($p < 0.05$) degraded from 15 minutes of photocatalysis by g-C₃N₄ coated and UV-A LED irradiation when catalyst loads of 0.14% - 0.56% (w/v) were used and from 30 minutes of photocatalysis when 0.70% (w/v) g-C₃N₄ catalyst load was used. The diuron concentration continued to decrease until it was completely degraded within 24 hours of photocatalytic treatment for all catalyst loads evaluated (Figure 4.14).

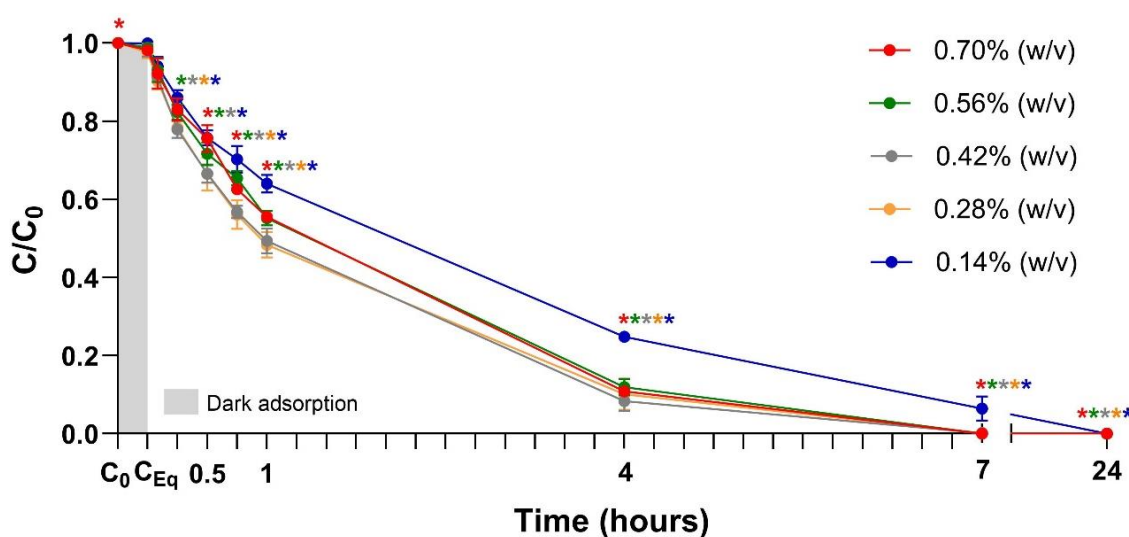


Figure 4.14: Diuron degradation after photocatalytic treatment by UV-A LED irradiation and glass beads coated with graphitic carbon nitride (g-C₃N₄) at different catalyst loads (0.14% – 0.70% w/v), initial solution pH 5 in phosphate buffer over 24 hours. (n = 3, error bars = 1SD). *Significantly different from T_{Eq}.

The diuron degradation rates were also evaluated to determine the optimal g-C₃N₄ catalyst load. All data for treatments using different g-C₃N₄ coated beads catalyst loads best fit into a pseudo-first order reaction with R² = 0.9630 for 0.14% (w/v) g-C₃N₄ catalyst load, R² = 0.9587 for 0.28% (w/v) g-C₃N₄, R² = 0.9866 for 0.42% (w/v) g-C₃N₄, R² = 0.9902 for 0.56% (w/v)

g-C₃N₄ and $R^2 = 0.9953$ for 0.70% (w/v) g-C₃N₄ (Figure 4.15). Contrary to what was previously observed, the diuron degradation rates increased when higher g-C₃N₄ catalyst loads were used from 0.14% to 0.42% (w/v) of g-C₃N₄ with a reaction rate constant $k = 0.006411 \text{ min}^{-1}$ when 0.14% (w/v) g-C₃N₄ was used $< k = 0.009471 \text{ min}^{-1}$ for 0.28% (w/v) g-C₃N₄ $< k = 0.01090 \text{ min}^{-1}$ for 0.42% (w/v) g-C₃N₄ (Figure 4.15).

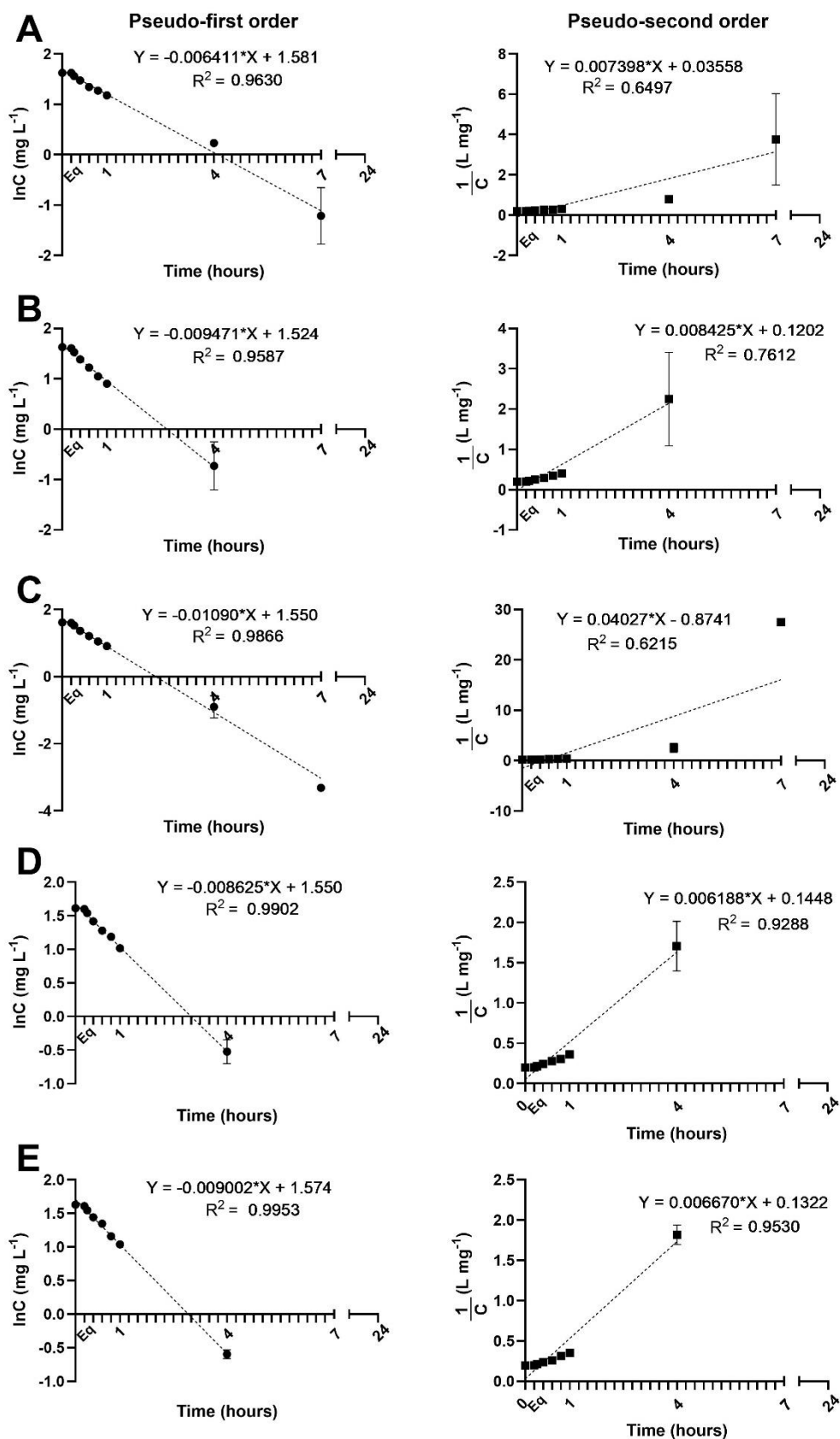


Figure 4.15: Kinetics of diuron photocatalytic degradation by graphitic carbon nitride (g-C₃N₄) coated beads at of A) 0.14%, B) 0.28%, C) 0.42%, D) 0.56% and E) 0.70% (w/v) catalyst load and UV-A LED irradiation at solution pH 5 in phosphate buffer. Kinetic models were calculated following pseudo-first order and pseudo-second order reactions. Diuron initial concentration was 5 mg L⁻¹. (n = 3, error bars = 1SD).

However, the diuron reaction rate constant k decreased as the catalyst load increased from 0.56% (w/v) g-C₃N₄ with a $k = 0.008625 \text{ min}^{-1}$ for 0.56% (w/v) g-C₃N₄ and $k = 0.009002 \text{ min}^{-1}$ for 0.70% (w/v) g-C₃N₄ (Figure 4.15), with no significant changes ($p > 0.05$) between all the sampling times for treatments where 0.56% and 0.70% (w/v) g-C₃N₄ were used as catalyst load (Table A4.2).

The decrease in the diuron degradation rates from 0.56% (w/v) g-C₃N₄ catalyst load could be explained by the light scattering effect (Fenoll et al. 2019), where the higher catalyst concentration present in solution might have prevented the UV-A LED irradiation to reach diuron molecules and therefore caused a decrease in the photocatalytic performance. Paul et al. (2019) also observed a decline in the photocatalytic activity of g-C₃N₄ towards methylene blue dye degradation when higher catalyst load of 0.07% (w/v) g-C₃N₄ was used in comparison with lower catalyst loads of 0.01%, 0.03% and 0.05% (w/v) g-C₃N₄. The same light scattering effect, where the larger amount of catalyst prevents the penetration of light, was observed when the concentration of powdered TiO₂ and UV irradiation were used in the degradation of the neonicotinoid thiacloprid. As the TiO₂ concentration increased from 0.02% to 0.05% (w/v) TiO₂ (0.2 – 0.5 g L⁻¹), the thiacloprid degradation rate also increased, however, further increase in the TiO₂ load from 0.05% to 0.15% w/v TiO₂ (0.5 – 1.5 g L⁻¹) resulted in a decline in the photocatalytic performance (Berberidou et al. 2019).

Even though the highest diuron degradation rate was achieved when 0.42% (w/v) g-C₃N₄ catalyst load was used, there were no significant ($p > 0.05$) differences between all sampling points for treatments where 0.42% and 0.28% (w/v) g-C₃N₄ were used as catalyst load (Table 43.2). Therefore, the optimal g-C₃N₄ coated beads catalyst load selected was 0.28% (w/v) g-C₃N₄, which was the most cost-effective option for diuron photocatalytic degradation between the catalyst loads evaluated (Figure 4.14).

The optimal catalyst load of 0.28% (w/v) g-C₃N₄ was used in the following photocatalytic experiments involving the degradation of pesticides by g-C₃N₄ coated beads and UV-A LED irradiation. The solution pH, however, was not adjusted to the optimal pH determined. The investigation to determine the optimal solution pH during g-C₃N₄ coated beads photocatalysis was not performed to suggest an adjustment of the solution pH in aquatic

environments during at source application of the photocatalytic system, but to better understand the optimal conditions during photocatalysis by g-C₃N₄ coated beads and UV-A LED irradiation and the effects of pH in the photocatalytic efficiency during the removal of pesticides.

4.3.5 Optimization of muffle furnace calcination time for g-C₃N₄ coated beads preparation

The optimization of calcination time of the g-C₃N₄ precursor is important especially when large amount of catalyst is required for large scale applications, such as water treatment, therefore, shorter times for the preparation of catalyst are desirable. g-C₃N₄ coated beads were prepared using different calcination times (2, 4, 6, 8 and 10 hours) and the photocatalytic performance was evaluated with UV-A LED irradiation on diuron degradation. All g-C₃N₄ coated beads prepared at different calcination times were able to degrade diuron. Diuron was significantly removed ($p < 0.05$) from 30 minutes for g-C₃N₄ coated beads calcinated for 2 and 8 hours, from 2 hours for 4 hours calcination time and from 15 minutes for 6 hours calcination time. Diuron continued to be degraded over 24 hours until the end of photocatalysis (Figure 4.16). g-C₃N₄ coated beads prepared with 10 hours calcination time demonstrated the best photocatalytic performance with diuron showing a significant degradation from 5 minutes of photocatalysis reaching complete degradation over 1 hour (Figure 4.16).

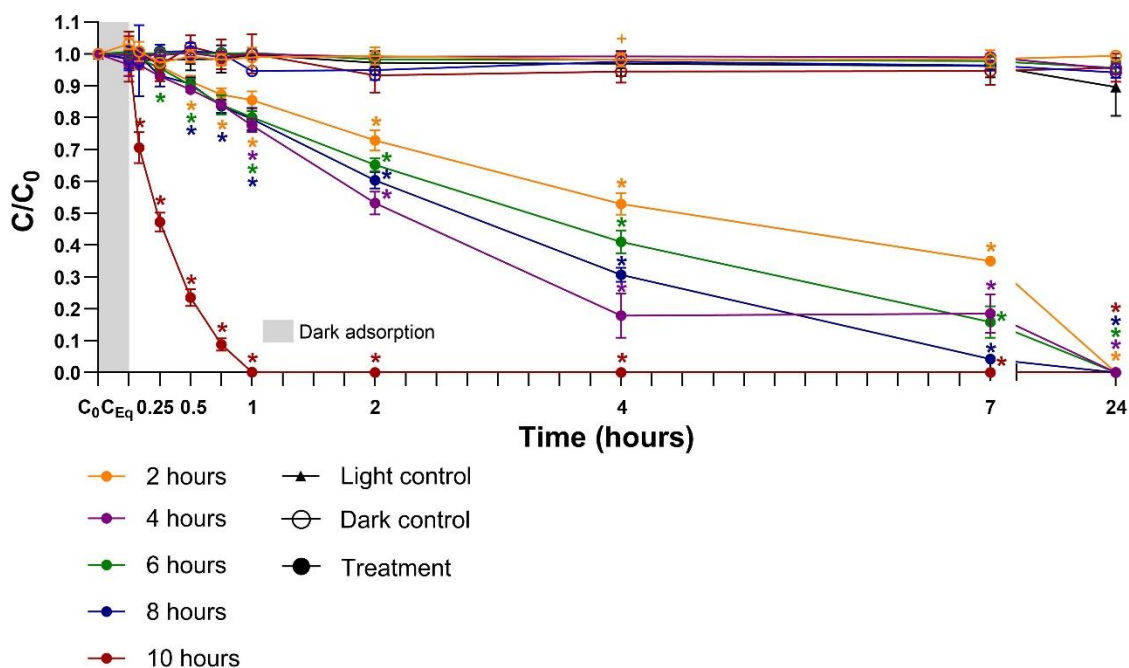


Figure 4.16: Diuron degradation after photocatalytic treatment by UV-A LED irradiation and glass beads coated with graphitic carbon nitride (g-C₃N₄) coated at different calcination times (2, 4, 6, 8 and 10 hours) over 24 hours. (n = 3, error bars = 1SD). *Significantly different from T_{Eq} (Treatment), +Significantly different from T_{Eq} (Dark control).

No significant changes ($p > 0.05$) were observed during light control experiments when only UV-A LED irradiation was applied on the diuron solution. Also, there were no significant changes ($p > 0.05$) during dark control samples where only g-C₃N₄ coated beads were used with no illumination (Figure 4.16).

Even though the highest photocatalytic performance during diuron degradation was achieved when g-C₃N₄ coated beads were prepared with 10 hours calcination time, most investigations report a calcination time of up to 4 hours during preparation of g-C₃N₄ (Zhao et al. 2015; Chen et al. 2021; Oluwole, Khoza and Olatunji 2022; Jadhav et al. 2023; Roškarič et al. 2023; Tarighati Sareshkeh et al. 2023). Wang et al. (2019a), however, investigated the effects of calcination time during the production of g-C₃N₄ (4, 6, 8 and 10 hours calcination time using 600 °C calcination temperature) during the photocatalytic degradation of Rhodamine B and the authors also observed that the best photocatalytic performance was achieved when 10 hours calcination time was used to prepare g-C₃N₄. Therefore, the optimal calcination time for g-C₃N₄ coated beads preparation was 10 hours.

The morphology of g-C₃N₄ coated beads prepared at different calcination times was evaluated on a scanning electron microscope (SEM, JSM-IT800, JEOL, Japan). Coating layers of g-C₃N₄ with rough surfaces were present on all samples. The g-C₃N₄ is moderately uniform for coated beads prepared with 2, 4 and 6 hours of calcination time, as some regions of exposed glass bead surface were observed (Figure 4.17). When g-C₃N₄ coated beads were prepared with 8 hours calcination time, the g-C₃N₄ layer was uniform with agglomerated particles deposited on the surface of the glass bead (Figure 4.17). g-C₃N₄ coated beads prepared with 10 hours calcination time presented multilayer of catalyst with tube and needle structures (Figure 4.17), which might have resulted in the higher photocatalytic performance observed during degradation of diuron.

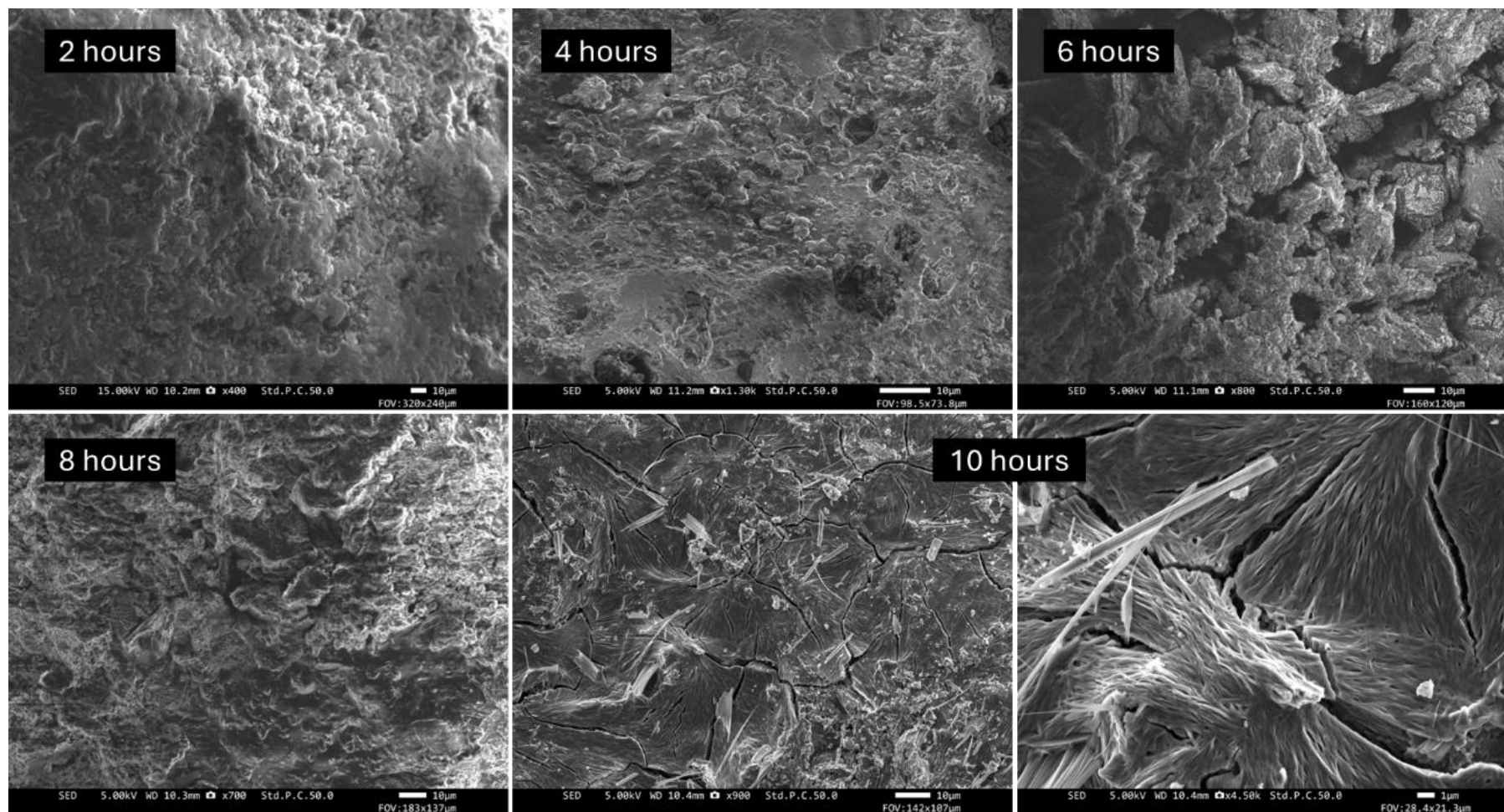


Figure 4.17: SEM images of graphitic carbon nitride (g-C₃N₄) coated glass beads at 500 °C and different calcination times (2, 4, 6, 8 and 10 hours).

Furthermore, the formation of g-C₃N₄ using melamine as precursor consists of the gathering of melamine molecules at lower temperatures (around 250 °C), followed by an increase in the temperature which results in the intermolecular condensation of melamine and production of small amount of ammonia. At around 450 °C, the thermal polycondensation among melam, melem and melamine occurs, which initially results in the formation of tri-s-triazine and then graphitic carbon nitride, however, this reaction occurs at a slow rate and g-C₃N₄ requires a longer time to be formed. In order to increase the reaction rate, the calcination temperature can be raised to 650 °C (Wang et al. 2019a). On the other hand, the increase in the calcination temperature could also decompose the polymer structure (Hui et al. 2021). Therefore, the calcination time during preparation of g-C₃N₄ coated beads could be further optimized at higher calcination temperatures.

4.3.6 Pesticide mixture degradation by photocatalysis using g-C₃N₄ coated beads and UV-A LED irradiation

The photocatalytic efficiency of g-C₃N₄ coated beads illuminated by low-cost UV-A 365 nm LEDs (~ £0.63 per LED) on nine different pesticides was evaluated. The pesticide mixture consisted of the herbicides diuron, atrazine, 2,4-D and the insecticides dimethoate, acetamiprid, clothianidin, imidacloprid, thiacloprid and thiamethoxam in AFW (1 mg L⁻¹ each). During photocatalytic treatment, the herbicides diuron and 2,4-D concentrations significantly decreased ($p < 0.05$) from 5 minutes and 1 hour of treatment and both herbicides were completely removed within 4 hours (Figure 4.18A). The concentration of imidacloprid and thiamethoxam significantly decreased ($p < 0.05$) from 15 minutes of photocatalysis while clothianidin presented a significant reduction from 45 minutes of treatment. The neonicotinoids imidacloprid, thiamethoxam and clothianidin continued to be degraded over 7 hours of photocatalysis until their concentration was not detected in the experimental solution (Figure 4.18A). The concentration of the neonicotinoid thiacloprid significantly decreased ($p < 0.05$) from 5 minutes of photocatalytic treatment and the concentration of both the herbicide atrazine and the insecticide dimethoate significantly decreased ($p < 0.05$) from 45 minutes. Within 24 hours of photocatalysis, atrazine,

dimethoate and thiacloprid were all completely degraded by g-C₃N₄ coated beads and UV-A LEDs (Figure 4.18A). Finally, the neonicotinoid acetamiprid was the pesticide evaluated that presented slower photocatalytic degradation with significant degradation ($p < 0.05$) from 45 minutes until complete removal by 48 hours of treatment, however, it is possible to observe that the acetamiprid concentration remains constant from 1 hour until at least the 7 hours of photocatalytic treatment, which then continues to decrease until complete degradation at 48 hours (Figure 4.18A). The plateau in the acetamiprid concentration observed between 1 and 7 hours of treatment could be explained by the fact that transformation products from the degradation of other pesticides were also present in the solution. These transformation products might present similar molecular structure as acetamiprid and were detected and accounted as acetamiprid as the photocatalytic degradation occurred. Kurwadkar et al. (2016) studied the degradation of imidacloprid in the presence of natural sunlight and observed the generation of transformation compounds containing chloropyridine rings, which are also found in the molecular structure of acetamiprid. Furthermore, Tampieri et al. (2019) evaluated the degradation of imidacloprid by non-thermal plasma and observed the production of a transformation product with similar structure as acetamiprid.

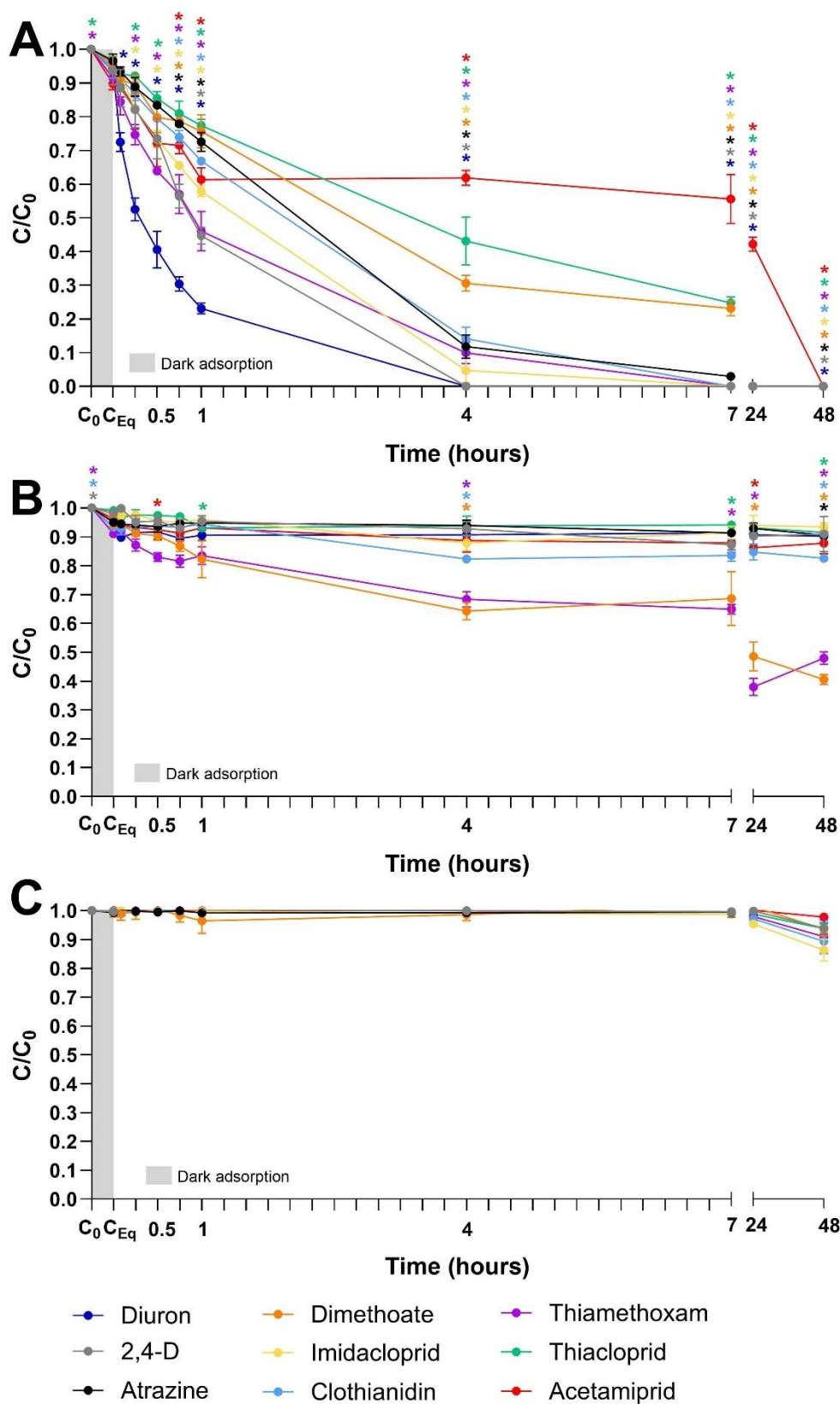


Figure 4.18: Degradation of a pesticide mixture containing the herbicides diuron, atrazine and 2,4-D and the insecticides dimethoate, acetamiprid, clothianidin, imidacloprid, thiacloprid and thiamethoxam after A) photocatalytic treatment by UV-A LED irradiation and graphitic carbon nitride (g-C₃N₄) coated beads, B) dark control (g-C₃N₄ coated beads only) and C) light control (UV-A LED irradiation) over 48 hours. (n = 3, error bars = 1SD). *Significantly different from T_{Eq}.

When no UV-A LED irradiation was applied onto the g-C₃N₄ coated beads (dark control samples), there was a significant decrease ($p < 0.05$) in the concentration of both thiamethoxam and dimethoate concentration from 4 hours until 48 hours of treatment, except for dimethoate at 7 hours, with a concentration reduction of 47% for thiamethoxam and of 57% for dimethoate at the end of the experiment (Figure 4.18B). On the other hand, there was only a decrease of 6.5% – 17.5% in the concentration of the other pesticides evaluated (Figure 4.18B). Usually, the dark adsorption equilibrium should be reached within a relatively short period of time after the pollutant and catalyst are in contact (Bairamis, Rapti and Konstantinou 2023). For instance, equilibrium of thiamethoxam onto TiO₂ (1 g L⁻¹ Degussa P25) was achieved in 15 minutes of dark adsorption during photocatalytic studies (Mir et al. 2013). Aliste et al. (2021) observed the dark adsorption of the pesticides chlorantraniliprole, imidacloprid, pirimicarb and thiamethoxam onto both TiO₂ and ZnO over 20 minutes of darkness. Complete equilibrium of adsorption/desorption of the pesticides oxydemeton-methyl, methidathion, carbaryl and dimethoate onto TiO₂ was obtained over 30 minutes in the dark (Vicente et al. 2014). However, both thiamethoxam and dimethoate showed a decrease in their concentration when only g-C₃N₄ coated beads were used in solution over 48 hours of dark control. It is possible that both thiamethoxam and dimethoate underwent a change in chemical stability due to an increase in the solution pH, which favored hydrolysis during the dark adsorption experiment. The addition of g-C₃N₄ coated beads into the pesticide solution also increase the pH to a more alkaline pH (from pH 7 at T₀ to pH 9 at 48 hours of dark adsorption), which could have interfered in the chemical stability of thiamethoxam and dimethoate (Figure 4.19).

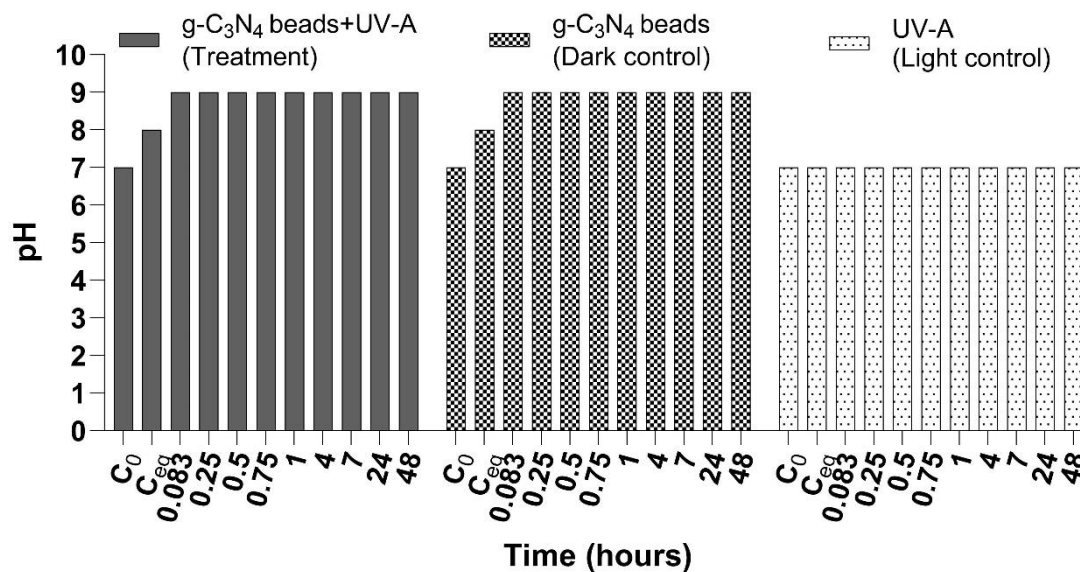


Figure 4.19: Solution pH determined during photocatalytic degradation of a pesticide mixture containing the herbicides diuron, atrazine and 2,4-D and the insecticides dimethoate, acetamiprid, clothianidin, imidacloprid, thiacloprid and thiamethoxam by graphitic carbon nitride (g-C₃N₄) coated beads and UV-A LED irradiation over 48 hours.

Dimethoate degradation by hydrolysis is favored by alkaline conditions and it was shown to be enhanced by the increase in the solution pH from 5 to 9 (Katagi 2002). Thiamethoxam also presented enhanced degradation by hydrolysis in alkaline solutions (pH 9.2) in comparison with neutral (pH 7) and acidic conditions (pH 4) (Karmakar, Singh and Kulshrestha 2009). During light control experiments, where only UV-A LED irradiation was applied and no g-C₃N₄ coated beads were added into the pesticide solution, a decrease of only 9% and 6% in the concentration of thiamethoxam and dimethoate, respectively, was observed (Figure 4.18C). These results further indicate the role of alkaline hydrolysis into the degradation of both dimethoate and thiamethoxam during dark control, as no beads were used during light control samples, therefore, the solution pH 7 remained constant over 24 hours of experiment and no increase in the solution pH was observed. No significant decrease ($p > 0.05$) was observed in the concentration of all pesticides over 48 hours during light control experiments (Figure 4.18C).

All pesticides were completely degraded over 48 hours of photocatalytic treatment by g-C₃N₄ coated beads and UV-A LED irradiation. Further, all pesticides evaluated followed a pseudo-first order kinetics reaction with R²

= 0.9604 for diuron, $R^2 = 0.9261$ for 2,4-D, $R^2 = 0.9876$ for atrazine, $R^2 = 0.9586$ for dimethoate, $R^2 = 0.9351$ for imidacloprid, $R^2 = 0.9768$ for clothianidin, $R^2 = 0.9720$ for thiamethoxam and $R^2 = 0.9842$ for thiacloprid, except for acetamiprid degradation data which best fit into a pseudo-second order with $R^2 = 0.7647$ in comparison with a $R^2 = 0.6604$ for pseudo-first order (Figure 4.20). However, all data were considered to follow pseudo-first order reaction.

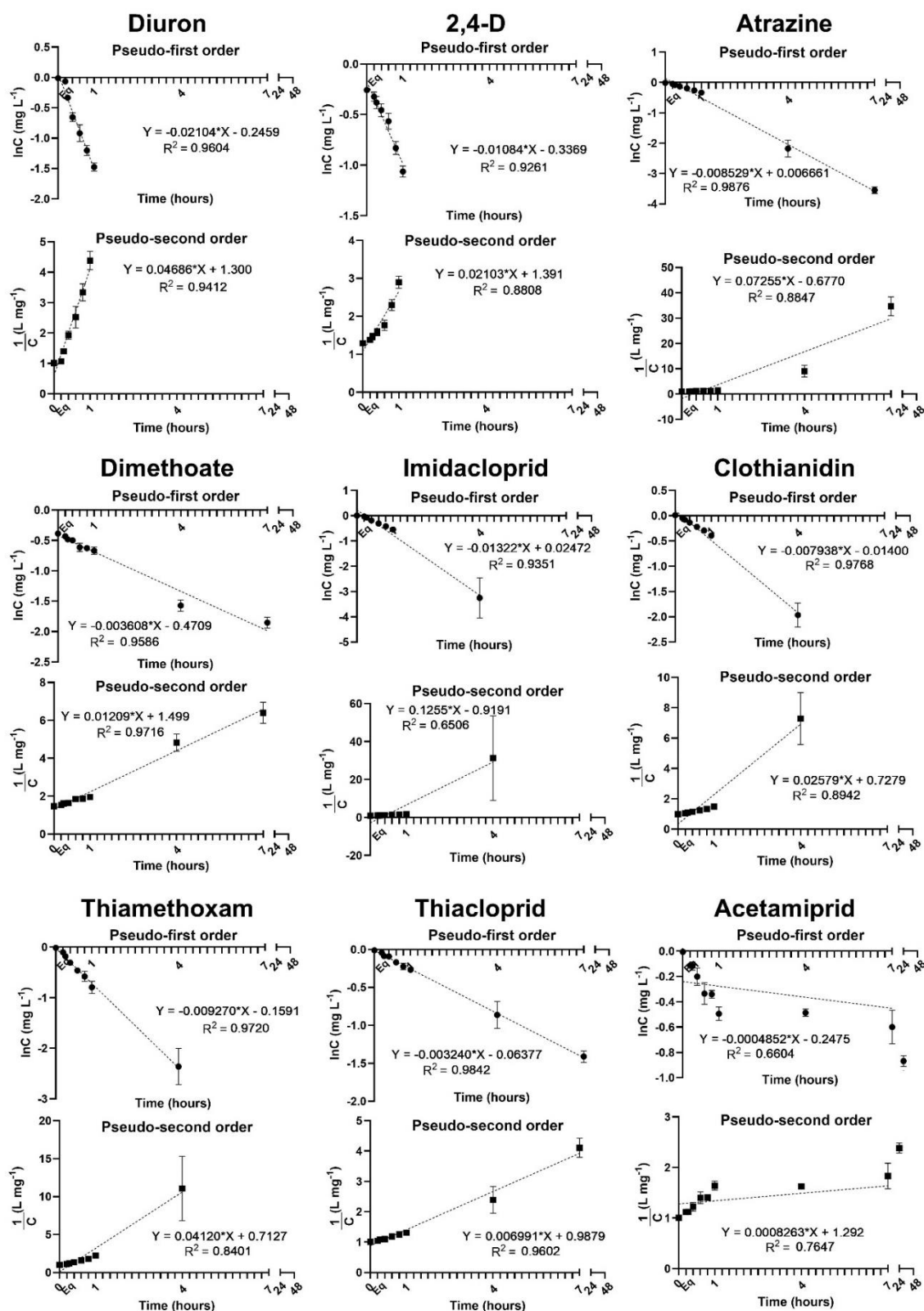


Figure 4.20: Kinetics of a pesticide mixture photocatalytic degradation by graphitic carbon nitride ($g\text{-C}_3\text{N}_4$) coated beads and UV-A LED irradiation over 48 hours. Kinetic models were calculated following pseudo-first order and pseudo-second order reactions. Pesticide mixture consisted of diuron, 2,4-D, atrazine, dimethoate, imidacloprid, clothianidin, thiamethoxam, thiachloprid and acetamiprid at an initial concentration of 1 mg L^{-1} each. ($n = 3$, error bars = 1SD).

Diuron demonstrated the fastest photocatalytic degradation from the pesticides evaluated with a reaction rate constant $k = 0.02104 \text{ min}^{-1}$, followed by imidacloprid with $k = 0.01322 \text{ min}^{-1}$, 2,4-D with $k = 0.01084 \text{ min}^{-1}$, thiamethoxam with $k = 0.009270 \text{ min}^{-1}$, atrazine with $k = 0.008529 \text{ min}^{-1}$, clothianidin with $k = 0.007938 \text{ min}^{-1}$, dimethoate with $k = 0.003608 \text{ min}^{-1}$, thiacloprid with $k = 0.003240 \text{ min}^{-1}$ and acetamiprid with $k = 0.0004852 \text{ min}^{-1}$ (Figure 4.20). The neonicotinoids are a group of insecticides that are chemically related to nicotine, therefore present similar chemical structure (Seifert 2005). Because of the similarity between this group of pesticides, neonicotinoids were expected to present similar degradation rates during photocatalysis by g-C₃N₄ coated beads and UV-A LED irradiation, however, imidacloprid, thiamethoxam and clothianidin were completely degraded within 7 hours of photocatalytic treatment and demonstrated higher degradation rates in comparison with thiacloprid and acetamiprid, which were fully degraded by 24 and 48 hours, respectively, and presented lower degradation rates (Figure 4.20). Liu et al. (2020a) evaluated the photocatalytic degradation of a mixture of neonicotinoids containing dinotefuran, nitenpyram, clothianidin, thiacloprid, imidacloprid, thiamethoxam and acetamiprid (2 mg L⁻¹) by powdered g-C₃N₄ and a xenon lamp over 5 hours. The authors observed that g-C₃N₄ was also successful in the removal of neonicotinoids even though the degradation efficiency of neonicotinoids was influenced by the precursor used to produce g-C₃N₄ (urea, thiourea or a mixture of the two chemicals). Liu et al. (2020a) used powdered g-C₃N₄ for the photocatalytic degradation of neonicotinoids, which presented higher surface area (21.55 m² g⁻¹ – 92.89 m² g⁻¹) than the surface area presented by the g-C₃N₄ coated beads used in the current study (2.3 m² g⁻¹; Hui et al. 2021). Even though the catalyst used in the current study showed smaller surface area and the combined pesticide concentration was higher (9 mg L⁻¹), there was still a marked removal of pesticides of at least 38% (acetamiprid) until complete degradation of 2,4-D and diuron over only 4 hours of photocatalysis, whereas Liu et al. (2020a) observed a degradation of up to 42% (dinotefuran), 21% (acetamiprid), 79% (clothianidin), 50% (thiacloprid), 99% (imidacloprid), 90% (nitenpyram) and 33% (thiamethoxam). Each pesticide demonstrated different amounts of degradation at the end of 5 hours of photocatalysis,

even though all pesticides studied were also from the same group of neonicotinoids (Liu et al. 2020a). Other advanced oxidation processes such as photolysis (Banić et al. 2014) and $\text{TiO}_2/\text{Na}_2\text{S}_2\text{O}_8$ photocatalysis (Fenoll et al. 2019) were also used on the degradation of neonicotinoids. Both studies observed that moieties such as nitroguanidine ($=\text{N}-\text{NO}_2$ present in imidacloprid, thiamethoxam and clothianidin) and cyanoimine ($\text{N}-\text{C}\equiv\text{N}$ present in thiacloprid and acetamiprid) were sufficient to cause the different degradation rates on neonicotinoids due to a faster oxidation of reactive oxygen species towards neonicotinoids containing nitroguanidine (Banić et al. 2014).

Other studies have reported the photocatalytic removal of pesticides by doped $\text{g-C}_3\text{N}_4$ catalyst. Photocatalysis by $\text{g-C}_3\text{N}_4/\text{Fe}_3\text{O}_4/\text{Ag}$ catalyst and UV irradiation was used in the successful removal of the pesticide diazinon (Ghodsi et al. 2020). Zinc vanadate/graphitic carbon nitride ($\text{Zn}_3\text{V}_2\text{O}_8/\text{g-C}_3\text{N}_4$) catalyst under visible light from a xenon lamp was able to degrade different pesticides in aqueous solution such as diazinon, malathion, glyphosate and chlorpyrifos (Thakur et al. 2023). This is the first time, however, that $\text{g-C}_3\text{N}_4$ coated beads and low-cost UV-A LEDs were applied in the photocatalytic removal of nine pesticides (including herbicides and insecticides) simultaneously. The degradation efficiency of the photocatalytic system used in the current study demonstrates the possibility of application of $\text{g-C}_3\text{N}_4$ coated beads and UV-A 365nm LEDs for the removal at source of pesticides.

4.3.7 Reusability analysis of $\text{g-C}_3\text{N}_4$ coated beads during the photocatalytic degradation of diuron

The reusability of $\text{g-C}_3\text{N}_4$ coated beads during the photocatalytic removal of diuron by UV-A LED irradiation was investigated to determine the practical photocatalytic efficiency of the system. The $\text{g-C}_3\text{N}_4$ coated beads were reused for 5 consecutive cycles. No substantial decrease in the photocatalytic efficiency of $\text{g-C}_3\text{N}_4$ coated beads was observed. Diuron removal over 24 hours of photocatalysis remained stable (96.2% – 99.9%) throughout the 5 cycles evaluated (Figure 4.21). A decrease in the photocatalytic performance was observed between cycle 2 and cycle 3 and between cycle 4 and cycle 5, however, these changes were only significant

($p < 0.05$) between 30 minutes and 4 hours for cycles 2 and 3 and between 7 and 24 hours for cycles 4 and 5 (Table A4.3). The results indicate the excellent photocatalytic reusability of g-C₃N₄ coated beads, suggesting that the coated catalyst could be recoverable and reusable. Other studies have also evaluated the reusability of g-C₃N₄ and modified g-C₃N₄ as photocatalyst (Liu et al. 2015; Ejeta and Imae 2021; Thakur et al. 2023).

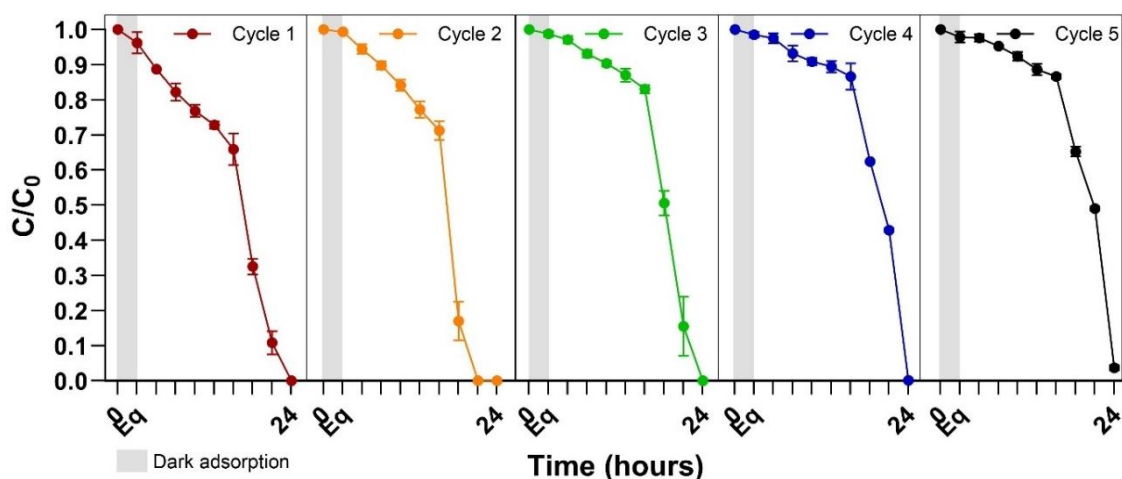


Figure 4.21: Reusability of graphitic carbon nitride coated beads for the photocatalytic degradation of diuron by UV-A LED irradiation over 5 successive cycles. ($n = 3$, error bars = 1SD).

The solution pH was recorded in order to evaluate if the solution pH would increase in all the photocatalytic cycles. The solution pH increased from pH 7 to pH 9 during cycle 1 over 24 hours of experiment, however, no change was observed in the solution pH from cycle 2 onwards (Figure 4.22). The fact that the solution pH remained constant from cycle 2 further suggests that the initial increase in the solution pH observed in cycle 1 might be related with the release of loose g-C₃N₄ and/or products that were not removed during the washing procedure during the preparation of g-C₃N₄ coated beads, which could have caused the increase in the solution pH during only the first photocatalytic cycle.

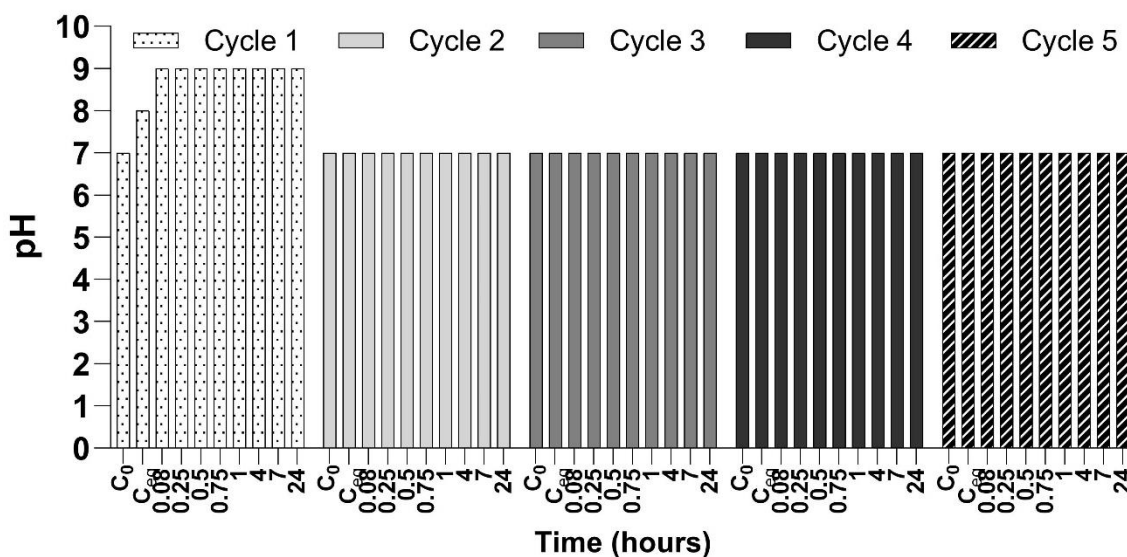


Figure 4.22: Solution pH determined during degradation of diuron by graphitic carbon nitride (g-C₃N₄) coated beads and UV-A LED irradiation over five successive photocatalytic cycles.

4.3.8 Diuron degradation by photocatalysis using g-C₃N₄ coated beads and UV-A LED irradiation in a continuous-flow system

The efficiency of g-C₃N₄ coated beads under UV-A LED irradiation in the photocatalytic degradation of diuron was evaluated using a continuous flow system. So far, only batch photocatalytic treatments were performed in the current study for the removal of pesticides by g-C₃N₄ coated beads under UV-A LED irradiation, however, both batch and flow through systems can be used during large scale applications. In an agricultural scenario, a photocatalytic reactor might be placed in a storage tank containing residual pesticides from spray tanks and the photocatalytic treatment would work as a batch system. On the other hand, the photocatalytic reactor could be applied as a flow through system in the case of application in drainage systems or in other aquatic environments such as ponds or reservoirs that might be contaminated by pesticides from crop runoff. The photocatalytic efficiency and stability of g-C₃N₄ coated beads was evaluated at flow rates of 5 and 10 mL min⁻¹. When the flow rate of 5 mL min⁻¹ was applied, a decrease in diuron concentration of around 20% was observed from 30 minutes photocatalysis, which remained constant over 6 hours photocatalysis (Figure 4.23A).

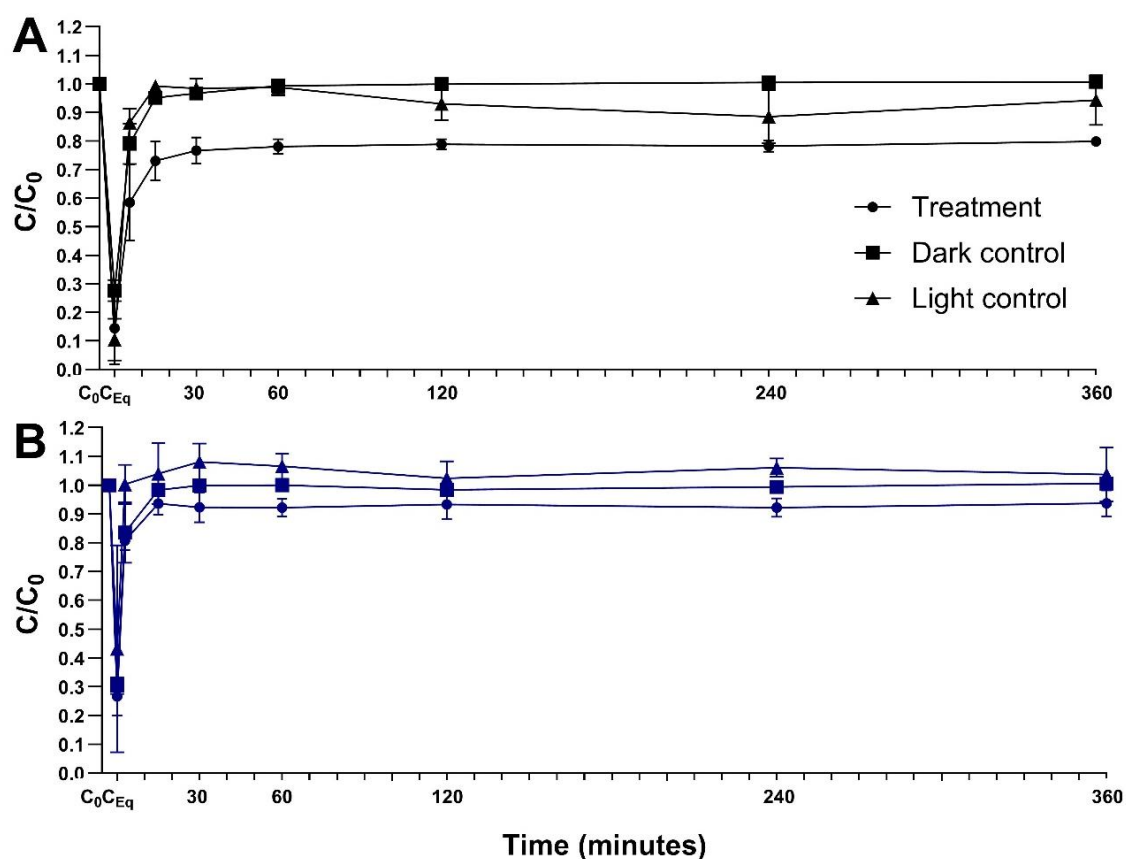


Figure 4.23: Photocatalytic degradation of diuron in artificial fresh water by graphitic carbon nitride (g-C₃N₄) coated beads and UV-A LED irradiation using a single-pass continuous flow reactor over 360 minutes at A) 5 mL min⁻¹ and B) 10 mL min⁻¹ flow rate. (n = 3, error bars = 1SD).

The diuron degradation decreased to around 7% when a higher flow rate of 10 mL min⁻¹ was applied to the photocatalytic system, however, the diuron removal also remained constant until the end of the experiment despite the lower photocatalytic performance (Figure 4.23B).

In order to further investigate the stability of g-C₃N₄ coated beads and considering a scenario where the photocatalytic reactor would be deployed at source for a longer period of time, the degradation of diuron g-C₃N₄ coated beads and UV-A LED irradiation was investigated using the same continuous flow system setup over 21 days. The experimental solution consisted of diuron in AFW at a lower concentration (1 mg L⁻¹) and the flow rate was 5 mL min⁻¹. A total volume of 115 L of the diuron experimental solution passed through the reactor over 21 days. This was an explorative experiment to verify a trend during longer exposure of the photocatalytic system, which would be more relevant to large scale applications, therefore, just one replicate was performed and no controls were evaluated. The

diuron final concentration relative to the initial concentration at the pesticide reservoir was obtained (Equation 4.1).

$$\text{Diuron concentration (\%)} = \frac{C}{C_0} \times 100 \quad (\text{Equation 4.1})$$

Where:

- C is the diuron concentration (mg L^{-1}) at the outlet tube before reaching the outlet reservoir.
- C_0 is the diuron concentration (mg L^{-1}) at the pesticide reservoir.

The remaining concentration of diuron was 60% on the first day of photocatalysis (Figure 4.24). The photocatalytic treatment was slightly less efficiency from day 2 with a diuron concentration of 70%, which remained stable from day 2 until day 15 of treatment. From day 16 of treatment until the end of the experiment, the diuron remaining concentration was around 80%, with the exception of day 20 where diuron concentration was 90% (Figure 4.24). The decrease in the diuron concentration from day 20 to day 21 of photocatalysis to the previous removal rate observed from day 16 to day 19 might indicate a sampling error during day 20.

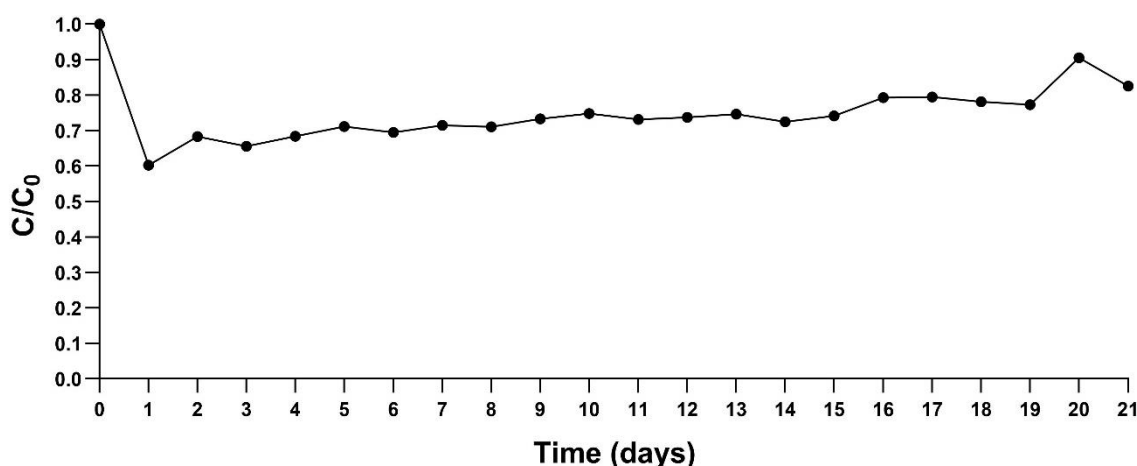


Figure 4.24: Photocatalytic degradation of diuron in artificial fresh water by graphitic carbon nitride ($\text{g-C}_3\text{N}_4$) coated beads and UV-A LED irradiation using a single-pass continuous flow reactor over 21 days at 5 mL min^{-1} flow rate.

The results suggest that the photocatalytic system using $\text{g-C}_3\text{N}_4$ coated beads and UV-A LED irradiation was not only efficient in the removal of the herbicide diuron, but it was also stable for a longer period of time (21 days) with a similar photocatalytic performance throughout the experiment. Even

though a lower diuron concentration (1 mg L^{-1}) was used for the long exposure experiments using a continuous flow reactor in comparison with the diuron concentration previously used in the present research (5 mg L^{-1}), the diuron concentration of 1 mg L^{-1} is considerably higher than the environmental concentrations reported for diuron in aquatic environments. For instance, diuron was detected in surface waters in Spain and China at maximum concentrations of 58 and 847 ng L^{-1} , respectively (de Souza et al. 2020). Also, diuron was detected at $5 \text{ } \mu\text{g L}^{-1}$ in La Rioja Alavesa area in Spain (Herrero-Hernández et al. 2017). There are also reports of diuron found in surface water at concentrations of $30 \text{ } \mu\text{g L}^{-1}$ (Meffe and de Bustamante 2014). When higher concentrations of pesticides are present in the water, a decrease in the available active sites of the catalyst occurs and there is a relatively low amount of ROS produced by the photocatalytic system (catalyst and light source), which reduces the photocatalytic efficiency (Dorrajji et al. 2017; Ghodsi et al. 2020; Lopes and Salgado 2021; Licht et al. 2023). Therefore, a better photocatalytic performance would be expected at large scale application when lower concentrations of pesticides are present in the water.

Further, the short retention time of 5 minutes and 36 seconds had an influence in the photocatalytic performance of the reactor. Kim et al. (2022) evaluated the degradation of the herbicide atrazine in a continuous flow photocatalytic experiment by g- C_3N_4 (derived from 0.5 M of nitric acid-modified melamine) and UV-A LED irradiation using a slurry-type reactor at several retention times (10, 20, 40 and 70 minutes) for 20 cycles. The atrazine removal efficiency increased when longer retention times were applied Kim et al. (2022). Fernandes et al. (2020) investigated the removal of parabens by a metal-free graphite-like carbon nitride coated in glass rings and LED irradiation (417 nm) under a continuous flow of 1.0 mL min^{-1} (retention time of around 30 minutes). The authors observed a similar removal of parabens between 25% and 30% after 90 minutes of photocatalysis which remained stable over 24 hours (Fernandes et al. 2020). The photocatalytic efficiency of a continuous flow system is strongly influenced by the retention time of the solution. The retention time should be considered when developing a reactor prototype for photocatalytic water treatment at source and an appropriate design for the retention time is

necessary to achieve sufficient photocatalytic performance. For instance, the retention time could be optimized by using batch applications for pesticide removal, changing the dimensions of the reactor or placing reactors in series.

4.4 Conclusion

The photocatalytic degradation of a pesticide mixture containing nine pesticides (diuron, 2,4-D, atrazine, dimethoate, acetamiprid, clothianidin, imidacloprid, thiacloprid and thiamethoxam) by g-C₃N₄ coated beads and economical UV-A LED irradiation was demonstrated. The proposed photocatalytic system was able to successfully remove several different pesticides at the same time even when higher concentrations were present. The optimal conditions of solution pH, catalyst load and calcination time required during the preparation of g-C₃N₄ coated beads were determined during the removal of the herbicide diuron. These conditions were evaluated to obtain a better understanding the photocatalytic system based on g-C₃N₄ coated beads and UV-A LEDs, however, even though the optimal solution pH was found to be pH 5, it is not practical to change the pH during at source application in aquatic environments for pesticide removal. The solution pH and catalyst load can be further optimized according to other conditions such as the targeted pollutant, aquatic matrix used, distribution of reactor components (e.g., distance between catalyst and LED). Various aspects of this work would benefit from further research, for example, the effect of natural organic matter (NOM) present in natural water or the influence of other complex matrices containing different types of pesticides in the photocatalytic performance of g-C₃N₄ coated beads and UV-A LEDs. Furthermore, a wider range of pesticides and a mixture of a different selection of compounds (e.g., pesticides and fertilizers) should also be evaluated to further confirm the effectiveness and feasibility of scaling up the photocatalytic system by g-C₃N₄ coated beads and UV-A LED irradiation for different water treatment applications.

The reusability of g-C₃N₄ coated beads was tested over 24 hours for 5 successive photocatalytic cycles and were effective in removing diuron. The stability of g-C₃N₄ coated beads was further evaluated using a continuous flow reactor system over 21 days of photocatalysis. The photocatalytic

system demonstrated consistent removal of diuron even when low retention times were applied. This indicates the potential application of the photocatalytic system in a real water treatment scenario for pesticide removal at source that would require batch or flow-through treatment. A simple, portable and cost-effective photocatalytic reactor prototype based on g-C₃N₄ coated beads and UV-A LED irradiation should be constructed and tested for the removal of pesticides at source. The photocatalytic reactor could be applied in several agricultural scenarios (e.g., inside storage tanks containing residual pesticides, connected to spray tanks through a vacuum pump, in drainage systems next to crops and in other aquatic environments such as ponds or reservoirs) and it should reduce pesticide contamination and improve water quality.

Chapter 5

Scale-up of a photocatalytic reactor for the degradation of pesticides at source from aquatic environments

5 SCALE-UP OF A PHOTOCATALYTIC REACTOR FOR THE DEGRADATION OF PESTICIDES AT SOURCE FROM AQUATIC ENVIRONMENTS.....	171
5.1 Introduction	173
5.1.1 Photocatalytic removal of pesticides at source from aquatic environments.....	173
5.2 Materials and methods	175
5.2.1 Reagents	175
5.2.2 Photocatalytic degradation of diuron by a photocatalytic reactor based on g-C ₃ N ₄ coated beads and UV-A LED irradiation.....	175
5.2.3 Ultra-performance liquid chromatography of diuron	177
5.3 Results and discussion	177
5.3.1 Rationale for scale-up of photocatalytic reactor	177
5.3.2 Diuron degradation by a photocatalytic reactor: Challenges and learnings	188
5.4 Conclusion.....	193

5.1 Introduction

5.1.1 Photocatalytic removal of pesticides at source from aquatic environments

Titanium dioxide (TiO_2) has been widely used in the photocatalytic removal of contaminants from aquatic environments, however, graphitic carbon nitride ($\text{g-C}_3\text{N}_4$) has only been recently applied as a photocatalyst, especially for the removal of pesticides. Powdered $\text{g-C}_3\text{N}_4$ was illuminated by UV-A light emitting diodes (LEDs; 400 nm) in a batch mode photocatalytic experiment and in a continuous flow system for the removal of the herbicide atrazine at initial concentration of 1 mg L^{-1} and 0.1 mg L^{-1} , respectively (Kim et al. 2022). Zhang et al. (2021) also investigated the removal of atrazine (2 mg L^{-1} initial concentration) by photocatalysis using powdered $\text{g-C}_3\text{N}_4$ (0.03% w/v) activated by visible light ($\lambda > 400 \text{ nm}$) in a circulating water system. Powdered $\text{g-C}_3\text{N}_4$ (0.05% w/v) was also applied in bench-scale photocatalysis with a Xenon lamp in addition to a UV-cut filter ($\lambda > 420 \text{ nm}$) for the removal of the insecticide nitenpyram at initial concentration of 5 mg L^{-1} (Tang et al. 2020; Zhou et al. 2021). Seven neonicotinoids (dinotefuran, acetamiprid, clothianidin, thiacloprid, imidacloprid, nitenpyram and thiamethoxam with an initial concentration of insecticides solution of 2 mg L^{-1}) were degraded by $\text{g-C}_3\text{N}_4$ (0.1% w/v) and a Xenon lamp with an UV-cut filter ($\lambda > 400 \text{ nm}$) in a 150 mL reactor with a double wall for water circulation (Liu et al. 2020a). The removal of the neonicotinoid imidacloprid was also investigated using $\text{g-C}_3\text{N}_4$ as catalyst activated by visible light LED irradiation (Raizada et al. 2019) and by visible-light ($\lambda > 400 \text{ nm}$) obtained from a Xenon lamp (Liu et al. 2015b). Ejeta and Imae (2021) investigated the degradation of the herbicide 2,4-Dichlorophenoxyacetic acid (2,4-D; 100 mg L^{-1} initial concentration) by $\text{g-C}_3\text{N}_4$ (0.006% w/v) using both UV and visible light irradiation. Natural sunlight was also applied to activate $\text{g-C}_3\text{N}_4$ (0.03% w/v) for the removal of the insecticide diazinon (10 mg L^{-1}) in tap and river water (Thakur et al. 2023).

So far, only bench-scale experiments were performed using $\text{g-C}_3\text{N}_4$ as catalyst during the photocatalytic removal of pesticides and there is no report of the application of a photocatalytic reactor for at source application using this catalyst. Very few reports of reactors or modular facilities using different photocatalysts for the removal of pesticides at source were found.

Fenoll et al. (2019) developed a modular facility based on TiO_2 tandem $\text{Na}_2\text{S}_2\text{O}_8$ and solar light photocatalysis to treat 180 L of wastewater from farms contaminated with neonicotinoids (thiamethoxam, imidacloprid, acetamiprid and thiacloprid). The modular facility consisted of a reservoir tank (180 L) and the photoreactor. The photoreactor had four borosilicate tubes in series (150 cm length x 14.6 cm internal diameter) mounted on curved polished aluminium reflectors. TiO_2 and $\text{Na}_2\text{S}_2\text{O}_8$ (300 mg L^{-1} each) were added to the reservoir tanks before the photoreactor. Finally, an ultrafiltration membrane was used at the end of the treatment to recover the catalyst. The same pilot plant photoreactor module was used to treat wastewater from farms contaminated with the pesticides chlorantraniliprole, difenoconazole, metalaxyl, myclobutanil and triadimenol (Garrido et al. 2021) and with the pesticides acetamiprid, cyproconazole, cyprodinil, difenoconazole, fenhexamid, hexythiazox, myclobutanil and thiamethoxam (Garrido et al. 2020). A similar system based on TiO_2 (200 mg L^{-1}) with addition of $\text{Na}_2\text{S}_2\text{O}_8$ (250 mg L^{-1}) and solar light photocatalysis was applied at pilot plant scale to remove a mixture of six pesticides (malathion, fenotrothion, quinalphos, vinclozoline, dimethoate and fenarimol with initial concentration of 0.30 mg L^{-1} each) spiked in 100 L of wastewater (Vela et al. 2018). The modular facility consisted of a photoreactor with five borosilicate tubes in series (200 cm length x 4 cm internal diameter) mounted on curved polished aluminium reflectors.

All pilot scale reactors reported were efficient in the removal of pesticides, however, the reactors are quite robust in relation to the presence of different tanks and other elements that cannot be easily transported. Furthermore, the system was applied to treat wastewater contaminated with pesticides that was stored and pumped into the photoreactor, therefore, the use of this reactor system in different water treatment scenarios in a farm could represent a challenge, for example, to treat pesticides present in small ponds, in drainage systems close to crops or in residual solutions from spray tanks after pesticide application. Therefore, a simple, easy to build, portable, environmentally friendly and cost-effective photocatalytic reactor capable of removing pesticides from aquatic environments at source would be desirable.

5.2 Materials and methods

5.2.1 Reagents

Acetonitrile, methanol and trifluoroacetic acid (Fisher Scientific, USA) were used for ultra-performance liquid chromatography tandem photo diode array (UPLC-PDA) analysis of diuron. Ultrapure water (18.2 M Ω) obtained by an ELGA PURELAB system (Veolia, UK) was used to prepare solutions. Solution containing the herbicide diuron (Fisher Scientific, UK), >95% purity, was prepared using tap water.

5.2.2 Photocatalytic degradation of diuron by a photocatalytic reactor based on g-C₃N₄ coated beads and UV-A LED irradiation

The photocatalytic efficiency of a reactor based on g-C₃N₄ coated beads and UV-A LEDs was evaluated for the removal of diuron in tap water. This would mimic the removal of residual pesticides obtained from spray tanks after pesticide application in a farm. The reactor was made of two concentric acrylic cylinders (external cylinder 10 x 0.3 cm and internal cylinder 8 x 0.2 cm) with 1 m length. Ten 1 meter long UV-A LEDs strips (60 individual UV-A LEDs 365 nm per strip; 380 – 420 nm and 66 W m⁻²) were placed within the walls of the two cylinders and the edges sealed using Wessex 4303 resin. The reactor was filled with g-C₃N₄ coated beads (1.16 kg) placed inside the internal cylinder (void volume of 1.6 L). A stainless-steel mesh (aperture of 1.2 x 1.2 mm and 0.4 mm wire strength) was placed in both top and bottom ends of the reactor to contain the g-C₃N₄ coated beads. A submersible water pump (SDO 75 M, Efaflu, Portugal) was connected to the bottom of the reactor (Figure 5.1) to direct water through the reactor at a flow rate of approximately 6 m³ h⁻¹.



Figure 5.1: Photocatalytic reactor based on graphitic carbon nitride ($g\text{-C}_3\text{N}_4$) coated beads and UV-A LEDs (365 nm) connected to submersible water pump and tank containing diuron experimental solution.

The pump and reactor were placed inside of a polyethylene tank (1000 L capacity) containing diuron solution in tap water (0.8 mg L^{-1}). An initial sample (1.5 mL) was removed from the diuron experimental solution for analysis (T_0) and the diuron solution was then exposed to UV-A LED irradiation. Other samples were removed at 1, 2, 3, 4, 5, 6, 7, 24, 42 and 72 hours. For each sampling point, two samples were taken from the top of the tank and two samples were taken from the bottom of the tank. Samples were placed in 1.5 mL Eppendorf tubes, centrifuged for 30 seconds at

13000×*g* and the supernatant analyzed by UPLC-PDA for diuron quantification.

5.2.3 Ultra-performance liquid chromatography of diuron

Quantification of diuron was achieved by a Waters Acquity UPLC system (Waters, UK) and an Acquity photodiode array (PDA) eλ detector (Waters, UK) (Table 5.1) at a detection wavelength of 250 nm. The limit of quantification for diuron was 0.02 mg L⁻¹.

Table 5.1: Analytic conditions of ultra-performance liquid chromatography for the quantification of diuron.

Parameters	Conditions					
Column	Acquity UPLC BEH C18 column (2.1 x 50 mm, 1.7 μm particle size; Waters, UK)					
Guard column	Acquity UPLC BEH C18 VanGuard pre-column (2.1 x 5 mm, 1.7 μm particle size; Waters, UK)					
Mobile phase	A: 0.05% trifluoroacetic acid in ultrapure water (18.2 MΩ) B: 0.05% trifluoroacetic acid in acetonitrile					
Gradient	Time (min)	0	0.5	5	5.6	8
	Solvent B (%)	5	5	80	5	5
	Elution profile	6	6	6	6	6
Flow rate	0.5 mL min ⁻¹					
Injection volume	10 μL					
Column temperature	40 °C					

5.3 Results and discussion

5.3.1 Rationale for scale-up of photocatalytic reactor

Pesticides are chemical compounds used to eliminate harmful organisms. Pesticides are mainly used in agriculture for pest control to increase and optimize agricultural production, however, they can also be applied in other activities such as sheep dipping and soft fruit wash. Pesticides can be carried by air drift during application in crops or by rainfall runoff (Stehle et al. 2019) and unintentional spillage (Damalas and Eleftherohorinos 2011) during and after their application, finding their way to aquatic environments. Furthermore, pesticides are applied using tractors with spray tanks and after application there could be some residual pesticide left in the

tank, which could be placed in wastewater storage tanks or also reach watercourses and drains (Ribeiro et al. 2015; Nasiri, Ahmadzadeh and Amiri 2020). The issue is that pesticides cannot be completely removed by conventional treatment methods and they can cause harmful effects to both human and animal health (Handford, Elliott and Campbell 2015; Yadav, Prajapati and Atri 2016; Sousa et al. 2018; Rani et al. 2020). Therefore, the development of alternatives for the removal of pesticides from aquatic environments at source is required, such as reactors based on photocatalysis that are simple, portable, cost-effective and environmentally safe.

Different factors need to be considered for the scale-up of a photocatalytic reactor, for instance, the catalyst. Powdered catalyst are commonly applied during bench-scale experiments based on photocatalysis, however, powdered catalysts represent a challenge during the practical application of this technology because they need to be recovered from water after the treatment occurs (Marcelino and Amorim 2019). An efficient method for recovering photocatalysts after treatment involves immobilizing powdered photocatalysts onto a substrate, also known as immobilization matrix, which can then be recovered. TiO_2 is commonly used during photocatalytic studies because it is an economical and efficient catalyst option, however, $\text{g-C}_3\text{N}_4$ can also be used as an alternative catalyst because it is also economical, environmentally safe and it can be activated by visible light. TiO_2 and $\text{g-C}_3\text{N}_4$ were successfully coated onto porous foamed glass beads made with recycled glass that float in aquatic medium and can be recovered after photocatalytic treatment. $\text{g-C}_3\text{N}_4$ coated beads demonstrated the highest photocatalytic performance during the degradation of a model compound (microcystin-LR; Chapter 3, Section 3.3), therefore, $\text{g-C}_3\text{N}_4$ coated beads were selected as the catalyst for the photocatalytic reactor.

Another important component in photocatalytic reactors is the light source used for catalyst activation. High intensity discharge lamps (e.g., Xenon lamps), fluorescent light, incandescent lamps and sunlight can be used for the activation of catalysts, however, LEDs were selected as the best light source option to be used in the photocatalytic reactor for the degradation of pesticides at source mainly because of the high luminous efficacy, long lifespan and LEDs are manufactured in a range of dimensions (shape and

sizes), which results in flexibility in deployment and configuration. Furthermore, LEDs have become an affordable option of illumination and, over the years, the LED chip styles have evolved. Dual In-Line Package (DIP) LEDs were first developed in 1962, which consisted of a chip inside a bulb head with 2 connecting pins. More recently, LED chips were developed in the form of Surface Mounted Diode (SMD), which have higher lumen efficacy and longer lifespan. SMDs present a smaller design and can usually be found in LED strip lighting (Take Three Lighting 2024). Around 20 years ago, an individual LED bulb was sold for around £30 (Halliwell 2014). In the last 5 years, ultraviolet light LED could be found for £0.63 per LED (https://www.amazon.co.uk/Ultraviolet-LightingWill-365nm-370nm-Non-Waterproof-Flexible/dp/B01N0EG9BB/ref=sr_1_2?keywords=uv%2Bled%2Bstrips%2B365nm&qid=1572364295&sr=8-2&th=1), being even more economical if visible light LED was required. More recently, LEDs have become even more affordable and ultraviolet LEDs were sold for £0.075 per LED (<https://www.amazon.co.uk/390nm-400nm-120LEDs-Waterproof-Fluorescent-Lighting/dp/B08LZ7CTRJ?th=1>). Besides all the advantages, UV-A LEDs were also effective on the activation of g-C₃N₄ coated beads during the photocatalytic degradation of pesticides and, therefore, were selected as the light source in the photocatalytic reactor.

The materials, format and dimensions of the reactor are also important factors that need to be taken in consideration when developing a reactor for at source application. The materials should be affordable, easy to obtain, long-lasting and should not require specialized maintenance. Initially, the idea was to manufacture a mesh to be used as the main structure of the reactor using glass fiber thread and a weaving loom (Figure 5.2A), however, the resulting mesh was very malleable and would not give an appropriate structure for the reactor. Then, a glass fiber mesh was evaluated (Figure 5.2B), however, the mesh presented the same structural issue and it would not be a suitable option. Instead of glass fibre mesh, a stainless-steel mesh (aperture of 1.2 x 1.2 mm and 0.4 mm wire strength; Figure 5.2C) could be an appropriate option to be used as the main structure of the reactor.

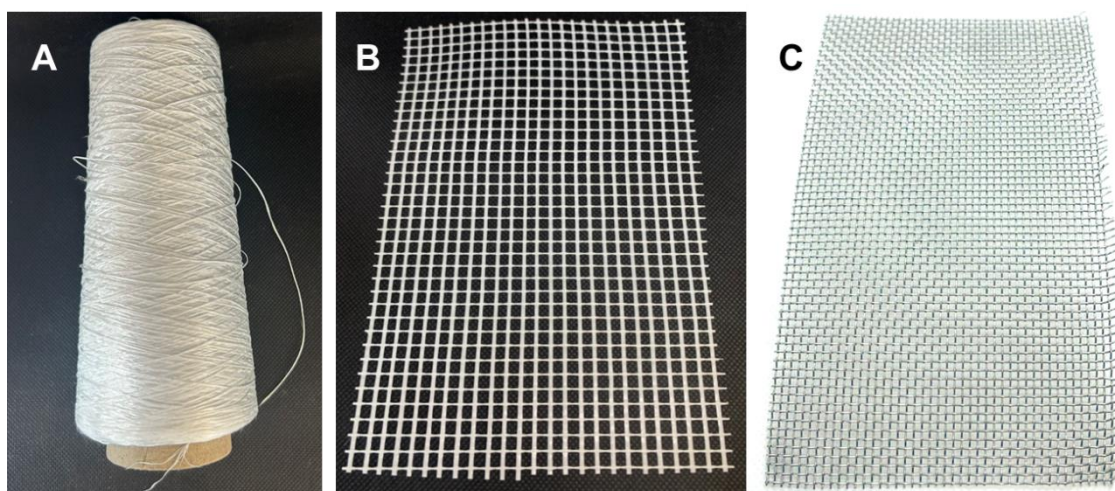


Figure 5.2: A) glass fiber thread, B) glass fiber mesh and C) stainless steel-mesh evaluated as materials for the construction of a photocatalytic reactor for at source application.

After selecting the stainless-steel mesh as the primary material for the reactor, it was necessary to explore options for containing the coated beads. Stainless-steel tea pods were initially tested (Figure 5.3A), however, the tea pods were not properly sealed and the coated beads would escape. Then, the idea was to make pods to contain the coated beads using the same stainless-steel mesh and close it with metal rings (Figure 5.3B), however, the metal rings did not work as the coated beads were not properly contained. Tetrahedral stainless-steel pods were then prepared by cutting the stainless-steel mesh sheets (15 x 13 cm) and then folding the edges into the final tetrahedral form of pods (Figure 5.3C). The reactor prototype consisted of placing the tetrahedral pods containing coated beads inside of an outer cylinder made of the stainless-steel mesh (1000 x 90 mm). The light source consisted of five waterproof UV-A LED strips (1 meter each strip with 120 individual LEDs; LightingWill, UK; 365-370 nm; IP68, 4.8 W m⁻¹, 120 LEDs m⁻¹) placed in five aluminum profiles attached to the cylindrical mesh.

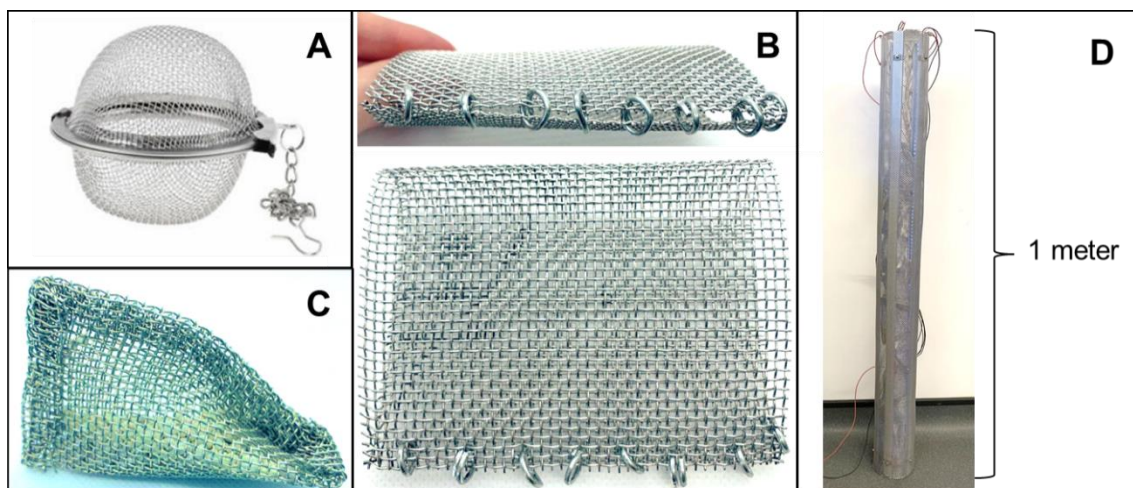


Figure 5.3: A) stainless-steel tea pods, B) metal rings and C) stainless-steel tetrahedral pods tested to contain graphitic carbon nitride coated beads. D) Initial reactor prototype based on photocatalysis for the removal of contaminants.

The reactor prototype was tested in a mesocosm study for the removal of cyanobacteria in a drinking water reservoir by photocatalysis using TiO_2 coated beads and UV-A LED strips (Pestana et al. 2022) and it was shown to be a promising photocatalytic reactor prototype for batch water treatment. In the context of pesticide removal at source, this prototype could be applied in the context of treating water contaminated with pesticides contained in storage tanks, however, the prototype would not be applied in other flow-through applications such as drainage systems or to treat residual pesticides pumped out of spray tanks. Furthermore, water tends to follow the path of least resistance in a system, unless there is an increase in momentum (Pedescoll et al. 2013), and the use of the wire mesh as the outer structure of the reactor could prevent water from flowing through the entire length of the reactor. This would result in a decrease in the retentional time and subsequent decrease in the photocatalytic performance of the reactor. To overcome these issues, acrylic tubes (Figure 5.4) were explored to be used as the reactor main structure, which would allow water treatment applications during both flow-through systems and batch treatments.



Figure 5.4: Acrylic tube evaluated as material during construction of photocatalytic reactor prototype.

Furthermore, another challenge with the initial reactor prototype was the waterproof UV-A LEDs used to activate the coated beads, which were not completely waterproof and stopped working after a few days when fully submerged in water. Therefore, it was essential to waterproof all the electric components of the reactor. Since waterproof LEDs were not appropriate, the idea was to place non waterproof UV LED strips inside acrylic tubes and waterproof both ends of the tube. The first option to seal the ends of the acrylic tubes containing LED strips was to use electrically insulated and water resistant heat shrink end caps that reduce dimensions and seal when briefly heated (Figure 5.5A), however, the caps would easily overheat and melt (Figure 5.5B).

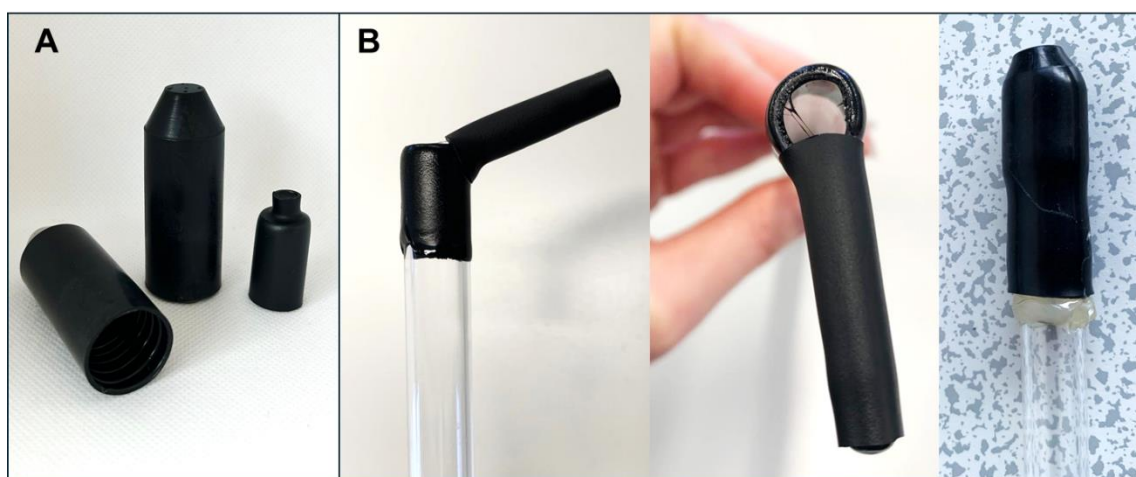


Figure 5.5: A) Heat shrink end caps tested to seal bottom and top ends of acrylic tubes and B) end caps melted after heated.

Different types of resins were explored to seal the ends of acrylic tubes and waterproof electric components. Pratley Quickset Putty was tested (Figure 5.6), however, this resin was hard to shape around the ends of the tube and no information about the reactivity of the resin with acrylic was found, so there was a possibility of the resin being removed from the acrylic tubes over time.

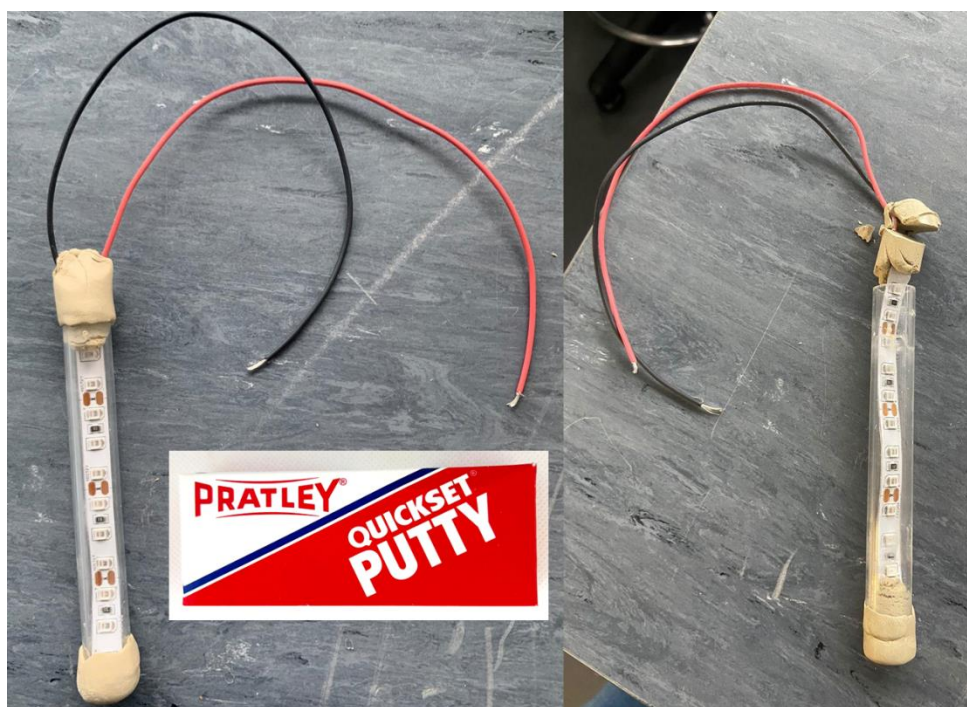


Figure 5.6: Pratley quick-set putty resin tested to seal bottom and top ends of acrylic tubes.

Quick-set epoxy resin was also tested to seal bottom and top ends of acrylic tubes and to waterproof wires from UV-A LED strips. This resin presented a very liquid consistency that would flow into the acrylic tube once applied at the ends (Figure 5.7A). Also, the resin did not present a gradual setting process and it cured almost immediately within around 5 minutes of application. Furthermore, acrylic tubes containing non waterproof UV-A LED strips were submerged in water for two weeks and the resin turned yellow, process also known as ambering (Figure 5.7B), which could have been caused by exposure to the UV light that resulted in a faster degradation of the resin (Felix 2021).

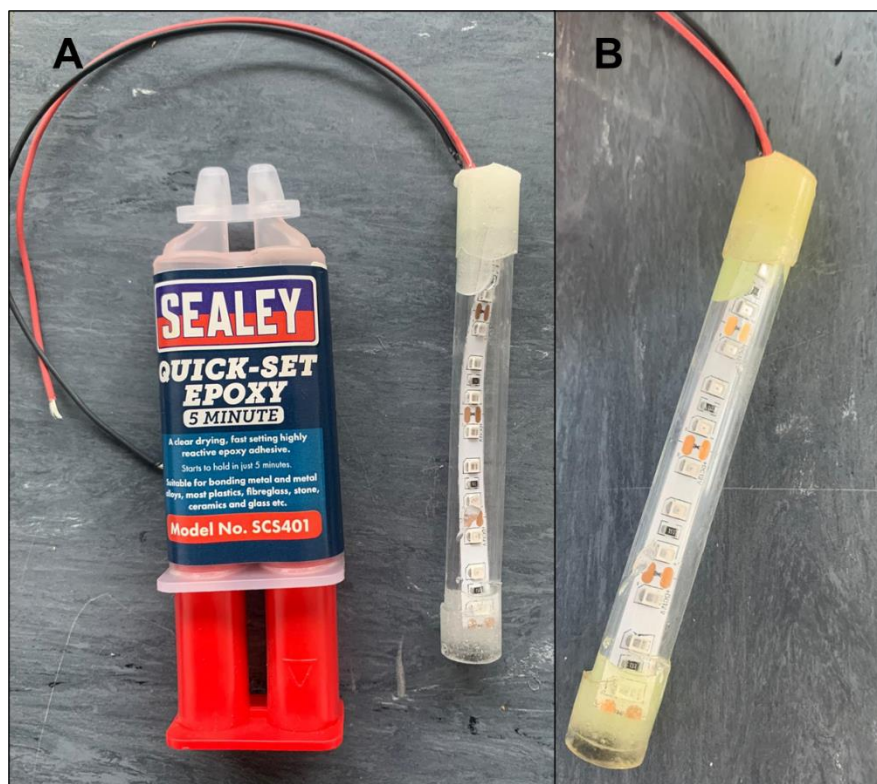


Figure 5.7: A) Quick-set epoxy resin tested to seal bottom and top ends of acrylic tubes and B) ambering process caused in the resin after exposure to UV irradiation.

A two-part epoxy resin was also evaluated (Figure 5.8A). The resin also presented a liquid formulation that would flow inside the acrylic tube (Figure 5.8B). Glass wool was placed at both ends of the acrylic tube before the resin was added to prevent the resin to run into the tube (Figure 5.8C), however, the glass wool application was not practical as the wool and resin were not easy to manipulate. Furthermore, the two-part epoxy resin also underwent ambering after a month in contact with water and exposure to UV-A LED irradiation (Figure 5.8D).

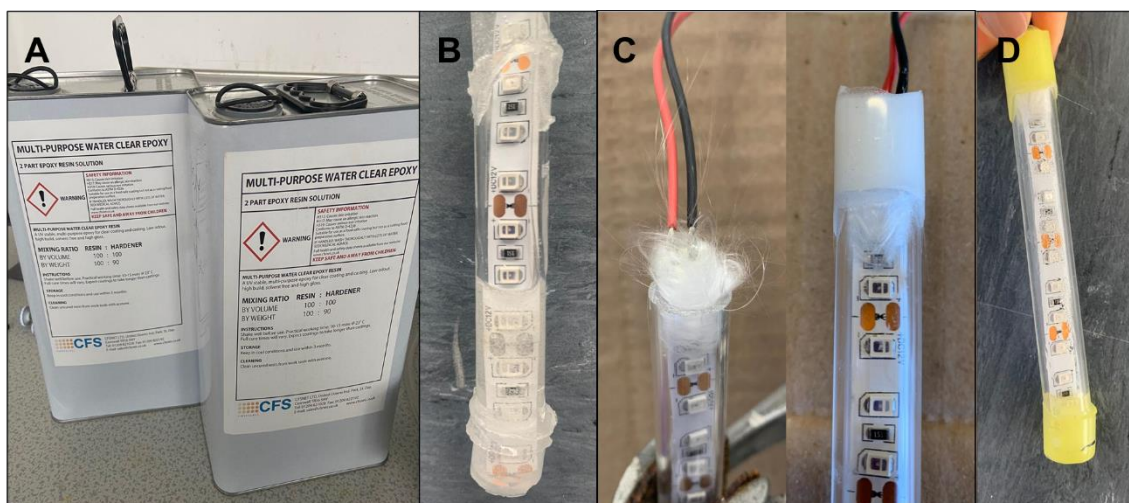


Figure 5.8: A) Two-part epoxy resin tested to seal bottom and top ends of acrylic tubes, B) resin flowing into acrylic tube, C) glass wool used to stop resin to enter the acrylic tube and D) ambering process caused in the resin after exposure to UV irradiation.

The Wessex 4303 resin was also tested as a sealant for acrylic tubes. The Wessex resins have many applications, including underwater services (Wessex Resins & Adhesives 2024), which means the Wessex 4303 resin would be a stable option for the reactor used for the removal of pesticides from aquatic environments at source. The resin consists of a yellow resin and blue hardener that show green coloration when mixed together (Figure 5.9). The Wessex 4303 resin was easy to apply and a suitable option to waterproof the electric components of the photocatalytic reactor.

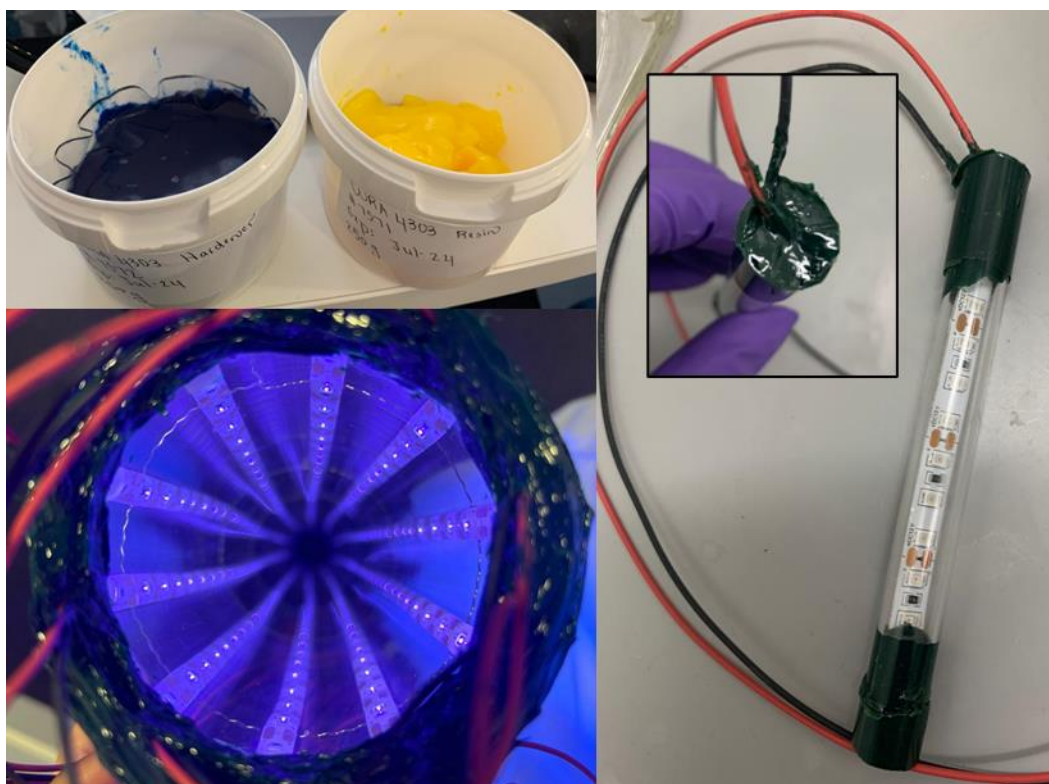


Figure 5.9: Wessex 4303 resin tested to seal bottom and top ends of acrylic tubes.

All the components of the photocatalytic reactor were determined, including $\text{g-C}_3\text{N}_4$ coated beads selected as catalyst because this catalyst is as easy to prepare, non-toxic, environmentally safe, requires low-cost precursor (melamine – around £0.06 per gram of melamine) and can be recovered from water after treatment. UV-A LED strips were used to activate $\text{g-C}_3\text{N}_4$ coated beads as a low-cost, low maintenance, flexible, long-life and efficient light source option to be used in photocatalysis. The format and dimensions of the photocatalytic reactor consisted of a cylinder, which could be used in different application for both flow through systems and batch treatment for pesticide removal. Electric components were sealed and waterproofed using Wessex 4303 resin. The final reactor prototype consisted of a portable double wall acrylic cylinder (76 mm inside diameter and 1 m length), ten LED strips (1 m each) were placed in between the two walls and then were waterproofed with the Wessex 4303 resin. Finally, $\text{g-C}_3\text{N}_4$ coated beads were place inside the acrylic tube (approximately 1.1 kg) and contained using a stainless-steel mesh at the top and bottom ends of the reactor (Figure 5.10).

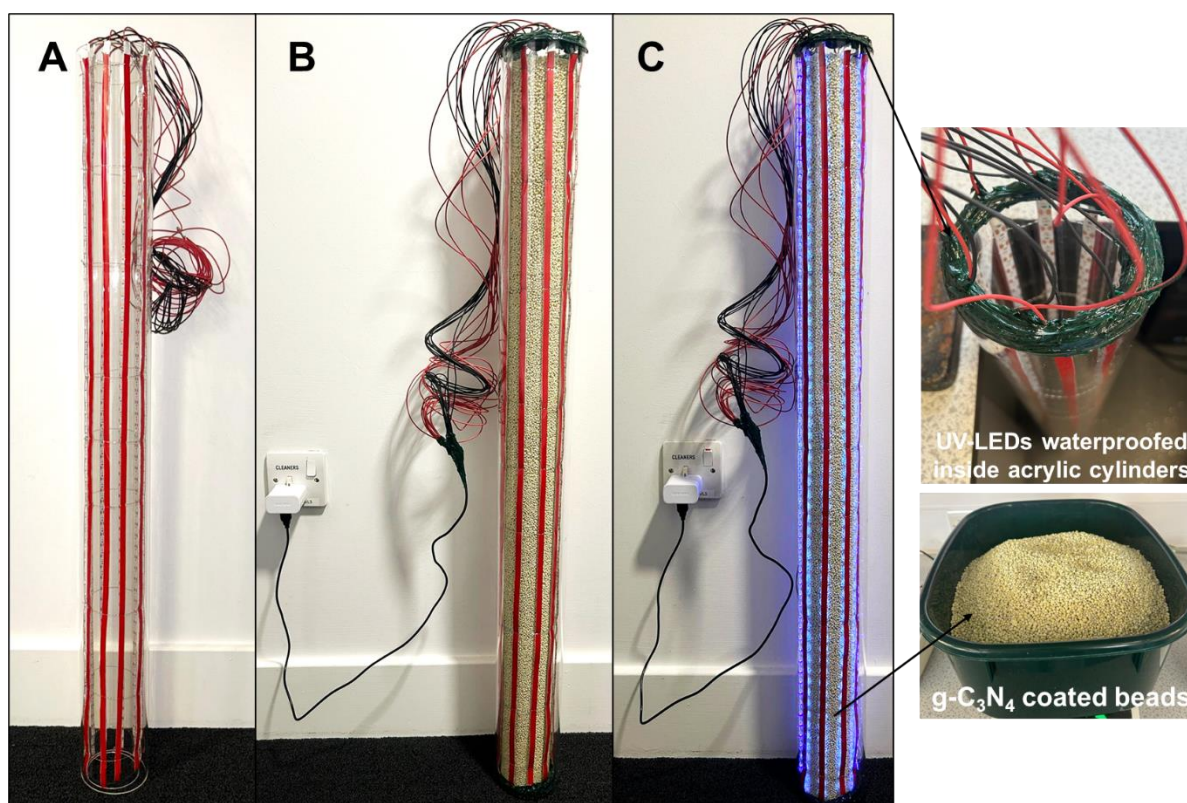


Figure 5.10: A) Concentric acrylic cylinders containing ten UV-A LED strips of 1 m each, B) photocatalytic reactor prototype based on graphitic carbon nitride ($\text{g-C}_3\text{N}_4$) coated beads and UV-A LED irradiation and C) electric components sealed and UV-A LED strips switched on for $\text{g-C}_3\text{N}_4$ coated beads activation.

One challenge during the scale-up of a photocatalytic reactor is the illumination of the catalyst since the absorption of photons by the catalyst and the photocatalytic efficiency depend on the reactor design (Marcelino and Amorim 2019). The design of the proposed prototype is very flexible and the irradiation of the catalyst by LEDs can be optimized by changing the internal diameter of the acrylic tube. Other parameters such as the length of the reactor and the number of treatment units in series can also change depending on the treatment requirements and local conditions in order to increase the photocatalytic performance.

Capital costs are the fixed costs related to the purchase all materials required for the preparation of the reactor. For the proposed reactor prototype, the capital costs included two acrylic cylinders, uncoated glass beads, melamine as the precursor for $\text{g-C}_3\text{N}_4$, UV-A LED strips, stainless-steel mesh to contain $\text{g-C}_3\text{N}_4$ coated, Wessex 4303 resin and electric wires, which represent an overall cost of £204 per treatment unit (Table 5.2).

Table 5.2: Total capital costs (£204 per treatment unit) for the construction of the photocatalytic reactor prototype.

Material	Amount required	Total cost (~£)
Acrylic cylinders	2 units	118
Uncoated glass beads	1 kg	2.5
Melamine	400 g	23
UV-A LED strip	10 m (600 individual LEDs)	45
Stainless-steel mesh	30 x 30 cm	2.5
Wessex 4303 resin	100 g	10
Electric wires	20 m	3

The total costs can only be determined on a case-by-case basis and the costs will depend on different factors such as the duration of treatment and the number of treatment units applied. Operational and maintenance costs should also be considered, including electric power consumption.

This is a small and portable reactor prototype that should be applied at source for the removal of pesticides from aquatic environments in both batch and flow-through systems. The associated costs to build and run the reactor can be supported by any farm and should be easily applied where the removal of pesticides is required.

5.3.2 Diuron degradation by a photocatalytic reactor: Challenges and learnings

So far, only bench-scale experiments using g-C₃N₄ coated beads and UV-A LED irradiation for the degradation of pesticides were performed, however, the reactor prototype should be tested in pilot-scale experiments to treat larger volumes of water contaminated with pesticides, for example, in 1000L storage tanks. These storage tanks are commonly used in farms to keep residual pesticides. Several challenges were observed during experiments involving the large-scale application of a photocatalytic reactor based on g-C₃N₄ and UV-A LEDs in comparison with bench scale experiment. Before working with environmental samples, the photocatalytic removal of pesticides by a reactor was evaluated using a solution consisting of diuron dissolved in tap water. The initial challenge was to prepare the diuron experimental solution by dissolving diuron (>95% purity) in tap water. First, chlorine has been used for water disinfection for over 100

years in Scotland (Scottish Water 2024). The residual chlorine in the tap water could be reactive and, therefore, could interfere in the photocatalytic degradation of organic pollutants, such as diuron, by oxidizing these compounds (Zhang and Pehkonen 1999; Ohno et al. 2008). To minimize a possible inhibition of photocatalysis by residual chlorine present in the tap water, the tank remained open for 72 hours after tap water was added to the tank to allow chlorine evaporation. Another issue was to completely dissolve diuron in large volumes of water. Diuron was added to the experimental solution and the diuron concentration was quantified until equilibrium was reached. The submersible water pump was used to mix the experimental solution until the diuron concentration was constant. Even though diuron is relatively soluble in water with a solubility of 42 mg L⁻¹ at 20 °C (Agriculture and Environment Research Unit 2007), equilibrium of the diuron concentration was only obtained after 48 hours of mixing. Diuron demonstrates lower solubility in lower temperatures (Araujo et al. 2023), therefore, one of the reasons why diuron was not quickly dissolved could be the water temperature, which was around 16 °C. The experiment could not be performed indoors because of the large volume of water used in the tank, therefore, environmental conditions like temperature could not be controlled.

Another challenge was to pump the experimental solution through the reactor. As previously mentioned, water tends to follow the path of least resistance in a system (Pedescoll et al. 2013), therefore, the experimental solution might not be treatment with only the natural flow of water inside the tank. A submersible pump was applied to direct the water flow through the reactor. The pump was connected to the bottom of the reactor using different plumbing parts connected to each other and sealed with Wessex 4303 resin (Figure 5.11).



Figure 5.11: Submersible water pump connected to the photocatalytic reactor for the removal of diuron at large-scale in a 1000 L tank.

The photocatalytic reactor initially fit inside of the tank containing the diuron experimental solution, however, when the pump and connectors were attached to the bottom of the reactor, the system would not completely pass through the top opening of the tank. Due to this, the top of the reactor was further opened to fit the pump connected to the reactor (Figure 5.12).

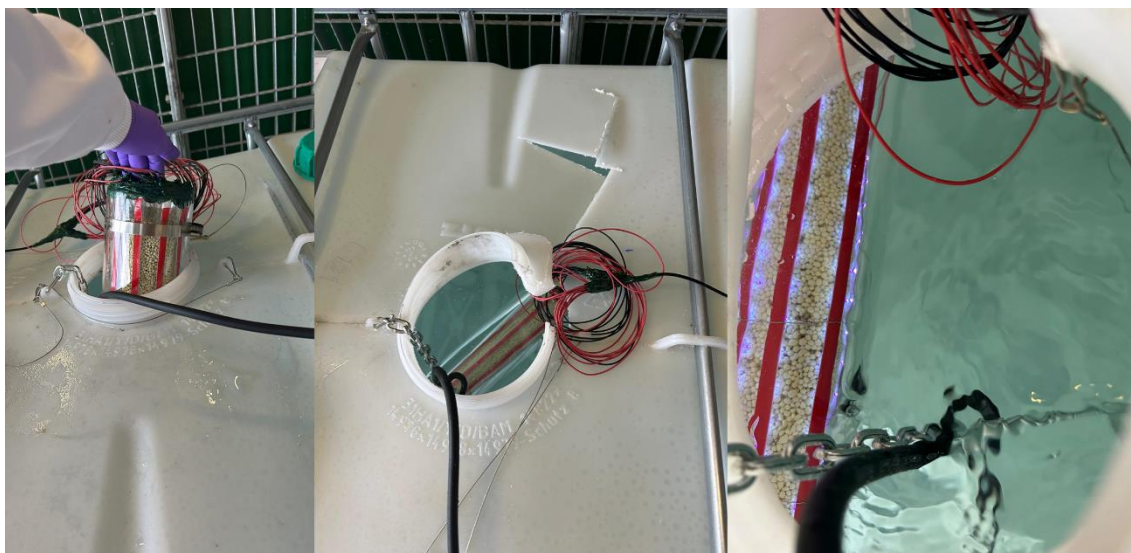


Figure 5.12: Pump and photocatalytic reactor inside of 1000 L tank containing diuron experimental solution.

After the pump and reactor were placed inside the tank, the pump was switched on, however, the pressure generated by the pump was too high, causing the connections between the pump and reactor to detach, despite the fact resin was used to join all the parts. Using three different plumbing parts to connect the pump to the bottom of the reactor likely resulted in lower stability of the connections compared to using a single connecting fitting. Consequently, the connections separated under the pressure generated from the pump flow, instead of directing the water through the reactor. A single custom-made connecting part could have been manufactured to connect the pump and the reactor, allowing the fitting to be more resistant to the pump pressure and the water would be directed through the reactor. Furthermore, the custom-made connecting part would be smaller, allowing the reactor to fit the tank. Another option would be to use a less powerful submersible water pump, which would ensure a higher contact time between the experimental solution and the catalyst inside the reactor.

Even though water was not pumped through the reactor, the water pump provided constant mixing of the experimental solution. It was possible that some water would flow through the photocatalytic reactor by placing the bottom of the reactor close to the pump. The diuron concentration was evaluated over 72 hours to verify if any diuron removal occurred by the

photocatalytic reactor based on g-C₃N₄ coated beads and UV-A LEDs, however, no removal of diuron was observed (Figure 5.13).

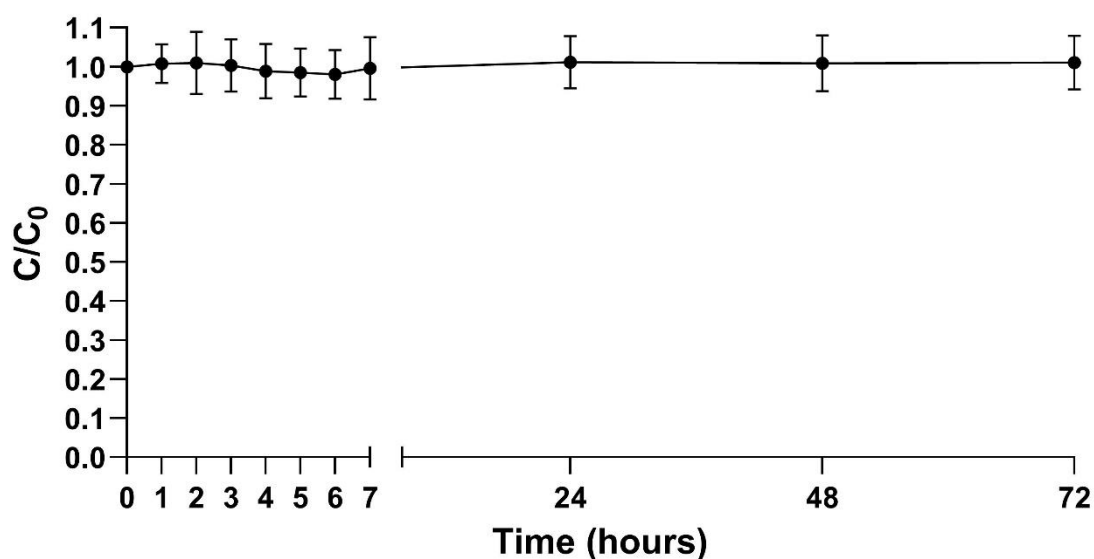


Figure 5.13: Photocatalytic degradation of diuron in tap water in a 1000 L tank by a reactor based on graphitic carbon nitride (g-C₃N₄) coated beads and UV-A LED irradiation over 72 hours. (n = 4, error bars = 1SD).

The results indicate that the mixing caused by the submersible water pump inside of the tank was not sufficient to promote an efficient photocatalytic degradation of diuron by the reactor. It is possible that a higher photocatalytic performance would be achieved once the experimental flows through the reactor.

Despite some challenges faced during the experiment, the prototype design can still be considered a success. The Wessex 4303 resin used for electric components and UV-A LED strips effectively sealed and waterproofed the reactor, enabling it to be fully submerged in the tank containing the diuron experimental solution. Furthermore, the g-C₃N₄ coated beads used as catalysts were contained within the reactor and did not escape into the experimental solution, even when water was pumped through the reactor. Longer periods of operation would be desirable to further evaluate the functionality of the photocatalytic reactor over time.

While many water treatment technologies are evaluated using bench-scale experiments, testing these technologies at a large scale presents numerous challenges. The current investigation highlights the importance of thoroughly assessing different technologies in large-scale implementations to identify possible challenges and to ensure reliability and effectiveness of

the proposed treatment. Some adjustments might be required to the proposed experimental protocol, however, the photocatalytic reactor has the potential to successfully remove pesticides from aquatic environments.

5.4 Conclusion

A photocatalytic reactor prototype was proposed to remove pesticides from aquatic environments at source by g-C₃N₄ coated beads and UV-A LED irradiation. Different challenges were observed during the pilot-scale investigation for the removal of diuron by the proposed photocatalytic reactor. New adjustments should be made to the photocatalytic system, for example, manufacture a custom-made connection (for instance, the connection could be manufactured using a 3D printer) or apply a less powerful water pump to guarantee water flow through the reactor to achieve a higher photocatalytic performance. Other future research includes the evaluation of photocatalytic degradation on a wide selection of pesticides and other agrochemicals (e.g., fertilizers), a mixture of pesticides and deployment at farms to confirm the effectiveness and feasibility of the photocatalytic reactor.

The photocatalytic treatment could also be applied in different activities. Pesticides are also applied in aquaculture as a medicine for the control of salmon lice. Different pesticides can be used as medicine, such as imidacloprid, azamethiphos, deltamethrin and cypermethrin. The medicine is applied during medicinal bath treatments, which consist of enclosing the fish cage and adding the medicine to the water. After treatment, the fish return to the pen and the water is discharged back into the sea, however, the discharged water might still contain residual medicine. A possible application of the proposed reactor is to treat the water used during medicinal bath treatment before its discharge to the sea by deploying the reactor inside of the tank.

In conclusion, the photocatalytic reactor is a low-cost, flexible, portable, easy to use and environmentally friendly prototype that can be used in different scenarios in any farm for the removal of pesticides in both batch and flow-through systems, depending on the required application.

Chapter 6

Conclusions and Future work

6.1 Conclusion and future work

The aim of the current research was to apply advanced oxidation processes (photolysis and photocatalysis) at source for the removal of harmful contaminants from aquatic environments. Photolysis and photocatalysis were able to successfully degrade cyanobacterial cells, cyanotoxins and pesticides, however, experiments performed in natural water will also enable further investigation of the degradation of pesticides and of the effects of water elements (e.g., organic matter and other nutrients) can impact the degradation of pollutants in aquatic environments.

Both photolysis and photocatalysis require UV irradiation, which would usually represent an increase in treatment costs. Low-cost UV-A LED irradiation, however, was successfully applied during both treatments. The lighting technology has improved over the years by replacing conventional light sources to Dual In-Line Package (DIP) LEDs and more recently to Surface Mounted Diode (SMD) LEDs, for example, which are smaller and more efficient LEDs. Even the SMD technology has improved by changing SMD 5050 and SMD 3528 LED diodes to SMD 2835 LED diodes. SMD 2835 LED diodes are thinner, present better light output (higher luminous flux and brightness) and longer working life, due to presence of an additional bottom heat sink that allows heat dissipation and subsequently avoids lumen depreciation. Future development in LED technology will decrease costs further and improve these water treatment technologies.

Furthermore, both photolytic and photocatalytic systems require energy supply. So far, all treatment units were powered by mains power, however, the use of renewable energy systems are desirable to further enhance the sustainability aspect of each treatment. Alternative energy supplies, such as photovoltaic cells or wind power that feed a battery system could be explored, depending on the local climatic conditions of each system.

A photocatalytic reactor based on g-C₃N₄ coated beads and UV-A LED irradiation was developed for the removal of pesticides. The reactor is a low-cost, flexible, portable and efficient reactor that could be applied in various scenarios in any farm. Potential deployment locations include storage tanks containing residual pesticides, ponds, drainage channels and other aquatic environments near farms. The photocatalytic reactor can also

be utilized in other activities. In aquaculture, pesticides (e.g., imidacloprid, azamethiphos, deltamethrin and cypermethrin) can be used in medicinal bath treatments as medicines to control salmon lice. During bath treatments, the salmon cage is enclosed and the medicine is added to the water. After the bath treatment, the salmon return to the pen and the remaining water containing residual medicine is discharged into the sea. The photocatalytic reactor could be used to treat the water containing residual medicines before it is discharged into the sea.

Pesticides have the potential of being very persistent and both parent compound and transformation products can still be detected in aquatic environments after years of the pesticide application. Transformation products can be generated during the photocatalytic degradation of pesticides at source and they can present equal or higher toxicity than the parent compound if they are not also degraded during treatment. Therefore, a critical component of future investigation is to evaluate the generation, degradation and toxicity of transformation products during the photocatalytic degradation of pesticides at source. Identification of transformation products can be achieved by liquid chromatography tandem quadrupole time-of-flight mass spectrometry.

The application of the photocatalytic reactor at source would require the preparation of g-C₃N₄ coated beads in larger scale. In laboratory, one batch of the g-C₃N₄ coating process onto glass beads would result in the preparation of approximately 240 g of g-C₃N₄ coated beads, considering the equipment available to sieve the precursor (melamine) onto the uncoated beads and the space available in the muffle furnace during the calcination step. The preparation of g-C₃N₄ coated beads in larger scale could be explored by using a cement mixer to deposit melamine onto the surface of uncoated beads. The cement mixer will allow the preparation of larger quantities of coated beads at the same time with little effort. Furthermore, muffle furnaces used to prepare resin sculptures could be used during the calcination of g-C₃N₄ coated beads.

To conclude, photolysis and photocatalysis are advanced oxidation processes that can be applied as environmentally safe, economical and efficient approaches for the removal of contaminants from aquatic environments at source. Further research is essential to comprehensively

understand the effects of these technologies on the degradation of contaminants in natural environments and to further improve the application of each treatment at source. Furthermore, these technologies have the potential to be applied in different water treatment scenarios, such as complimentary steps to ease the burden on potable water treatment, as localized treatment in lakes or reservoirs, as a polishing step before the discharge of treated water into the environment and as main water treatment in agriculture and aquaculture industries.

Chapter 7

References

ABD EL-HACK, M.E. et al., 2022. Undesirable odour substances (geosmin and 2-methylisoborneol) in water environment: Sources, impacts and removal strategies. *Marine Pollution Bulletin*, 178, p. 113579.

ADAMS, D.G., 1997. Cyanobacteria. In: SHAPIRO J. and DWORKIN M., eds. *Bacteria as Multicellular Organisms*. New York: Oxford University Press. pp. 109–148.

AFFAM, A.C. and CHAUDHURI, M., 2013. Degradation of pesticides chlorpyrifos, cypermethrin and chlorothalonil in aqueous solution by TiO₂ photocatalysis. *Journal of Environmental Management*, 130, pp. 160–165.

AGRICULTURE AND ENVIRONMENT RESEARCH UNIT, 2007. *Pesticide properties database*. [online]. Available from: <http://sitem.herts.ac.uk/aeru/ppdb/> [Accessed 17 February 2022].

AJIBOYE, T.O., KUVAREGA, A.T. and ONWUDIWE, D.C., 2020. Recent strategies for environmental remediation of organochlorine pesticides. *Applied Sciences*, 10(18), p. 6286.

AKBARI SHORGOLI, A. and SHOKRI, M., 2017. Photocatalytic degradation of imidacloprid pesticide in aqueous solution by TiO₂ nanoparticles immobilized on the glass plate. *Chemical Engineering Communications*, 204(9), pp. 1061–1069.

AKKANEN, J. and KUKKONEN, J.V.K., 2003. Measuring the bioavailability of two hydrophobic organic compounds in the presence of dissolved organic matter. *Environmental Toxicology and Chemistry*, 22(3), pp. 518–524.

AKTER, S. et al., 2017. Rapid and highly sensitive non-competitive immunoassay for specific detection of nodularin. *Microorganisms*, 5(3), p. 58.

ALABAANI, S.M.M., 2013. Assessment of evolution in LEDs lighting as energy-saving. In: *2nd International Conference on Energy Systems and Technologies*. Cairo, Egypt. Available from: <https://www.researchgate.net/publication/330839472>.

DE ALBUQUERQUE, F.P. et al., 2020. An overview of the potential impacts of atrazine in aquatic environments: Perspectives for tailored solutions based on nanotechnology. *Science of the Total Environment*, 700, p. 134868.

ALISTE, M. et al., 2021. Photocatalytic oxidation of chlorantraniliprole, imidacloprid, pirimicarb, thiamethoxam and their main photoreaction intermediates as impacted by water matrix composition under UVA-LED exposure. *Catalysts*, 11(5), p. 609.

ALJUAID, A. et al., 2023. g-C₃N₄ Based Photocatalyst for the Efficient Photodegradation of Toxic Methyl Orange Dye: Recent Modifications and Future Perspectives. *Molecules*, 28(7), p. 3199.

AMALRAJ, A. and PIUS, A., 2015. Photocatalytic degradation of monocrotophos and chlorpyrifos in aqueous solution using TiO₂ under UV radiation. *Journal of Water Process Engineering*, 7, pp. 94–101.

AMETA, R. et al., 2018. Photocatalysis. In: *Advanced Oxidation Processes for Wastewater Treatment: Emerging Green Chemical Technology*. Elsevier Inc. pp. 135–175.

- ANDRÉS, C.M.C. et al., 2023. Superoxide Anion Chemistry—Its Role at the Core of the Innate Immunity. *International Journal of Molecular Sciences*, 24(3), p. 1841.
- ANJUMOL, K.S. et al., 2022. Graphitic carbon nitride-based nanocomposites. In: *Synthesis, Characterization, and Applications of Graphitic Carbon Nitride: An Emerging Carbonaceous Material*. Elsevier. pp. 59–76.
- ANUPAM, K. et al., 2022. Technologies for pesticide removal from water and wastewater— A bibliometric survey. In: *Pesticides Remediation Technologies from Water and Wastewater*. Elsevier. pp. 77–95.
- ARAUJO, G.R. et al., 2023. Cucumber bioassay and HPLC analysis to detect diuron residues in remineralized soils following *Canavalia ensiformis* cultivation as a phytoremediator. *Horticulturae*, 9(12), p. 1251.
- ATSDR, 1997. *Public health statement chlorfenvinphos*. [online]. Available from: <https://wwwn.cdc.gov/TSP/PHS/PHS.aspx?phsid=930&toxid=193> [Accessed 12 April 2024].
- AZEVEDO, S.M.F.O. et al., 2002. Human intoxication by microcystins during renal dialysis treatment in Caruaru-Brazil. *Toxicology*, 181–182, pp. 441–446.
- BAIRAMIS, F., RAPTI, I. and KONSTANTINO, I., 2023. g-C₃N₄ based Z-scheme photocatalysts for environmental pollutants removal. *Current Opinion in Green and Sustainable Chemistry*, 40, p. 100749.
- BAKER, B.H., ALDRIDGE, C.A. and OMER, A., 2016. Water Availability and use. *Mississippi State University* , pp. 1–4.

- BANIĆ, N.D. et al., 2014. Photodegradation of neonicotinoid active ingredients and their commercial formulations in water by different advanced oxidation processes. *Water, Air, and Soil Pollution*, 225(5).
- BARUAH, A. et al., 2019. Nanotechnology based solutions for wastewater treatment. In: *Nanotechnology in Water and Wastewater Treatment: Theory and Applications*. Elsevier. pp. 337–368.
- BEASLEY, V.R., 2020. Harmful Algal Blooms (Phycotoxins). In: *Earth Systems and Environmental Sciences*. Elsevier.
- BEIRAS, R., 2018. Nonpersistent Inorganic Pollution. In: *Marine Pollution. Sources, Fate and Effects of Pollutants in Coastal Ecosystems*. Elsevier. pp. 31–39.
- BERBERIDOU, C. et al., 2019. Decomposition and detoxification of the insecticide thiacloprid by TiO₂-mediated photocatalysis: kinetics, intermediate products and transformation pathways. *Journal of Chemical Technology and Biotechnology*, 94(8), pp. 2475–2486.
- BERMAN, F.W., GERWICK, W.H. and MURRAY, T.F., 1999. Antillatoxin and kalkitoxin, ichthyotoxins from the tropical cyanobacterium *Lyngbya majuscula*, induce distinct temporal patterns of NMDA receptor-mediated neurotoxicity. *Toxicon*, 37, pp. 1645–1648.
- BERRY, J.P., 2008. Cyanobacterial toxins as allelochemicals with potential applications as algaecides, herbicides and insecticides. *Marine Drugs*, 6(2), pp. 117–146.

BORAH, P., KUMAR, M. and DEVI, P., 2020. Types of inorganic pollutants: metals/metalloids, acids, and organic forms. In: *Inorganic Pollutants in Water*. Elsevier. pp. 17–31.

BOUQUET-SOMRANI, C. et al., 2000. Photocatalytic degradative oxidation of Diuron in organic and semi-aqueous systems over titanium dioxide catalyst. *New Journal of Chemistry*, 24(12), pp. 999–1002.

BOURKE, A.T.C. et al., 1983. An outbreak of hepato-enteritis (the Palm Island mystery disease) possibly caused by algal intoxication. *Toxicon*, 21(3), pp. 45–48.

BRUCKMANN, F.S. et al., 2022. Adsorption and photocatalytic degradation of pesticides into nanocomposites: A review. *Molecules*, 27(19), p. 6261.

BYRNE, C., SUBRAMANIAN, G. and PILLAI, S.C., 2018. Recent advances in photocatalysis for environmental applications. *Journal of Environmental Chemical Engineering*, 6(3), pp. 3531–3555.

CAMACHO-MUÑOZ, D. et al., 2020. Degradation of microcystin-LR and cylindrospermopsin by continuous flow UV-A photocatalysis over immobilised TiO₂. *Journal of Environmental Management*, 276, p. 111368.

CAMPBELL, D. et al., 1998. Chlorophyll fluorescence analysis of cyanobacterial photosynthesis and acclimation. *Microbiology and Molecular Biology Reviews: MMBR*, 62(3), pp. 667–683.

CARAZO-ROJAS, E. et al., 2018. Pesticide monitoring and ecotoxicological risk assessment in surface water bodies and sediments of a tropical agro-ecosystem. *Environmental Pollution*, 241, pp. 800–809.

- CARMICHAEL, W., MAHMOOD, N.A. and HYDE, E.G., 1990. Natural toxins from cyanobacteria (blue-green algae). In: *Marine Toxins*. pp. 87–106.
- CARMICHAEL, W.W. and BOYER, G.L., 2016. Health impacts from cyanobacteria harmful algae blooms: Implications for the North American Great Lakes. *Harmful Algae*, 54, pp. 194–212.
- ČERNIGOJ, U., ŠTANGAR, U.L. and TREBŠE, P., 2007. Degradation of neonicotinoid insecticides by different advanced oxidation processes and studying the effect of ozone on TiO₂ photocatalysis. *Applied Catalysis B: Environmental*, 75(3–4), pp. 229–238.
- CHAE, S. et al., 2019. Effective removal of emerging dissolved cyanotoxins from water using hybrid photocatalytic composites. *Water Research*, 149, pp. 421–431.
- CHAKRABORTY, G., GOSWAMI, A.D. and ROY, J., 2023. Study of the Harmonic Analysis of the High-Intensity Discharge Lamps. *Light & Engineering*, (04–2023), pp. 50–56.
- CHANG, C.W., HUO, X. and LIN, T.F., 2018. Exposure of *Microcystis aeruginosa* to hydrogen peroxide and titanium dioxide under visible light conditions: Modeling the impact of hydrogen peroxide and hydroxyl radical on cell rupture and microcystin degradation. *Water Research*, 141, pp. 217–226. Available from: <https://doi.org/10.1016/j.watres.2018.05.023>.
- CHANG, S.Y. et al., 2015. An environmentally friendly method for testing photocatalytic inactivation of cyanobacterial propagation on a hybrid Ag-TiO₂ photocatalyst under solar illumination. *International Journal of Environmental Research and Public Health*, 12(12), pp. 15819–15833.

- CHEMISTRY STEPS, 2016. *Determining Reaction Order Using Graphs*.
[online]. Available from: <https://general.chemistrysteps.com/determining-reaction-order-using-graphs/> [Accessed 8 March 2024].
- CHEN, G., DING, X. and ZHOU, W., 2020. Study on ultrasonic treatment for degradation of Microcystins (MCs). *Ultrasonics Sonochemistry*, 63, p. 104900.
- CHEN, J. et al., 2021. Porous g-C₃N₄ with defects for the efficient dye photodegradation under visible light. *Water Science and Technology*, 84(6), pp. 1354–1365.
- CHEN, L. et al., 2015. TiO₂ photocatalytic degradation and detoxification of cylindrospermopsin. *Journal of Photochemistry and Photobiology A: Chemistry*, 307–308, pp. 115–122.
- CHEN, P. et al., 2012. Photocatalytic degradation efficiency and mechanism of microcystin-RR by mesoporous Bi₂WO₆ under near ultraviolet light. *Environmental Science and Technology*, 46(4), pp. 2345–2351.
- CHEUNG, M.Y., LIANG, S. and LEE, J., 2013. Toxin-producing cyanobacteria in freshwater: A review of the problems, impact on drinking water safety, and efforts for protecting public health. *Journal of Microbiology*, 51(1), pp. 1–10.
- CHINTALAPATI, P. and MOHSENI, M., 2018. Effect of vacuum UV irradiation on the concentration of dissolved cyanobacterial toxin microcystin-LR. *Water Science and Technology: Water Supply*, 18(4), pp. 1466–1471.

CHRISTIANSEN, G. et al., 2003. Microcystin biosynthesis in *Planktothrix*: Genes, evolution, and manipulation. *Journal of Bacteriology*, 185(2), pp. 564–572.

CHU, S., 1942. The influence of the mineral composition of the medium on the growth of planktonic algae. *Journal of Ecology*, 30, pp. 284–325.

CLEMENTE, A. et al., 2020. The role of hydraulic conditions of coagulation and flocculation on the damage of cyanobacteria. *Science of the Total Environment*, 740, p. 139737.

COMMISSION IMPLEMENTING DECISION (EU) 2018/840, 2018.
Implementing decision 2018/840 - Watch list of substances for Union-wide monitoring in the field of water policy pursuant to Directive 2008/105/EC repealing Commission Implementing Decision (EU) 2015/495.

COX, P.A. et al., 2005. Diverse taxa of cyanobacteria produce-N-methylamino-L-alanine, a neurotoxic amino acid. [online]. Available from: www.pnas.org/cgi/doi/10.1073/pnas.0501526102.

CUMMING, H. and RÜCKER, C., 2017. Octanol-Water Partition Coefficient Measurement by a Simple ¹H NMR Method. *ACS Omega*, 2(9), pp. 6244–6249.

CUNHA, D.L. et al., 2018. Immobilized TiO₂ on glass spheres applied to heterogeneous photocatalysis: Photoactivity, leaching and regeneration process. *PeerJ*, 2018(3), pp. 1–19.

DALHAT, M.H. and AHMAD, A., 2021. Removal of pesticides from water and wastewater by solar-driven photocatalysis. In: *Development in Wastewater*

Treatment Research and Processes: Removal of Emerging Contaminants from Wastewater through Bio-Nanotechnology. Elsevier. pp. 435–458.

DAMALAS, C.A. and ELEFTHEROHORINOS, I.G., 2011. Pesticide exposure, safety issues, and risk assessment indicators. *International Journal of Environmental Research and Public Health*, 8(5), pp. 1402–1419.

DIAZ-ANGULO, J., LARA-RAMOS, J.A. and MACHUCA-MARTÍNEZ, F., 2021. Dye photosensitization on heterogeneous photocatalysis process, fundamentals, and applications. In: *Nanostructured Photocatalysts: From Fundamental to Practical Applications*. Elsevier. pp. 331–362.

DODDS, W.K. et al., 2009. Eutrophication of U.S. freshwaters: Analysis of potential economic damages. *Environmental Science and Technology*, 43(1), pp. 12–19.

DOKULIL, M.T. and TEUBNER, K., 2011. Eutrophication and climate change: Present situation and future scenarios. In: A.A. ANSARI et al., eds. *Eutrophication: Causes, Consequences and Control*. pp. 1–16.

DONG, H. et al., 2015. An overview on limitations of TiO₂-based particles for photocatalytic degradation of organic pollutants and the corresponding countermeasures. *Water Research*, 79, pp. 128–146.

DORRAJI, M.S.S. et al., 2017. Photocatalytic activity of g-C₃N₄: An empirical kinetic model, optimization by neuro-genetic approach and identification of intermediates. *Chemical Engineering Research and Design*, 127, pp. 113–125.

DRAYER, L., 2017. *The importance of hydration*. [online]. Harvard School of Public Health . Available from: <https://www.hsph.harvard.edu/news/hsph->

in-the-news/the-importance-of-

hydration/#:~:text=Drinking%20enough%20water%20each%20day,qualit
y%2C%20cognition%2C%20and%20mood. [Accessed 7 June 2024].

DU, S., LIAN, J. and ZHANG, F., 2022. Visible light-responsive N-doped TiO₂ photocatalysis: Synthesis, characterizations, and applications. *Transactions of Tianjin University*.

ECHAVIA, G.R.M., MATZUSAWA, F. and NEGISHI, N., 2009. Photocatalytic degradation of organophosphate and phosphonoglycine pesticides using TiO₂ immobilized on silica gel. *Chemosphere*, 76(5), pp. 595–600.

EDDY, D.R. et al., 2023. Heterophase polymorph of TiO₂ (anatase, rutile, brookite, TiO₂ (B)) for efficient photocatalyst: Fabrication and activity. *Nanomaterials*, 13(4), p. 704.

EDWARDS, D.J. et al., 2004. Structure and biosynthesis of the Jamaicamides, new mixed polyketide-peptide neurotoxins from the marine cyanobacterium *Lyngbya majuscula*. *Chemistry & Biology*, 11, pp. 817–833.

EHLING-SCHULZ, M. and SCHERER, S., 1999. UV protection in cyanobacteria. *European Journal of Phycology*, 34(4), pp. 329–338.

EJETA, S.Y. and IMAE, T., 2021. Photodegradation of pollutant pesticide by oxidized graphitic carbon nitride catalysts. *Journal of Photochemistry and Photobiology A: Chemistry*, 404, p. 112955.

ELMOLLA, E.S. and CHAUDHURI, M., 2010. Photocatalytic degradation of amoxicillin, ampicillin and cloxacillin antibiotics in aqueous solution using UV/TiO₂ and UV/H₂O₂/TiO₂ photocatalysis. *Desalination*, 252(1–3), pp. 46–52.

EL-SHEEKH, M.M. et al., 2021. Detrimental effect of UV-B radiation on growth, photosynthetic pigments, metabolites and ultrastructure of some cyanobacteria and freshwater chlorophyta. *International Journal of Radiation Biology*, 97(2), pp. 265–275.

EPA, 2000. *Trifluralin*. [online]. Available from: <https://www.epa.gov/sites/default/files/2016-09/documents/trifluralin.pdf> [Accessed 12 April 2024].

EPA, 2006. *Permethrin Facts (Reregistration Eligibility Decision (RED) Fact Sheet)*. [online]. Available from: https://www3.epa.gov/pesticides/chem_search/reg_actions/reregistration/facts_PC-109701_1-Jun-06.pdf [Accessed 12 April 2024].

EPA, 2024a. *Chlorpyrifos*. [online]. Available from: <https://www.epa.gov/ingredients-used-pesticide-products/chlorpyrifos#:~:text=Chlorpyrifos%20is%20an%20organophosphate%20insecticide,and%20soil%2Dborne%20insect%20pests>. [Accessed 15 March 2024].

EPA, 2024b. *DDT - A Brief History and Status*. [online]. Available from: <https://www.epa.gov/ingredients-used-pesticide-products/ddt-brief-history-and-status> [Accessed 12 April 2024].

ESCOBAR-SÁNCHEZ, H. et al., 2023. Plasmonic and photothermal effects of CuS nanoparticles biosynthesized from acid mine drainage with potential drug delivery applications. *International Journal of Molecular Sciences*, 24(22), p. 16489.

EVGENIDOU, E. et al., 2023. Photocatalytic performance of buoyant TiO₂-immobilized poly(ethylene terephthalate) beads for the removal of the anticonvulsant drug pregabalin from water and leachate. *Journal of Environmental Chemical Engineering*, 11(5), p. 110697.

FAGAN, R. et al., 2016a. Photocatalytic properties of g-C₃N₄-TiO₂ heterojunctions under UV and visible light conditions. *Materials*, 9(4), p. 286.

FAGAN, R. et al., 2016b. A review of solar and visible light active TiO₂ photocatalysis for treating bacteria, cyanotoxins and contaminants of emerging concern. *Materials Science in Semiconductor Processing*, 42, pp. 2–14.

FAWZI SULEIMAN KHASAWNEH, O. and PALANIANDY, P., 2019. Photocatalytic degradation of pharmaceuticals using TiO₂ based nanocomposite catalyst - Review. *Civil and Environmental Engineering Reports*, 29(3), pp. 1–33.

FELIX, J., 2021. *Why Epoxy resin turns yellow and how to prevent it*. [online]. Life Specialty Coatings. Available from: <https://lifespecialtycoatings.com/deep-dive-into-the-discoloration-of-epoxy-resin-over-time/#:~:text=Exposure%20to%20UV%20light%20is,turning%20the%20epoxy%20resin%20yellowish>. [Accessed 30 May 2024].

FENG, S. and LI, F., 2021. Photocatalytic dyes degradation on suspended and cement paste immobilized TiO₂/g-C₃N₄ under simulated solar light. *Journal of Environmental Chemical Engineering*, 9(4), p. 105488.

- FENOLL, J. et al., 2013. Photocatalytic degradation of substituted phenylurea herbicides in aqueous semiconductor suspensions exposed to solar energy. *Chemosphere*, 91(5), pp. 571–578.
- FENOLL, J. et al., 2019. Implementation of a new modular facility to detoxify agro-wastewater polluted with neonicotinoid insecticides in farms by solar photocatalysis. *Energy*, 175, pp. 722–729.
- FERNANDES, R.A. et al., 2020. Efficient removal of parabens from real water matrices by a metal-free carbon nitride photocatalyst. *Science of the Total Environment*, 716, p. 135346.
- FERNANDES, T.C.C., PIZANO, M.A. and MARIN-MORALES, M.A., 2013. Characterization, modes of action and effects of trifluralin: A review. In: A.J. PRICE and J.A. KELTON, eds. *Herbicides - Current Research and Case Studies in Use*.
- FLESCH, P., 2006. *Light and light sources: high-intensity discharge lamps*. Springer-Verlag.
- FRANK, S.N. and BARD, A.J., 1977. Heterogeneous photocatalytic oxidation of cyanide ion in aqueous solutions at TiO₂ powder. *Journal of the American Chemical Society*, 99(1), pp. 303–304.
- FUJIKI, H. et al., 1981. Indole alkaloids: Dihydroteleocidin B, teleocidin, and lyngbyatoxin A as members of a new class of tumor promoters. *Medical Sciences*, 78(6), pp. 3872–3876.
- GAHLOT, S. et al., 2021. High surface area g-C₃N₄ and g-C₃N₄-TiO₂ photocatalytic activity under UV and Visible light: Impact of individual

component. *Journal of Environmental Chemical Engineering*, 9(4), p. 105587.

GANESAN, S. et al., 2024. Efficient photocatalytic degradation of textile dye pollutants using thermally exfoliated graphitic carbon nitride (TE-g-C₃N₄). *Scientific Reports*, 14(1), p. 2284.

GAO, R.H. et al., 2022. Graphitic carbon nitride (g-C₃N₄)-based photocatalytic materials for hydrogen evolution. *Frontiers in Chemistry*, 10, p. 1048504.

GAR ALALM, M. et al., 2018. Immobilization of S-TiO₂ on reusable aluminum plates by polysiloxane for photocatalytic degradation of 2,4-dichlorophenol in water. *Journal of Water Process Engineering*, 26, pp. 329–335.

GARRIDO, I. et al., 2020. Solar reclamation of agro-wastewater polluted with eight pesticides by heterogeneous photocatalysis using a modular facility. A case study. *Chemosphere*, 249, p. 126156.

GARRIDO, I. et al., 2021. Solar photocatalysis as strategy for on-site reclamation of agro-wastewater polluted with pesticide residues on farms using a modular facility. *Environmental Science and Pollution Research*, 28, pp. 23647–23656.

GHODSI, S. et al., 2020. Synthesis and evaluation of the performance of g-C₃N₄/Fe₃O₄/Ag photocatalyst for the efficient removal of diazinon: Kinetic studies. *Journal of Photochemistry and Photobiology A: Chemistry*, 389, p. 112279.

GIACOMAZZI, S. and COCHET, N., 2004. Environmental impact of diuron transformation: A review. *Chemosphere*, 56(11), pp. 1021–1032.

- GOLDSTEIN, S. and RABANI, J., 2007. Mechanism of nitrite formation by nitrate photolysis in aqueous solutions: the role of peroxyxynitrite, nitrogen dioxide, and hydroxyl radical. *Journal of the American Chemical Society*, 129(34), pp. 10597–10601.
- GONÇALVES, C. et al., 2021. Zinc oxide immobilized on alginate beads as catalyst for photocatalytic degradation of textile dyes – an evaluation of matrix effects. *Desalination and Water Treatment*, 210, pp. 250–257.
- GONZÁLEZ-BORRERO, P.P. et al., 2010. Optical band-gap determination of nanostructured WO₃ film. *Applied Physics Letters*, 96(6), p. 061909.
- GÓRECKI, K., 2013. The influence of power supply voltage on exploitive parameters of the selected lamps. *Journal of Microelectronics, Electronic Components and Materials*, 43(3), pp. 193–198.
- GORHAM, P.R. et al., 1964. Isolation and culture of toxic strains of *Anabaena flos-aquae* (Lyngb.) de Bréb. *SIL Proceedings, 1922-2010*, 15(2), pp. 796–804.
- GRANDO, G. et al., 2023. Graphitic carbon nitride meets molecular oxygen: New sustainable photocatalytic ways for the oxidation of organic molecules. *Nano Trends*, 4, p. 100028.
- GREIM, H., 2024. Pendimethalin. In: P. WEXLER, ed. *Encyclopedia of Toxicology*. pp. 293–297.
- GU, W. et al., 2017. Face-to-Face Interfacial Assembly of Ultrathin g-C₃N₄ and Anatase TiO₂ Nanosheets for Enhanced Solar Photocatalytic Activity. *ACS Applied Materials and Interfaces*, 9(34), pp. 28674–28684.

GUERRERO-ESTÉVEZ, S.M. and LÓPEZ-LÓPEZ, E., 2016. Effects of endocrine disruptors on reproduction in viviparous teleosts with intraluminal gestation. *Reviews in Fish Biology and Fisheries*, 26(3), pp. 563–587.

HALLIWELL, J., 2014. *The LED evolution: Colourful story of the light-emitting diode*. [online]. The Grocer. Available from: <https://www.thegrocer.co.uk/store-design/the-led-evolution-colourful-story-of-the-light-emitting-diode/374188.article> [Accessed 29 May 2024].

HAN, W., TIAN, Y. and SHEN, X., 2018. Human exposure to neonicotinoid insecticides and the evaluation of their potential toxicity: An overview. *Chemosphere*, 192, pp. 59–65.

HANDFORD, C.E., ELLIOTT, C.T. and CAMPBELL, K., 2015. A review of the global pesticide legislation and the scale of challenge in reaching the global harmonization of food safety standards. *Integrated Environmental Assessment and Management*, 11(4), pp. 525–536.

HANSON, M.J. and STEFAN, H.G., 1984. Side effects of 58 years of copper sulfate treatment of the Fairmont Lakes, Minnesota. *JAWRA Journal of the American Water Resources Association*, 20(6), pp. 889–900.

HAO, R. et al., 2017. *In situ* hydrothermal synthesis of g-C₃N₄/TiO₂ heterojunction photocatalysts with high specific surface area for Rhodamine B degradation. *Applied Surface Science*, 411, pp. 400–410.

HARKE, M.J. et al., 2016. A review of the global ecology, genomics, and biogeography of the toxic cyanobacterium, *Microcystis* spp. *Harmful Algae*, 54, pp. 4–20.

HASSAAN, M.A. et al., 2023. Principles of Photocatalysts and Their Different Applications: A Review. *Topics in Current Chemistry*, 381(6), p. 31.

HE, X. et al., 2015. Destruction of microcystins (cyanotoxins) by UV-254nm-based direct photolysis and advanced oxidation processes (AOPs): Influence of variable amino acids on the degradation kinetics and reaction mechanisms. *Water Research*, 74, pp. 227–238.

HEERING, W., 2004a. UV-sources - Basics, Properties and Applications. *International Ultraviolet Association*, 6(4), pp. 7–13.

HEERING, W., 2004b. UV-sources - Basics, Properties and Applications. *International Ultraviolet Association*, 6(4), pp. 7–13.

HERCA WG, 2014. *Information paper on lamps containing small amount of radioactive substances*. Lithuania. Available from: https://www.herca.org/wp-content/uploads/uploaditems/documents/Information%20paper%20on%20lamps%20containing%20small%20amount%20of%20radioactive%20substances_%20June%202014.pdf [Accessed 6 March 2024].

HERESZTYN, T. and NICHOLSON, B.C., 2001. Determination of cyanobacterial hepatotoxins directly in water using a protein phosphatase inhibition assay. *Water Research*, 35(13), pp. 3049–3056.

HERRERO-HERNÁNDEZ, E. et al., 2017. Seasonal distribution of herbicide and insecticide residues in the water resources of the vineyard region of La Rioja (Spain). *Science of the Total Environment*, 609, pp. 161–171.

HERRMANN, J.-M., 1999. Heterogeneous photocatalysis: fundamentals and applications to the removal of various types of aqueous pollutants. *Catalysis Today*, 53, pp. 115–129.

HODGES, G. et al., 2019. A comparison of log K_{ow} (n-octanol–water partition coefficient) values for non-ionic, anionic, cationic and amphoteric surfactants determined using predictions and experimental methods. *Environmental Sciences Europe*, 31, p. 1.

HODGSON, E., 2012. Toxins and Venoms. In: *Progress in Molecular Biology and Translational Science*. Cambridge: Academic Press. pp. 373–415.

VAN DEN HOEK, C., MANN D.G. and JAHNS, H.M., 1997. *Algae. An Introduction to Phycology*. Cambridge: Cambridge University Press.

HONG, J.F. et al., 2021. In silico assessment of human health risks caused by cyanotoxins from cyanobacteria. *Biocell*, 45(1), pp. 65–77.

HORAK, I., HORN, S. and PIETERS, R., 2021. Agrochemicals in freshwater systems and their potential as endocrine disrupting chemicals: A South African context. *Environmental Pollution*, 268(A), p. 115718.

HU, X. et al., 2017. Mechanisms underlying degradation pathways of microcystin-LR with doped TiO₂ photocatalysis. *Chemical Engineering Journal*, 330, pp. 355–371.

HUH, J.H. and AHN, J.W., 2017. A perspective of chemical treatment for cyanobacteria control toward sustainable freshwater development. *Environmental Engineering Research*, 22(1), pp. 1–11.

HUI, J. et al., 2021. Graphitic-C₃N₄ coated floating glass beads for photocatalytic destruction of synthetic and natural organic compounds in

water under UV light. *Journal of Photochemistry and Photobiology A: Chemistry*, 405, p. 112935.

HUSSEIN, B.H. et al., 2022. Effect of copper on physical properties of CdO thin films and n-CdO: Cu/p-Si heterojunction. *Journal of Ovonic Research*, 18(1), pp. 37–42.

HUSSIEN, M.S.A. and YAHIA, I.S., 2021. Hybrid multifunctional core/shell g-C₃N₄ @TiO₂ heterojunction nano-catalytic for photodegradation of organic dye and pharmaceutical compounds. *Environmental Science and Pollution Research*, 28, pp. 29665–29680.

IGARASHI, N., ONOUE, S. and TSUDA, Y., 2007. Photoreactivity of amino acids: Tryptophan-induced photochemical events via reactive oxygen species generation. *Analytical Sciences*, 23(8), pp. 943–948.

IGHALO, J.O., ADENIYI, A.G. and ADELODUN, A.A., 2020. Recent advances on the adsorption of herbicides and pesticides from polluted waters: Performance evaluation via physical attributes. *Journal of Industrial and Engineering Chemistry*, 93, pp. 117–137.

INAGAKI, M. et al., 2019. Graphitic carbon nitrides (g-C₃N₄) with comparative discussion to carbon materials. *Carbon*, 141, pp. 580–607.

ISLAM, F. et al., 2018. Potential impact of the herbicide 2,4-dichlorophenoxyacetic acid on human and ecosystems. *Environment International*, 111, pp. 332–351.

ISLAM, M.A., BEARDALL, J. and COOK, P., 2019. Intra-strain Variability in the Effects of Temperature on UV-B Sensitivity of Cyanobacteria. *Photochemistry and Photobiology*, 95(1), pp. 306–314.

- ISLAS, G. et al., 2014. Determination of glyphosate and aminomethylphosphonic acid in soils by HPLC with pre-column derivatization using 1,2-naphthoquinone-4-sulfonate. *Journal of Liquid Chromatography and Related Technologies*, 37(9), pp. 1298–1309.
- ISMAEL, M., 2020. A review on graphitic carbon nitride (g-C₃N₄) based nanocomposites: Synthesis, categories, and their application in photocatalysis. *Journal of Alloys and Compounds*, 846, p. 156446.
- JACINAVICIUS, F.R. et al., 2021. Effect of ultraviolet radiation on the metabolomic profiles of potentially toxic cyanobacteria. *FEMS Microbiology Ecology*, 97(1), pp. 1–16.
- JACOBS, L.C.V. et al., 2013. Photocatalytic degradation of microcystin-LR in aqueous solutions. *Chemosphere*, 90(4), pp. 1552–1557.
- JACOBY, J.M. et al., 2000. Environmental factors associated with a toxic bloom of *Microcystis aeruginosa*. *Canadian Journal of Fisheries and Aquatic Sciences*, 57(1), pp. 231–240.
- JADHAV, A. et al., 2023. Effect of calcination temperature on synthesis of g-C₃N₄ and its application in photocatalytic degradation of methylene blue dye. *International Research Journal of Science and Engineering*, (A12), pp. 65–73.
- JALILI, F. et al., 2022. Evidence-based framework to manage cyanobacteria and cyanotoxins in water and sludge from drinking water treatment plants. *Toxins*, 14(6), p. 410.
- JANSE, I. et al., 2004. Toxic and nontoxic *Microcystis* colonies in natural populations can be differentiated on the basis of rRNA gene internal

transcribed spacer diversity. *Applied and Environmental Microbiology*, 70(7), pp. 3979–3987.

JOCHIMSEN, E.M. et al., 1998. Liver failure and death after exposure to microcystins. *The New England Journal of Medicine*, 338(13), pp. 873–878.

DE JULIO, M. et al., 2010. A methodology for optimising the removal of cyanobacteria cells from a brazilian eutrophic water. *Brazilian Journal of Chemical Engineering*, 27(1), pp. 113–126.

JUNAID, M. et al., 2023. Band gap analysis of zinc oxide for potential bio glucose sensor. *Results in Chemistry*, 5, p. 100961.

KAEBERNICK, M. and NEILAN, B.A., 2006. Ecological and molecular investigations of cyanotoxin production. *FEMS Microbiology Ecology*, 35(1), pp. 1–9.

KAMINSKI, A. et al., 2021. Anatoxin-a degradation by using titanium dioxide. *Science of the Total Environment*, 756, p. 143590.

KANAN, S. et al., 2020. Recent advances on TiO₂-based photocatalysts toward the degradation of pesticides and major organic pollutants from water bodies. *Catalysis Reviews - Science and Engineering*, 62(1), pp. 1–65.

KANE, A. et al., 2022. g-C₃N₄/TiO₂ S-scheme heterojunction photocatalyst with enhanced photocatalytic Carbamazepine degradation and mineralization. *Journal of Photochemistry and Photobiology A: Chemistry*, 430, p. 113971.

KARMAKAR, R., SINGH, S.B. and KULSHRESTHA, G., 2009. Kinetics and mechanism of the hydrolysis of thiamethoxam. *Journal of Environmental*

Science and Health - Part B Pesticides, Food Contaminants, and Agricultural Wastes, 44(5), pp. 435–441.

KATAGI, T., 2002. Abiotic hydrolysis of pesticides in the aquatic environment. *Reviews of Environmental Contamination and Toxicology*, (175), pp. 79–261.

KATSUMATA, H. et al., 2009. Photocatalytic degradation of diuron in aqueous solution by platinized TiO₂. *Journal of Hazardous Materials*, 171(1–3), pp. 1081–1087.

KHATRI, N. and TYAGI, S., 2015. Influences of natural and anthropogenic factors on surface and groundwater quality in rural and urban areas. *Frontiers in Life Science*, 8(1), pp. 23–39.

KIM, H. et al., 2022. Insight into the role of charge carrier mediation zone for singlet oxygen production over rod-shape graphitic carbon nitride: Batch and continuous-flow reactor. *Journal of Hazardous Materials*, 424, p. 127652.

KOBKEATTTHAWIN, T. et al., 2022. Photocatalytic activity of TiO₂/g-C₃N₄ nanocomposites for removal of monochlorophenols from water. *Nanomaterials*, 12(16), p. 2852.

KOMÁREK, J. et al., 2002. Review of the European *Microcystis*-morphospecies (Cyanoprokaryotes) from nature Two common *Microcystis* species (*Chroococcales*, Cyanobacteria) from tropical America, including *M. panniformis* sp. *Cryptogamie, Algol.*, 23(2), pp. 159–177.

KUHL, A. and LORENZEN, H., 1964. Handling and Culturing of Chlorella. In: *Methods in Cell Biology*. pp. 159–187.

- KUMAR, A., TYAGI, M.B. and JHA, P.N., 2004. Evidences showing ultraviolet-B radiation-induced damage of DNA in cyanobacteria and its detection by PCR assay. *Biochemical and Biophysical Research Communications*, 318(4), pp. 1025–1030.
- KUMAR, R. et al., 2022. Photocatalytic activity of graphene oxide-TiO₂ nanocomposite on dichlorvos and malathion and assessment of toxicity changes due to photodegradation. *Chemosphere*, 308, p. 136402.
- KURWADKAR, S. et al., 2016. Modeling photodegradation kinetics of three systemic neonicotinoids—dinotefuran, imidacloprid, and thiamethoxam—in aqueous and soil environment. *Environmental Toxicology and Chemistry*, 35(7), pp. 1718–1726.
- LANDSBERG, J.H., 2002. The Effects of Harmful Algal Blooms on Aquatic Organisms. *Reviews in Fisheries Science*, 10(2), pp. 113–390.
- LAWTON, L.A. and EDWARDS, C., 2001. Purification of microcystins. *Journal of Chromatography A*, 912(2), pp. 191–209.
- LEONTIE, L. et al., 2002. Structural and optical characteristics of bismuth oxide thin films. *Surface Science*, 507–510, pp. 480–485.
- LI, M. et al., 2024. How does the neurotoxin β-N-methylamino-L-alanine exist in biological matrices and cause toxicity? *Science of the Total Environment*, 922.
- LI, Y. et al., 2017. Hybridization of rutile TiO₂ (rTiO₂) with g-C₃N₄ quantum dots (CN QDs): An efficient visible-light-driven Z-scheme hybridized photocatalyst. *Applied Catalysis B: Environmental*, 202, pp. 611–619.

- LI, Y. et al., 2020. Recent advances in g-C₃N₄-based heterojunction photocatalysts. *Journal of Materials Science and Technology*, 56, pp. 1–17.
- LIAO, X. et al., 2009. Photocatalytic inhibition of cyanobacterial growth using silver-doped TiO₂ under UV-C light. *Journal Wuhan University of Technology, Materials Science Edition*, 24(3), pp. 402–408.
- LICHT, K. et al., 2023. Removal of the neonicotinoid insecticide acetamiprid from wastewater using heterogeneous photocatalysis. *Environmental Technology*, 44(8), pp. 1125–1134.
- LIN, J.Y., 2012. Optogenetic excitation of neurons with channelrhodopsins: Light instrumentation, expression systems, and channelrhodopsin variants. In: T. KNÖPFEL and E.S. BOYDEN, eds. *Progress in Brain Research*. pp. 29–47.
- LIN, L., YANG, H. and XU, X., 2022. Effects of water pollution on human health and disease heterogeneity: A review. *Frontiers in Environmental Science*, 10, p. 880246.
- LIU, I. et al., 2005. The photocatalytic destruction of the cyanotoxin, nodularin using TiO₂. *Applied Catalysis B: Environmental*, 60(3–4), pp. 245–252.
- LIU, J., 2010. Phenylurea Herbicides. In: *Hayes' Handbook of Pesticide Toxicology*. Elsevier. pp. 1725–1731.
- LIU, L. et al., 2015a. Organic Semiconductor g-C₃N₄ Modified TiO₂ Nanotube Arrays for Enhanced Photoelectrochemical Performance in Wastewater Treatment. *Energy Technology*, 3(9), pp. 982–988.

- LIU, L. et al., 2023. ZnO-ZnS heterostructure as a potent photocatalyst in the preparation of some substituted chromenes and remarkable antigastrointestinal cancer activity. *ACS Omega*, 8(46), pp. 44276–44286.
- LIU, M., FENG TIAN, X. and LONG CHANG, Y., 2020. Preparation and kinetics of g-C₃N₄/TiO₂ nanomaterials for the photodegradation of pyridine under solar-light irradiation. *ChemistrySelect*, 5(21), pp. 6389–6402.
- LIU, S. et al., 2016. Degradation of microcystins from *Microcystis aeruginosa* by 185-nm UV irradiation. *Water, Air, and Soil Pollution*, 227(4), p. 129.
- LIU, X. et al., 2010. Degradation and detoxification of microcystin-LR in drinking water by sequential use of UV and ozone. *Journal of Environmental Sciences*, 22(12), pp. 1897–1902.
- LIU, X. et al., 2015b. Photodegradation of imidacloprid in aqueous solution by the metal-free catalyst graphitic carbon nitride using an energy-saving lamp. *Journal of Agricultural and Food Chemistry*, 63(19), pp. 4754–4760.
- LIU, X. et al., 2020a. A facile strategy for photocatalytic degradation of seven neonicotinoids over sulfur and oxygen co-doped carbon nitride. *Chemosphere*, 253, p. 126672.
- LIU, Y. et al., 2020b. Thermal-sprayed photocatalytic coatings for biocidal applications: A review. *Journal of Thermal Spray Technology*, 30(3), pp. 1–24.
- LOOMIS, D. et al., 2015. Carcinogenicity of lindane, DDT, and 2,4-dichlorophenoxyacetic acid. *The Lancet Oncology*, 16(8), pp. 891–892.

- LOPES, J.Q. and SALGADO, B.C.B., 2021. Photocatalytic performance of titanium and zinc oxides in diuron degradation. *Environmental Challenges*, 4, p. 100186.
- LU, L. et al., 2018. Effects of calcining temperature on formation of hierarchical TiO₂/g-C₃N₄ hybrids as an effective Z-scheme heterojunction photocatalyst. *Applied Surface Science*, 441, pp. 1012–1023.
- LU, R., LIU, P. and CHEN, X., 2015. Study the toxicity to *Microcystis aeruginosa* induced by TiO₂ nanoparticles photocatalysis under UV light. *Bulletin of Environmental Contamination and Toxicology*, 94(4), pp. 484–489.
- LUO, Y. et al., 2023. g-C₃N₄-based photocatalysts for organic pollutant removal: a critical review. *Carbon Research*, 2(1), p. 14.
- LÜRLING, M. and FAASSEN, E.J., 2013. Dog poisonings associated with a *Microcystis aeruginosa* bloom in the Netherlands. *Toxins*, 5(3), pp. 556–567.
- MA, J. et al., 2016. Fabrication of g-C₃N₄/TiO₂ hierarchical spheres with reactive {001} TiO₂ crystal facets and its visible-light photocatalytic activity. *International Journal of Hydrogen Energy*, 41(6), pp. 3877–3887.
- MACHADO, J. et al., 2017. Effects of microcystin-LR and cylindrospermopsin on plant-soil systems: A review of their relevance for agricultural plant quality and public health. *Environmental Research*, 153, pp. 191–204.
- MACK, J. and BOLTON, J.R., 1999. Photochemistry of nitrite and nitrate in aqueous solution: a review. *Journal of Photochemistry and Photobiology A: Chemistry*, 128, pp. 1–13.

MACKINTOSH, C. et al., 1990. Cyanobacterial microcystin-LR is a potent and specific inhibitor of protein phosphatases 1 and 2A from both mammals and higher plants, 264(2), pp. 187–192.

MADKOUR, M. et al., 2016. Nano-heterostructured photo-stable $\text{Cd}_x\text{Zn}_{1-x}\text{S}$ heterojunction as a non-photocorrosive visible light active photocatalyst. *Optical Materials Express*, 6(9), p. 2857.

MAK, K.F. et al., 2010. Atomically thin MoS_2 : A new direct-gap semiconductor. *Physical Review Letters*, 105(13), p. 136805.

MAMBA, G. and MISHRA, A.K., 2016a. Graphitic carbon nitride ($\text{g-C}_3\text{N}_4$) nanocomposites: A new and exciting generation of visible light driven photocatalysts for environmental pollution remediation. *Applied Catalysis B: Environmental*, 198, pp. 347–377.

MAMBA, G. and MISHRA, A., 2016b. Advances in magnetically separable photocatalysts: Smart, Recyclable materials for water pollution mitigation. *Catalysts*, 6(6), p. 79.

MARCELINO, R.B.P. and AMORIM, C.C., 2019. Towards visible-light photocatalysis for environmental applications: band-gap engineering versus photons absorption—a review. *Environmental Science and Pollution Research*, 26(5), pp. 4155–4170.

MARSHALL, C., 2021. *Legal threat over bee-harming pesticide use*. [online]. BBC. Available from: <https://www.bbc.co.uk/news/science-environment-55766035> [Accessed 18 March 2024].

- MARTIN, D.J. et al., 2014. Highly efficient photocatalytic H₂ evolution from water using visible light and structure-controlled graphitic carbon nitride. *Angewandte Chemie*, 126(35), pp. 9394–9399.
- MCGRATH, M., 2018. *EU member states support near-total neonicotinoids ban*. [online]. BBC. Available from: <https://www.bbc.co.uk/news/science-environment-43910536> [Accessed 18 March 2024].
- MEEPHON, S. et al., 2019. Heterogeneous photocatalytic degradation of diuron on zinc oxide: Influence of surface-dependent adsorption on kinetics, degradation pathway, and toxicity of intermediates. *Journal of Environmental Sciences (China)*, 84, pp. 97–111.
- MEFFE, R. and DE BUSTAMANTE, I., 2014. Emerging organic contaminants in surface water and groundwater: A first overview of the situation in Italy. *Science of the Total Environment*, 481(1), pp. 280–295.
- MEFTAUL, I.M. et al., 2020. Controversies over human health and ecological impacts of glyphosate: Is it to be banned in modern agriculture? *Environmental Pollution*, 263, p. 114372.
- MENEZES, I. et al., 2021a. Comparison of UV-A photolytic and UV/TiO₂ photocatalytic effects on *Microcystis aeruginosa* PCC7813 and four microcystin analogues: A pilot scale study. *Journal of Environmental Management*, 298, p. 113519.
- MENEZES, I. et al., 2021b. Oxidative stress in the cyanobacterium *Microcystis aeruginosa* PCC 7813: Comparison of different analytical cell stress detection assays. *Chemosphere*, 269, p. 128766.

MEREL, S. et al., 2013. State of knowledge and concerns on cyanobacterial blooms and cyanotoxins. *Environment International*, 59, pp. 303–327.

MICELI, M. et al., 2021. Recovery/reuse of heterogeneous supported spent catalysts. *Catalysts*, 11(5), p. 591.

MILLS, A. and LE HUNTE, S., 1997. An overview of semiconductor photocatalysis. *Journal of Photochemistry and Photobiology A: Chemistry*, 108, pp. 1–35.

MIR, N.A. et al., 2013. Photocatalytic degradation of a widely used insecticide Thiamethoxam in aqueous suspension of TiO₂: Adsorption, kinetics, product analysis and toxicity assessment. *Science of the Total Environment*, 458–460, pp. 388–398.

MOHAN, R. et al., 2023. Occurrence and toxicity of cyanobacterium *Microcystis aeruginosa* in freshwater ecosystems of the Indian subcontinent: a review. *Energy, Ecology and Environment*, 8(4), pp. 332–343.

MOHINI, R. and LAKSHMINARASIMHAN, N., 2016. Coupled semiconductor nanocomposite g-C₃N₄/TiO₂ with enhanced visible light photocatalytic activity. *Materials Research Bulletin*, 76, pp. 370–375.

MORRISSEY, C.A. et al., 2015. Neonicotinoid contamination of global surface waters and associated risk to aquatic invertebrates: A review. *Environment International*, 74, pp. 291–303.

MUNAWAROH, H.S.H. et al., 2018. Characterization of phycocyanin from *Spirulina fusiformis* and its thermal stability. *Journal of Physics: Conference Series*, 1013(1), p. 012205.

MUÑOZ, J.P., BLEAK, T.C. and CALAF, G.M., 2020. Glyphosate and the key characteristics of an endocrine disruptor: A review. *Chemosphere*, 270, p. 128619.

MUNOZ, M. et al., 2021. Overview of toxic cyanobacteria and cyanotoxins in Ibero-American freshwaters: Challenges for risk management and opportunities for removal by advanced technologies. *Science of the Total Environment*, 761, p. 143197.

MUR, L., SKULBERG, O. and UTKILEN, H., 1999. Cyanobacteria in the environment. In: I. CHROUS and J. BARTRAM, eds. *Toxic Cyanobacteria in Water: A Guide to Their Public Health Consequences, Monitoring and Management*. New York: E & FN Spon: pp. 113–132.

MURCHIE, E.H. and LAWSON, T., 2013. Chlorophyll fluorescence analysis: A guide to good practice and understanding some new applications. *Journal of Experimental Botany*, 64(13), pp. 3983–3998.

MURRAY, K.E., THOMAS, S.M. and BODOUR, A.A., 2010. Prioritizing research for trace pollutants and emerging contaminants in the freshwater environment. *Environmental Pollution*, 158(12), pp. 3462–3471.

NAGCU, C. et al., 1997. Spray pyrolysis deposition of CuS thin films. *Materials Letters*, 32, pp. 73–77.

NASIRI, M., AHMADZADEH, H. and AMIRI, A., 2020. Sample preparation and extraction methods for pesticides in aquatic environments: A review. *TrAC - Trends in Analytical Chemistry*, 123, p. 115772.

NATIONAL CENTER FOR BIOTECHNOLOGY INFORMATION, 2024. *PubChem Compound Summary for CID 25429, Carbendazim*. [online]. Available from:

<https://pubchem.ncbi.nlm.nih.gov/compound/Carbendazim> [Accessed 15 March 2024].

NEELAM, A. and CHAND RAI, L., 2003. Differential responses of three cyanobacteria to UV-B and Cd. *Journal of Microbiology and Biotechnology*, 13(4), pp. 544–551.

NEGISHI, N. et al., 2012. Photocatalytic detoxification of aqueous organophosphorus by TiO₂ immobilized silica gel. *Applied Catalysis B: Environmental*, 128, pp. 105–118.

NICOLAIDIS, S., 1998. Physiology of thirst. In: M.J. ARNAUD, ed. *Hydration Throughout Life*. p. 247.

NIETO-SANDOVAL, J. et al., 2023. Application of g-C₃N₄-PVDF membrane for the photocatalytic degradation of micropollutants in continuous flow mode: Impact of water matrix. *Journal of Environmental Chemical Engineering*, 11(5), p. 110586.

NIU, J. et al., 2020. Application of g-C₃N₄ matrix composites photocatalytic performance from degradation of antibiotics. *ChemistrySelect*, 5(40), pp. 12353–12364.

NOYMA, N.P. et al., 2021. Increasing temperature counteracts the negative effect of UV radiation on growth and photosynthetic efficiency of *Microcystis aeruginosa* and *Raphidiopsis raciborskii*. *Photochemistry and Photobiology*, 97(4), pp. 753–762.

OBINNAA, I.B. and EBERE, E.C., 2019. Water pollution by heavy metal and organic pollutants: Brief review of sources, effects and progress on

remediation with aquatic plants. *Analytical Methods in Environmental Chemistry Journal*, 2(3), pp. 5–38.

ODLING, G. and ROBERTSON, N., 2019. Bridging the gap between laboratory and application in photocatalytic water purification. *Catalysis Science and Technology*, 9(3), pp. 533–545.

OGAWA, T., MISUMI, M. and SONOIKE, K., 2017. Estimation of photosynthesis in cyanobacteria by pulse-amplitude modulation chlorophyll fluorescence: problems and solutions. *Photosynthesis Research*, 133(1–3), pp. 63–73.

OHNO, K. et al., 2008. Effects of chlorine on organophosphorus pesticides adsorbed on activated carbon: Desorption and oxon formation. *Water Research*, 42, pp. 1753–1759.

OHTA, T. et al., 2015. Nodularin, a potent inhibitor of protein phosphatases 1 and 2A, is a new environmental carcinogen in male F344 rat liver. *Cancer Research*, 54(24), pp. 6402–6406.

OLA, O. and MAROTO-VALER, M.M., 2015. Review of material design and reactor engineering on TiO₂ photocatalysis for CO₂ reduction. *Journal of Photochemistry and Photobiology C: Photochemistry Reviews*, 24, pp. 16–42.

OLIVER, R.L. et al., 2012. Physiology, Blooms and Prediction of Planktonic Cyanobacteria. In: B.A. WHITTON, ed. *Ecology of Cyanobacteria II, Their Diversity in Space and Time*. Springer. pp. 155–194.

OLUWOLE, A.O., KHOZA, P. and OLATUNJI, O.S., 2022. Synthesis and characterization of g-C₃N₄ doped with activated carbon (AC) prepared from

grape leaf litters for the photocatalytic degradation of enrofloxacin in aqueous systems. *ChemistrySelect*, 7(45), p. e202203601.

ONG, W.J. et al., 2016. Graphitic carbon nitride (g-C₃N₄)-based photocatalysts for artificial photosynthesis and environmental remediation: Are we a step closer to achieving sustainability? *Chemical Reviews*, 116(12), pp. 7159–7329.

OSRAM OPTO SEMICONDUCTORS, 2009. *Life Cycle Assessment of Illuminants: A Comparison of Light Bulbs, Compact Fluorescent Lamps and LED Lamps*. Available from: http://seeds4green.net/sites/default/files/OSRAM_LED_LCA_Summary_November_2009.pdf [Accessed 12 February 2024].

OTERO, P. and SILVA, M., 2022. The role of toxins: Impact on human health and aquatic environments. In: *The Pharmacological Potential of Cyanobacteria*. Elsevier. pp. 173–199.

OU, H.S. et al., 2014. Integrated principal component analysis of *Microcystis aeruginosa* dissolved organic matter and assessment of UV-C pre-treatment on cyanobacteria-containing water. *Clean - Soil, Air, Water*, 42(4), pp. 442–448.

OU, H. et al., 2011. Mechanistic studies of *Microcystic aeruginosa* inactivation and degradation by UV-C irradiation and chlorination with polysynchronous analyses. *Desalination*, 272(1–3), pp. 107–119.

PAERL, H.W., 1996. Microscale physiological and ecological studies of aquatic cyanobacteria: Macroscale implications. *Microscopy Research and Technique*, 33(1), pp. 47–72.

- PAERL, H.W. and OTTEN, T.G., 2013. Harmful Cyanobacterial Blooms: Causes, Consequences, and Controls. *Microbial Ecology*, 65(4), pp. 995–1010.
- PANDEY, S. et al., 2023. A review on the effect of blue green 11 medium and its constituents on microalgal growth and lipid production. *Journal of Environmental Chemical Engineering*, 11(3), p. 109984.
- PARK, J.A. et al., 2018. Removal of microcystin-LR using UV-assisted advanced oxidation processes and optimization of photo-Fenton-like process for treating Nak-Dong River water, South Korea. *Chemical Engineering Journal*, 348, pp. 125–134.
- PATTANASUPONG, A. et al., 2004. Ability of a microbial consortium to remove pesticide, carbendazim and 2,4-dichlorophenoxyacetic acid. *World Journal of Microbiology and Biotechnology*, 20(5), pp. 517–522.
- PATTISON, P.M., HANSEN, M. and TSAO, J.Y., 2018. LED lighting efficacy: Status and directions. *Comptes Rendus Physique*, 19(3), pp. 134–145.
- PAUL, D.R. et al., 2019. Effect of calcination temperature, pH and catalyst loading on photodegradation efficiency of urea derived graphitic carbon nitride towards methylene blue dye solution. *RSC Advances*, 9(27), pp. 15381–15391.
- PAWAR, R.C. and LEE, C.S., 2015. Basics of Photocatalysis. In: *Heterogeneous Nanocomposite-Photocatalysis for Water Purification*. pp. 1–23.
- PECK, J., ASHBURNER, G. and SCHRATZ, M., 2011. Solid state LED lighting technology for hazardous environments; Lowering total cost of ownership

while improving safety, quality of light and reliability. *2011 European Conference on Electrical and Instrumentation Applications in the Petroleum and Chemical Industry, PCIC EUROPE*, pp. 1–8.

PEDESCOLL, A. et al., 2013. Design configurations affecting flow pattern and solids accumulation in horizontal free water and subsurface flow constructed wetlands. *Water Research*, 47(3), pp. 1448–1458.

PENG, G. et al., 2015. Photodegradation of microcystin-LR catalyzed by metal phthalocyanines immobilized on TiO₂-SiO₂ under visible-light irradiation. *Water Science and Technology*, 72(10), pp. 1824–1831.

PESTANA, C.J. et al., 2015. Photocatalytic degradation of eleven microcystin variants and nodularin by TiO₂ coated glass microspheres. *Journal of Hazardous Materials*, 300, pp. 347–353.

PESTANA, C.J. et al., 2019. The effect of water treatment unit processes on cyanobacterial trichome integrity. *Science of the Total Environment*, 659, pp. 1403–1414.

PESTANA, C.J. et al., 2020. Photocatalytic removal of the cyanobacterium *Microcystis aeruginosa* PCC7813 and four microcystins by TiO₂ coated porous glass beads with UV-LED irradiation. *Science of the Total Environment*, 745, p. 141154.

PESTANA, C.J. et al., 2022. Suppressing cyanobacterial dominance by UV-LED TiO₂-photocatalysis in a drinking water reservoir: A mesocosm study. *Water Research*, 226, p. 119299.

- PESTANA, C.J. et al., 2023. Solar-driven semi-conductor photocatalytic water treatment (TiO_2 , g- C_3N_4 , and TiO_2 +g- C_3N_4) of cyanotoxins: Proof-of-concept study with microcystin-LR. *Chemosphere*, 310, p. 136828.
- PETROSKI, J., 2002. Thermal challenges facing new-generation light-emitting diodes (LEDs) for lighting applications. *Solid State Lighting II*, 4776, p. 215.
- PHAM, T.T.H. et al., 2023. Synthesis of cuprous oxide/silver ($\text{Cu}_2\text{O}/\text{Ag}$) hybrid as surface-enhanced Raman scattering probe for trace determination of methyl orange. *Royal Society Open Science*, 10(5), p. 221623.
- PIETRZAK, D. et al., 2019. Pesticides from the EU First and Second Watch Lists in the Water Environment. *Clean - Soil, Air, Water*, 47(7), p. 1800376.
- PIMENTA, E.M. et al., 2020. Quantification of glyphosate and AMPA by HPLC-ICP-MS/MS and HPLC-DAD: A comparative study. *Journal of the Brazilian Chemical Society*, 31(2), pp. 298–304.
- PINHO, L.X. et al., 2015a. Oxidation of microcystin-LR and cylindrospermopsin by heterogeneous photocatalysis using a tubular photoreactor packed with different TiO_2 coated supports. *Chemical Engineering Journal*, 266, pp. 100–111.
- PINHO, L.X. et al., 2015b. Effect of TiO_2 photocatalysis on the destruction of *Microcystis aeruginosa* cells and degradation of cyanotoxins microcystin-LR and cylindrospermopsin. *Chemical Engineering Journal*, 268, pp. 144–152.
- PINHO, L.X. et al., 2015c. Oxidation of microcystin-LR and cylindrospermopsin by heterogeneous photocatalysis using a tubular

photoreactor packed with different TiO₂ coated supports. *Chemical Engineering Journal*, 266, pp. 100–111.

PINKANJANANAVEE, K. et al., 2021. Potential impacts on treated water quality of recycling dewatered sludge supernatant during harmful cyanobacterial blooms. *Toxins*, 13(2), p. 99.

PÍŠKOVÁ, V. et al., 2015. Photocatalytic degradation of β -blockers by using immobilized titania/silica on glass slides. *Journal of Photochemistry and Photobiology A: Chemistry*, 305, pp. 19–28.

PISUPATI, S., 2022a. *Types of Lighting: High-intensity Discharge*. [online]. Available from: <https://www.e-education.psu.edu/egee102/node/2048> [Accessed 6 March 2024].

PISUPATI, S., 2022b. *Types of Lighting: Fluorescent Bulbs*. [online]. Available from: <https://www.e-education.psu.edu/egee102/node/2047> [Accessed 7 March 2024].

PISUPATI, S., 2022c. *Types of Lighting: LED*. [online]. Available from: <https://www.e-education.psu.edu/egee102/node/2049> [Accessed 7 March 2024].

PRASAD, C. et al., 2020. A latest overview on photocatalytic application of g-C₃N₄ based nanostructured materials for hydrogen production. *International Journal of Hydrogen Energy*, 45(1), pp. 337–379.

PRIOR, M., 2024. *Bee-harming neonicotinoid use 'makes a mockery' of ban*. [online]. BBC. Available from: <https://www.bbc.co.uk/news/science-environment-68471101> [Accessed 18 March 2024].

QAMAR, M. and MUNEER, M., 2005. Comparative photocatalytic study of two selected pesticide derivatives, indole-3-acetic acid and indole-3-butyric acid in aqueous suspensions of titanium dioxide. *Journal of Hazardous Materials*, 120(1–3), pp. 219–227.

QAMAR, M., MUNEER, M. and BAHNEMANN, D., 2006. Heterogeneous photocatalysed degradation of two selected pesticide derivatives, triclopyr and daminozid in aqueous suspensions of titanium dioxide. *Journal of Environmental Management*, 80(2), pp. 99–106.

QIN, H., LI, S. and LI, D., 2015. Differential responses of different phenotypes of *Microcystis* (Cyanophyceae) to UV-B radiation. *Phycologia*, 54(2), pp. 118–129.

QUAN, C. et al., 2015. Research on lumen depreciation related to LED packages by *in-situ* measurement method. In: *Microelectronics Reliability*. Elsevier Ltd. pp. 2269–2275.

RAIZADA, P. et al., 2019. Silver-mediated Bi₂O₃ and graphitic carbon nitride nanocomposite as all solid state z scheme photocatalyst for imidacloprid pesticide abatement from water. *Desalination and Water Treatment*, 171, pp. 344–355.

RANI, L. et al., 2020. An extensive review on the consequences of chemical pesticides on human health and environment. *Journal of Cleaner Production*, 283, p. 124657.

RASTOGI, R.P. et al., 2010. Molecular mechanisms of ultraviolet radiation-induced DNA damage and repair. *Journal of Nucleic Acids*, 2010, p. 592980.

- RASTOGI, R.P., MADAMWAR, D. and INCHAROENSAKDI, A., 2015. Bloom dynamics of cyanobacteria and their toxins: Environmental health impacts and mitigation strategies. *Frontiers in Microbiology*, 6, p. 1254.
- RASTOGI, R.P. et al., 2014. Ultraviolet radiation and cyanobacteria. *Journal of Photochemistry and Photobiology B: Biology*, 141, pp. 154–169.
- REDDY, P.V.L. and KIM, K.H., 2015. A review of photochemical approaches for the treatment of a wide range of pesticides. *Journal of Hazardous Materials*, 285, pp. 325–335.
- RIBEIRO, A.R. et al., 2015. An overview on the advanced oxidation processes applied for the treatment of water pollutants defined in the recently launched Directive 2013/39/EU. *Environment International*, 75, pp. 33–51.
- RINEHART, K.L., NAMIKOSHI, M. and CHOI, B.W., 1994. Structure and biosynthesis of toxins from blue-green algae (cyanobacteria). *Journal of Applied Phycology*, 6(2), pp. 159–176.
- RITCHIE, H., ROSER, M. and ROSADO, P., 2022. *Pesticides*. [online]. Our World in Data. Available from: <https://ourworldindata.org/pesticides> [Accessed 17 April 2024].
- ROBERTSON, P.K.J., LAWTON, L.A. and CORNISH, B.J.P.A., 1999. The Involvement of Phycocyanin Pigment in the Photodecomposition of the Cyanobacterial Toxin, Microcystin-LR. *Journal of Porphyrins and Phthalocyanines*, 3(6–7), pp. 544–551.
- ROBERTSON, P.K.J., ROBERTSON, J.M.C. and BAHNEMANN, D.W., 2012. Removal of microorganisms and their chemical metabolites from water

using semiconductor photocatalysis. *Journal of Hazardous Materials*, 211–212, pp. 161–171.

RODRIGUEZ-GONZALEZ, L. et al., 2019. Oxidation of off flavor compounds in recirculating aquaculture systems using UV-TiO₂ photocatalysis. *Aquaculture*, 502, pp. 32–39.

RODRIGUEZ-NARVAEZ, O.M. et al., 2017. Treatment technologies for emerging contaminants in water: A review. *Chemical Engineering Journal*, 323, pp. 361–380.

RONO, N. et al., 2021. A review of the current status of graphitic carbon nitride. *Critical Reviews in Solid State and Materials Sciences*, 46(3), pp. 189–217.

ROŠKARIČ, M. et al., 2023. Influence of the calcination duration of g-C₃N₄/TiO₂ “veggie-toast-like” photocatalyst on the visible-light triggered photocatalytic oxidation of bisphenol A. *Journal of Alloys and Compounds*, 947, p. 169585.

SAKAI, H. et al., 2007. Effects of low- or medium-pressure ultraviolet lamp irradiation on *Microcystis aeruginosa* and *Anabaena variabilis*. *Water Research*, 41(1), pp. 11–18.

SAKAI, H. et al., 2009. Kinetics of *Microcystis aeruginosa* growth and intracellular microcystins release after UV irradiation. *Environmental Science and Technology*, 43(3), pp. 896–901.

SALEH, I.A., ZOUARI, N. and AL-GHOUTI, M.A., 2020. Removal of pesticides from water and wastewater: Chemical, physical and biological treatment approaches. *Environmental Technology and Innovation*, 19, p. 101026.

SANGWAN, K.S. et al., 2014. Life cycle assessment of incandescent, fluorescent, compact fluorescent and light emitting diode lamps in an Indian scenario. *Procedia CIRP*, 15, pp. 467–472.

SANTOS, A.A. et al., 2021. Effect of hydrogen peroxide on natural phytoplankton and bacterioplankton in a drinking water reservoir: Mesocosm-scale study. *Water Research*, 197, p. 117069.

SCHNEIDER, M. and BLÁHA, L., 2020. Advanced oxidation processes for the removal of cyanobacterial toxins from drinking water. *Environmental Sciences Europe*, 32(1), p. 94.

SCOTTISH GOVERNMENT, 2019. *Pesticide usage in Scotland*. [online]. Available from: <https://www.gov.scot/news/pesticide-usage-in-scotland-5/#:~:text=A%20National%20Statistics%20Publication%20for,2018%20th an%20reported%20in%202016>. [Accessed 18 March 2024].

SCOTTISH WATER, 2024. *Why am I able to taste and smell chlorine in my water supply?* [online]. Water Quality FAQs. Available from: Water Quality FAQs [Accessed 18 June 2024].

SEIFERT, J., 2005. Neonicotinoids. In: *Encyclopedia of Toxicology*. pp. 196–200.

SHAIKH, G.Y. et al., 2022. Structural, optical, photoelectrochemical, and electronic properties of the photocathode CuS and the efficient CuS/CdS heterojunction. *ACS Omega*, 7(34), pp. 30233–30240.

SHANKS, C., 2022. *Aberdeenshire pet owners warned after dogs die in suspected blue-green algae poisonings*. [online]. AberdeenLive. Available

from: <https://www.aberdeenlive.news/news/health/aberdeenshire-pet-owners-warned-after-7465571> [Accessed 31 January 2024].

SHARMA, A. et al., 2019. Worldwide pesticide usage and its impacts on ecosystem. *SN Applied Sciences*, 1(11), p. 1446.

SHARMA, P. et al., 2022. One-step synthesis of highly reactive g-C₃N₄. *Journal of Materials Science: Materials in Electronics*, 33(12), pp. 1–10.

SHETGAONKAR, S.S. et al., 2023. Coupling of photocatalytic and bioremediation processes for enhanced mitigation of xenobiotic pollutants from wastewater. In: *Advances in Nano and Biochemistry: Environmental and Biomedical Applications*. Elsevier. pp. 3–38.

SILVA, D.B. et al., 2022. Performance of TiO₂/UV-LED-based processes for degradation of pharmaceuticals: Effect of matrix composition and process variables. *Nanomaterials*, 12(2), p. 295.

SINGH, J. et al., 2020. Water pollutants: Origin and status. In: D. POOJA et al., eds. *Sensors in Water Pollutants Monitoring: Role of Material Advanced Functional Material*. pp. 5–20.

SINGH, N.K. et al., 2015. The phycobilisomes: An early requisite for efficient photosynthesis in cyanobacteria. *EXCLI Journal*, 14, pp. 268–289.

SINHA, A.K., EGGLETON, M.A. and LOCHMANN, R.T., 2018. An environmentally friendly approach for mitigating cyanobacterial bloom and their toxins in hypereutrophic ponds: Potentiality of a newly developed granular hydrogen peroxide-based compound. *Science of the Total Environment*, 637–638, pp. 524–537.

SIVONEN, K. et al., 1989. Occurrence of the hepatotoxic cyanobacterium *Nodularia spumigena* in the Baltic Sea and structure of the toxin. *Applied and Environmental Microbiology*, 55(8), pp. 1990–1995.

SIVONEN, K., 2009. Cyanobacterial Toxins. In: *Encyclopedia of Microbiology*. Elsevier. pp. 290–307.

ŠNYRYCHOVÁ, I., POSPÍŠIL, P. and NAUŠ, J., 2006. The effect of metal chelators on the production of hydroxyl radicals in thylakoids. *Photosynthesis Research*, 88(3), pp. 323–329.

SONG, J. et al., 2018a. Removal of *Microcystis aeruginosa* and Microcystin-LR using a graphitic-C₃N₄/TiO₂ floating photocatalyst under visible light irradiation. *Chemical Engineering Journal*, 348(April), pp. 380–388.

SONG, J. et al., 2018b. Visible-light-driven *in situ* inactivation of *Microcystis aeruginosa* with the use of floating g-C₃N₄ heterojunction photocatalyst: Performance, mechanisms and implications. *Applied Catalysis B: Environmental*, 226, pp. 83–92.

SONG, W., BARDOWELL, S. and O'SHEA, K.E., 2007. Mechanistic study and the influence of oxygen on the photosensitized transformations of microcystins (Cyanotoxins). *Environmental Science and Technology*, 41(15), pp. 5336–5341.

SOUSA, J.C.G. et al., 2018. A review on environmental monitoring of water organic pollutants identified by EU guidelines. *Journal of Hazardous Materials*, 344, pp. 146–162.

- DE SOUZA, D.F. et al., 2019. Efficiency, quality, and environmental impacts: A comparative study of residential artificial lighting. *Energy Reports*, 5, pp. 409–424.
- DE SOUZA, R.M. et al., 2020. Occurrence, impacts and general aspects of pesticides in surface water: A review. *Process Safety and Environmental Protection*, 135, pp. 22–37.
- SPEIGHT, J.G., 2020. Sources of water pollution. In: *Natural Water Remediation*. Elsevier. pp. 165–198.
- SPOOF, L. and CATHERINE, A., 2017. Cyanobacteria samples: preservation, abundance and biovolume measurements. In: J. MERILUOTO, L. SPOOF and G. A. CODD, eds. *Handbook of Cyanobacterial Monitoring and Cyanotoxin Analysis*. Chichester, UK: John Wiley & Sons. pp. 526–537.
- SRAW, A. et al., 2018. Fixed bed recirculation type photocatalytic reactor with TiO₂ immobilized clay beads for the degradation of pesticide polluted water. *Journal of Environmental Chemical Engineering*, 6(6), pp. 7035–7043.
- STANIER, R.Y. et al., 1971. Purification and properties of unicellular blue-green algae (order *Chroococcales*). *Bacteriological Reviews*, 35(2), pp. 171–205.
- STEHLE, S. et al., 2019. Aquatic pesticide exposure in the U.S. as a result of non-agricultural uses. *Environment International*, 133, p. 105234.
- STIRBET, A. et al., 2018. Chlorophyll *a* Fluorescence in Cyanobacteria: Relation to Photosynthesis. *Cyanobacteria: From Basic Science to Applications*, pp. 79–130.

- STRANDBERG, M. and SCOTT-FORDSMAND, J.J., 2004. Effects of pendimethalin at lower trophic levels - A review. *Ecotoxicology and Environmental Safety*, 57(2), pp. 190–201.
- SUFFET, I.H. (Mel), KHIARI, D. and BRUCHET, A., 1999. The drinking water taste and odor wheel for the millennium: Beyond geosmin and 2-methylisoborneol. *Water Science and Technology*, 40(6), pp. 1–13.
- SUKENIK, A. and KAPLAN, A., 2021. Cyanobacterial harmful algal blooms in aquatic ecosystems: A comprehensive outlook on current and emerging mitigation and control approaches. *Microorganisms*, 9(7), p. 1472.
- SULANIA, I. et al., 2016. Investigations of electrical and optical properties of low energy ion irradiated α -Fe₂O₃ (hematite) thin films. *AIP Conference Proceedings*, 1731.
- SUN, L. et al., 2017. Determination of glyphosate in soil/sludge by high performance liquid chromatography. *Journal of Chromatography A*, 1502, pp. 8–13.
- SUURNÄKKI, S. et al., 2015. Identification of geosmin and 2-methylisoborneol in cyanobacteria and molecular detection methods for the producers of these compounds. *Water Research*, 68, pp. 56–66.
- TAKE THREE LIGHTING, 2024. *LED Chip Styles: What's Best for Your Application?* [online]. Available from: [https://www.takethreelighting.com/led-technology-chip-comparison.html#:~:text=Surface%20Mounted%20Diode%20\(SMD\)%20LED,less%20energy%20than%20DIP%20LEDs](https://www.takethreelighting.com/led-technology-chip-comparison.html#:~:text=Surface%20Mounted%20Diode%20(SMD)%20LED,less%20energy%20than%20DIP%20LEDs). [Accessed 29 May 2024].

- TAMPIERI, F. et al., 2019. Kinetics and Products of Air Plasma Induced Oxidation in Water of Imidacloprid and Thiamethoxam Treated Individually and in Mixture. *Plasma Chemistry and Plasma Processing*, 39(3), pp. 545–559.
- TAN, Y. et al., 2023. Supercritical carbon dioxide-assisted $\text{TiO}_2/\text{g-C}_3\text{N}_4$ heterostructures tuning for efficient interfacial charge transfer and formaldehyde photo-degradation. *Journal of Environmental Chemical Engineering*, 11(5), p. 110992.
- TANG, M. et al., 2020. Facile synthesis of dual Z-scheme $\text{g-C}_3\text{N}_4/\text{Ag}_3\text{PO}_4/\text{AgI}$ composite photocatalysts with enhanced performance for the degradation of a typical neonicotinoid pesticide. *Applied Catalysis B: Environmental*, 268, p. 118395.
- TAO, Y. et al., 2013. Mechanisms of photosynthetic inactivation on growth suppression of *Microcystis aeruginosa* under UV-C stress. *Chemosphere*, 93(4), pp. 637–644.
- TARIGHATI SARESHKEH, A. et al., 2023. Preparation of high-crystalline and non-metal modified $\text{g-C}_3\text{N}_4$ for improving ultrasound-accelerated white-LED-light-driven photocatalytic performances. *Scientific Reports*, 13(1), p. 15079.
- THAKUR, P.R. et al., 2023. Fabrication of a Z-scheme $\text{Zn}_3\text{V}_2\text{O}_8/\text{g-C}_3\text{N}_4$ nano-heterojunction with high interfacial charge transfer for superior photocatalytic removal of diazinon pesticide under visible light. *Applied Nanoscience*, 13(6), pp. 3643–3658.

THIOUR-MAUPRIVEZ, C. et al., 2019. Effects of herbicide on non-target microorganisms: Towards a new class of biomarkers? *Science of the Total Environment*, 684, pp. 314–325.

THOMPSON, D.A. et al., 2020. A critical review on the potential impacts of neonicotinoid insecticide use: Current knowledge of environmental fate, toxicity, and implications for human health. *Environmental Science: Processes and Impacts*, 22(6), pp. 1315–1346.

TOKODE, O., 2014. *Photocatalytic destruction of volatile organic compounds from the oil and gas industry*. Robert Gordon University. Available from: <http://openair.rgu.ac.uk> [Accessed 21 March 2024].

TOMA, F.L. et al., 2014. Parameters influencing the photocatalytic activity of suspension-sprayed TiO₂ coatings. *Journal of Thermal Spray Technology*, 23(7), pp. 1037–1053.

TONGAY, S. et al., 2012. Thermally driven crossover from indirect toward direct bandgap in 2D Semiconductors: MoSe₂ versus MoS₂. *Nano Letters*, 12(11), pp. 5576–5580.

TOPPR, 2024. *Chemical kinetics. Pseudo First Order Reaction*. [online]. Available from: <https://www.toppr.com/guides/chemistry/chemical-kinetics/pseudo-first-order-reaction/> [Accessed 8 March 2024].

TOZE, S., 1999. PCR and the detection of microbial pathogens in water and wastewater. *Water Research*, 33(17), pp. 3545–3556.

TSAI, K.P., 2015. Effects of two copper compounds on *Microcystis aeruginosa* cell density, membrane integrity, and microcystin release. *Ecotoxicology and Environmental Safety*, 120, pp. 428–435.

TSUJI, K. et al., 1995. Stability of microcystins from cyanobacteria-II. Effect of UV light on decomposition and isomerization. *Toxicon*, 33(12), pp. 1619–1631.

TUDI, M. et al., 2021. Agriculture development, pesticide application and its impact on the environment. *International Journal of Environmental Research and Public Health*, 18(3), pp. 1–24.

TUFAIL, A. et al., 2021. A critical review of advanced oxidation processes for emerging trace organic contaminant degradation: Mechanisms, factors, degradation products, and effluent toxicity. *Journal of Water Process Engineering*, 40, p. 101778.

TURNER, A.D. et al., 2018. Development and single-laboratory validation of a UHPLC-MS/MS method for quantitation of microcystins and nodularin in natural water, cyanobacteria, shellfish and algal supplement tablet powders. *Journal of Chromatography B: Analytical Technologies in the Biomedical and Life Sciences*, 1074–1075, pp. 111–123.

TURNER, P.C. et al., 1990. Pneumonia associated with contact with cyanobacteria. *Br Med J*, 300, pp. 1440–1441.

UNITED NATIONS, 2015. *Sustainable Development Goals*. [online]. The 17 Goals. Available from: <https://sdgs.un.org/goals> [Accessed 7 June 2024].

VARSHNEY, P. et al., 2015. Extremophilic micro-algae and their potential contribution in biotechnology. *Bioresource Technology*, 184, pp. 363–372.

VELA, N. et al., 2015. Photocatalytic mitigation of triazinone herbicide residues using titanium dioxide in slurry photoreactor. *Catalysis Today*, 252, pp. 70–77.

- VELA, N. et al., 2018. Photocatalytic oxidation of six pesticides listed as endocrine disruptor chemicals from wastewater using two different TiO₂ samples at pilot plant scale under sunlight irradiation. *Journal of Photochemistry and Photobiology A: Chemistry*, 353, pp. 271–278.
- VEMURI, R.S., ENGELHARD, M.H. and RAMANA, C. V., 2012. Correlation between surface chemistry, density, and band gap in nanocrystalline WO₃ thin films. *ACS Applied Materials and Interfaces*, 4(3), pp. 1371–1377.
- VERMA, A., PRAKASH, N.T. and TOOR, A.P., 2014. Photocatalytic degradation of herbicide isoproturon in TiO₂ aqueous suspensions: Study of reaction intermediates and degradation pathways. *Environmental Progress and Sustainable Energy*, 33(2), pp. 402–409.
- VICENTE, R. et al., 2014. Comparison of different TiO₂ samples as photocatalyst for the degradation of a mixture of four commercial pesticides. *Journal of Chemical Technology and Biotechnology*, 89(8), pp. 1259–1264.
- VILELA, W.F.D. et al., 2012. Degradation of [D-Leu]-Microcystin-LR by solar heterogeneous photocatalysis (TiO₂). *Solar Energy*, 86(9), pp. 2746–2752.
- VINGE, S.L. et al., 2020. Nitrate with benefits: Optimizing radical production during UV water treatment. *Environmental Science: Water Research and Technology*, 6(4), pp. 1163–1175.
- VOUDOUKIS, N. and OIKONOMIDIS, S., 2017. Inverse square law for light and radiation: A unifying educational approach. *European Journal of Engineering Research and Science*, 2(11), p. 23.

WANG, J. et al., 2018a. Robust photocatalytic hydrogen evolution over amorphous ruthenium phosphide quantum dots modified g-C₃N₄ nanosheet. *Applied Catalysis B: Environmental*, 239, pp. 578–585.

WANG, K. et al., 2022. Superhydrophobic and photocatalytic synergistic Self-Cleaning ZnS coating. *Applied Surface Science*, 595, p. 153565.

WANG, L. et al., 2019a. One-step, high-yield synthesis of g-C₃N₄ nanosheets for enhanced visible light photocatalytic activity. *RSC Advances*, 9(67), pp. 39304–39314.

WANG, P. et al., 2018b. A weak-light-responsive TiO₂/g-C₃N₄ composite film: photocatalytic activity under low-intensity light irradiation. *Environmental Science and Pollution Research*, 25(20), pp. 20206–20216.

WANG, S. et al., 2020. Photodegradation of microcystin-LR by pyridyl iron porphyrin immobilized on NaY zeolite. *Water Science and Technology*, 81(1), pp. 121–130.

WANG, W. et al., 2017. Compact and uniform TiO₂@g-C₃N₄ core-shell quantum heterojunction for photocatalytic degradation of tetracycline antibiotics. *Applied Catalysis B: Environmental*, 217, pp. 57–64.

WANG, W. et al., 2019b. TiO₂@g-C₃N₄ heterojunction with directional charge migration behavior for photodegradation of tetracycline antibiotics. *Materials Letters*, 236, pp. 622–624.

WANG, Y. et al., 2021a. An efficient floating adsorption-photocatalyst to decarboxylate D-Glu and D-MeAsp of Microcystin-LR via holes direct oxidation. *Chemical Engineering Journal*, 413, p. 127543.

WANG, Z. et al., 2021b. Cyanobacterial dominance and succession: Factors, mechanisms, predictions, and managements. *Journal of Environmental Management*, 297, p. 113281.

WEAVER, A.J. et al., 2001. The UVic earth system climate model: Model description, climatology, and applications to past, present and future climates. *Atmosphere - Ocean*, 39(4), pp. 361–428.

WEIR, A. et al., 2012. Titanium dioxide nanoparticles in food and personal care products. *Environmental Science and Technology*, 46(4), pp. 2242–2250.

WELKER, M. and VON DÖHREN, H., 2006. Cyanobacterial peptides — Nature’s own combinatorial biosynthesis. *FEMS Microbiology Reviews*, 30(4), pp. 530–563.

WELKER, M. and STEINBERG, C., 1999. Indirect photolysis of cyanotoxins: One possible mechanism for their low persistence. *Water Research*, 33(5), pp. 1159–1164.

WESSEX RESINS & ADHESIVES, 2024. *Our applications*. [online]. Wessex. Available from: <https://wessexresins.co.uk/about/our-applications/> [Accessed 30 May 2024].

WIEGAND, C. and PFLUGMACHER, S., 2005. Ecotoxicological effects of selected cyanobacterial secondary metabolites a short review. *Toxicology and Applied Pharmacology*, 203(3), pp. 201–218.

WIERZYŃSKA, E. et al., 2023. Comparative studies of g-C₃N₄ and C₃N₃S₃ organic semiconductors—synthesis, properties, and application in the catalytic oxygen reduction. *Molecules*, 28(6), p. 2469.

- WIESE, M. et al., 2010. Neurotoxic alkaloids: Saxitoxin and its analogues. *Marine Drugs*, 8(7), pp. 2185–2211.
- WIMMER, K.M., STRANGMAN, W.K. and WRIGHT, J.L.C., 2014. 7-Deoxy-desulfo-cylindrospermopsin and 7-deoxy-desulfo-12-acetylcylindrospermopsin: Two new cylindrospermopsin analogs isolated from a Thai strain of *Cylindrospermopsis raciborskii*. *Harmful Algae*, 37, pp. 203–206.
- WHO, 1999. *Toxic cyanobacteria in water: a guide to their public health consequences, monitoring, and management*. Edited by: CHORUS, I. and BARTRAM, J., E & FN Spon.
- WOLF, D., GEORGIC, W. and KLAIBER, H.A., 2017. Reeling in the damages: Harmful algal blooms' impact on Lake Erie's recreational fishing industry. *Journal of Environmental Management*, 199, pp. 148–157.
- WOLS, B.A. and HOFMAN-CARIS, C.H.M., 2012. Review of photochemical reaction constants of organic micropollutants required for UV advanced oxidation processes in water. *Water Research*, 46(9), pp. 2815–2827.
- WOOD, R., 2016. Acute animal and human poisonings from cyanotoxin exposure - A review of the literature. *Environment International*, 91, pp. 276–282.
- WORLD HEALTH ORGANIZATION, 2019. *The WHO recommended classification of pesticides by hazard and guidelines to classification*. [online]. Available from: <https://www.who.int/publications/i/item/9789240005662> [Accessed 16 January 2021].

- XIAO, M., LI, M. and REYNOLDS, C.S., 2018. Colony formation in the cyanobacterium *Microcystis*. *Biological Reviews*, 93(3), pp. 1399–1420.
- XING, Z. et al., 2018. Recent advances in floating TiO₂-based photocatalysts for environmental application. *Applied Catalysis B: Environmental*, 225, pp. 452–467.
- XU, L. et al., 2022. Efficient generation of singlet oxygen on modified g-C₃N₄ photocatalyst for preferential oxidation of targeted organic pollutants. *Chemical Engineering Journal*, 431, p. 134241.
- YADAV, S., PRAJAPATI, R. and ATRI, N., 2016. Effects of UV-B and heavy metals on nitrogen and phosphorus metabolism in three cyanobacteria. *Journal of Basic Microbiology*, 56(1), pp. 2–13.
- EL YADINI, A. et al., 2014. Supported TiO₂ on borosilicate glass plates for efficient photocatalytic degradation of fenamiphos. *Journal of Catalysts*, 2014, pp. 1–8.
- YAN, S.C., LI, Z.S. and ZOU, Z.G., 2010. Photodegradation of rhodamine B and methyl orange over boron-doped g-C₃N₄ under visible light irradiation. *Langmuir*, 26(6), pp. 3894–3901.
- YANG, C. et al., 2017. Highly-efficient photocatalytic degradation of methylene blue by PoPD-modified TiO₂ nanocomposites due to photosensitization-synergetic effect of TiO₂ with PoPD. *Scientific Reports*, 7(1), p. 3973.
- YANG, D. et al., 2019. Synthesis of g-C₃N₄ nanosheet/TiO₂ heterojunctions inspired by bioadhesion and biomineralization mechanism. *Industrial and Engineering Chemistry Research*, 58(14), pp. 5516–5525.

- YANG, X.E. et al., 2008. Mechanisms and assessment of water eutrophication. *Journal of Zhejiang University: Science B*, 9(3), pp. 197–209.
- YANG, Y. et al., 2014. Degradation and transformation of atrazine under catalyzed ozonation process with TiO₂ as catalyst. *Journal of Hazardous Materials*, 279, pp. 444–451.
- YANG, Z. et al., 2015. Effects of UV-B radiation on microcystin production of a toxic strain of *Microcystis aeruginosa* and its competitiveness against a non-toxic strain. *Journal of Hazardous Materials*, 283, pp. 447–453.
- YANG, Z. et al., 2016. g-C₃N₄/TiO₂ nanocomposites for degradation of ciprofloxacin under visible light irradiation. *ChemistrySelect*, 1(18), pp. 5679–5685.
- YING, L. et al., 2014. White polymer light-emitting devices for solid-state lighting: Materials, devices, and recent progress. *Advanced Materials*, 26(16), pp. 2459–2473.
- YOUNES, M. et al., 2021. Safety assessment of titanium dioxide (E171) as a food additive. *EFSA Journal*, 19(5).
- YU, B. et al., 2024. Advanced oxidation processes for synchronizing harmful *Microcystis* blooms control with algal metabolites removal: From the laboratory to practical applications. *Science of the Total Environment*, 906, p. 167650.
- ŽABAR, R. et al., 2012. Photocatalytic degradation with immobilised TiO₂ of three selected neonicotinoid insecticides: Imidacloprid, thiamethoxam and clothianidin. *Chemosphere*, 89(3), pp. 293–301.

ZHAN, M. et al., 2023. Visible light-driven photocatalytic degradation of Microcystin-LR by Bi₂WO₆/Reduced graphene oxide heterojunctions: Mechanistic insight, DFT calculation and degradation pathways. *Chemosphere*, 321, p. 138105.

ZHAN, M. and HONG, Y., 2022. Recent advances in technologies for removal of microcystins in water: a review. *Current Pollution Reports*, 8(2), pp. 113–127.

ZHANG, B. et al., 2021. Improved photocatalyst: Elimination of triazine herbicides by novel phosphorus and boron co-doping graphite carbon nitride. *Science of the Total Environment*, 757, p. 143810.

ZHANG, L., MCMILLON, L. and MCNATT, J., 2013. Gas-dependent bandgap and electrical conductivity of Cu₂O thin films. In: *Solar Energy Materials and Solar Cells*. pp. 230–234.

ZHANG, Q. and PEHKONEN, S.O., 1999. Oxidation of diazinon by aqueous chlorine: Kinetics, mechanisms, and product studies. *Journal of Agricultural and Food Chemistry*, 47(4), pp. 1760–1766.

ZHANG, W. et al., 2022. The impact of cyanobacteria blooms on the aquatic environment and human health. *Toxins*, 14(10), p. 658.

ZHAO, C. et al., 2014. UV and visible light activated TiO₂ photocatalysis of 6-hydroxymethyl uracil, a model compound for the potent cyanotoxin cylindrospermopsin. *Catalysis Today*, 224, pp. 70–76.

ZHAO, M. et al., 2015. Synthesis of g-C₃N₄ at different temperatures for superior visible/UV photocatalytic performance and photoelectrochemical sensing of MB solution. *RSC Advances*, 5(123), pp. 101552–101562.

ZHAO, W. et al., 2020. Facile construction of all-solid-state Z-scheme G-C₃N₄/TiO₂ thin film for the efficient visible-light degradation of organic pollutant. *Nanomaterials*, 10(4), p. 600.

ZHOU, D. et al., 2016. *In-situ* construction of all-solid-state Z-scheme g-C₃N₄/TiO₂ nanotube arrays photocatalyst with enhanced visible-light-induced properties. *Solar Energy Materials and Solar Cells*, 157, pp. 399–405.

ZHOU, S. et al., 2021. *In-situ* construction of Z-scheme g-C₃N₄/WO₃ composite with enhanced visible-light responsive performance for nitenpyram degradation. *Chinese Chemical Letters*, 32(7), pp. 2179–2182.

ZUANAZZI, N.R., GHISI, N. de C. and OLIVEIRA, E.C., 2020. Analysis of global trends and gaps for studies about 2,4-D herbicide toxicity: A scientometric review. *Chemosphere*, 241, p. 125016.

APPENDIX

Table A2.1: Coefficient of variation (COV), standard deviation and average of replicates used to determine data statistical analysis used in chapter 2. – means data is not applicable for COV determination.

	Replicate 1	Replicate 2	Replicate 3	Average	Standard deviation (%)	COV (%)
SCIENTO						
Time	F_v'/F_m' - UV-A LED					
Eq	0.4870	0.4967	0.4631	0.4823	1.7	3.6
0	0.4151	0.4615	0.3889	0.4218	3.7	8.7
1	0.0690	0.0333	0.0632	0.0552	1.9	34.7
2	0.0778	0.0000	0.0213	0.0330	4.0	121.7
3	0.0370	0.0000	0.0000	0.0123	2.1	173.2
4	0.0317	0.0217	0.0000	0.0178	1.6	91.0
7	0.0000	0.1429	0.0000	0.0476	8.2	173.2
Time	F_v'/F_m' - Visible light LED					
Eq	0.4797	0.4774	0.4902	0.4824	0.7	1.4
0	0.4262	0.4182	0.3962	0.4135	1.6	3.8
1	0.4474	0.4299	0.4479	0.4417	1.0	2.3
2	0.4706	0.4495	0.4867	0.4690	1.9	4.0
3	0.5373	0.5088	0.5043	0.5168	1.8	3.5
4	0.5714	0.5280	0.5159	0.5384	2.9	5.4
7	0.4643	0.4444	0.4211	0.4433	2.2	4.9
Time	F_v'/F_m' - No LED					
Eq	0.5161	0.4899	0.4710	0.4923	2.3	4.6
0	0.5723	0.5570	0.5234	0.5509	2.5	4.5
1	0.5793	0.5549	0.5503	0.5615	1.6	2.8
2	0.5632	0.5730	0.5549	0.5637	0.9	1.6
3	0.5882	0.5789	0.5824	0.5832	0.5	0.8
4	0.5957	0.5758	0.5870	0.5862	1.0	1.7
7	0.4479	0.4444	0.4699	0.4541	1.4	3.0
NIES 1099						
Time	F_v'/F_m' - UV-A LED					
Eq	0.4909	0.4968	0.4675	0.4851	1.5	3.2
0	0.3692	0.3682	0.4030	0.3801	2.0	5.2
1	0.0950	0.0779	0.0485	0.0738	2.4	31.9
2	0.0204	0.0283	0.0359	0.0282	0.8	27.5
3	0.0000	0.0421	0.0262	0.0228	2.1	93.3
4	0.0000	0.0000	0.0000	0.0000	0.0	###
7	0.0833	0.1818	0.0000	0.0884	9.1	103.0
Time	F_v'/F_m' - Visible light LED					
Eq	0.5000	0.5000	0.5000	0.5000	0.0	0.0
0	0.3897	0.3777	0.3389	0.3688	2.7	7.2
1	0.3212	0.3247	0.3280	0.3247	0.3	1.0
2	0.3046	0.3232	0.3298	0.3192	1.3	4.1
3	0.2700	0.2906	0.2690	0.2766	1.2	4.4

4	0.2256	0.2550	0.2437	0.2414	1.5	6.1
7	0.1230	0.1453	0.1238	0.1307	1.3	9.7
Time	F_v'/F_m' - No LED					
Eq	0.4805	0.4452	0.4937	0.4731	2.5	5.3
0	0.5093	0.5096	0.4444	0.4878	3.8	7.7
1	0.5229	0.4977	0.4220	0.4809	5.3	10.9
2	0.4783	0.4064	0.3551	0.4133	6.2	15.0
3	0.4871	0.4055	0.3397	0.4108	7.4	18.0
4	0.4144	0.3367	0.2892	0.3468	6.3	18.2
7	0.2449	0.2139	0.1803	0.2131	3.2	15.2
B2666						
Time	F_v'/F_m' - UV-A LED					
Eq	0.5083	0.5141	0.5169	0.5131	0.4	0.9
0	0.4372	0.5063	0.5043	0.4826	3.9	8.2
1	0.2138	0.1677	0.1250	0.1688	4.4	26.3
2	0.0144	0.0064	0.0000	0.0069	0.7	104.2
3	0.0000	0.0000	0.0000	0.0000	0.0	-
4	0.0000	0.0000	0.0000	0.0000	0.0	-
7	0.1429	0.0000	0.0000	0.0476	8.2	173.2
Time	F_v'/F_m' - Visible light LED					
Eq	0.5225	0.5054	0.5291	0.5190	1.2	2.4
0	0.4769	0.4545	0.4488	0.4601	1.5	3.2
1	0.4811	0.4372	0.4795	0.4659	2.5	5.3
2	0.4804	0.4036	0.4808	0.4549	4.4	9.8
3	0.4393	0.3742	0.5182	0.4439	7.2	16.3
4	0.2750	0.1888	0.5308	0.3315	17.8	53.6
7	0.0000	0.0000	0.5417	0.1806	31.3	173.2
Time	F_v'/F_m' - No LED					
Eq	0.5287	0.5220	0.5249	0.5252	0.3	0.6
0	0.5394	0.5309	0.5020	0.5241	2.0	3.7
1	0.4978	0.5041	0.5316	0.5112	1.8	3.5
2	0.4581	0.4509	0.5067	0.4719	3.0	6.4
3	0.3850	0.3211	0.4350	0.3804	5.7	15.0
4	0.2216	0.1414	0.3005	0.2212	8.0	36.0
7	0.0044	0.0000	0.0135	0.0060	0.7	115.4
PCC 7820						
Time	F_v'/F_m' - UV-A LED					
Eq	0.4785	0.4943	0.4743	0.4824	1.1	2.2
0	0.3883	0.3906	0.4066	0.3952	1.0	2.5
1	0.1294	0.0455	0.0714	0.0821	4.3	52.4
2	0.0000	0.0000	0.0000	0.0000	0.0	-
3	0.0127	0.0000	0.0000	0.0042	0.7	173.2
4	0.0000	0.0000	0.0000	0.0000	0.0	-
7	0.0476	0.0250	0.0625	0.0450	1.9	41.9
Time	F_v'/F_m' - Visible light LED					
Eq	0.4913	0.4551	0.4689	0.4718	1.8	3.9
0	0.3862	0.3583	0.3897	0.3781	1.7	4.6
1	0.3814	0.3714	0.3704	0.3744	0.6	1.6
2	0.3596	0.3756	0.3812	0.3721	1.1	3.0
3	0.2973	0.2660	0.2762	0.2798	1.6	5.7

4	0.0221	0.0414	0.0000	0.0212	2.1	97.9
7	0.0556	0.0952	0.1053	0.0854	2.6	30.8
Time	F_v'/F_m' - No LED					
Eq	0.4889	0.4778	0.5000	0.4889	1.1	2.3
0	0.4597	0.4787	0.4314	0.4566	2.4	5.2
1	0.4893	0.4812	0.4367	0.4690	2.8	6.0
2	0.4809	0.4698	0.4192	0.4566	3.3	7.2
3	0.4244	0.4182	0.3710	0.4045	2.9	7.2
4	0.2644	0.2602	0.1905	0.2384	4.2	17.4
7	0.0881	0.0857	0.0472	0.0737	2.3	31.1
PCC 7813						
Time	F_v'/F_m' - UV-A LED					
Eq	0.4550	0.4570	0.4497	0.4539	0.4	0.8
0	0.4010	0.4044	0.3895	0.3983	0.8	2.0
1	0.0909	0.0602	0.0827	0.0779	1.6	20.4
2	0.0000	0.0000	0.0000	0.0000	0.0	-
3	0.0000	0.0000	0.0000	0.0000	0.0	-
4	0.0000	0.0000	0.0000	0.0000	0.0	-
7	0.1429	0.0000	0.0000	0.0476	8.2	173.2
Time	F_v'/F_m' - Visible light LED					
Eq	0.4301	0.4301	0.4402	0.4335	0.6	1.3
0	0.3257	0.3314	0.4021	0.3531	4.3	12.1
1	0.3929	0.4171	0.4000	0.4033	1.2	3.1
2	0.3757	0.3862	0.3886	0.3835	0.7	1.8
3	0.3490	0.2929	0.2714	0.3044	4.0	13.2
4	0.1789	0.1075	0.1720	0.1528	3.9	25.8
7	0.3088	0.2281	0.2258	0.2542	4.7	18.6
Time	F_v'/F_m' - No LED					
Eq	0.4560	0.4603	0.4486	0.4550	0.6	1.3
0	0.4619	0.4426	0.4511	0.4518	1.0	2.1
1	0.4111	0.3813	0.3902	0.3942	1.5	3.9
2	0.3165	0.3084	0.3060	0.3103	0.5	1.8
3	0.2079	0.1959	0.2011	0.2016	0.6	3.0
4	0.0658	0.0197	0.0000	0.0285	3.4	118.4
7	0.3118	0.1957	0.2131	0.2402	6.3	26.1
PCC 7806						
Time	F_v'/F_m' - UV-A LED					
Eq	0.3493	0.3474	0.3445	0.3471	0.2	0.7
0	0.3200	0.2677	0.3214	0.3030	3.1	10.1
1	0.0502	0.0540	0.0100	0.0380	2.4	64.0
2	0.0372	0.0000	0.0000	0.0124	2.1	173.2
3	0.0249	0.0000	0.0038	0.0096	1.3	140.2
4	0.0000	0.0000	0.0000	0.0000	0.0	-
7	0.0341	0.0000	0.0000	0.0114	2.0	173.2
Time	F_v'/F_m' - Visible light LED					
Eq	0.3398	0.3544	0.3689	0.3544	1.5	4.1
0	0.2585	0.2575	0.3013	0.2724	2.5	9.2
1	0.2008	0.2076	0.2556	0.2213	3.0	13.5
2	0.1410	0.1092	0.1320	0.1274	1.6	12.9
3	0.2535	0.2525	0.2241	0.2434	1.7	6.8

4	0.3216	0.3235	0.2905	0.3119	1.9	5.9
7	0.3036	0.2946	0.3019	0.3000	0.5	1.6
Time	F_v'/F_M' - No LED					
Eq	0.3412	0.3547	0.3586	0.3515	0.9	2.6
0	0.4126	0.4029	0.3918	0.4024	1.0	2.6
1	0.4542	0.3987	0.4219	0.4250	2.8	6.6
2	0.4406	0.4322	0.4453	0.4394	0.7	1.5
3	0.4520	0.3983	0.4492	0.4332	3.0	7.0
4	0.3992	0.3793	0.4251	0.4012	2.3	5.7
7	0.3094	0.2335	0.3636	0.3022	6.5	21.6
SCIENTO						
Time	F_v/F_M - UV-A LED					
Eq	0.4768	0.4726	0.4558	0.4684	1.1	2.4
0	0.3981	0.4425	0.3592	0.3999	4.2	10.4
1	0.1000	0.0645	0.0326	0.0657	3.4	51.3
2	0.0978	0.0088	0.0515	0.0527	4.5	84.5
3	0.0488	0.0109	0.0222	0.0273	1.9	71.3
4	0.0896		0.0345	0.0620	3.9	62.8
7				-	-	-
Time	F_v/F_M - Visible light LED					
Eq	0.4690	0.4706	0.4765	0.4720	0.4	0.8
0	0.3913	0.3962	0.3786	0.3887	0.9	2.3
1	0.4220	0.4190	0.4362	0.4257	0.9	2.1
2	0.4324	0.4286	0.4082	0.4231	1.3	3.1
3	0.4918	0.4717	0.4528	0.4721	1.9	4.1
4	0.5000	0.4587	0.4455	0.4681	2.8	6.1
7	0.3939	0.3820	0.3956	0.3905	0.7	1.9
Time	F_v/F_M - No LED					
Eq	0.4966	0.4899	0.4605	0.4824	1.9	4.0
0	0.5359	0.5302	0.5308	0.5323	0.3	0.6
1	0.5208	0.5166	0.5074	0.5149	0.7	1.3
2	0.5159	0.5250	0.4966	0.5125	1.5	2.8
3	0.5276	0.5210	0.5422	0.5302	1.1	2.0
4	0.5449	0.5030	0.5280	0.5253	2.1	4.0
7	0.4340	0.4118	0.4172	0.4210	1.2	2.7
NIES 1099						
Time	F_v/F_M - UV-A LED					
Eq	0.4362	0.4348	0.4015	0.4242	2.0	4.6
0	0.3090	0.3135	0.3370	0.3198	1.5	4.7
1	0.0385	0.0318	0.0270	0.0324	0.6	17.7
2	0.0154	0.0144	0.0309	0.0202	0.9	45.9
3	0.0000	0.0000	0.0000	0.0000	0.0	-
4	0.0072	0.0000	0.0000	0.0024	0.4	173.2
7				-	-	-
Time	F_v/F_M - Visible light LED					
Eq	0.4437	0.4552	0.4444	0.4478	0.6	1.4
0	0.3200	0.3158	0.3000	0.3119	1.1	3.4
1	0.3105	0.3177	0.3135	0.3139	0.4	1.1
2	0.2789	0.2834	0.2849	0.2824	0.3	1.1
3	0.2474	0.2727	0.2500	0.2567	1.4	5.4

4	0.1925	0.2199	0.2032	0.2052	1.4	6.7
7	0.1087	0.1207	0.0923	0.1072	1.4	13.3
Time	F_V/F_M - No LED					
Eq	0.4245	0.3944	0.4406	0.4198	2.3	5.6
0	0.4324	0.4426	0.3646	0.4132	4.2	10.3
1	0.4667	0.4559	0.3854	0.4360	4.4	10.1
2	0.4286	0.3720	0.3460	0.3822	4.2	11.1
3	0.4465	0.3676	0.3268	0.3803	6.1	16.0
4	0.3659	0.3125	0.2602	0.3129	5.3	16.9
7	0.2128	0.1771	0.1758	0.1886	2.1	11.1
B2666						
Time	F_V/F_M - UV-A LED					
Eq	0.5000	0.5086	0.5086	0.5057	0.5	1.0
0	0.4227	0.4957	0.4820	0.4668	3.9	8.3
1	0.1259	0.0671	0.0278	0.0736	4.9	67.1
2	0.0284	0.0311	0.0000	0.0198	1.7	86.9
3	0.0000	0.0000	0.0000	0.0000	0.0	-
4	0.0160	0.0000	0.0000	0.0053	0.9	173.2
7				-	-	-
Time	F_V/F_M - Visible light LED					
Eq	0.5115	0.5000	0.5215	0.5110	1.1	2.1
0	0.4593	0.4439	0.4350	0.4461	1.2	2.8
1	0.4667	0.4046	0.4540	0.4418	3.3	7.4
2	0.4686	0.3889	0.4564	0.4379	4.3	9.8
3	0.4294	0.3701	0.4762	0.4252	5.3	12.5
4	0.2611	0.1944	0.4959	0.3172	15.8	49.9
7	0.0000	0.0067	0.5000	0.1689	28.7	169.8
Time	F_V/F_M - No LED					
Eq	0.5205	0.5167	0.5249	0.5207	0.4	0.8
0	0.5236	0.5190	0.4768	0.5065	2.6	5.1
1	0.4844	0.4894	0.5132	0.4957	1.5	3.1
2	0.4332	0.4306	0.4885	0.4507	3.3	7.3
3	0.3627	0.3102	0.4235	0.3654	5.7	15.5
4	0.1749	0.1277	0.2889	0.1971	8.3	42.0
7	0.0088	0.0000	0.0395	0.0161	2.1	128.9
PCC 7820						
Time	F_V/F_M - UV-A LED					
Eq	0.4097	0.4331	0.4026	0.4151	1.6	3.8
0	0.3466	0.3390	0.3533	0.3463	0.7	2.1
1	0.0513	0.0329	0.0530	0.0457	1.1	24.4
2	0.0059	0.0000	0.0062	0.0040	0.3	86.7
3	0.0000	0.0000	0.0000	0.0000	0.0	-
4	0.0000	0.0000	0.0000	0.0000	0.0	-
7				-	-	-
Time	F_V/F_M - Visible light LED					
Eq	0.4248	0.3446	0.3896	0.3863	4.0	10.4
0	0.3333	0.3143	0.3352	0.3276	1.2	3.5
1	0.3416	0.3623	0.3524	0.3521	1.0	2.9
2	0.3209	0.3416	0.3521	0.3382	1.6	4.7
3	0.2529	0.2291	0.2202	0.2341	1.7	7.2

4	0.0167	0.0357	0.0099	0.0207	1.3	64.6
7				-	-	-
Time	F_V/F_M - No LED					
Eq	0.4177	0.4013	0.4194	0.4128	1.0	2.4
0	0.4271	0.4118	0.3830	0.4073	2.2	5.5
1	0.3834	0.3769	0.3485	0.3696	1.9	5.0
2	0.3679	0.3971	0.3480	0.3710	2.5	6.6
3	0.3568	0.3436	0.3085	0.3363	2.5	7.4
4	0.2388	0.2120	0.1685	0.2064	3.5	17.2
7	0.0938	0.0857	0.0320	0.0705	3.4	47.6
PCC 7813						
Time	F_V/F_M - UV-A LED					
Eq	0.3481	0.3648	0.3376	0.3502	1.4	3.9
0	0.3656	0.3626	0.3371	0.3551	1.6	4.4
1	0.0698	0.0672	0.0394	0.0588	1.7	28.7
2	0.0325	0.0000	0.0172	0.0166	1.6	98.1
3	0.0089	0.0000	0.0000	0.0030	0.5	173.2
4	0.0000	0.0000	0.0000	0.0000	0.0	-
7				-	-	-
Time	F_V/F_M - Visible light LED					
Eq	0.3375	0.3205	0.3522	0.3367	1.6	4.7
0	0.2892	0.2901	0.3506	0.3100	3.5	11.4
1	0.3533	0.3895	0.3422	0.3617	2.5	6.8
2	0.3295	0.3520	0.3408	0.3408	1.1	3.3
3	0.3310	0.2667	0.2444	0.2807	4.5	16.0
4	0.1522	0.1170	0.1538	0.1410	2.1	14.7
7				-	-	-
Time	F_V/F_M - No LED					
Eq	0.3438	0.3462	0.3462	0.3454	0.1	0.4
0	0.3865	0.3850	0.3798	0.3838	0.3	0.9
1	0.3660	0.3234	0.3243	0.3379	2.4	7.2
2	0.2957	0.2798	0.2682	0.2812	1.4	4.9
3	0.1878	0.1832	0.1793	0.1835	0.4	2.3
4	0.0470	0.0261	0.0388	0.0373	1.0	28.1
7	0.2889	0.1494	0.1724	0.2036	7.5	36.7
PCC 7806						
Time	F_V/F_M - UV-A LED					
Eq	0.2229	0.2191	0.2216	0.2212	0.2	0.9
0	0.2609	0.1959	0.2400	0.2323	3.3	14.3
1	0.0070	0.0000	0.0000	0.0023	0.4	173.2
2	0.0127	0.0000	0.0000	0.0042	0.7	173.2
3	0.0036	0.0038	0.0000	0.0025	0.2	86.7
4	0.0000	0.0000	0.0000	0.0000	0.0	-
7	0.0341	0.0000	0.0364	0.0235	2.0	86.7
Time	F_V/F_M - Visible light LED					
Eq	0.2047	0.2130	0.2353	0.2177	1.6	7.3
0	0.1972	0.2064	0.2233	0.2090	1.3	6.3
1	0.1471	0.1652	0.1895	0.1673	2.1	12.7
2	0.1373	0.1207	0.1457	0.1346	1.3	9.5
3	0.2050	0.2176	0.1964	0.2063	1.1	5.2

4	0.2795	0.2988	0.2446	0.2743	2.7	10.0
7	0.2909	0.3009	0.3019	0.2979	0.6	2.0
Time	F_V/F_M - No LED					
Eq	0.2102	0.2156	0.2303	0.2187	1.0	4.8
0	0.2941	0.2876	0.2716	0.2844	1.2	4.1
1	0.3239	0.3004	0.3230	0.3157	1.3	4.2
2	0.4206	0.3881	0.3613	0.3900	3.0	7.6
3	0.4219	0.3395	0.4198	0.3937	4.7	11.9
4	0.3540	0.2653	0.4008	0.3400	6.9	20.2
7	0.2770	0.2525	0.3378	0.2891	4.4	15.2
Degradation of dissolved MC-LR						
Time	BG-11 - UV-A LED					
Eq	1.0000	1.0000	1.0000	1.0000	0.0	0.0
0	0.9049	0.9233	0.9639	0.9307	3.0	3.2
1	0.7169	0.7862	0.8875	0.7969	8.6	10.8
2	0.6474	0.7028	0.8555	0.7353	10.8	14.7
3	0.5698	0.6340	0.7811	0.6616	10.8	16.4
4	0.4893	0.5441	0.7054	0.5796	11.2	19.4
7	0.3274	0.3990	0.5827	0.4364	13.2	30.2
Time	BG-11 - No LED					
Eq	1.0000	1.0000	1.0000	1.0000	0.0	0.0
0	1.0083	0.9732	0.9851	0.9889	1.8	1.8
1	0.9940	0.9512	0.9526	0.9659	2.4	2.5
2	1.0051	0.9665	0.9803	0.9840	2.0	2.0
3	0.9996	0.9411	0.9631	0.9679	3.0	3.1
4	0.9630	0.9315	0.9536	0.9493	1.6	1.7
7	0.9410	0.9118	0.8971	0.9166	2.2	2.4
Time	Pure water - UV-A LED					
Eq	1.0000	1.0000	1.0000	1.0000	0.0	0.0
0	1.0095	0.9791	0.9815	0.9901	1.7	1.7
1	0.9643	0.9460	0.9353	0.9485	1.5	1.5
2	0.9134	0.9176	0.9063	0.9124	0.6	0.6
3	0.8636	0.8862	0.8519	0.8672	1.7	2.0
4	0.8342	0.8446	0.8686	0.8491	1.8	2.1
7	0.7439	0.7518	0.8298	0.7752	4.7	6.1
Time	Pure water - No LED					
Eq	1.0000	1.0000	1.0000	1.0000	0.0	0.0
0	0.9782	1.0483	0.9551	0.9939	4.9	4.9
1	0.9584	1.1168	1.0121	1.0291	8.1	7.8
2	0.9244	0.9963	0.9048	0.9418	4.8	5.1
3	0.8813	0.9144	0.8546	0.8834	3.0	3.4
4	0.9425	0.9890	0.8925	0.9413	4.8	5.1
7	1.1006	1.1866	1.0738	1.1203	5.9	5.3
Time	AFW - UV-A LED					
Eq	1.0000	1.0000	1.0000	1.0000	0.0	0.0
0	1.0096	0.9989	1.0358	1.0148	1.9	1.9
1	1.0197	0.9692	1.0257	1.0049	3.1	3.1
2	1.0266	1.0038	1.0211	1.0171	1.2	1.2
3	0.9949	0.9982	1.0191	1.0041	1.3	1.3
4	0.9534	0.9653	1.0313	0.9833	4.2	4.3

7	0.9528	0.9316	0.9624	0.9489	1.6	1.7
Time	AFW - No LED					
Eq	1.0000	1.0000	1.0000	1.0000	0.0	0.0
0	1.0119	0.9998	1.0707	1.0274	3.8	3.7
1	1.0503	1.0721	1.0599	1.0607	1.1	1.0
2	1.1317	1.1045	1.1063	1.1141	1.5	1.4
3	1.1063	1.1172	1.1540	1.1259	2.5	2.2
4	1.1521	1.1417	1.1902	1.1613	2.6	2.2
7	1.1468	1.1369	1.1766	1.1534	2.1	1.8
Time	FeSO₄.7H₂O - UV-A LED					
Eq	1.0000	1.0000	1.0000	1.0000	0.0	0.0
0	0.9428	0.8900	0.9145	0.9158	2.6	2.9
1	0.6672	0.6165	0.7089	0.6642	4.6	7.0
2	0.4823	0.4291	0.5514	0.4876	6.1	12.6
3	0.3641	0.3289	0.4538	0.3823	6.4	16.8
4	0.2642	0.2450	0.3373	0.2821	4.9	17.3
7	0.1526	0.1230	0.2146	0.1634	4.7	28.6
Time	BG-11 - FeSO₄.7H₂O - UV-A LED					
Eq	1.0000	1.0000	1.0000	1.0000	0.0	0.0
0	0.9062	0.8909	0.9202	0.9058	1.5	1.6
1	0.7440	0.6917	0.7477	0.7278	3.1	4.3
2	0.6187	0.5581	0.6350	0.6040	4.1	6.7
3	0.5122	0.4463	0.5289	0.4958	4.4	8.8
4	0.4402	0.3859	0.4496	0.4252	3.4	8.1
7	0.2897	0.2603	0.3178	0.2893	2.9	9.9

Table A2.2: Two-way ANOVA comparing the results of the concentration of total combined microcystins from each *M. aeruginosa* strain exposed to UV-A LED irradiation, visible light LED irradiation and no additional LED irradiation. The significance level was 0.05. The color red represents $p < 0.05$, treatments are significantly different from each other.

	No LED vs. Vis light LED	No LED vs. UV-A LED	Vis light LED vs. UV-A LED
Time	SCIENTO		
Eq	0.7480	0.4469	0.3668
0	0.6456	0.5087	0.6940
1	0.0318	0.0078	0.0005
2	0.1093	0.0183	0.0002
3	0.0381	0.0003	0.0005
4	0.8297	0.0002	0.0007
7	0.1539	<0.0001	<0.0001
Time	NIES 1099		
Eq	0.7091	0.6386	0.8393
0	0.2634	0.2541	0.9992
1	0.1167	0.0017	0.0016
2	0.1267	0.0015	<0.0001
3	0.1223	0.0064	0.0044
4	0.0109	<0.0001	<0.0001
7	0.0679	<0.0001	<0.0001
Time	B2666		
Eq	0.7533	0.9918	0.4517
0	0.4135	0.2080	0.4290
1	0.7163	0.3827	0.6201
2	0.7610	0.1339	0.0844
3	0.1844	0.0293	0.0093
4	0.2959	0.0211	0.0055
7	0.5702	0.0038	0.0305
Time	PCC 7820		
Eq	0.5897	0.7115	0.5454
0	0.0504	0.1470	0.0034
1	0.0888	0.8494	0.0886
2	0.0038	0.0150	0.0018
3	0.0033	0.0086	0.0004
4	0.0311	0.0059	<0.0001
7	0.0011	<0.0001	<0.0001
Time	PCC 7813		
Eq	0.0067	0.3379	0.9815
0	0.0047	0.7203	0.0111
1	0.0048	0.4658	0.0052
2	0.0006	0.0075	0.0002
3	0.0023	0.0128	0.0023
4	0.0055	0.0001	0.0012
7	0.0003	0.0045	0.0002
Time	PCC 7806		
Eq	0.2286	0.4999	0.9160
0	0.0212	0.0287	0.0642
1	0.0093	0.0005	0.4803
2	0.1022	0.0009	0.0027
3	0.3925	0.0003	0.0043
4	0.9670	<0.0001	<0.0001
7	0.0073	<0.0001	<0.0001

Table A3.1: Coefficient of variation (COV), standard deviation and average of replicates used to determine data statistical analysis used in chapter 3. – means data is not applicable for COV determination.

	Replicate 1	Replicate 2	Replicate 3	Average	Standard deviation (%)	COV (%)
Time	g-C₃N₄ coated beads + UV-A LED					
0	1.0000	1.0000	1.0000	1.0000	0.0	0.0
Eq	0.9515	0.9235	0.9324	0.9358	1.4	1.5
1	0.9453	0.9195	0.9093	0.9247	1.9	2.0
3	0.9000	0.9045	0.8849	0.8964	1.0	1.1
5	0.8729	0.8430	0.8908	0.8689	2.4	2.8
7	0.8730	0.7821	0.8482	0.8345	4.7	5.6
10	0.8382	0.7792	0.8220	0.8131	3.0	3.8
15	0.7746	0.6655	0.7323	0.7241	5.5	7.6
30	0.6346	0.4569	0.5499	0.5471	8.9	16.3
45	0.4696	0.2724	0.3859	0.3760	9.9	26.3
60	0.3132	0.1922	0.2894	0.2649	6.4	24.2
90	0.1659	0.0761	0.1356	0.1259	4.6	36.3
120	0.0935	0.0342	0.0642	0.0640	3.0	46.3
180	0.0223	0.0000	0.0000	0.0074	1.3	173.2
Time	g-C₃N₄/TiO₂ coated beads + UV-A LED					
0	1.0000	1.0000	1.0000	1.0000	0.0	0.0
Eq	1.0017	1.0025	0.9920	0.9987	0.6	0.6
1	0.9923	0.9923	0.9932	0.9926	0.1	0.1
3	0.9918	0.9866	0.9958	0.9914	0.5	0.5
5	0.9724	0.9834	0.9942	0.9834	1.1	1.1
7	0.9779	0.9744	0.9867	0.9797	0.6	0.6
10	0.9756	0.9508	0.9783	0.9682	1.5	1.6
15	0.9576	0.9033	0.9485	0.9365	2.9	3.1
30	0.8166	0.7989	0.8389	0.8182	2.0	2.5
45	0.7122	0.6765	0.7515	0.7134	3.7	5.3
60	0.6357	0.5797	0.6427	0.6193	3.5	5.6
90	0.4403	0.3620	0.4422	0.4148	4.6	11.0
120	0.2683	0.2062	0.2693	0.2479	3.6	14.6
180	0.0689	0.0537	0.0851	0.0692	1.6	22.7
Time	UV-A LED (light control)					
0	1.0000	1.0000	1.0000	1.0000	0.0	0.0
Eq	0.9596	0.9976	0.9949	0.9840	2.1	2.2
1	0.9783	1.0020	0.9899	0.9901	1.2	1.2
3	0.9659	1.0122	0.9820	0.9867	2.4	2.4
5	0.9997	0.9862	0.9775	0.9878	1.1	1.1
7	0.9723	0.9937	0.9978	0.9879	1.4	1.4
10	0.9809	0.9942	0.9831	0.9861	0.7	0.7
15	0.9740	0.9935	1.0020	0.9898	1.4	1.4
30	0.9831	0.9905	0.9952	0.9896	0.6	0.6
45	0.9645	0.9909	0.9813	0.9789	1.3	1.4
60	0.9607	0.9876	0.9650	0.9711	1.4	1.5
90	0.9614	0.9931	0.9742	0.9762	1.6	1.6
120	0.9494	1.0142	0.9903	0.9847	3.3	3.3

180	0.9978	0.9809	0.9685	0.9824	1.5	1.5
Time	g-C₃N₄ coated beads (dark control)					
0	1.0000	1.0000	1.0000	1.0000	0.0	0.0
Eq	0.9684	0.9838	0.9857	0.9793	0.9	1.0
1	0.9882	0.9782	0.9947	0.9870	0.8	0.8
3	0.9768	0.9968	0.9874	0.9870	1.0	1.0
5	0.9793	0.9894	0.9830	0.9839	0.5	0.5
7	0.9909	0.9828	0.9726	0.9821	0.9	0.9
10	0.9923	0.9793	0.9763	0.9826	0.9	0.9
15	0.9951	0.9831	0.9796	0.9859	0.8	0.8
30	0.9705	0.9696	0.9723	0.9708	0.1	0.1
45	0.9784	0.9822	0.9848	0.9818	0.3	0.3
60	0.9815	0.9778	0.9764	0.9786	0.3	0.3
90	0.9826	0.9697	0.9822	0.9782	0.7	0.7
120	0.9920	0.9913	0.9954	0.9929	0.2	0.2
180	1.0001	0.9911	0.9948	0.9954	0.5	0.5
Time	g-C₃N₄/TiO₂ coated beads (dark control)					
0	1.0000	1.0000	1.0000	1.0000	0.0	0.0
Eq	0.9740	1.0052	0.9897	0.9896	1.6	1.6
1	0.9794	1.0003	0.9966	0.9921	1.1	1.1
3	0.9840	1.0047	0.9956	0.9948	1.0	1.0
5	0.9710	0.9755	0.9991	0.9819	1.5	1.5
7	0.9930	0.9968	0.9958	0.9952	0.2	0.2
10	0.9856	1.0006	0.9872	0.9911	0.8	0.8
15	0.9904	1.0009	0.9881	0.9931	0.7	0.7
30	0.9760	1.0087	1.0103	0.9984	1.9	1.9
45	0.9769	0.9896	0.9992	0.9886	1.1	1.1
60	0.9889	0.9809	1.0124	0.9940	1.6	1.6
90	0.9905	0.9945	1.0028	0.9959	0.6	0.6
120	0.9913	1.0021	1.0189	1.0041	1.4	1.4
180	0.9966	0.9966	1.0100	1.0011	0.8	0.8
Time	g-C₃N₄ coated beads + White LED					
0	1.0000	1.0000	1.0000	1.0000	0.0	0.0
Eq	0.9115	0.9530	0.9213	0.9286	2.2	2.3
1	0.9198	0.9241	0.9255	0.9231	0.3	0.3
3	0.8997	0.9289	0.9142	0.9143	1.5	1.6
5	0.9131	0.9322	0.9106	0.9186	1.2	1.3
7	0.9234	0.9230	0.9128	0.9197	0.6	0.7
10	0.8973	0.9350	0.9287	0.9203	2.0	2.2
15	0.8891	0.9140	0.9154	0.9062	1.5	1.6
30	0.8712	0.9066	0.9100	0.8960	2.1	2.4
45	0.8857	0.9295	0.8898	0.9016	2.4	2.7
60	0.8964	0.9312	0.9028	0.9101	1.9	2.0
90	0.9040	0.9331	0.9170	0.9180	1.5	1.6
120	0.9182	0.9428	0.9184	0.9265	1.4	1.5
180	0.8956	0.9378	0.9196	0.9177	2.1	2.3
Time	White LED (light control)					
0	1.0000	1.0000	1.0000	1.0000	0.0	0.0
Eq	0.9881	0.9944	1.0024	0.9950	0.7	0.7
1	0.9757	0.9867	1.0040	0.9888	1.4	1.4

3	0.9655	0.9929	0.9855	0.9813	1.4	1.4
5	0.9609	0.9805	0.9942	0.9785	1.7	1.7
7	0.9740	0.9918	0.9844	0.9834	0.9	0.9
10	0.9848	0.9960	1.0006	0.9938	0.8	0.8
15	0.9910	0.9790	0.9835	0.9845	0.6	0.6
30	0.9766	1.0057	0.9823	0.9882	1.5	1.6
45	0.9894	1.0031	0.9719	0.9881	1.6	1.6
60	1.0052	0.9910	0.9869	0.9944	1.0	1.0
90	0.9604	0.9825	1.0116	0.9849	2.6	2.6
120	0.9869	1.0221	0.9933	1.0008	1.9	1.9
180	0.9987	0.9862	1.0031	0.9960	0.9	0.9
Time	g-C₃N₄ coated beads (dark control)					
0	1.0000	1.0000	1.0000	1.0000	0.0	0.0
Eq	0.9684	0.9838	0.9857	0.9793	0.9	1.0
1	0.9882	0.9782	0.9947	0.9870	0.8	0.8
3	0.9768	0.9968	0.9874	0.9870	1.0	1.0
5	0.9793	0.9894	0.9830	0.9839	0.5	0.5
7	0.9909	0.9828	0.9726	0.9821	0.9	0.9
10	0.9923	0.9793	0.9763	0.9826	0.9	0.9
15	0.9951	0.9831	0.9796	0.9859	0.8	0.8
30	0.9705	0.9696	0.9723	0.9708	0.1	0.1
45	0.9784	0.9822	0.9848	0.9818	0.3	0.3
60	0.9815	0.9778	0.9764	0.9786	0.3	0.3
90	0.9826	0.9697	0.9822	0.9782	0.7	0.7
120	0.9920	0.9913	0.9954	0.9929	0.2	0.2
180	1.0001	0.9911	0.9948	0.9954	0.5	0.5
Time	g-C₃N₄ coated beads + Blue LED bulbs					
0	1.0000	1.0000	1.0000	1.0000	0.0	0.0
Eq	0.9845	0.9780	0.9921	0.9849	0.7	0.7
1	0.9787	0.9891	0.9985	0.9887	1.0	1.0
3	0.9792	0.9932	0.9985	0.9903	1.0	1.0
5	0.9766	0.9896	0.9935	0.9866	0.9	0.9
7	0.9942	0.9816	1.0094	0.9951	1.4	1.4
10	0.9821	0.9867	0.9998	0.9895	0.9	0.9
15	0.9747	0.9916	1.0075	0.9913	1.6	1.7
30	0.9882	0.9867	1.0178	0.9976	1.8	1.8
45	0.9640	0.9869	1.0043	0.9850	2.0	2.1
60	0.9956	0.9918	1.0151	1.0008	1.2	1.2
90	1.0101	0.9927	1.0185	1.0071	1.3	1.3
120	1.0020	1.0014	1.0140	1.0058	0.7	0.7
180	1.0084	1.0036	1.0188	1.0103	0.8	0.8
Time	Blue LED bulbs (light control)					
0	1.0000	1.0000	1.0000	1.0000	0.0	0.0
Eq	1.0332	1.0030	1.0068	1.0143	1.6	1.6
1	1.0425	1.0436	1.0165	1.0342	1.5	1.5
3	1.0193	1.0409	1.0325	1.0309	1.1	1.1
5	1.1449	1.0252	1.0284	1.0662	6.8	6.4
7	1.0961	1.0205	1.0375	1.0514	4.0	3.8
10	1.0337	1.0272	1.0330	1.0313	0.4	0.3
15	1.0488	1.0172	1.0291	1.0317	1.6	1.5

30	1.0030	1.0466	1.0260	1.0252	2.2	2.1
45	1.0780	1.0357	1.0481	1.0539	2.2	2.1
60	1.0693	1.0078	1.0092	1.0288	3.5	3.4
90	1.0150	1.0095	1.0127	1.0124	0.3	0.3
120	1.0480	1.1147	1.0435	1.0687	4.0	3.7
180	1.0353	1.0708	1.0161	1.0408	2.8	2.7
Time	g-C₃N₄ coated beads (dark control)					
0	1.0000	1.0000	1.0000	1.0000	0.0	0.0
Eq	0.9684	0.9838	0.9857	0.9793	0.9	1.0
1	0.9882	0.9782	0.9947	0.9870	0.8	0.8
3	0.9768	0.9968	0.9874	0.9870	1.0	1.0
5	0.9793	0.9894	0.9830	0.9839	0.5	0.5
7	0.9909	0.9828	0.9726	0.9821	0.9	0.9
10	0.9923	0.9793	0.9763	0.9826	0.9	0.9
15	0.9951	0.9831	0.9796	0.9859	0.8	0.8
30	0.9705	0.9696	0.9723	0.9708	0.1	0.1
45	0.9784	0.9822	0.9848	0.9818	0.3	0.3
60	0.9815	0.9778	0.9764	0.9786	0.3	0.3
90	0.9826	0.9697	0.9822	0.9782	0.7	0.7
120	0.9920	0.9913	0.9954	0.9929	0.2	0.2
180	1.0001	0.9911	0.9948	0.9954	0.5	0.5
Time	g-C₃N₄ coated beads + Blue LED bulbs - 3 cm from solution					
0	1.0000	1.0000	1.0000	1.0000	0.0	0.0
Eq	0.9815	0.9688	0.9825	0.9776	0.8	0.8
1	0.9737	0.9804	0.9854	0.9798	0.6	0.6
3	0.9882	0.9717	0.9910	0.9836	1.0	1.1
5	0.9969	0.9866	0.9948	0.9928	0.5	0.5
7	0.9724	0.9704	0.9818	0.9749	0.6	0.6
10	0.9898	0.9474	0.9714	0.9695	2.1	2.2
15	0.9929	0.9782	0.9820	0.9844	0.8	0.8
30	0.9806	0.9822	0.9717	0.9782	0.6	0.6
45	0.9405	0.9626	0.9690	0.9574	1.5	1.6
60	1.0009	0.9822	0.9786	0.9872	1.2	1.2
90	0.9659	0.9187	0.9287	0.9378	2.5	2.7
120	0.9733	0.9326	0.9213	0.9424	2.7	2.9
180	0.9695	0.9339	0.9139	0.9391	2.8	3.0
Time	Blue LED bulbs (light control) - 3 cm from solution					
0	1.0000	1.0000	1.0000	1.0000	0.0	0.0
Eq	1.0241	1.0171	0.9971	1.0128	1.4	1.4
1	0.9963	1.0080	1.0052	1.0032	0.6	0.6
3	1.0082	1.0268	0.9840	1.0063	2.1	2.1
5	1.0130	1.0084	1.0043	1.0086	0.4	0.4
7	1.0016	1.0226	1.0266	1.0169	1.3	1.3
10	0.9900	1.0146	0.9993	1.0013	1.2	1.2
15	0.9950	1.0228	0.9856	1.0011	1.9	1.9
30	1.0005	1.0305	0.9995	1.0102	1.8	1.7
45	1.0128	1.0359	1.0260	1.0249	1.2	1.1
60	1.0077	1.0352	1.0106	1.0178	1.5	1.5
90	0.9988	1.0215	0.9679	0.9960	2.7	2.7
120	1.0009	1.0339	1.0032	1.0127	1.8	1.8

180	1.0475	1.0325	1.0095	1.0298	1.9	1.9
Time	g-C₃N₄ coated beads (dark control)					
0	1.0000	1.0000	1.0000	1.0000	0.0	0.0
Eq	0.9752	0.9739	0.9882	0.9791	0.8	0.8
1	0.9864	0.9907	0.9738	0.9836	0.9	0.9
3	0.9855	0.9692	0.9703	0.9750	0.9	0.9
5	0.9749	0.9776	0.9819	0.9781	0.4	0.4
7	0.9790	0.9673	0.9830	0.9764	0.8	0.8
10	0.9846	0.9673	0.9778	0.9766	0.9	0.9
15	0.9902	0.9973	0.9973	0.9949	0.4	0.4
30	0.9841	0.9723	0.9817	0.9794	0.6	0.6
45	0.9714	0.9771	0.9693	0.9726	0.4	0.4
60	0.9756	0.9866	0.9908	0.9843	0.8	0.8
90	0.9816	0.9832	0.9821	0.9823	0.1	0.1
120	0.9864	0.9778	1.0007	0.9883	1.2	1.2
180	1.0126	1.0204	1.0322	1.0217	1.0	1.0
Time	g-C₃N₄ coated beads + UV-A LED - 3 cm from solution					
0	1.0000	1.0000	1.0000	1.0000	0.0	0.0
Eq	0.9552	0.9132	0.9463	0.9382	2.2	2.4
1	0.8749	0.8692	0.8775	0.8739	0.4	0.5
3	0.7427	0.7533	0.8064	0.7675	3.4	4.5
5	0.6106	0.6242	0.7131	0.6493	5.6	8.6
7	0.4960	0.5430	0.6191	0.5527	6.2	11.2
10	0.3567	0.4143	0.5103	0.4271	7.8	18.2
15	0.2151	0.2460	0.3485	0.2699	7.0	25.9
30	0.0409	0.0575	0.1038	0.0674	3.3	48.3
45	0.0000	0.0153	0.0321	0.0158	1.6	101.7
60	0.0000	0.0000	0.0135	0.0045	0.8	173.2
90	0.0000	0.0000	0.0000	0.0000	0.0	###
120	0.0000	0.0000	0.0000	0.0000	0.0	###
180	0.0000	0.0000	0.0000	0.0000	0.0	###
Time	UV-A LED (light control) - 3 cm from solution					
0	1.0000	1.0000	1.0000	1.0000	0.0	0.0
Eq	1.0136	0.9993	0.9955	1.0028	1.0	1.0
1	1.0218	1.0468	1.0085	1.0257	1.9	1.9
3	1.0055	0.9843	0.9861	0.9920	1.2	1.2
5	1.0011	0.9948	1.0196	1.0052	1.3	1.3
7	0.9871	1.0067	1.0193	1.0044	1.6	1.6
10	1.0020	1.0192	1.0169	1.0127	0.9	0.9
15	0.9898	1.0094	1.0114	1.0035	1.2	1.2
30	0.9803	0.9966	1.0036	0.9935	1.2	1.2
45	1.0020	0.9895	1.0097	1.0004	1.0	1.0
60	0.9701	0.9729	1.0014	0.9815	1.7	1.8
90	0.9889	1.0161	0.9932	0.9994	1.5	1.5
120	1.0000	0.9998	1.0058	1.0019	0.3	0.3
180	0.9902	1.0023	1.0011	0.9979	0.7	0.7
Time	TiO₂ coated beads + UV-A LED (light control) - 3 cm from solution					
0	1.0000	1.0000	1.0000	1.0000	0.0	0.0
Eq	1.0209	1.0144	1.0057	1.0137	0.8	0.8
1	0.9886	1.0052	0.9770	0.9903	1.4	1.4

3	0.9469	0.9888	0.9683	0.9680	2.1	2.2
5	0.9424	0.9261	0.9443	0.9376	1.0	1.1
7	0.9620	0.9118	0.8922	0.9220	3.6	3.9
10	0.8941	0.9042	0.8666	0.8883	1.9	2.2
15	0.8758	0.8987	0.8255	0.8666	3.7	4.3
30	0.7383	0.7357	0.6908	0.7216	2.7	3.7
45	0.6600	0.6537	0.5900	0.6346	3.9	6.1
60	0.5605	0.5322	0.4997	0.5308	3.0	5.7
90	0.4226	0.4076	0.3640	0.3981	3.0	7.7
120	0.3291	0.2992	0.2610	0.2964	3.4	11.5
180	0.1558	0.1384	0.1114	0.1352	2.2	16.6
Time	UV-A LED (light control) - 3 cm from solution					
0	1.0000	1.0000	1.0000	1.0000	0.0	0.0
Eq	1.0136	0.9993	0.9955	1.0028	1.0	1.0
1	1.0218	1.0468	1.0085	1.0257	1.9	1.9
3	1.0055	0.9843	0.9861	0.9920	1.2	1.2
5	1.0011	0.9948	1.0196	1.0052	1.3	1.3
7	0.9871	1.0067	1.0193	1.0044	1.6	1.6
10	1.0020	1.0192	1.0169	1.0127	0.9	0.9
15	0.9898	1.0094	1.0114	1.0035	1.2	1.2
30	0.9803	0.9966	1.0036	0.9935	1.2	1.2
45	1.0020	0.9895	1.0097	1.0004	1.0	1.0
60	0.9701	0.9729	1.0014	0.9815	1.7	1.8
90	0.9889	1.0161	0.9932	0.9994	1.5	1.5
120	1.0000	0.9998	1.0058	1.0019	0.3	0.3
180	0.9902	1.0023	1.0011	0.9979	0.7	0.7
Time	TiO₂ coated beads (dark control)					
0	1.0000	1.0000	1.0000	1.0000	0.0	0.0
Eq	0.9914	1.0193	0.9818	0.9975	2.0	2.0
1	0.9006	1.0217	1.0063	0.9762	6.6	6.8
3	0.9856	1.0144	0.9922	0.9974	1.5	1.5
5	0.9776	1.0106	0.9935	0.9939	1.7	1.7
7	0.9930	1.0034	0.9979	0.9981	0.5	0.5
10	0.9806	1.0004	0.9956	0.9922	1.0	1.0
15	0.9934	1.0170	0.9876	0.9993	1.6	1.6
30	0.9819	1.0229	1.0206	1.0085	2.3	2.3
45	0.9724	1.0121	1.0004	0.9950	2.0	2.0
60	0.9502	0.9943	0.9849	0.9764	2.3	2.4
90	0.9794	1.0204	0.9899	0.9966	2.1	2.1
120	0.9757	0.9904	0.9931	0.9864	0.9	0.9
180	0.9669	0.9781	0.9803	0.9751	0.7	0.7

Table A3.2: Two-way ANOVA comparing the results of the concentration of microcystin-LR exposed to photocatalytic treatment (UV-A LED irradiation plus g-C₃N₄ or g-C₃N₄/TiO₂ coated beads), light control (UV-A LED irradiation only) or dark control (g-C₃N₄ or g-C₃N₄/TiO₂ coated beads only). The significance level was 0.05. The color red represents p<0.05, treatments are significantly different from each other.

	Treatment vs. Light control	Treatment vs. Dark control	Light control vs. Dark control
Time	g-C₃N₄ coated beads and UV-A LEDs		
Eq	0.0765	0.0338	0.9341
1	0.0218	0.0316	0.9306
3	0.0228	0.0009	0.9998
5	0.0112	0.0217	0.8552
7	0.0429	0.0523	0.8223
10	0.0142	0.0134	0.858
15	0.0191	0.0238	0.9139
30	0.0235	0.0261	0.0527
45	0.0147	0.0159	0.9306
60	0.0034	0.0046	0.6998
90	0.0002	0.0005	0.9799
120	<0.0001	<0.0001	0.9062
180	<0.0001	<0.0001	0.4419
Time	g-C₃N₄/TiO₂ coated beads and UV-A LEDs		
Eq	0.5652	0.6585	0.9291
1	0.9304	0.9965	0.9754
3	0.9408	0.87	0.8578
5	0.8778	0.9894	0.853
7	0.6542	0.0763	0.6843
10	0.304	0.1959	0.7211
15	0.13	0.1291	0.9325
30	0.0047	0.0008	0.7609
45	0.0061	0.0068	0.6369
60	0.0019	0.0013	0.2767
90	0.0016	0.0029	0.2774
120	<0.0001	<0.0001	0.657
180	<0.0001	<0.0001	0.2685
Time	g-C₃N₄ coated beads and white LEDs		
Eq	0.0468	0.0774	0.1767
1	0.0234	0.0049	0.9819
3	0.0102	0.0069	0.8445
5	0.0201	0.0089	0.8636
7	0.0021	0.0026	0.9827
10	0.0277	0.0403	0.3311
15	0.0105	0.0069	0.9682
30	0.011	0.0471	0.3236
45	0.0207	0.0497	0.7939
60	0.0122	0.0398	0.1736
90	0.054	0.0165	0.9057
120	0.0144	0.0242	0.7767
180	0.0264	0.0374	0.9933

Table A4.1: Coefficient of variation (COV), standard deviation and average of replicates used to determine data statistical analysis used in chapter 4. – means data is not applicable for COV determination.

	Replicate 1	Replicate 2	Replicate 3	Average	Standard deviation (%)	COV (%)
Time	Reactor design: beaker					
0	1.0000	1.0000	1.0000	1.0000	0.0	0.0
Eq	1.0043	1.0021	0.9953	1.0006	0.5	0.5
5	0.9605	0.9409	0.9424	0.9480	1.1	1.2
15	0.9206	0.8884	0.8737	0.8942	2.4	2.7
30	0.8846	0.8395	0.8347	0.8529	2.8	3.2
45	0.8638	0.7886	0.7772	0.8099	4.7	5.8
60	0.8289	0.7501	0.7421	0.7737	4.8	6.2
240	0.6224	0.6138	0.4494	0.5619	9.7	17.4
420	0.3267	0.1267	0.2378	0.2304	10.0	43.5
1440	0.0000	0.0000	0.0000	0.0000	0.0	-
Time	Reactor design: crystallizing dish					
0	1.0000	1.0000	1.0000	1.0000	0.0	0.0
Eq	0.9932	0.9986	0.9825	0.9915	0.8	0.8
5	0.9426	0.9199	0.9234	0.9286	1.2	1.3
15	0.8693	0.8601	0.8668	0.8654	0.5	0.5
30	0.8204	0.8015	0.8009	0.8076	1.1	1.4
45	0.7660	0.7638	0.7574	0.7624	0.4	0.6
60	0.7390	0.7108	0.7103	0.7201	1.6	2.3
240	0.3409	0.3064	0.2695	0.3056	3.6	11.7
420	0.0529	0.0362	0.0119	0.0337	2.1	61.3
1440	0.0000	0.0000	0.0000	0.0000	0.0	-
Time	Catalyst load optimization: 0.14% (w/v)					
0	1.0000	1.0000	1.0000	1.0000	0.0	0.0
Eq	0.9932	0.9986	0.9825	0.9915	0.8	0.8
5	0.9426	0.9199	0.9234	0.9286	1.2	1.3
15	0.8693	0.8601	0.8668	0.8654	0.5	0.5
30	0.8204	0.8015	0.8009	0.8076	1.1	1.4
45	0.7660	0.7638	0.7574	0.7624	0.4	0.6
60	0.7390	0.7108	0.7103	0.7201	1.6	2.3
240	0.3409	0.3064	0.2695	0.3056	3.6	11.7
420	0.0529	0.0362	0.0119	0.0337	2.1	61.3
1440	0.0000	0.0000	0.0000	0.0000	0.0	-
Time	Catalyst load optimization: 0.28% (w/v)					
0	1.0000	1.0000	1.0000	1.0000	0.0	0.0
Eq	0.9961	1.0097	0.9884	0.9981	1.1	1.1
5	0.9075	0.8978	0.9234	0.9096	1.3	1.4
15	0.8567	0.8271	0.8611	0.8483	1.8	2.2
30	0.7978	0.7698	0.7859	0.7845	1.4	1.8
45	0.7564	0.7304	0.7457	0.7441	1.3	1.8
60	0.7244	0.6773	0.7063	0.7027	2.4	3.4
240	0.3440	0.2805	0.2709	0.2985	4.0	13.3
420	0.1220	0.0814	0.1267	0.1101	2.5	22.6
1440	0.0000	0.0000	0.0000	0.0000	0.0	-

Time	Catalyst load optimization: 0.42% (w/v)					
0	1.0000	1.0000	1.0000	1.0000	0.0	0.0
Eq	0.9939	0.9919	0.9799	0.9885	0.8	0.8
5	0.9034	0.9099	0.9072	0.9068	0.3	0.4
15	0.8357	0.8505	0.8617	0.8493	1.3	1.5
30	0.7809	0.7954	0.8134	0.7966	1.6	2.0
45	0.7519	0.7537	0.7614	0.7557	0.5	0.7
60	0.7166	0.7112	0.7005	0.7094	0.8	1.1
240	0.3674	0.3226	0.3744	0.3548	2.8	7.9
420	0.1647	0.1231	0.1791	0.1556	2.9	18.7
1440	0.0000	0.0000	0.0000	0.0000	0.0	-
Time	Catalyst load optimization: 0.56% (w/v)					
0	1.0000	1.0000	1.0000	1.0000	0.0	0.0
Eq	0.9983	0.9927	1.0032	0.9981	0.5	0.5
5	0.9400	0.8902	0.9441	0.9247	3.0	3.2
15	0.8987	0.8598	0.9021	0.8869	2.4	2.7
30	0.8326	0.8224	0.8357	0.8302	0.7	0.8
45	0.7609	0.7815	0.7773	0.7732	1.1	1.4
60	0.7552	0.7381	0.7269	0.7401	1.4	1.9
240	0.4080	0.3576	0.4381	0.4012	4.1	10.1
420	0.1932	0.1561	0.1853	0.1782	2.0	11.0
1440	0.0000	0.0000	0.0000	0.0000	0.0	-
Time	Catalyst load optimization: 0.70% (w/v)					
0	1.0000	1.0000	1.0000	1.0000	0.0	0.0
Eq	0.9903	0.9915	1.0036	0.9951	0.7	0.7
5	0.9350	0.9209	0.9460	0.9340	1.3	1.3
15	0.8611	0.8683	0.8869	0.8721	1.3	1.5
30	0.8427	0.8172	0.8410	0.8336	1.4	1.7
45	0.7813	0.7600	0.7982	0.7798	1.9	2.5
60	0.7434	0.7363	0.7537	0.7445	0.9	1.2
240	0.3810	0.3607	0.4298	0.3905	3.5	9.1
420	0.1901	0.1933	0.2255	0.2030	2.0	9.7
1440	0.0000	0.0000	0.0000	0.0000	0.0	-
Time	pH optimization: pH 2					
0	1.0000	1.0000	1.0000	1.0000	0.0	0.0
Eq	0.9694	0.9897	0.9916	0.9836	1.2	1.3
5	0.9026	0.9224	0.9209	0.9153	1.1	1.2
15	0.7731	0.8355	0.8452	0.8180	3.9	4.8
30	0.6734	0.7285	0.7354	0.7124	3.4	4.8
45	0.5659	0.6327	0.6659	0.6215	5.1	8.2
60	0.5074	0.5877	0.6046	0.5666	5.2	9.2
240	0.0959	0.1750	0.1832	0.1513	4.8	31.8
420	0.0157	0.0352	0.0405	0.0305	1.3	42.8
1440	0.0108	0.0000	0.0107	0.0071	0.6	86.6
Time	pH optimization: pH 5					
0	1.0000	1.0000	1.0000	1.0000	0.0	0.0
Eq	0.9869	0.9977	0.9829	0.9892	0.8	0.8
5	0.8599	0.8350	0.8605	0.8518	1.5	1.7
15	0.6830	0.6331	0.6901	0.6687	3.1	4.6
30	0.4702	0.4316	0.5619	0.4879	6.7	13.7

45	0.3039	0.2482	0.4184	0.3235	8.7	26.8
60	0.1935	0.1627	0.3135	0.2233	8.0	35.7
240	0.0112	0.0000	0.0302	0.0138	1.5	110.8
420	0.0000	0.0000	0.0000	0.0000	0.0	-
1440	0.0000	0.0000	0.0000	0.0000	0.0	-
Time	pH optimization: pH 8					
0	1.0000	1.0000	1.0000	1.0000	0.0	0.0
Eq	0.9829	0.9955	0.9947	0.9910	0.7	0.7
5	0.9336	0.9038	0.9164	0.9179	1.5	1.6
15	0.8806	0.8681	0.8675	0.8721	0.7	0.8
30	0.8070	0.7624	0.7899	0.7864	2.3	2.9
45	0.7437	0.7068	0.7441	0.7315	2.1	2.9
60	0.7184	0.7109	0.6945	0.7079	1.2	1.7
240	0.3631	0.3102	0.3054	0.3262	3.2	9.8
420	0.0847	0.0579	0.0210	0.0545	3.2	58.6
1440	0.0000	0.0000	0.0000	0.0000	0.0	-
Time	pH optimization: pH 10					
0	1.0000	1.0000	1.0000	1.0000	0.0	0.0
Eq	0.9911	0.9897	0.9938	0.9915	0.2	0.2
5	0.9091	0.9057	0.8990	0.9046	0.5	0.6
15	0.8125	0.8572	0.8691	0.8463	3.0	3.5
30	0.7473	0.7832	0.7462	0.7589	2.1	2.8
45	0.7405	0.7398	0.7033	0.7279	2.1	2.9
60	0.6650	0.7152	0.6353	0.6718	4.0	6.0
240	0.2658	0.2731	0.1618	0.2335	6.2	26.7
420	0.0294	0.0403	0.0000	0.0232	2.1	89.7
1440	0.0000	0.0000	0.0000	0.0000	0.0	-
Time	Catalyst load optimization with buffer: 0.14% (w/v)					
0	1.0000	1.0000	1.0000	1.0000	0.0	0.0
Eq	0.9952	1.0016	1.0028	0.9998	0.4	0.4
5	0.9124	0.9485	0.9596	0.9402	2.5	2.6
15	0.8485	0.8831	0.8492	0.8603	2.0	2.3
30	0.7360	0.7625	0.7740	0.7575	1.9	2.6
45	0.6748	0.6913	0.7412	0.7024	3.5	4.9
60	0.6175	0.6399	0.6636	0.6404	2.3	3.6
240	0.2542	0.2362	0.2550	0.2485	1.1	4.3
420	0.0307	0.0726	0.0900	0.0644	3.1	47.3
1440	0.0000	0.0000	0.0000	0.0000	0.0	-
Time	Catalyst load optimization with buffer: 0.28% (w/v)					
0	1.0000	1.0000	1.0000	1.0000	0.0	0.0
Eq	0.9599	0.9787	0.9894	0.9760	1.5	1.5
5	0.9144	0.8785	0.9174	0.9034	2.2	2.4
15	0.7770	0.7755	0.7975	0.7833	1.2	1.6
30	0.7139	0.6336	0.6481	0.6652	4.3	6.4
45	0.5609	0.5245	0.5976	0.5610	3.7	6.5
60	0.4827	0.4519	0.5167	0.4838	3.2	6.7
240	0.1306	0.0552	0.1177	0.1012	4.0	39.9
420	0.0000	0.0000	0.0000	0.0000	0.0	-
1440	0.0000	0.0000	0.0000	0.0000	0.0	-
Time	Catalyst load optimization with buffer: 0.42% (w/v)					

0	1.0000	1.0000	1.0000	1.0000	0.0	0.0
Eq	0.9628	0.9879	0.9946	0.9818	1.7	1.7
5	0.9127	0.9214	0.9009	0.9117	1.0	1.1
15	0.7968	0.7546	0.7863	0.7792	2.2	2.8
30	0.6583	0.6472	0.6929	0.6662	2.4	3.6
45	0.5811	0.5492	0.5722	0.5675	1.6	2.9
60	0.5253	0.4614	0.4947	0.4938	3.2	6.5
240	0.0954	0.0553	0.1003	0.0837	2.5	29.5
420	0.0073	0.0000	0.0000	0.0024	0.4	173.2
1440	0.0000	0.0000	0.0000	0.0000	0.0	-
Time	Catalyst load optimization with buffer: 0.56% (w/v)					
0	1.0000	1.0000	1.0000	1.0000	0.0	0.0
Eq	0.9905	0.9967	0.9787	0.9886	0.9	0.9
5	0.9622	0.9000	0.9319	0.9314	3.1	3.3
15	0.8044	0.8208	0.8436	0.8229	2.0	2.4
30	0.7128	0.6895	0.7486	0.7170	3.0	4.1
45	0.6542	0.6360	0.6723	0.6542	1.8	2.8
60	0.5727	0.5360	0.5474	0.5521	1.9	3.4
240	0.1211	0.0980	0.1396	0.1196	2.1	17.5
420	0.0000	0.0000	0.0000	0.0000	0.0	-
1440	0.0000	0.0000	0.0000	0.0000	0.0	-
Time	Catalyst load optimization with buffer: 0.70% (w/v)					
0	1.0000	1.0000	1.0000	1.0000	0.0	0.0
Eq	0.9808	0.9803	0.9858	0.9823	0.3	0.3
5	0.9578	0.9269	0.8822	0.9223	3.8	4.1
15	0.8285	0.8595	0.8023	0.8301	2.9	3.4
30	0.7864	0.7616	0.7186	0.7555	3.4	4.5
45	0.6203	0.6369	0.6206	0.6259	0.9	1.5
60	0.5576	0.5675	0.5396	0.5549	1.4	2.5
240	0.0998	0.1105	0.1147	0.1084	0.8	7.1
420	0.0000	0.0000	0.0000	0.0000	0.0	-
1440	0.0000	0.0000	0.0000	0.0000	0.0	-
Time	Calcination time optimization: Treatment - 2 hours					
0	1.0000	1.0000	1.0000	1.0000	0.0	0.0
Eq	1.0141	0.9711	1.0123	0.9992	2.4	2.4
5	0.9978	0.9671	0.9547	0.9732	2.2	2.3
15	0.9447	0.9692	0.9706	0.9615	1.5	1.5
30	0.9268	0.8921	0.9213	0.9134	1.9	2.0
45	0.8945	0.8574	0.8649	0.8723	2.0	2.2
60	0.8792	0.8250	0.8605	0.8549	2.8	3.2
120	0.7617	0.6969	0.7273	0.7287	3.2	4.4
240	0.5626	0.4934	0.5337	0.5299	3.5	6.6
420	0.3578	0.3467	0.3466	0.3504	0.6	1.8
1440	0.0000	0.0000	0.0000	0.0000	0.0	-
Time	Calcination time optimization: Dark control - 2 hours					
0	1.0000	1.0000	1.0000	1.0000	0.0	0.0
Eq	1.0116	1.0435	1.0399	1.0317	1.8	1.7
5	1.0103	1.0367	0.9761	1.0077	3.0	3.0
15	0.9692	0.9714	0.9762	0.9723	0.4	0.4
30	0.9768	0.9858	1.0138	0.9921	1.9	1.9

45	0.9826	0.9993	0.9620	0.9813	1.9	1.9
60	0.9736	1.0259	0.9708	0.9901	3.1	3.1
120	0.9820	1.0254	0.9741	0.9938	2.8	2.8
240	0.9596	1.0012	0.9837	0.9815	2.1	2.1
420	1.0154	0.9719	0.9642	0.9838	2.8	2.8
1440	0.9964	1.0087	0.9773	0.9941	1.6	1.6
Time	Calcination time optimization: Treatment - 4 hours					
0	1.0000	1.0000	1.0000	1.0000	0.0	0.0
Eq	0.9499	0.9409	1.0062	0.9656	3.5	3.7
5	0.9546	0.9681	0.9763	0.9663	1.1	1.1
15	0.9162	0.9306	0.9432	0.9300	1.4	1.5
30	0.8841	0.8775	0.9026	0.8881	1.3	1.5
45	0.8244	0.8453	0.8522	0.8406	1.4	1.7
60	0.7840	0.7520	0.7919	0.7760	2.1	2.7
120	0.5339	0.4959	0.5675	0.5324	3.6	6.7
240	0.1655	0.1172	0.2549	0.1792	7.0	39.0
420	0.1587	0.1421	0.2548	0.1852	6.1	32.9
1440	0.0000	0.0000	0.0000	0.0000	0.0	-
Time	Calcination time optimization: Dark control - 4 hours					
0	1.0000	1.0000	1.0000	1.0000	0.0	0.0
Eq	0.9966	0.9929	0.9998	0.9965	0.3	0.3
5	0.9940	1.0028	0.9995	0.9988	0.4	0.4
15	0.9872	1.0037	0.9970	0.9960	0.8	0.8
30	0.9971	0.9998	1.0144	1.0038	0.9	0.9
45	0.9948	1.0047	0.9707	0.9901	1.7	1.8
60	0.9846	1.0162	0.9995	1.0001	1.6	1.6
120	0.9771	0.9974	1.0006	0.9917	1.3	1.3
240	0.9753	1.0032	0.9996	0.9927	1.5	1.5
420	0.9778	0.9970	0.9945	0.9898	1.0	1.1
1440	0.9340	0.9699	0.9544	0.9528	1.8	1.9
Time	Calcination time optimization: Treatment - 6 hours					
0	1.0000	1.0000	1.0000	1.0000	0.0	0.0
Eq	1.0223	1.0092	0.9904	1.0073	1.6	1.6
5	0.9911	0.9877	0.9805	0.9864	0.5	0.6
15	0.9671	0.9623	0.9383	0.9559	1.5	1.6
30	0.9079	0.9190	0.8792	0.9020	2.1	2.3
45	0.8655	0.8056	0.8492	0.8401	3.1	3.7
60	0.8153	0.7787	0.8090	0.8010	2.0	2.4
120	0.6695	0.6300	0.6580	0.6525	2.0	3.1
240	0.4306	0.3692	0.4320	0.4106	3.6	8.7
420	0.1613	0.1080	0.2080	0.1591	5.0	31.5
1440	0.0000	0.0000	0.0000	0.0000	0.0	-
Time	Calcination time optimization: Dark control - 6 hours					
0	1.0000	1.0000	1.0000	1.0000	0.0	0.0
Eq	0.9951	1.0057	1.0008	1.0005	0.5	0.5
5	0.9972	1.0005	1.0024	1.0000	0.3	0.3
15	1.0134	1.0029	0.9952	1.0038	0.9	0.9
30	1.0129	0.9878	1.0106	1.0037	1.4	1.4
45	1.0039	1.0096	0.9878	1.0004	1.1	1.1
60	1.0079	1.0041	0.9984	1.0035	0.5	0.5

120	0.9806	0.9814	0.9867	0.9829	0.3	0.3
240	0.9801	0.9926	0.9736	0.9821	1.0	1.0
420	0.9780	0.9671	0.9884	0.9779	1.1	1.1
1440	0.9666	0.9708	0.9339	0.9571	2.0	2.1
Time	Calcination time optimization: Treatment - 8 hours					
0	1.0000	1.0000	1.0000	1.0000	0.0	0.0
Eq	1.0062	0.9896	0.9919	0.9959	0.9	0.9
5	1.0203	0.9822	0.9803	0.9943	2.3	2.3
15	0.9072	0.9709	0.9177	0.9319	3.4	3.7
30	0.9296	0.8927	0.8966	0.9063	2.0	2.2
45	0.8532	0.8116	0.8421	0.8356	2.1	2.6
60	0.8365	0.7745	0.7772	0.7961	3.5	4.4
120	0.6322	0.5812	0.5959	0.6031	2.6	4.4
240	0.3187	0.2812	0.3219	0.3072	2.3	7.4
420	0.0537	0.0236	0.0491	0.0421	1.6	38.4
1440	0.0000	0.0000	0.0000	0.0000	0.0	-
Time	Calcination time optimization: Dark control - 8 hours					
0	1.0000	1.0000	1.0000	1.0000	0.0	0.0
Eq	1.0001	0.9434	1.0147	0.9861	3.8	3.8
5	0.8592	0.9970	1.0803	0.9788	11.2	11.4
15	1.0133	0.9831	1.0250	1.0071	2.2	2.1
30	0.9945	0.9924	1.0387	1.0085	2.6	2.6
45	1.0077	1.0083	0.9902	1.0021	1.0	1.0
60	0.9522	0.9311	0.9569	0.9467	1.4	1.5
120	0.9502	0.9181	0.9798	0.9494	3.1	3.2
240	0.9675	0.9795	0.9819	0.9763	0.8	0.8
420	0.9582	0.9591	0.9758	0.9644	1.0	1.0
1440	0.9293	0.9347	0.9625	0.9422	1.8	1.9
Time	Calcination time optimization: Treatment - 10 hours					
0	1.0000	1.0000	1.0000	1.0000	0.0	0.0
Eq	1.0330	1.0477	0.9205	1.0004	7.0	7.0
5	0.7516	0.7112	0.6547	0.7058	4.9	6.9
15	0.5052	0.4462	0.4679	0.4731	3.0	6.3
30	0.2656	0.2272	0.2148	0.2358	2.6	11.2
45	0.1069	0.0683	0.0897	0.0883	1.9	21.9
60	0.0040	0.0000	0.0000	0.0013	0.2	173.2
120	0.0000	0.0000	0.0000	0.0000	0.0	-
240	0.0000	0.0000	0.0000	0.0000	0.0	-
420	0.0000	0.0000	0.0000	0.0000	0.0	-
1440	0.0000	0.0000	0.0000	0.0000	0.0	-
Time	Calcination time optimization: Dark control - 10 hours					
0	1.0000	1.0000	1.0000	1.0000	0.0	0.0
Eq	0.9006	1.0219	1.0289	0.9838	7.2	7.3
5	0.9925	0.9936	1.0224	1.0028	1.7	1.7
15	0.9121	0.9727	1.0139	0.9662	5.1	5.3
30	1.0322	0.9821	1.0527	1.0223	3.6	3.6
45	0.9504	1.0436	1.0035	0.9992	4.7	4.7
60	0.9327	1.0186	1.0515	1.0009	6.1	6.1
120	0.8770	0.9363	0.9853	0.9329	5.4	5.8
240	0.9102	0.9457	0.9797	0.9452	3.5	3.7

420	0.8957	0.9644	0.9791	0.9464	4.5	4.7
1440	0.9081	0.9701	0.9927	0.9570	4.4	4.6
Time	Calcination time optimization: Light control - UV-A LED					
0	1.0000	1.0000	1.0000	1.0000	0.0	0.0
Eq	0.9984	1.0054	0.9502	0.9847	3.0	3.1
5	0.9985	0.9993	0.9460	0.9813	3.1	3.1
15	1.0003	0.9993	0.9420	0.9805	3.3	3.4
30	0.9916	1.0138	0.9449	0.9834	3.5	3.6
45	1.0039	1.0138	0.9344	0.9840	4.3	4.4
60	0.9934	1.0047	0.9961	0.9981	0.6	0.6
120	0.9825	1.0030	0.9314	0.9723	3.7	3.8
240	0.9851	0.9998	0.9247	0.9699	4.0	4.1
420	0.9699	0.9934	0.9233	0.9622	3.6	3.7
1440	0.8963	0.9867	0.8048	0.8959	9.1	10.2
Time	Pesticide mix - Treatment: Acetamiprid					
0	1.0000	1.0000	1.0000	1.0000	0.0	0.0
Eq	0.9178	0.8924	0.8822	0.8975	1.8	2.0
5	0.9333	0.8878	0.8624	0.8945	3.6	4.0
15	0.8707	0.7560	0.8453	0.8240	6.0	7.3
30	0.8006	0.6816	0.6808	0.7210	6.9	9.6
45	0.7368	0.7214	0.6875	0.7152	2.5	3.5
60	0.6407	0.5741	0.6269	0.6139	3.5	5.7
240	0.6414	0.5973	0.6161	0.6182	2.2	3.6
420	0.6039	0.4713	0.5915	0.5556	7.3	13.2
1440	0.4446	0.4190	0.4032	0.4223	2.1	4.9
2880	0.0000	0.0000	0.0000	0.0000	0.0	-
Time	Pesticide mix - Dark control: Acetamiprid					
0	1.0000	1.0000	1.0000	1.0000	0.0	0.0
Eq	0.9745	0.9543	0.9587	0.9625	1.1	1.1
5	0.9244	0.9517	0.9447	0.9403	1.4	1.5
15	0.9124	0.9664	0.9205	0.9331	2.9	3.1
30	0.9387	0.9190	0.9151	0.9243	1.3	1.4
45	0.8998	0.8930	0.9457	0.9129	2.9	3.1
60	0.9393	0.9310	0.9234	0.9312	0.8	0.9
240	0.8652	0.8631	0.9345	0.8876	4.1	4.6
420	0.8561	0.9175	0.8642	0.8793	3.3	3.8
1440	0.8561	0.8678	0.8638	0.8626	0.6	0.7
2880	0.9023	0.8962	0.8354	0.8780	3.7	4.2
Time	Pesticide mix - Light control: Acetamiprid					
0	1.0000	1.0000	1.0000	1.0000	0.0	0.0
Eq	1.0025	1.0045	0.9910	0.9993	0.7	0.7
5	0.9960	1.0042	1.0005	1.0002	0.4	0.4
15	0.9975	1.0047	0.9961	0.9994	0.5	0.5
30	1.0025	0.9969	0.9899	0.9964	0.6	0.6
45	1.0092	0.9953	0.9931	0.9992	0.9	0.9
60	1.0069	1.0011	0.9914	0.9998	0.8	0.8
240	1.0046	1.0021	0.9986	1.0018	0.3	0.3
420	1.0026	1.0095	0.9959	1.0027	0.7	0.7
1440	0.9935	1.0027	1.0073	1.0012	0.7	0.7
2880	0.9828	0.9634	0.9874	0.9779	1.3	1.3

Time	Pesticide mix - Treatment: Clothianidin					
0	1.0000	1.0000	1.0000	1.0000	0.0	0.0
Eq	0.9106	0.9726	0.9597	0.9476	3.3	3.5
5	0.9341	0.9088	0.9033	0.9154	1.6	1.8
15	0.8839	0.8476	0.8671	0.8662	1.8	2.1
30	0.8062	0.7964	0.7825	0.7951	1.2	1.5
45	0.7244	0.7330	0.7622	0.7398	2.0	2.7
60	0.6816	0.6630	0.6609	0.6685	1.1	1.7
240	0.1779	0.1095	0.1370	0.1415	3.4	24.3
420	0.0000	0.0000	0.0000	0.0000	0.0	-
1440	0.0000	0.0000	0.0000	0.0000	0.0	-
2880	0.0000	0.0000	0.0000	0.0000	0.0	-
Time	Pesticide mix - Dark control: Clothianidin					
0	1.0000	1.0000	1.0000	1.0000	0.0	0.0
Eq	0.9313	0.9343	0.9353	0.9336	0.2	0.2
5	0.9202	0.9142	0.9557	0.9300	2.2	2.4
15	0.9213	0.9142	0.9632	0.9329	2.6	2.8
30	0.9192	0.9451	0.9473	0.9372	1.6	1.7
45	0.9464	0.9343	0.9172	0.9326	1.5	1.6
60	0.9552	0.9402	0.9379	0.9445	0.9	1.0
240	0.8174	0.8216	0.8314	0.8235	0.7	0.9
420	0.8287	0.8206	0.8584	0.8359	2.0	2.4
1440	0.8697	0.8160	0.8556	0.8471	2.8	3.3
2880	0.8378	0.8111	0.8275	0.8255	1.3	1.6
Time	Pesticide mix - Light control: Clothianidin					
0	1.0000	1.0000	1.0000	1.0000	0.0	0.0
Eq	1.0082	0.9981	0.9960	1.0008	0.7	0.7
5	1.0047	0.9970	0.9990	1.0002	0.4	0.4
15	1.0055	0.9978	1.0006	1.0013	0.4	0.4
30	1.0043	0.9991	0.9986	1.0007	0.3	0.3
45	1.0152	1.0053	1.0079	1.0095	0.5	0.5
60	1.0105	1.0093	1.0035	1.0078	0.4	0.4
240	1.0106	0.9880	1.0112	1.0033	1.3	1.3
420	0.9976	0.9998	1.0038	1.0004	0.3	0.3
1440	0.9816	0.9549	0.9785	0.9717	1.5	1.5
2880	0.9311	0.8499	0.9002	0.8937	4.1	4.6
Time	Pesticide mix - Treatment: Imidacloprid					
0	1.0000	1.0000	1.0000	1.0000	0.0	0.0
Eq	0.9810	0.9481	0.9689	0.9660	1.7	1.7
5	0.9203	0.9277	0.9370	0.9283	0.8	0.9
15	0.8277	0.8177	0.8225	0.8226	0.5	0.6
30	0.7481	0.7494	0.7032	0.7336	2.6	3.6
45	0.6666	0.6511	0.6486	0.6554	1.0	1.5
60	0.5797	0.5616	0.5940	0.5784	1.6	2.8
240	0.0887	0.0179	0.0364	0.0477	3.7	77.0
420	0.0000	0.0000	0.0000	0.0000	0.0	-
1440	0.0000	0.0000	0.0000	0.0000	0.0	-
2880	0.0000	0.0000	0.0000	0.0000	0.0	-
Time	Pesticide mix - Dark control: Imidacloprid					
0	1.0000	1.0000	1.0000	1.0000	0.0	0.0

Eq	0.9869	0.9828	0.9730	0.9809	0.7	0.7
5	0.9794	0.9691	0.9765	0.9750	0.5	0.5
15	0.9684	0.9812	0.9796	0.9764	0.7	0.7
30	0.9583	0.9696	0.9389	0.9556	1.6	1.6
45	0.9641	0.9509	0.9385	0.9512	1.3	1.3
60	0.9603	0.9718	0.9481	0.9600	1.2	1.2
240	0.8929	0.8493	0.8949	0.8790	2.6	2.9
420	0.9394	0.9006	0.9017	0.9139	2.2	2.4
1440	0.9619	0.8993	0.9574	0.9395	3.5	3.7
2880	0.9442	0.9430	0.9175	0.9349	1.5	1.6
Time	Pesticide mix - Light control: Imidacloprid					
0	1.0000	1.0000	1.0000	1.0000	0.0	0.0
Eq	0.9995	1.0016	0.9924	0.9978	0.5	0.5
5	1.0002	0.9963	1.0029	0.9998	0.3	0.3
15	0.9994	1.0008	0.9952	0.9985	0.3	0.3
30	0.9998	0.9989	0.9980	0.9989	0.1	0.1
45	0.9994	0.9889	0.9963	0.9949	0.5	0.5
60	0.9987	0.9999	0.9961	0.9982	0.2	0.2
240	0.9947	0.9831	0.9951	0.9910	0.7	0.7
420	0.9812	0.9886	0.9885	0.9861	0.4	0.4
1440	0.9615	0.9410	0.9594	0.9540	1.1	1.2
2880	0.8958	0.8221	0.8714	0.8631	3.8	4.3
Time	Pesticide mix - Treatment: Thiacloprid					
0	1.0000	1.0000	1.0000	1.0000	0.0	0.0
Eq	0.9703	0.9676	0.9695	0.9691	0.1	0.1
5	0.9345	0.9334	0.9137	0.9272	1.2	1.3
15	0.9230	0.9198	0.9220	0.9216	0.2	0.2
30	0.8724	0.8323	0.8584	0.8543	2.0	2.4
45	0.8525	0.7845	0.7906	0.8092	3.8	4.7
60	0.7915	0.7541	0.7753	0.7736	1.9	2.4
240	0.4693	0.3489	0.4763	0.4315	7.2	16.6
420	0.2605	0.2267	0.2548	0.2473	1.8	7.3
1440	0.0000	0.0000	0.0000	0.0000	0.0	-
2880	0.0000	0.0000	0.0000	0.0000	0.0	-
Time	Pesticide mix - Dark control: Thiacloprid					
0	1.0000	1.0000	1.0000	1.0000	0.0	0.0
Eq	0.9999	0.9854	0.9887	0.9913	0.8	0.8
5	0.9954	0.9597	0.9498	0.9683	2.4	2.5
15	0.9974	0.9618	0.9682	0.9758	1.9	1.9
30	0.9724	0.9758	0.9757	0.9746	0.2	0.2
45	0.9790	0.9729	0.9592	0.9704	1.0	1.0
60	0.9384	0.9320	0.9240	0.9315	0.7	0.8
240	0.9635	0.9512	0.8986	0.9378	3.4	3.7
420	0.9452	0.9337	0.9456	0.9415	0.7	0.7
1440	0.9375	0.9424	0.9132	0.9310	1.6	1.7
2880	0.9246	0.9076	0.9143	0.9155	0.9	0.9
Time	Pesticide mix - Light control: Thiacloprid					
0	1.0000	1.0000	1.0000	1.0000	0.0	0.0
Eq	0.9982	1.0040	0.9924	0.9982	0.6	0.6
5	0.9920	0.9981	0.9988	0.9963	0.4	0.4

15	0.9975	0.9980	1.0011	0.9989	0.2	0.2
30	1.0017	0.9935	0.9883	0.9945	0.7	0.7
45	1.0069	1.0117	1.0076	1.0087	0.3	0.3
60	1.0107	1.0112	1.0006	1.0075	0.6	0.6
240	1.0069	1.0030	1.0092	1.0064	0.3	0.3
420	1.0051	1.0120	1.0103	1.0091	0.4	0.4
1440	0.9741	0.9922	0.9984	0.9882	1.3	1.3
2880	0.9235	0.9344	0.9571	0.9384	1.7	1.8
Time	Pesticide mix - Treatment: Thiamethoxam					
0	1.0000	1.0000	1.0000	1.0000	0.0	0.0
Eq	0.9208	0.9062	0.9192	0.9154	0.8	0.9
5	0.8559	0.8761	0.8015	0.8445	3.9	4.6
15	0.7694	0.7125	0.7579	0.7466	3.0	4.0
30	0.6374	0.6316	0.6491	0.6393	0.9	1.4
45	0.6232	0.5778	0.5089	0.5699	5.8	10.1
60	0.5180	0.4012	0.4617	0.4603	5.8	12.7
240	0.1240	0.1113	0.0633	0.0995	3.2	32.2
420	0.0000	0.0000	0.0000	0.0000	0.0	-
1440	0.0000	0.0000	0.0000	0.0000	0.0	-
2880	0.0000	0.0000	0.0000	0.0000	0.0	-
Time	Pesticide mix - Dark control: Thiamethoxam					
0	1.0000	1.0000	1.0000	1.0000	0.0	0.0
Eq	0.9146	0.8988	0.9178	0.9104	1.0	1.1
5	0.9117	0.9215	0.9298	0.9210	0.9	1.0
15	0.8939	0.8513	0.8682	0.8711	2.1	2.5
30	0.8259	0.8465	0.8171	0.8298	1.5	1.8
45	0.8380	0.8126	0.7971	0.8159	2.1	2.5
60	0.8373	0.8033	0.8648	0.8351	3.1	3.7
240	0.7143	0.6717	0.6642	0.6834	2.7	4.0
420	0.6646	0.6312	0.6522	0.6493	1.7	2.6
1440	0.3655	0.3602	0.4139	0.3799	3.0	7.8
2880	0.4926	0.4543	0.4925	0.4798	2.2	4.6
Time	Pesticide mix - Light control: Thiamethoxam					
0	1.0000	1.0000	1.0000	1.0000	0.0	0.0
Eq	1.0019	0.9982	1.0001	1.0001	0.2	0.2
5	1.0011	0.9970	1.0040	1.0007	0.4	0.4
15	1.0010	0.9976	1.0043	1.0010	0.3	0.3
30	0.9972	1.0054	1.0003	1.0010	0.4	0.4
45	1.0094	1.0031	1.0084	1.0070	0.3	0.3
60	1.0101	1.0019	1.0060	1.0060	0.4	0.4
240	1.0071	0.9907	1.0015	0.9998	0.8	0.8
420	0.9907	0.9960	1.0033	0.9966	0.6	0.6
1440	0.9937	0.9506	0.9936	0.9793	2.5	2.5
2880	0.9692	0.8516	0.9090	0.9099	5.9	6.5
Time	Pesticide mix - Treatment: Dimethoate					
0	1.0000	1.0000	1.0000	1.0000	0.0	0.0
Eq	0.9745	0.9445	0.9529	0.9573	1.5	1.6
5	0.9407	0.8778	0.9143	0.9109	3.2	3.5
15	0.9140	0.8629	0.9086	0.8952	2.8	3.1
30	0.7628	0.7834	0.8489	0.7983	4.5	5.6

45	0.7944	0.7739	0.7942	0.7875	1.2	1.5
60	0.8036	0.7614	0.7050	0.7566	4.9	6.5
240	0.2831	0.3049	0.3305	0.3061	2.4	7.8
420	0.2257	0.2127	0.2559	0.2314	2.2	9.6
1440	0.0000	0.0000	0.0000	0.0000	0.0	-
2880	0.0000	0.0000	0.0000	0.0000	0.0	-
Time	Pesticide mix - Dark control: Dimethoate					
0	1.0000	1.0000	1.0000	1.0000	0.0	0.0
Eq	0.9653	0.9306	0.9526	0.9495	1.8	1.8
5	0.9497	0.9446	0.9450	0.9464	0.3	0.3
15	0.9173	0.8974	0.9223	0.9124	1.3	1.4
30	0.9220	0.8966	0.8920	0.9035	1.6	1.8
45	0.8801	0.8783	0.8473	0.8685	1.8	2.1
60	0.8773	0.8378	0.7510	0.8220	6.5	7.9
240	0.6492	0.6105	0.6694	0.6430	3.0	4.7
420	0.6105	0.6573	0.7897	0.6858	9.3	13.5
1440	0.4287	0.5216	0.5064	0.4856	5.0	10.3
2880	0.4184	0.3858	0.4136	0.4059	1.8	4.3
Time	Pesticide mix - Light control: Dimethoate					
0	1.0000	1.0000	1.0000	1.0000	0.0	0.0
Eq	0.9868	1.0199	0.9857	0.9975	1.9	1.9
5	0.9632	1.0020	1.0047	0.9900	2.3	2.3
15	0.9817	1.0246	0.9802	0.9955	2.5	2.5
30	1.0059	1.0060	1.0030	1.0050	0.2	0.2
45	1.0117	0.9704	0.9703	0.9841	2.4	2.4
60	1.0140	0.9495	0.9312	0.9649	4.4	4.5
240	0.9961	1.0003	0.9624	0.9863	2.1	2.1
420	0.9786	1.0443	1.0367	1.0199	3.6	3.5
1440	1.0085	1.0155	1.0159	1.0133	0.4	0.4
2880	0.9564	0.9103	0.9428	0.9365	2.4	2.5
Time	Pesticide mix - Treatment: Diuron					
0	1.0000	1.0000	1.0000	1.0000	0.0	0.0
Eq	0.9479	0.9294	0.9648	0.9474	1.8	1.9
5	0.7252	0.6963	0.7524	0.7246	2.8	3.9
15	0.5184	0.4961	0.5623	0.5256	3.4	6.4
30	0.4421	0.3435	0.4319	0.4058	5.4	13.4
45	0.2821	0.3048	0.3251	0.3040	2.2	7.1
60	0.2444	0.2132	0.2364	0.2313	1.6	7.0
240	0.0000	0.0000	0.0000	0.0000	0.0	-
420	0.0000	0.0000	0.0000	0.0000	0.0	-
1440	0.0000	0.0000	0.0000	0.0000	0.0	-
2880	0.0000	0.0000	0.0000	0.0000	0.0	-
Time	Pesticide mix - Dark control: Diuron					
0	1.0000	1.0000	1.0000	1.0000	0.0	0.0
Eq	0.9080	0.9328	0.9579	0.9329	2.5	2.7
5	0.9050	0.8844	0.9049	0.8981	1.2	1.3
15	0.9271	0.9031	0.9148	0.9150	1.2	1.3
30	0.9270	0.9366	0.8882	0.9172	2.6	2.8
45	0.8900	0.8913	0.9026	0.8946	0.7	0.8
60	0.9257	0.8979	0.8925	0.9054	1.8	2.0

240	0.9313	0.8938	0.8966	0.9073	2.1	2.3
420	0.9254	0.9046	0.9117	0.9139	1.1	1.2
1440	0.9221	0.8943	0.9054	0.9072	1.4	1.5
2880	0.9101	0.9091	0.8884	0.9025	1.2	1.4
Time	Pesticide mix - Light control: Diuron					
0	1.0000	1.0000	1.0000	1.0000	0.0	0.0
Eq	1.0150	0.9864	0.9977	0.9997	1.4	1.4
5	1.0132	0.9818	1.0022	0.9991	1.6	1.6
15	1.0150	0.9929	0.9989	1.0023	1.1	1.1
30	1.0154	0.9908	0.9916	0.9993	1.4	1.4
45	1.0237	0.9818	1.0045	1.0033	2.1	2.1
60	1.0198	0.9864	0.9976	1.0013	1.7	1.7
240	1.0275	0.9850	1.0093	1.0073	2.1	2.1
420	1.0117	0.9924	1.0208	1.0083	1.5	1.4
1440	1.0300	0.9758	1.0601	1.0220	4.3	4.2
2880	1.0095	0.9150	1.1025	1.0090	9.4	9.3
Time	Pesticide mix - Treatment: 2,4-D					
0	1.0000	1.0000	1.0000	1.0000	0.0	0.0
Eq	0.9680	0.8887	0.9552	0.9373	4.3	4.5
5	0.9372	0.8914	0.8270	0.8852	5.5	6.3
15	0.8789	0.7728	0.8101	0.8206	5.4	6.6
30	0.8039	0.7115	0.6918	0.7357	6.0	8.1
45	0.5797	0.5892	0.5241	0.5644	3.5	6.2
60	0.4432	0.4235	0.4737	0.4468	2.5	5.7
240	0.0000	0.0000	0.0000	0.0000	0.0	-
420	0.0000	0.0000	0.0000	0.0000	0.0	-
1440	0.0000	0.0000	0.0000	0.0000	0.0	-
2880	0.0000	0.0000	0.0000	0.0000	0.0	-
Time	Pesticide mix - Dark control: 2,4-D					
0	1.0000	1.0000	1.0000	1.0000	0.0	0.0
Eq	0.9834	0.9786	0.9841	0.9820	0.3	0.3
5	1.0112	0.9899	0.9947	0.9986	1.1	1.1
15	0.9768	0.9316	0.9458	0.9514	2.3	2.4
30	0.9629	0.9661	0.9379	0.9557	1.5	1.6
45	0.9010	0.9640	0.9228	0.9293	3.2	3.4
60	0.9497	0.9742	0.9370	0.9536	1.9	2.0
240	0.9236	0.9539	0.9065	0.9280	2.4	2.6
420	0.8630	0.8932	0.8618	0.8727	1.8	2.0
1440	0.9436	0.9059	0.8572	0.9022	4.3	4.8
2880	0.9396	0.9496	0.8399	0.9097	6.1	6.7
Time	Pesticide mix - Light control: 2,4-D					
0	1	1	1	1.0000	0.0	0.0
Eq	0.9942392	1.0029168	0.9907252	0.9960	0.6	0.6
5	0.9998989	1.0054266	0.9988533	1.0014	0.4	0.4
15	0.9946771	1.0042735	1.0042833	1.0011	0.6	0.6
30	1.000977	1.0087844	1.0015514	1.0038	0.4	0.4
45	1.0148569	1.0103106	1.0015851	1.0089	0.7	0.7
60	1.0158675	0.995523	0.9977403	1.0030	1.1	1.1
240	1.0144189	0.992301	0.9908264	0.9992	1.3	1.3
420	1.0108142	1.0027472	0.9743678	0.9960	1.9	1.9

1440	0.9982819	1.0088183	0.9880271	0.9984	1.0	1.0
2880	0.9617966	0.9224671	0.9337948	0.9394	2.0	2.2
Time	Pesticide mix - Treatment: Atrazine					
0	1.0000	1.0000	1.0000	1.0000	0.0	0.0
Eq	0.9439	0.9662	0.9852	0.9651	2.1	2.1
5	0.9213	0.9345	0.9481	0.9346	1.3	1.4
15	0.9202	0.8694	0.8750	0.8882	2.8	3.1
30	0.8360	0.8444	0.8233	0.8345	1.1	1.3
45	0.7793	0.7678	0.7901	0.7791	1.1	1.4
60	0.7165	0.7035	0.7569	0.7256	2.8	3.8
240	0.0950	0.1003	0.1579	0.1177	3.5	29.6
420	0.0330	0.0262	0.0287	0.0293	0.3	11.6
1440	0.0000	0.0000	0.0000	0.0000	0.0	-
2880	0.0000	0.0000	0.0000	0.0000	0.0	-
Time	Pesticide mix - Dark control: Atrazine					
0	1.0000	1.0000	1.0000	1.0000	0.0	0.0
Eq	0.9467	0.9439	0.9607	0.9505	0.9	0.9
5	0.9353	0.9480	0.9507	0.9447	0.8	0.9
15	0.9326	0.9504	0.9389	0.9406	0.9	1.0
30	0.9159	0.9374	0.9558	0.9364	2.0	2.1
45	0.9491	0.9594	0.9318	0.9468	1.4	1.5
60	0.9359	0.9540	0.9529	0.9476	1.0	1.1
240	0.9567	0.9426	0.9204	0.9399	1.8	2.0
420	0.9133	0.9109	0.9166	0.9136	0.3	0.3
1440	0.9062	0.9398	0.9402	0.9288	2.0	2.1
2880	0.9080	0.9030	0.9091	0.9067	0.3	0.4
Time	Pesticide mix - Light control: Atrazine					
0	1.0000	1.0000	1.0000	1.0000	0.0	0.0
Eq	0.9971	0.9967	0.9855	0.9931	0.7	0.7
5	1.0040	1.0004	1.0059	1.0034	0.3	0.3
15	1.0035	0.9927	0.9975	0.9979	0.5	0.5
30	1.0000	0.9903	0.9961	0.9955	0.5	0.5
45	1.0062	0.9946	0.9978	0.9995	0.6	0.6
60	0.9932	0.9928	0.9907	0.9923	0.1	0.1
240	1.0015	0.9813	0.9971	0.9933	1.1	1.1
420	0.9850	1.0024	0.9961	0.9945	0.9	0.9
1440	1.0286	0.9918	1.0006	1.0070	1.9	1.9
2880	1.0427	0.9765	1.0054	1.0082	3.3	3.3
Time	Reusability: cycle 1					
0	1.0000	1.0000	1.0000	1.0000	0.0	0.0
Eq	0.9852	0.9282	0.9743	0.9626	3.0	3.1
5	0.8770	0.8943	0.8915	0.8876	0.9	1.0
15	0.8503	0.8041	0.8122	0.8222	2.5	3.0
30	0.7882	0.7558	0.7618	0.7686	1.7	2.2
45	0.7383	0.7292	0.7175	0.7283	1.0	1.4
60	0.7001	0.6660	0.6114	0.6592	4.5	6.8
240	0.3503	0.3180	0.3083	0.3255	2.2	6.8
420	0.1438	0.1031	0.0787	0.1085	3.3	30.3
1440	0.0007	0.0007	0.0007	0.0007	0.0	0.1
Time	Reusability: cycle 2					

0	1.0000	1.0000	1.0000	1.0000	0.0	0.0
Eq	0.9906	0.9915	0.9980	0.9934	0.4	0.4
5	0.9413	0.9338	0.9594	0.9448	1.3	1.4
15	0.9090	0.8857	0.8997	0.8981	1.2	1.3
30	0.8512	0.8233	0.8503	0.8416	1.6	1.9
45	0.7988	0.7540	0.7653	0.7727	2.3	3.0
60	0.7434	0.6973	0.6970	0.7126	2.7	3.7
240	0.2327	0.1452	0.1317	0.1699	5.5	32.3
420	0.0006	0.0006	0.0006	0.0006	0.0	0.2
1440	0.0006	0.0006	0.0006	0.0006	0.0	0.2
Time	Reusability: cycle 3					
0	1.0000	1.0000	1.0000	1.0000	0.0	0.0
Eq	0.9949	0.9792	0.9890	0.9877	0.8	0.8
5	0.9787	0.9592	0.9750	0.9710	1.0	1.1
15	0.9432	0.9212	0.9299	0.9314	1.1	1.2
30	0.9121	0.8948	0.9046	0.9038	0.9	1.0
45	0.8903	0.8682	0.8530	0.8705	1.9	2.2
60	0.8433	0.8242	0.8236	0.8304	1.1	1.3
240	0.5418	0.4722	0.5040	0.5060	3.5	6.9
420	0.0644	0.1714	0.2297	0.1552	8.4	54.1
1440	0.0007	0.0006	0.0006	0.0006	0.0	0.6
Time	Reusability: cycle 4					
0	1.0000	1.0000	1.0000	1.0000	0.0	0.0
Eq	0.9929	0.9768	0.9877	0.9858	0.8	0.8
5	0.9901	0.9617	0.9746	0.9755	1.4	1.5
15	0.9499	0.9071	0.9404	0.9325	2.2	2.4
30	0.9167	0.8972	0.9138	0.9092	1.1	1.2
45	0.9085	0.8768	0.8983	0.8945	1.6	1.8
60	0.8873	0.8230	0.8892	0.8665	3.8	4.3
240	0.6264	0.6238	0.6219	0.6241	0.2	0.4
420	0.4328	0.4313	0.4227	0.4289	0.5	1.3
1440	0.0010	0.0007	0.0011	0.0009	0.0	26.0
Time	Reusability: cycle 5					
0	1.0000	1.0000	1.0000	1.0000	0.0	0.0
Eq	0.9636	0.9775	0.9950	0.9787	1.6	1.6
5	0.9654	0.9777	0.9867	0.9766	1.1	1.1
15	0.9519	0.9517	0.9554	0.9530	0.2	0.2
30	0.9243	0.9111	0.9362	0.9239	1.3	1.4
45	0.8693	0.9009	0.8893	0.8865	1.6	1.8
60	0.8595	0.8726	0.8666	0.8662	0.7	0.8
240	0.6655	0.6379	0.6553	0.6529	1.4	2.1
420	0.4964	0.4843	0.4905	0.4904	0.6	1.2
1440	0.0437	0.0385	0.0291	0.0371	0.7	19.9

Table A4.2: Two-way ANOVA comparing the results of the concentration of diuron exposed to photocatalytic treatment (UV-A LED irradiation and g-C₃N₄ coated beads) at different initial solution pH (pH 2, 5, 8 and 10). The significance level was 0.05. The color red represents p<0.05, treatments are significantly different from each other. *Not applicable as compared treatments demonstrated diuron concentration equal to 0.

	pH 2 vs. pH 5	pH 2 vs. pH 8	pH 2 vs. pH 10	pH 5 vs. pH 8	pH 5 vs. pH 10	pH 8 vs. pH 10
Time (hours)	g-C ₃ N ₄ coated beads and UV-A LEDs					
Eq	0.9038	0.8018	0.7208	0.9880	0.9484	0.9992
0.083	0.0159	0.9941	0.5255	0.0184	0.0438	0.5633
0.25	0.0251	0.3144	0.7608	0.0145	0.0071	0.5708
0.50	0.0423	0.1256	0.3374	0.0277	0.0361	0.4923
0.75	0.0366	0.1317	0.1419	0.0292	0.0299	0.9961
1	0.0174	0.0928	0.1608	0.0198	0.0101	0.5566
4	0.0778	0.0294	0.3919	0.0024	0.0538	0.2788
7	0.1353	0.6683	0.9506	0.2304	0.4248	0.5568
24	0.4061	0.4061	0.4061	*	*	*

Table A4.2: Two-way ANOVA comparing the results of the concentration of diuron exposed to photocatalytic treatment (UV-A LED irradiation and g-C₃N₄ coated beads) using different catalyst load (0.14% – 0.70% w/v g-C₃N₄). The significance level was 0.05. The color red represents p<0.05, treatments are significantly different from each other. *Not applicable as compared treatments demonstrated diuron concentration equal to 0.

	0.14% vs. 0.28%	0.14% vs. 0.42%	0.14% vs. 0.56%	0.14% vs. 0.70%	0.28% vs. 0.42%	0.28% vs. 0.56%	0.28% vs. 0.70%	0.42% vs. 0.56%	0.42% vs. 0.70%	0.56% vs. 0.70%
Time (hours)	solution at pH 5 and phosphate buffer									
Eq	0.3005	0.5214	0.4585	0.0216	0.9889	0.7350	0.9373	0.9617	>0.9999	0.7848
0.083	0.4238	0.4929	0.9935	0.9493	0.9663	0.7194	0.9317	0.8251	0.9844	0.9967
0.25	0.0321	0.0409	0.2995	0.6140	0.9979	0.1925	0.2855	0.2404	0.2753	0.9948
0.50	0.1632	0.0333	0.4231	>0.9999	>0.9999	0.5177	0.1901	0.3077	0.1016	0.6245
0.75	0.0371	0.0378	0.3832	0.1666	0.9978	0.1098	0.2505	0.0170	0.0435	0.3180
1	0.0152	0.0181	0.0334	0.0374	0.9936	0.1705	0.1580	0.2368	0.2114	0.9993
4	0.0607	0.0100	0.0099	0.0005	0.9584	0.9430	0.9967	0.4304	0.5731	0.8894
7	0.1951	0.2045	0.1951	0.1951	0.8410	*	*	0.8410	0.8410	*
24	*	*	*	*	*	*	*	*	*	*

Table A4.3: Two-way ANOVA comparing the results of the concentration of diuron exposed to five successive photocatalytic treatment cycles (UV-A LED irradiation and g-C₃N₄ coated beads) over 24 hours. The significance level was 0.05. The color red represents p<0.05, treatments are significantly different from each other.

	cycle 1 vs. cycle 2	cycle 1 vs. cycle 3	cycle 1 vs. cycle 4	cycle 1 vs. cycle 5	cycle 2 vs. cycle 3	cycle 2 vs. cycle 4	cycle 2 vs. cycle 5	cycle 3 vs. cycle 4	cycle 3 vs. cycle 5	cycle 4 vs. cycle 5
Time (hours)	Reusability									
Eq	0.5522	0.6799	0.7255	0.9097	0.8036	0.6565	0.6106	0.9977	0.8840	0.9446
0.083	0.0216	0.0024	0.0072	0.0021	0.2183	0.2060	0.1363	0.9889	0.9569	>0.9999
0.25	0.0697	0.0284	0.0215	0.0344	0.0996	0.3270	0.0405	>0.9999	0.2177	0.6127
0.50	0.0264	0.0052	0.0032	0.0017	0.0336	0.0233	0.0116	0.9485	0.3258	0.5896
0.75	0.2120	0.0047	0.0013	0.0015	0.0244	0.0118	0.0149	0.5297	0.7893	0.9662
1	0.5029	0.0560	0.0178	0.0428	0.0305	0.0263	0.0234	0.5988	0.0581	>0.9999
4	0.0911	0.0131	0.0054	0.0005	0.0076	0.0148	0.0091	0.0828	0.0355	0.1965
7	0.0888	0.8813	0.0093	0.0065	0.2446	<0.0001	<0.0001	0.0887	0.0602	0.0010
24	0.1598	0.9656	0.4742	0.0408	0.8980	0.4674	0.0408	0.4715	0.0408	0.0413